University of Alberta
Department of Civil &
Environmental Engineering

Structural Engineering Report No. 224

Behaviour of Large Diameter Line Pipe Under Combined Loads

by

Patrick R, DelCol

Gilbert Y. Grondin

Roger J.J. Cheng

and

D.W. Murray

September, 1998

Behaviour of Large Diameter Line Pipe Under Combined Loads

by

Patrick R. DelCol

Gilbert Y. Grondin

Roger J.J. Cheng

David W. Murray

Structural Engineering Report 224

Department of Civil and Environmental Engineering
University of Alberta
Edmonton, Alberta

September 1998

ABSTRACT

Experimental testing of four full-size pipes with diameter (762 mm) to thickness (8.3 mm) ratio of 92 was conducted to investigate the behaviour of pipelines deformed into the post-buckling range under combinations of internal pressure, axial compression and imposed curvature. The specimens were subjected to internal pressure causing hoop stresses of 0, 20, 40 and 80 percent of the yield strength of the pipe material to determine the effect of the local buckling mode. The non-pressurized specimen failed in a "diamond shape" mode whereas the pressurized pipes failed in a single "outward bulge" mode. Increased internal pressure was found to lower the buckling moment but stabilize the post-buckling behaviour.

Non-linear finite element models of the tests were developed using ABAQUS software incorporating measured initial imperfections and material properties. Good correlation between the analytical and test results was observed. An analytical study of initial imperfections concluded that increased magnitude of imperfection causes a significant reduction in peak moment and buckling curvature.

ACKNOWLEDGEMENTS

Financial support for this project was provided by the Natural Sciences and Engineering Research Council of Canada. The test specimens were donated by Nova Corporation.

TABLE OF CONTENTS

1. INTRODUCTION 1

1.1 PIPELINE RESEARCH 2

1.1.1 Current Research 2

1.1.2 Research at the University of Alberta 5

1.2 OBJECTIVES OF RESEARCH 6

2. EXPERIMENTAL INVESTIGATION 8

2.1 SCOPE 8

2.2 SPECIMENS 8

2.3 TEST PARAMETERS 9

2.3.1 Axial Compression 9

2.3.2 Internal Pressure 10

2.3.3 Monotonically Increasing Curvature 11

2.4 TEST SET-UP 12

2.5 TEST PROCEDURE 13

2.5.1 Assembly and Alignment Procedures 13

2.5.2 Control of Tests 13

2.5.3 Expected Failure Values as Calculated by Mohareb and Murray Equation (1994) 16

2.6 INSTRUMENTATION 17

2.6.1 Electrical Resistance Strain Gauges 17

2.6.2 Demec Gauges 18

2.6.3 Rotation Meters 18

2.6.4 Linear Variable Differential Transformers (LVDT's) 18

2.6.5 Change in Diameter Measurements 18

2.6.6 Loads 19

2.7 ANCILLARY TESTS 19

2.7.1 Determination of Material Properties 19

2.7.2 Measurement of Initial Imperfections 20

3. RESULTS OF EXPERIMENTAL INVESTIGATION 31

3.1 INTRODUCTION 31
3.2 MATERIAL PROPERTIES 31
3.3 MEASURED INITIAL IMPERFECTIONS 32
3.4 MOMENT VERSUS CURVATURE RELATIONSHIP 33
3.4.1 Calculation of Moment 34
3.4.2 Calculation of Curvature 36
3.5 RESULTS FROM EXPERIMENTS 38
3.5.1 Results from Specimen C45P00 38
3.5.1.1 C45P00 – Moment Versus Curvature 38
3.5.1.2 C45P00 - Deformations 39
3.5.1.3 C45P00 - Strains 41
3.5.2 Results from Specimen C45P20 43
3.5.2.1 C45P20 – Moment Versus Curvature 43
3.5.2.3 C45P20 – Deformations 44
3.5.2.3 C45P20 - Strains 45
3.5.3 Results from Specimen C45P40 46
3.5.3.1 C45P40 – Moment Versus Curvature 47
3.5.3.2 C45P40 - Deformations 47
3.5.3.3 C45P40 - Strains 48
3.5.4 Results from Specimen C45P80 49
3.5.4.1 C45P80 – Moment Versus Curvature 50
3.5.4.2 C45P80 - Deformations 50
3.5.4.3 C45P80 - Strains 51
3.5.5 General Results 52

4. FINITE ELEMENT ANALYSIS 104
4.1 MODELLING OF TEST SPECIMENS 104
4.1.1 Symmetry of Model 104
4.1.2 Boundary Conditions 105
4.1.3 Residual Stresses 106
4.1.4 Material Properties 106
4.1.5 Loading 107
4.2 FINITE ELEMENT MESH SIZE STUDY 107

4.2.1 Results and Discussion of Mesh Size Study 108
4.3 INITIAL IMPERFECTIONS 109
4.3.1 Study of Model Sensitivity to Initial Imperfections 109
4.3.2 Pattern of Assumed Initial Imperfections 109
4.3.3 Analysis of Initial Imperfections 110
4.3.4 Measured Initial Imperfections 112

5. PREDICTION OF TEST RESULTS 128
5.1 FINITE ELEMENT ANALYSIS 128
5.1.1 Moment versus Curvature Relationship 128
5.1.2 Post-Buckling Configuration 130
5.1.3 Critical Strains 133
5.1.4 Change in Diameter 134
5.1.5 Compression Face Deformations 137
5.2 PREDICTION USING THE PLASTIC EQUATION BY MOHAREB AND MURRAY (1994) 139
5.3 IMPROVEMENTS TO THE ANALYTICAL MODEL 139
5.3.1 Sensitivity Analysis of the Model 141

6. CONCLUSIONS AND RECOMMENDATIONS 167
6.1 CONCLUSIONS 167
6.2 RECOMMENDATIONS 170

REFERENCES

LIST OF TABLES

Table 2.1 Experimental Parameters and Predicted Values 22

Table 3.1 Measured Static Engineering Material Properties from Tension Coupon Tests 54

Table 3.2 Magnitude of Measured Initial Imperfections 54

Table 3.3 Summary of Experimental Results 55

Table 4.1 Piecewise Material Property Definition Used in Finite Element Analysis 113

Table 5.1 Comparison of Experimental and Predicted Values for Peak Moment and Limit Point Curvature 144

Table 5.2 Critical Compressive Local Strains ($\mu\varepsilon$) 144

Table 5.3 Experimental and Predicted Peak Moment 145

Table 5.4 Sensitivity of Model for Specimen C45P00 145

LIST OF FIGURES

Figure 2.1 Diagram of Test Set-Up 23

Figure 2.2 Curved roller bearing 24

Figure 2.3 End Collar 24

Figure 2.4 Top loading arm in inverted position 25

Figure 2.5 Lifting the top loading arm and test specimen assembly 26

Figure 2.6 LVDT's used for measurement of compression face displacements 27

Figure 2.7 Gauge used to measure changes in diameter 28

Figure 2.8 Device to measure initial imperfections (showing carriage with LVDT) 29

Figure 2.9 Initial imperfection measurement apparatus inside test specimen 30

Figure 3.1 Static engineering material properties from tension coupon tests 56

Figure 3.2 Elastic and first yield static engineering material properties from tension coupon tests 56

Figure 3.3 Measured initial imperfection pattern for specimen C45P00 57

Figure 3.4 Measured initial imperfection pattern for specimen C45P20 57

Figure 3.5 Measured initial imperfection pattern for specimen C45P40 58

Figure 3.6 Measured initial imperfection pattern for specimen C45P80 58

Figure 3.7 Free body diagram of top loading arm for calculation of top end moment 59

Figure 3.8 Free body diagram used for calculation of moment at the top end of segment D 60

Figure 3.9 Symmetric cross-section distortion 61

Figure 3.10 Pipe segment of length D used to define local curvature 61

Figure 3.11 C45P00 – Global moment and axial load versus curvature diagram 62

Figure 3.12 C45P00 – Comparison of global and local moment versus curvature 62

Figure 3.13 C45P00 – Buckled configuration, compression face 63

Figure 3.14 C45P00 – Buckled configuration, profile 63

Figure 3.15 C45P00 – Compression face displacements: initial loading stage 64

Figure 3.16 C45P00 – Compression face displacements 64

Figure 3.17 C45P00 – Progression of compression face displacements 65

Figure 3.18 C45P00 – Measured changes in diameter 66

Figure 3.19 C45P00 – Compression face strain gauge measurements: initial loading stage 67

Figure 3.20 C45P00 – Compression face strain gauge measurements: pre- and post-buckling 67
Figure 3.21 C45P00 – Tension face strain gauge measurements: initial loading stage 68
Figure 3.22 C45P00 – Tension face strain gauge measurements: pre- and post-buckling 68
Figure 3.23 C45P00 – Compression face Demec measurements: initial loading stage.... 69
Figure 3.24 C45P00 – Compression face Demec measurements: pre- and post-buckling 69
Figure 3.25 C45P00 – Tension face Demec measurements: initial loading stage 70
Figure 3.26 C45P00 – Tension face Demec measurements: pre- and post-buckling 70
Figure 3.27 C45P00 – Determination of critical longitudinal compressive strain 71
Figure 3.28 C45P20 – Global moment, axial load and pressure versus curvature diagram 72
Figure 3.29 C45P20 – Comparison of global and local moment versus curvature 72
Figure 3.30 C45P20 – Buckled configuration, compression face 73
Figure 3.31 C45P20 – Buckled configuration, profile 73
Figure 3.32 C45P20 – Compression face displacements: initial loading stage 74
Figure 3.33 C45P20 – Compression face displacements 74
Figure 3.34 C45P20 – Progression of compression face displacements 75
Figure 3.35 C45P20 – Measured changes in diameter 76
Figure 3.36 C45P20 – Compression face strain gauge measurements: initial loading stage 77
Figure 3.37 C45P20 – Compression face strain gauge measurements: pre- and post-buckling 77
Figure 3.38 C45P20 – Tension face strain gauge measurements: initial loading stage.... 78
Figure 3.39 C45P20 – Tension face strain gauge measurements: pre- and post-buckling 78
Figure 3.40 C45P20 – Compression face Demec measurements: initial loading stage 79
Figure 3.41 C45P20 – Compression face Demec measurements: pre- and post-buckling 79
Figure 3.42 C45P20 – Tension face Demec measurements: initial loading stage 80
Figure 3.43 C45P20 – Tension face Demec measurements: pre- and post-buckling 80

Figure 3.44 C45P20 – Determination of critical longitudinal compressive strain 81
Figure 3.45 C45P40 – Global moment, axial load and pressure versus curvature diagram 82
Figure 3.46 C45P40 – Comparison of global and local moment versus curvature 82
Figure 3.47 C45P40 – Buckled configuration, compression face 83
Figure 3.48 C45P40 – Buckled configuration, profile.....83
Figure 3.49 C45P40 – Compression face displacements: initial loading stage 84
Figure 3.50 C45P40 – Compression face displacements.....84
Figure 3.51 C45P40 – Progression of compression face displacements 85
Figure 3.52 C45P40 – Measured changes in diameter 86
Figure 3.53 C45P40 – Compression face strain gauge measurements: initial loading stage.....87
Figure 3.54 C45P40 – Compression face strain gauge measurements: pre- and post-buckling 87
Figure 3.55 C45P40 – Tension face strain gauge measurements: initial loading stage.....88
Figure 3.56 C45P40 – Tension face strain gauge measurements: pre- and post-buckling 88
Figure 3.57 C45P40 – Compression face Demec measurements: initial loading stage.....89
Figure 3.58 C45P40 – Compression face Demec measurements: pre- and post-buckling 89
Figure 3.59 C45P40 – Tension face Demec measurements: initial loading stage.....90
Figure 3.60 C45P40 – Tension face Demec measurements: pre- and post-buckling 90
Figure 3.61 C45P40 – Determination of critical longitudinal compressive strain 91
Figure 3.62 C45P80 – Global moment, axial load and pressure versus curvature diagram 92
Figure 3.63 C45P80 – Comparison of global and local moment versus curvature 92
Figure 3.64 C45P80 – Buckled configuration, compression face 93
Figure 3.65 C45P80 – Buckled configuration, profile.....93
Figure 3.66 C45P80 – Compression face displacements: initial loading stage 94
Figure 3.67 C45P80 – Compression face displacements.....94
Figure 3.68 C45P80 – Progression of compression face displacements 95
Figure 3.69 C45P80 – Measured changes in diameter 96

Figure 3.70 C45P80 – Compression face strain gauge measurements: initial loading stage 97
Figure 3.71 C45P80 – Compression face strain gauge measurements: pre- and post-buckling 97
Figure 3.72 C45P80 – Tension face strain gauge measurements: initial loading stage 98
Figure 3.73 C45P80 – Tension face strain gauge measurements: pre- and post-buckling 98
Figure 3.74 C45P80 – Compression face Demec measurements: initial loading stage 99
Figure 3.75 C45P80 – Compression face Demec measurements: pre- and post-buckling 99
Figure 3.76 C45P80 – Tension face Demec measurements: initial loading stage 100
Figure 3.77 C45P80 – Tension face Demec measurements: pre- and post-buckling 100
Figure 3.78 C45P80 – Determination of critical longitudinal compressive strain 101
Figure 3.79 Comparison of Global moment versus curvature for all tests 102
Figure 3.80 Peak moment as a function of internal pressure 102
Figure 3.81 Curvature at peak moment as a function of internal pressure 103
Figure 3.82 Critical longitudinal compressive strain as a function of internal pressure. 103
Figure 4.1 Material properties used in the finite element model 114
Figure 4.2 Moment versus curvature results from mesh size study 115
Figure 4.3 Buckled configuration for Grid 24x46 116
Figure 4.4 Buckled configuration for Grid 36x70 117
Figure 4.5 Buckled configuration for Grid 40x78 118
Figure 4.6 Assumed initial imperfection pattern 119
Figure 4.7 Imperfections along compression face of assumed pattern 119
Figure 4.8 Effect of initial imperfections on moment versus curvature relationship 120
Figure 4.9 Effect of magnitude of initial imperfections on moment capacity and limit point curvature 120
Figure 4.10 Buckled configuration for 100% of assumed initial imperfections 121
Figure 4.11 Buckled configuration for 50% of assumed initial imperfections 122
Figure 4.12 Buckled configuration for 10% of assumed initial imperfections 123
Figure 4.13 Mapped initial imperfection pattern for specimen C45P00 124
Figure 4.14 Mapped initial imperfections along compression face of C45P00 124

Figure 4.15 Mapped initial imperfection pattern for specimen C45P20 125
Figure 4.16 Mapped initial imperfections along compression face of C45P20 125
Figure 4.17 Mapped initial imperfection pattern for specimen C45P40 126
Figure 4.18 Mapped initial imperfections along compression face of C45P40 126
Figure 4.19 Mapped initial imperfection pattern for specimen C45P80 127
Figure 4.20 Mapped initial imperfections along compression face of C45P80 127
Figure 5.1 C45P00 – Comparison of moment versus curvature relationship 146
Figure 5.2 C45P20 – Comparison of moment versus curvature relationship 146
Figure 5.3 C45P40 – Comparison of moment versus curvature relationship 147
Figure 5.4 C45P80 – Comparison of moment versus curvature relationship 147
Figure 5.5 Predicted buckled configuration for specimen C45P00 148
Figure 5.6 Comparison of analytical and experimental configurations for specimen C45P00 148
Figure 5.7 Predicted buckled configuration for specimen C45P20 149
Figure 5.8 Comparison of analytical and experimental configurations for specimen C45P20 149
Figure 5.9 Predicted elastic buckling modes for specimen C45P20 150
Figure 5.10 Predicted buckled configuration for specimen C45P40 151
Figure 5.11 Comparison of analytical and experimental configurations for specimen C45P40 151
Figure 5.12 Predicted buckled configuration for specimen C45P80 152
Figure 5.13 Comparison of analytical and experimental configurations for specimen C45P80 152
Figure 5.14 C45P00 – Determination of critical compressive strain from FEA 153
Figure 5.15 C45P20 – Determination of critical compressive strain from FEA 153
Figure 5.16 C45P40 – Determination of critical compressive strain from FEA 154
Figure 5.17 C45P80 – Determination of critical compressive strain from FEA 154
Figure 5.18 C45P00 – Change in diameter results from FEA 155
Figure 5.19 C45P00 – Maximum cross-sectional deformations 156
Figure 5.20 C45P20 – Change in diameter results from FEA 157
Figure 5.21 C45P20 – Maximum cross-sectional deformations 158
Figure 5.22 C45P40 – Change in diameter results from the FEA 159

Figure 5.23 C45P40 – Maximum cross-sectional deformations....160
Figure 5.24 C45P80 – Change in diameter results from FEA....161
Figure 5.25 C45P80 – Maximum cross-sectional deformations....162
Figure 5.26 C45P00 – Compression face displacements from finite element method...163
Figure 5.27 C45P20 – Compression face displacements from finite element method...163
Figure 5.28 C45P40 – Compression face displacements from finite element method...164
Figure 5.29 C45P80 – Compression face displacements from finite element method...164
Figure 5.30 Idealized material properties used to study model sensitivity....165
Figure 5.31 Influence of material properties and magnitude of initial imperfections on response of specimen C45P00....166
Figure 5.32 Comparison of FEA and Experimental....166

LIST OF SYMBOLS

A	cross-sectional area of specimen based on nominal dimensions
C	net axial load in pipe due to all effects
C_{pe}	axial load on pipe due to pressure acting on end plates
C_{ph}	axial load resulting from Poisson's ratio effect Poisson's ratio
C_t	axial load resulting from temperature differential
C_y	axial load causing yield in the pipe
D	nominal outside diameter of pipe
d	distance from pivot point to end of specimen
dl	increment along length of pipe
D/t	ratio of pipe diameter to wall thickness
E	Modulus of elasticity
e	eccentricity of jacks
F	eccentric jack force
F_y	yield strength of steel
i	sub or superscript variable to designate a top value, t, or a bottom value, b
LVDT	linear variable differential transformer
l_d	deformed gauge length of tension coupon
l_0	initial gauge length of tension coupon
M_p^p	plastic moment capacity reduced for circumferential stress due to internal pressure
M_P^{pC}	plastic moment capacity reduced for axial load and circumferential stress due to internal pressure
M_G	global moment
M_i	end moment
M_L	local moment
P	concentric load
p	internal pressure
p_y	pressure causing yield in hoop direction
r_{av}	average pipe radius
SMYS	specified minimum yield strength
t	pipe wall thickness

V_i	force in bracing member
α	coefficient of thermal expansion for steel
ΔT	temperature differential
ν	Poisson's ratio for steel
ε_c	compression face strain
ε_t	tension face strain
ε_e	engineering strain
ε_T	true strain
ϕ_G	global curvature
ϕ_L	local curvature
θ_i	end rotation
$\mu\varepsilon$	micro strain
σ_e	engineering stress
σ_T	true stress

1. INTRODUCTION

Recent economic activity throughout the world has prompted the search for oil and gas reserves in ever more remote regions of the globe. Exploration and development are therefore located in increasingly severe environments such as the Arctic and sub-Arctic. Development of such resources requires efficient, safe, reliable and cheap systems to transport the supply to the demand. Buried pipelines are often the preferred system for this important task. As a result, these transportation systems are subjected to increasingly severe environmental conditions. This impels an understanding of the strength and behavioural characteristics of buried pipelines to establish reasonable design procedures and limits that govern this type of structure.

Pipelines buried in Arctic and sub-Arctic regions are often subjected to combinations of internal pressure due to the fluid being transported, axial compression due to extreme temperature variations and increasing curvatures resulting from any imposed deformation of the structure from soil. These imposed deformations are typically caused by differential settlements and slope instability. Applying the concept of limit states philosophy to the design of buried pipelines requires that such limits be identified and quantified. In addition, suitable analysis tools able to reliably predict the behaviour of buried pipe with regard to the individual limit state must be made available. The governing limit states can generally be divided into two categories. The first type of limits are those that affect the integrity of the pipeline and are referred to as ultimate limit states. These include bursting of the pipeline, fracture, collapse of the cross-section and corrosion leading to catastrophic failure. The second type of limit states affect the functionality of the pipeline and are typically based on the deformations of the pipe and less on the strength. These types of limit states are generally termed serviceability limit states and include excessive local deformations and cross-section distortion but also include corrosion that requires special provisions such as a reduced level of internal pressure. Other limit states in both categories have been identified but are not discussed here since the above mentioned problem of imposed curvature typically involves large deformations and serviceability limits are likely to govern. The study of the deformational aspects of behaviour, however, also contributes to the understanding of strength limit states in that it provides the measurable limits (i.e.: critical compressive

strains) that indicate impending failure. These measurable limits are needed to establish suitable monitoring and maintenance programs for buried pipeline systems.

1.1 PIPELINE RESEARCH

The study of pipeline and cylindrical shell behaviour up to 1994 is summarized in previous work by Yoosef-Ghodsi et al. (1994), including discussions regarding the establishment of limit states, experimental programs and analytical studies. The following sections will therefore discuss the most current research pertaining to pipeline behaviour emphasizing testing and analysis of combinations of axial load, internal pressure and bending. Particular attention will be focused on the research conducted at the University of Alberta since it forms the basis for the research program presented in the following chapters.

1.1.1 Current Research

Karamanos and Tassoulas (1996a) performed a numerical investigation of the stability of tubular members subjected to external pressure and bending. A tube finite element was developed for this purpose. The formulation included large strains, large displacements, initial imperfections, and residual stresses. Pressure versus moment interaction diagrams were calculated and good agreement was obtained between a tube element solution and a shell element solution. Further analytical investigations of pipes with diameter to thickness ratios of 42 indicated that, with no external pressure, the moment carrying capacity of a segment of pipe is only slightly affected by the level of initial imperfection. Also, for members subjected to axial load and bending, residual stresses were found to only affect the behaviour of a pipe when the axial load component is greater than approximately 50 percent of the yield axial load.

Karamanos and Tassoulas (1996b) performed several experiments with tubes subjected to combinations of external pressure and bending. Tests on long tubes with a length to diameter ratio, L/D, from 18 to 25 and diameter to thickness ratios, D/t, of 63 and 42 were used to develop pressure versus moment interaction diagrams and to assess the performance of the analytical model previously described. Good agreement was obtained between the analytical and experimental results. Also, an analytical investigation of the length effects indicated that the ductility of the pipe decreases with an increase in pipe length.

Zimmerman et al. (1995) conducted a series of five full size tests subjected to combinations of internal pressure, axial tension and imposed curvature. The specimens had diameter to thickness ratios of 41 and 87 with a girth weld placed at the centre of the test region. A non-linear finite element model was then used to perform an analytical study including the effects of initial imperfections and residual stresses due to the girth weld. The imperfections were incorporated using an idealized axisymmetric imperfection of roughly the same average amplitude as those measured around the girth weld. However, it is not clear how the level of imperfection was measured experimentally. Critical strain limits were proposed and compared to existing empirical equations. The proposed limits recognise the fact that pipelines may deform plastically without impairment to the functionality of the segment.

Bruschi et al. (1995a) investigated the use of non-linear finite element methods to predict the behaviour of pipelines subjected to internal pressure, axial load and bending. ABAQUS finite element software was used to model a quarter section of a length of pipe assuming symmetry along the plane of bending and across the centreline. Also, assumed imperfections were included to trigger buckling at a desired location. The analyses were validated using previously published test results. It was concluded that the finite element method, once calibrated using experimental results, can be used as a "numerical testing laboratory" to study pipeline behaviour.

Bruschi et al. (1995b) used the finite element method to study pipeline behaviour subjected to soil movements. A case study was used to assess the effects of direction of slope movement relative to pipe axis, magnitude of displacement and soil properties on the failure modes of buried pipelines. Compressive shell failure (local wrinkling or bulging), fracture and Euler buckling were identified as possible failure modes dependant of the above factors.

Tseng et al. (1995) examined the applicability of a set of strain based performance criteria for the fitness-for-service evaluation of underground pipelines. The authors suggest failure modes that include tensile failure by fracture, compression failure by local buckling leading to cracking and leaking and large local deformations. They also propose the use of strain based criteria to avoid such failures. The finite element method was then employed to apply the criteria to a specific pipeline segment. By relating the critical

values to the curvature of the pipe a comparison with pipeline inspection data could be made.

Chiou and Chi (1996) conducted a numerical investigation of the interactions between the beam mode and shell mode of buckling in buried pipelines induced by ground failure along the length of the pipe causing axial compression. The authors found that the buckling mode is governed by the diameter to thickness ratio, buried depth, initial imperfection, soil-pipe friction, and soil foundation.

Estefen et al. (1995) investigated the behaviour of tubes subjected to external pressure and bending. Tests were carried out on small-scale specimens with diameter to thickness ratios commonly used for deepwater pipelines. Aluminium specimens included D/t ratios of 20, 25 and 32 and steel specimens included D/t ratios of 21 and 24. An analytical program was also developed using non-linear shell theory to determine suitable ultimate limit states for submerged pipelines. The model incorporated the initial geometric imperfections for each specimen. A parametric study was also conducted to determine the effect of the value of the strain hardening parameter in the Tvergaard expression on the ultimate strain for pipe subjected to bending only. It was found that the strain hardening properties of the material significantly affect the ultimate strain under bending. Doubling the strain hardening parameter from 8 to 16 resulted in a reduction in the ultimate strain of approximately 15 percent for a range of diameter to thickness ratios of 15 to 35.

Nicolella and Smith (1997) investigated the wrinkling behaviour of corroded pipelines experimentally and numerically. One specimen with an outside diameter of 1219 mm and a wall thickness of 12.6 mm was tested under internal pressure, axial load and bending. Corrosion was simulated experimentally by grinding a patch into the pipe, reducing the wall thickness. A numerical model was constructed using ABAQUS finite element software including a customized multi-linear kinematic hardening material model. Corrosion was simulated numerically using reduced wall thicknesses for elements corresponding to the reduced area on the specimen. Good agreement between experimental and predicted moment capacities was achieved. Reasonable agreement between the experimental and predicted curvatures and displacements was also achieved with the numerical values consistently higher. The authors concluded that the finite element model proposed is well suited for the wrinkling analysis of corroded pipe.

Schneider (1998) performed two full-scale tests on pipeline specimens subjected to axial compression, internal pressure and bending. The effect of sleeve length used for pipe repair was examined for pipes with a D/t of 64. It was found that failure took the form of a single outward bulge in the carrier pipe adjacent to the sleeve. Also failure occurred after significant inelastic behaviour. A simple analytical model was developed to predict the response of the test specimens. It was found that the Tresca yield criterion produced a reasonable estimate of the yield strength and a conservative estimate of the inelastic deformations.

1.1.2 Research at the University of Alberta

Research at the University of Alberta has included experimental and analytical investigations of pipeline behaviour as well as the development of computer aided design tools.

Zhou et al. (1993) performed three dimensional shell analyses, using the finite element method, of a segment of pipe subjected to combinations of axial load, internal pressure and large imposed curvature. Cross-sectional stiffness coefficients were defined by characteristic stiffness properties of the cross-section from the analysis. These pipe properties were then included in a soil-structure interaction beam model to generate a predictive analysis tool for differential settlement problems. Deformation localization was found to be a fundamental characteristic of predicted response. Local buckling, wrinkling, and properties of the surrounding soil were found to have a great influence on the behaviour of pipelines.

Mohareb et al. (1994) conducted a series of seven tests on full size segments of pipeline to determine the deformational behaviour of these structures. The test specimens were subjected to axial compression, internal pressure and increasing curvature. Three specimens had a diameter to thickness ratio, D/t, of 51 and four had a D/t of 64. All specimens in the test series were 1690 mm long and were subjected to various load combinations. This test program also examined the effect of active and reactive end conditions for applying axial load. An active condition maintains the axial load as a constant force and a reactive condition maintains the length of the specimen constant. In the reactive cases, the axial load was found to decrease from its starting value as the specimen is deformed. Two buckling modes were observed experimentally as a function

of internal pressure. It was found that the non-pressurized specimens exhibited a "diamond" shape buckle and the specimens pressurized at 36 percent of specified minimum yield strength, SMYS, or higher exhibited an "outward bulge" shape. There was no evidence that this mode of local buckling would prevail at lower internal pressure. In addition, a numerical model was developed using the ABAQUS finite element software to first predict the experimental results and then to perform a parametric study. Good agreement between the experimental results and the finite element solutions was obtained. An isotropic material model was used with material properties measured in the longitudinal direction of the specimens. Geometric imperfections were not included in the study.

Yoosef-Ghodsi et al. (1994) tested the same number and size of specimens as Mohareb et al. (1994) with the addition of a girth-weld at mid-length. The investigation adopted the active boundary condition for all tests. A computer program was written to perform an incremental analysis to predict the moment versus curvature results. In addition, a more comprehensive method for determining the critical compressive strains was outlined. This method uses a local strain versus global strain plot to define the onset of localization. It was found that the critical compressive strains of girth-welded segments of pipe were approximately 60 percent of those found by Mohareb et al. (1994) for plain pipe.

Souza and Murray (1994) used the finite element method to predict the behaviour of girth-welded pipelines. Residual stress effects due to welding and geometric misalignments at the weld were incorporated into the model. The work included studies of the choice of shell element used, boundary conditions, mesh type and size, as well as the type of imperfection included. Comparison of the analytical and experimental results showed good agreement. Recommendations were made regarding the most suitable modelling for capturing the wrinkling behaviour of pipe.

1.2 SCOPE AND OBJECTIVES

The research discussed in Section 1.1 indicates the large variety of aspects that must be addressed to fully understand pipeline behaviour. The problem of differential settlements, however, is generally governed by local deformations. Although many researchers have investigated this problem, the number of variables studied is still

limited. Most pipes studied have had diameter to thickness ratios ranging from 20 to 60 with few specimens covering up to 110. It is therefore the intention of this research to investigate the behaviour of pipelines with large diameter to thickness ratios subjected to combined loads. The deformational characteristics of pipe, particularly local buckling, will be investigated experimentally for the pre- and post-buckling ranges to expand the database of experimental results to higher diameter to thickness ratios. Four full size segments of pipeline with a D/t of 92 are subjected to combinations of axial compression, internal pressure and bending. The test specimens and loading were chosen to complement the work previously performed at the University of Alberta and elsewhere. The tests are also considered to add to the general database of experimental results. Mohareb et al. (1994) observed that the local buckling mode is dependent on the level of internal pressure and the transition between modes is between 0 and 36 percent SMYS. It is also an objective of this project to investigate the internal pressure at which the buckling mode changes from the "diamond shape" to the "bulge shape". Internal pressure causing a circumferential stress of 20 percent of SMYS is included to determine more precisely the pressure at which the transition occurs. In addition, test conditions include internal pressures of 0, 40 and 80 percent of SMYS. Because of the large diameter to thickness ratio of the test specimens, the effect of initial imperfections will be investigated in the following study. Consequently, initial imperfections for the specimens are measured prior to testing to assess their magnitude and distribution.

It has been shown that modern finite element methods are a powerful tool to examine pipeline behaviour compared to costly experimentation. Parameters that need to be investigated include the diameter to thickness ratio, material strength and behaviour, loading conditions, weld location, and initial imperfections. Although useful, the numerical models must first be validated by comparing with the results of carefully conducted tests on full size pipe specimens. A non-linear finite element model will therefore be constructed to incorporate measured initial imperfections and material properties and will be validated using the test results. The magnitude of initial imperfections and the sensitivity of the model to variations in the material definition will also be examined numerically.

2. EXPERIMENTAL INVESTIGATION

2.1 SCOPE

The purpose of this experimental investigation is to study the behavioural response of pipelines subjected to combined bending, axial load, and internal pressure in order to expand the database of test results already existing in this area. It is therefore necessary to test and evaluate the response of line pipe from elastic, through plastic, and post-buckling ranges. Testing methods and procedures have been developed to simulate specific field loading conditions. The following sections describe the test specimens, the test parameters, the test set-up, the testing procedure, the instrumentation used during this experimental investigation and the ancillary tests that were conducted.

2.2 SPECIMENS

The selection of the test specimens has to satisfy two primary objectives. First, specimens have to be representative of pipe currently used by the industry. Secondly, the specimens have to complement earlier tests conducted at the University of Alberta (Mohareb *et al.* 1994 and Yoosef-Ghodsi *et al.* 1994) in order to expand the existing database of experimental results. Previous experiments were conducted using 324 mm (12.75 inch) and 508 mm (20 inch) diameter pipes with diameter to thickness ratios, D/t, of 50 and 63, respectively. With this in mind, a 762 mm (30 inches) diameter pipe (NPS 30) with a wall thickness of 8.3 mm was selected. This pipe has a diameter to thickness ratio, D/t, of 92, extending the database previously acquired to the higher limits that are customarily used by the industry. All specimens had a single longitudinal seam weld fabricated using the double submerged arc welding process, DSAW, and were of Grade X70 steel with a specified minimum yield strength, SMYS, of 483 MPa. The SMYS will henceforth be referred to as the yield strength, F_y. The influence of the fabrication process and the location of the seam weld on the deformational response of the pipe were not included in this study. Based on previous experience, all specimens were chosen to be 2700 mm long, or 3.5 times the diameter, to ensure that a good portion of the specimen was undisturbed by boundary effects. Also, the outside surface of the specimens was sandblasted to remove paint and other debris to facilitate the installation

of gauges and to provide a clean surface for the detection of deformations. In addition, a coarse grid was painted on the surface of the specimens for control of measurements and to help visualize the pipe deformations in photographs.

The general designation that will be used to identify the individual tests has the form CaPb. "Ca" indicates the axial force applied to the specimen due to a difference in temperature (only compression is considered in this test program), with "a" indicating the value of the difference in temperature in degrees Celsius causing that force. "Pb" indicates the level of internal pressure in the pipe where "b" is the percentage of pressure that would yield the pipe in the hoop direction, p_y, based on F_y. For example, C45P80 indicates a specimen subjected to an axial compression of the magnitude caused by a 45 degree Celsius difference in temperature and an internal pressure of 80 percent of p_y. Discussions of the above parameters are included in the following sections.

2.3 TEST PARAMETERS

The test parameters were chosen to simulate loads and imposed deformations consistent with those experienced by buried pipelines. The test specimens were subjected to axial compression, internal pressure and monotonically increasing curvature. A description of each experimental loading parameter and its corresponding simulated field condition follows.

2.3.1 Axial Compression

Axial compression in pipelines is generally caused by the effect of a temperature difference between the tie-in and operating conditions. The tie-in restraint can be due to the friction between the soil and the structure or from more direct sources such as compressor/pumping stations and bends. Axial compression due to temperature effects was held constant during all four tests at a design temperature difference of 45 degrees Celsius. The assumption that the tie-in or construction temperature is -45 degrees Celsius, the operating temperature is 0 degrees Celsius, and that the segment of pipe is fully restrained, is based on winter construction and an operating temperature that will not disturb permafrost. This is consistent with industry practice for oil pipelines in regions of discontinuous permafrost. Compressive forces may also be imposed on pipelines that are placed in sloping ground when subject to earth movements along the length of the pipe.

In addition, axial tension is induced in pipelines due to caternary action on the pipe resulting from geotechnical movement. However, the axial force in this study was limited to compression caused by a difference in temperature.

The compressive axial load that results from the temperature effect, C_t, is calculated as follows:

$$C_t = A \cdot E \cdot \alpha \cdot \Delta T \tag{2.1}$$

where A is the nominal area of the pipe, E is the elastic modulus, α is the coefficient of thermal expansion for the material and ΔT is the difference in temperature with respect to the tie-in temperature. The axial load was held constant throughout the tests for all four specimens although in the field, local buckling of a segment of pipe would relieve some of the restraint causing the axial load. It was decided that a constant load, active end condition, would be more suitable to understand the fundamental behaviour of the pipe. Consequently, the test conditions during the post buckling behaviour are more severe than those that can be expected from similar conditions in the field where the axial load would likely decrease with increased deformations.

2.3.2 Internal Pressure

The internal pressure in a buried pipeline is caused by the action of the fluid that is being transported. The internal pressure in the test specimens was varied from 0 to 80 percent of the nominal pressure that would cause the yield stress in the hoop direction, p_y, given as:

$$p_y = \frac{2t \cdot F_y}{(D - 2t)} \tag{2.2}$$

where t is the wall thickness, F_y the nominal yield strength, and D the nominal pipe diameter.

The individual specimens were subjected to pressures of 0, 20, 40 and 80 percent of p_y. This upper value is based on the limit given in the design standard CAN/CSA-Z662-94 as the maximum design pressure for pipelines. The point of maximum internal pressure represents a point downstream of a pumping/compression station and the point of minimum internal pressure is located upstream of a pumping/compression station. A previous study by Mohareb *et al.* (1994) have indicated that there is a transition in

buckling mode, from a "diamond shape" local buckle to an outward "bulge" local buckle in the lower pressure range. This prior experimental program included specimens subjected to $0.0p_y$, $0.4p_y$ and $0.8p_y$ for pipes with outside diameters of 508 mm, and pressures of $0.0p_y$, $0.36p_y$ and $0.72p_y$ for pipes with outside diameters of 324 mm. The outward "bulge" buckle was observed for all pressurized specimens. For this reason, a test with an internal pressure of $0.2p_y$ was included to determine more accurately the pressure where the buckling mode may change.

Internal pressure produces an axial load in a pipeline due to the Poisson ratio effect, C_{ph}, depending on the restraint provided to the pipe. It was assumed in Section 2.3.1 that the pipe is fully restrained for the calculation of temperature effects. A consistent assumption must be made for calculation of the axial load due to the Poisson ratio effect. Internal pressure causes the pipe to expand in the radial direction which, by Poisson's effect, causes shortening in the longitudinal direction. Since the pipe is restrained against this shortening, the effect induces an axial tension in the pipe calculated as follows:

$$C_{ph} = -A \cdot \nu \cdot \frac{p}{p_y} \cdot F_y \tag{2.3}$$

where A is the nominal area of the pipe, p is the internal pressure, p_y is the pressure causing yield in the hoop direction and ν is Poisson's ratio. The negative sign is used to indicate tension in this case.

Pressure reductions in buried pipelines occur during shutdown of the pipeline. Pipelines may also be operated with reduced internal pressure due to a decrease in pipe capacity as a result of corrosion or reduced shipping demand. It is of interest to determine if a segment of pipe that is subjected to axial compression and an imposed curvature can be induced to buckle if subjected to a reduction in internal pressure. In order to investigate this phenomenon, the specimens were depressurized at various stages during the tests.

2.3.3 Monotonically Increasing Curvature

Monotonically increasing curvature in a buried pipeline is commonly caused by differential settlements or slope instability. During the tests, the monotonically increasing

curvature was imposed by increasing the stroke of eccentrically placed jacks as described in the following section.

2.4 TEST SET-UP

The test set-up used for this project is similar to that used in previous test programs of this type (Mohareb *et al.* 1994; Yoosef-Ghodsi *et al.* 1994). As shown in Figure 2.1, a concentric load, P, was applied to the specimen using the MTS 6000 Universal Testing Machine in the I.F Morrison Structural Laboratory at the University of Alberta. An eccentric load, F, was applied to the ends of the loading arms using two 1750 kN compression jacks positioned in line with each other. This dual jack system was used to ensure adequate stroke was available to impose the desired end rotations. The eccentric jacks were controlled by a manually controlled air-over-hydraulic system. Internal pressure was applied by filling the pipe with water and pressurizing it using a manually controlled air driven pump.

The supports at the top and bottom of the specimen consisted of rollers on curved plates as shown in Figure 2.2. This special end condition provides a known instantaneous centre of rotation, or pivot point. This system was used with success in previous research at the University of Alberta (Ibrahim and MacGregor, 1994). The test set-up was then braced at the pivot points using 12 mm high strength steel tension rods. Two sets of tension rods, one on each side of the test specimen, and aligned through the top and bottom pivot points were provided. This bracing system was included to provide stability in case of accidental eccentricities or misalignments in the system. An additional knife edge was placed at the top of the test set-up to allow rotation in the out-of-plane direction eliminating undue stresses on the loading head of the testing machine due to small misalignments.

The ends of the test specimens were welded to 76 mm thick end plates as shown in Figure 2.1. In addition, a set of collars, shown in Figure 2.3, 225 mm wide was fabricated and placed around the ends of the specimens in an attempt to avoid buckling near the boundaries.

2.5 TEST PROCEDURE

The procedures followed during the experimental program for the assembly of the test and for the control of the test is described in the following.

2.5.1 Assembly and Alignment Procedures

The assembly and alignment of the test set-up followed a procedure that ensured consistency among the four tests. The following steps were adopted for setting up each test specimen.

1) The top loading beam assembly, with the end plate bolted to the beam, was placed and levelled on the floor in an inverted position.
2) The specimen was centred and aligned vertically with the use of markings on the end plate as well as a transit and plumbs. The specimen was shimmed as needed.
3) The end of the pipe was then welded to the end plate resulting in the L-shaped assembly shown in Figure 2.4.
4) Using a crane and chain hoist, the L-shaped assembly was picked up, as seen in Figure 2.5, inverted, and placed in position in the MTS Universal Testing Machine. Prior to this stage the bottom loading beam assembly had already been positioned and levelled in the MTS.
5) The specimen and top loading beam were adjusted and aligned into position.
6) The bottom end of the pipe was welded to the bottom end plate. This process enabled both end welds to be done in the down hand position.
7) The jacking assembly, bracing system, pressure hoses and instrumentation were then added.
8) Prior to the commencement of a test, the bracing system was tightened and slightly pretensioned. The adjustment of the braces also allowed some fine-tuning of the alignment of the top and bottom ends of the specimen.

2.5.2 Control of Tests

The main objective for the control of the tests is to maintain the desired level of internal pressure, axial load and imposed curvature parameters. The concentric load applied to the specimen was the most difficult to maintain simply because it is a function of the current internal pressure and jack load and, consequently, changes throughout the

test. The load P, applied using the MTS Universal Testing Machine, accounts for the effects of the following: axial load in the pipe due to simulated temperature effects or load, C_t; Poisson ratio restraint effect due to the pressure in the hoop direction, C_{ph}; pressure acting on the end plates of the specimen, C_{pe}; and the jack force F applied to the loading arms. The load P is calculated from:

$$P = C_t + C_{ph} + C_{pe} + F \tag{2.4}$$

where C_t and C_{ph} are as calculated using Eq. (2.1) and Eq. (2.3), respectively. P can also be expressed in terms of the net axial load in the pipe, C, which includes the effects of temperature and Poisson ratio. C may be expressed as:

$$C = C_t + C_{ph} \tag{2.5}$$

It follows that P can be defined as:

$$P = C + C_{pe} + F \tag{2.6}$$

The axial force in the pipe due to the pressure acting on the end plates of the specimen, C_{pe}, is a function of the current internal pressure, p, and is obtained from:

$$C_{pe} = \frac{\pi \cdot (D - 2t)^2}{4} p \tag{2.7}$$

The jack force, F, applied to the system to impose the curvature, causes a tensile axial load in the specimen that must also be counteracted by the MTS load. This force changes throughout the test and requires continuous adjustment of the load P.

It was decided that the above adjustments to the load, P, could be accomplished using manual stroke control of the MTS Universal Testing Machine. Also, the eccentric jacks were used with a displacement control system. With this control arrangement, loss of capacity in the specimen could not cause sudden collapse damaging the specimen or equipment. As indicated above, the load P applied by the Universal Testing Machine is the result of a series of calculations dependent upon the current values of: the desired net axial load, C, the internal pressure, p, and the jack force, F. For this reason, a channel was dedicated in the FLUKE data acquisition system to monitor the current values of the test parameters and calculate and display the target value of the concentric load, P. The

MTS displacement was therefore adjusted manually to attain the desired load level P. The test procedure was as follows:

STEP 1: Pressurize the pipe

1) Using a manually controlled pump, the internal pressure was increased to the desire level.
2) The MTS load was increased to compensate for the pressure on the end plates.

STEP 2: Apply the axial load

1) The MTS load was increased by an amount equal to the net axial load desired on the specimen.
2) At this stage the MTS load was the sum of the internal pressure effect and the desired net axial load on the pipe.

STEP 3: Increase the pipe curvature

1) The eccentric jacks were then advanced in increments of approximately 100 kN corresponding to approximately 150 kN·m in applied moment.
2) Simultaneously, or following the jack load, the MTS load was adjusted to compensate for the jacking force. Before the MTS load adjustment was made, the net axial load in the pipe was reduced placing the specimen in a more stable situation than the desired load condition.

STEP 4: Depressurization

1) With jack displacement kept constant, the MTS load was reduced slightly.
2) A portion of the internal pressure was then released using the relief valve on the hand pump.
3) The MTS load was readjusted to the target value. It was the intention at this point to maintain relatively constant curvature which limited the amount of MTS adjustments that could be made.
4) 1) to 3) were repeated until the internal pressure was reduced to zero.
5) The pipe was then repressurized to its desired value before resuming the test loading sequence.

STEP 5: Peak Load and Post-Buckling Descending Branch

1) The peak load of the test can be determined when increasing the curvature as in STEP 3 and the MTS is not able to increase the load sufficiently to compensate for the additional jack force. At this point the jack force was decreased slightly and the concentric load P was adjusted. It was found during the testing of the non-pressurized specimen, C45P00, that further increase in MTS displacement without a reduction in jack load caused an increase in curvature in the test specimen with a state of stress in the pipe that has an axial load below the required value. This will be discussed further in Chapter 3.
2) Loading past the peak load proceeded by reducing the jack load in small increments. The reduction occurred naturally when the jack displacements were increased.
3) At each increment, the MTS was readjusted as needed to maintain the desired axial load.

2.5.3 Expected Values as Calculated by Mohareb–Murray Plastic Equation

Based on equations presented in previous work by Mohareb *et al.* (1994), the expected fully plastic moment capacity reduced for the circumferential stress caused by internal pressure, M_p^p, is calculated using:

$$M_p^p = 2r_{av}^2 t \cdot F_y \sqrt{4 - 3\left(\frac{p}{p_y}\right)^2} \tag{2.8}$$

The expected values of the plastic moment capacity reduced for axial load and the circumferential stress due to internal pressure, M_p^{pC}, can be calculated using:

$$M_p^{pC} = \pm M_p^p \cdot \cos\left\{\pi \frac{\left[\frac{C}{C_y} - \frac{1}{2}\frac{p}{p_y}\right]}{\sqrt{4 - 3\left(\frac{p}{p_y}\right)^2}}\right\} \tag{2.9}$$

In the above equations, r_{av} is the average of the internal and external radii of the pipe, p_y and C are defined by Eq. (2.2) and Eq. (2.5) respectively and the axial load required to develop the yield stress over the pipe cross-section, C_y, is given as:

$$C_y = A \cdot F_y \tag{2.10}$$

The above equations are derived assuming an ideal, bi-linear elastic–plastic material response and a fully plastic cross section. Previous tests by Mohareb *et al.* (1994), have shown that these equations yield reliable results if the internal pressure is relatively low, up to $0.4p_y$, but tend to underestimate the capacity when the internal pressure is increased to the maximum. These predicted values were used during the design of the components of the testing apparatus. Table 2.1 outlines the test parameters used during the experiments as well as the calculated values of C_t, C_{ph}, C_{pe} and the expected values for M_p^p, M_p^{pc}, F and P.

2.6 INSTRUMENTATION

Extensive instrumentation was used during the experimental program to capture the behaviour of the specimens. The following sections describe the various instruments used to monitor each test specimen.

2.6.1 Electrical Resistance Strain Gauges

A line of electrical resistance strain gauges was placed on the extreme compression face at intervals of 254 mm starting at 461 mm from the ends. This interval was chosen such that the strain gauges were located at mid-distance between Demec points as discussed in the following section. A line of gauges was also placed on the tension face opposite the compression gauges. These pairs of gauges at various elevations were used for the calculation of local curvature as indicated in Chapter 3. The gauges on the compression face were also used as an indication of the strains at buckling of the specimen as discussed in Chapter 3. It was expected that the strain gauge measurements would have a non-uniform distribution along the length after local buckling began since strain gauges provide localized surface strain measurements. However, the strain gauges can be used in the elastic portion of the test and also to confirm the Demec gauge readings. Additional rings of six gauges were placed at four elevations about the midsection of the specimen. These gauges, along with the compression and tension face gauges were equidistant around the pipe to detect any out-

of-plane bending or alignment errors. Data from these instruments were recorded using a FLUKE electronic data acquisition system.

2.6.2 Demec Gauges

Demec gauges are used to measure strains over a longer gauge length than strain gauges. During the test, Demec gauges with a gauge length of 254 mm were used to obtain average strain values over the length of the extreme compression and tension faces of the test specimens. Strains measured over a longer gauge length are not as sensitive to local effects and can therefore be more representative of average behaviour once local buckling has occurred. Demec gauge readings were recorded manually.

2.6.3 Rotation Meters

Electronic rotation meters were fixed to the top and bottom 76 mm end plates in line with the centroid of the pipe in order to measure the absolute rotation of the end plates. Rotations of the end plates are used in the calculation of global curvature of the specimen as described in Chapter 3.

2.6.4 Linear Variable Differential Transformers (LVDT's)

A series of nine LVDT's were attached to a column at intervals of 254 mm as shown in Figure 2.6. The column holding the LVDT's was placed 3 m from the specimen to minimize the effect of vertical displacements of the compression face on the measured horizontal displacements. The LVDT's were connected to the compression face of the specimen using thin wire that is too fine to be seen in Figure 2.6. Consequently, the LVDT's were used to record the horizontal displacement of the compression face of the specimen as it deformed. Compression face displacements were used for a number of applications as discussed in Chapter 3.

2.6.5 Change in Diameter Measurements

Change in diameters in the directions in and out of the plane of bending were measured during each test. A special gauge, shown in Figure 2.7, was fabricated for this purpose. The gauge consisted of a U-shaped aluminium frame constructed using 25 mm square aluminium tubing with struts across the corners to increase the overall stiffness. A sharpened point was affixed to the end of one leg and a depth gauge on the end of the

other leg. Specific cross sections were marked on the specimen at which the diameter was measured throughout the test.

2.6.6 Loads

All the loads applied to the test specimens were measured. The concentric load, P, applied by the MTS Universal Testing Machine was measured with an internal load cell. A pressure transducer was employed to measure internal water pressure for the pressurized specimens. The eccentric jack load, F, was measured using a load cell incorporated into the jacking assembly as shown in Figure 2.1. The bracing members at the pivot points were also designed and calibrated as load cells.

2.7 ANCILLARY TESTS

2.7.1 Determination of Material Properties

For line pipe, it is generally accepted that the material properties in the longitudinal direction differ from those in the circumferential direction, (Workman, 1988). Tension coupons were therefore obtained from the longitudinal and circumferential directions. Static material properties were determined for both types and subsequently included in the numerical analysis.

Three tension coupons with a gauge length of 51 mm were obtained from the compression face (opposite the seam weld) of a segment of pipe in the longitudinal direction. Tension specimens for pipe are generally taken from material 90 degrees from the seam weld. However, it is believed in this case the material properties from the compression face, 180 degrees from the seam weld, are more representative of the material likely to affect the buckling behaviour of the specimen. The tension coupons were otherwise prepared and tested in accordance to ASTM Standard A 370 – 94 (1994). Elongation of the tension coupons was monitored during the material tests using a 51 mm clip-on extensometer.

An additional set of three tension coupons with a gauge length of 51 mm were prepared from the compression face of a segment of pipe in the circumferential direction. The ASTM Standard for this type of material test indicates that the coupons are to be

flattened before testing. However, it is not known how the flattening process affects the material properties of the pipe.

2.7.2 Measurement of Initial Imperfections

Initial geometric imperfections of the pipe specimens were measured on the interior surface of each test specimen prior to testing. The measured initial imperfections were incorporated into the analytical model as described in Section 4.3. Measurements were taken at 16 points around 14 different cross-sections located at roughly equal spacing along the length of the specimen.

The apparatus used to measure initial imperfections was similar to that used for previous work at the University of Alberta (Chen *et al.* 1993). The apparatus, shown in Figure 2.8 and Figure 2.9, consisted of a 50 mm diameter aluminium tube, roughly the length of the specimens. This tube was placed along the centre of the specimen and secured to the ends of the pipe. The tube was free to rotate about its longitudinal axis. An aluminium track was mounted along the length of the tube along which a carriage was able to move. An LVDT was mounted to the end of an arm attached to the carriage. The LVDT was used to measure the radial distance from the pipe specimen inner surface to the tube, which served as a reference axis. Each measurement, therefore, consisted of: the angle at which the arm was rotated, the length along the specimen at which the carriage was placed, and the radial distance from the reference axis to the pipe wall. The test specimen and apparatus were placed in the vertical position to avoid sagging of the tube under the weight of the apparatus. In addition, the configuration of the reference axis was obtained by taking measurements along a reference line, the MTS Universal Testing Machine column, considered to be close to perfectly straight. This enabled the measurements of the specimens to be corrected for the initial out-of-straightness of the tube itself.

Although precautions were taken to minimize errors, some sources could not be eliminated. Imperfection measurements on the inside surface of the pipe were affected by features such as corrosion, debris and surface imperfections (bumps or pits). Also, the position of the LVDT at the time a measurement was recorded could not be controlled accurately. The angle of the instrument was the most difficult degree of freedom to

control. This lateral deviation may cause error if there are abrupt changes in the pipe configuration such as small dents. It was therefore difficult to quantify the experimental error associated with these measurements. Furthermore, it should be noted that the initial imperfection measurements were recorded before the ends of the specimens were welded to the end plates. Although the welding can potentially affect the initial imperfections, it was decided that the measured imperfections be used in the analytical model as a general indication of imperfections that can be expected in this type of pipe. The initial imperfection measurements were therefore considered sufficiently accurate for this purpose.

Table 2.1
Experimental Parameters and Predicted Values

Specimen	p/p_y	C_t [1] kN	C_{ph} [2] kN	C_{pe} [3] kN	M_p^p [4] kN·m	M_p^{pC} [5] kN·m	F [6] kN	P [7] kN
C45P00	0	2069	0	0	2277	2145	1430	3499
C45P20	0.2	2069	-570	939	2243	2233	1489	3927
C45P40	0.4	2069	-1139	1878	2136	2105	1403	4211
C45P80	0.8	2069	-2278	3757	1642	996	664	4208

1) calculated using Eq. (2.1) based on $\Delta T = 45$ °C
2) calculated using Eq. (2.3)
3) calculated using Eq. (2.7)
4) calculated using Eq. (2.8)
5) predicted value based on Eq. (2.9)
6) predicted jack force, F, required to produce M_p^{pC} based on an eccentricity of 1.5 m
7) predicted MTS load required to compensate for all effects

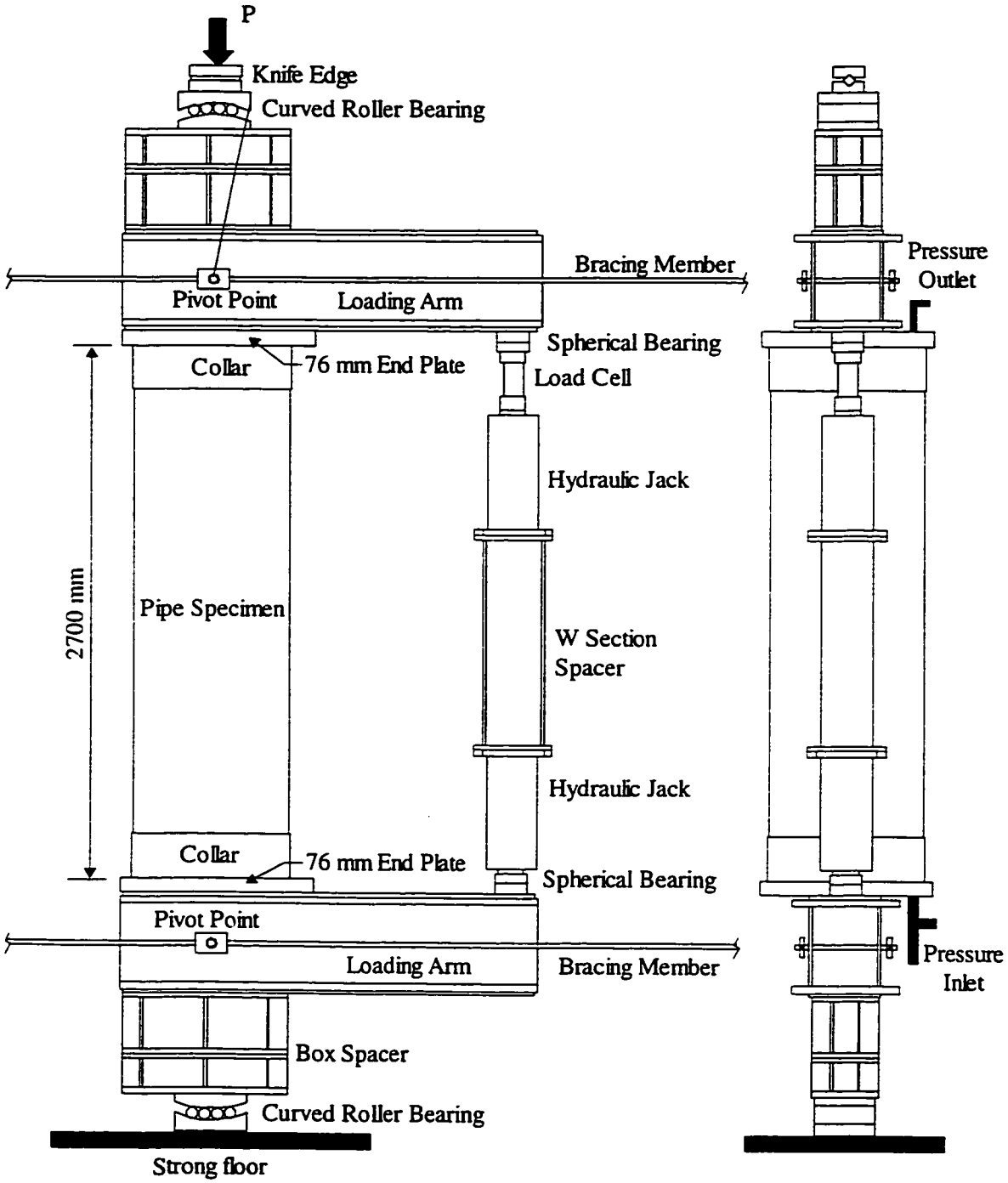

Figure 2.1 Diagram of Test Set-Up

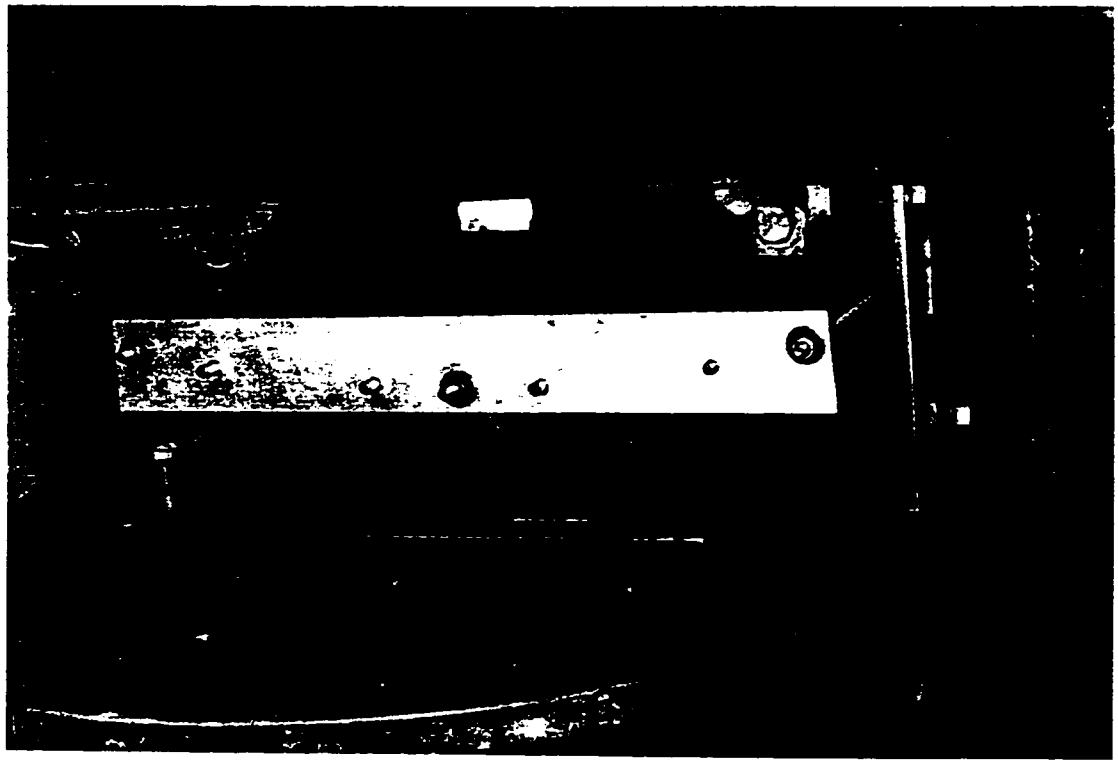

Figure 2.2 Curved roller bearing

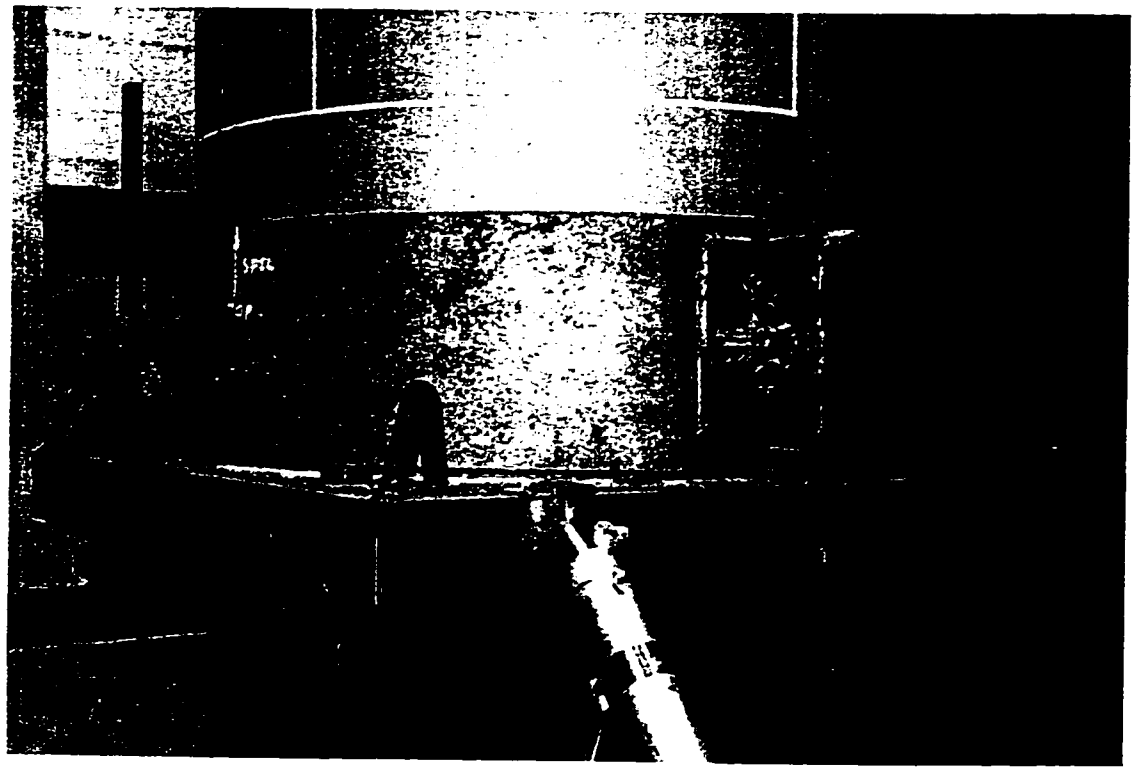

Figure 2.3 End Collar

Figure 2.4 Top loading arm in inverted position

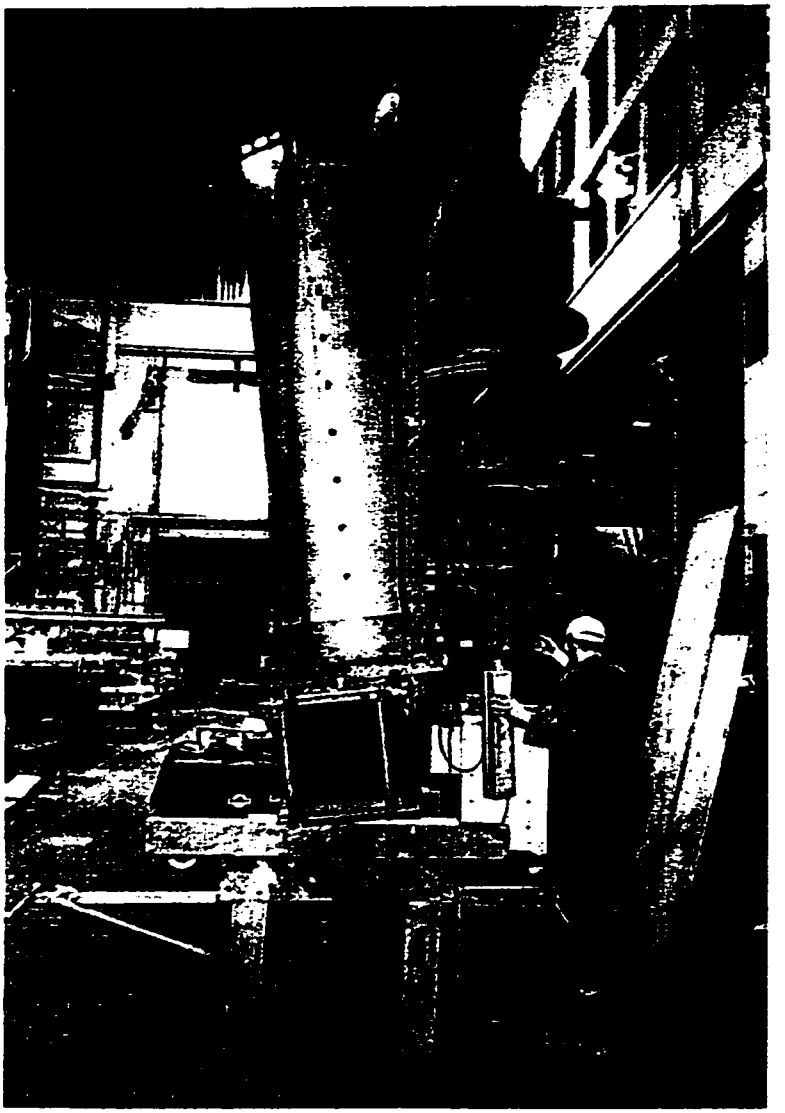

Figure 2.5 Lifting the top loading arm and test specimen assembly

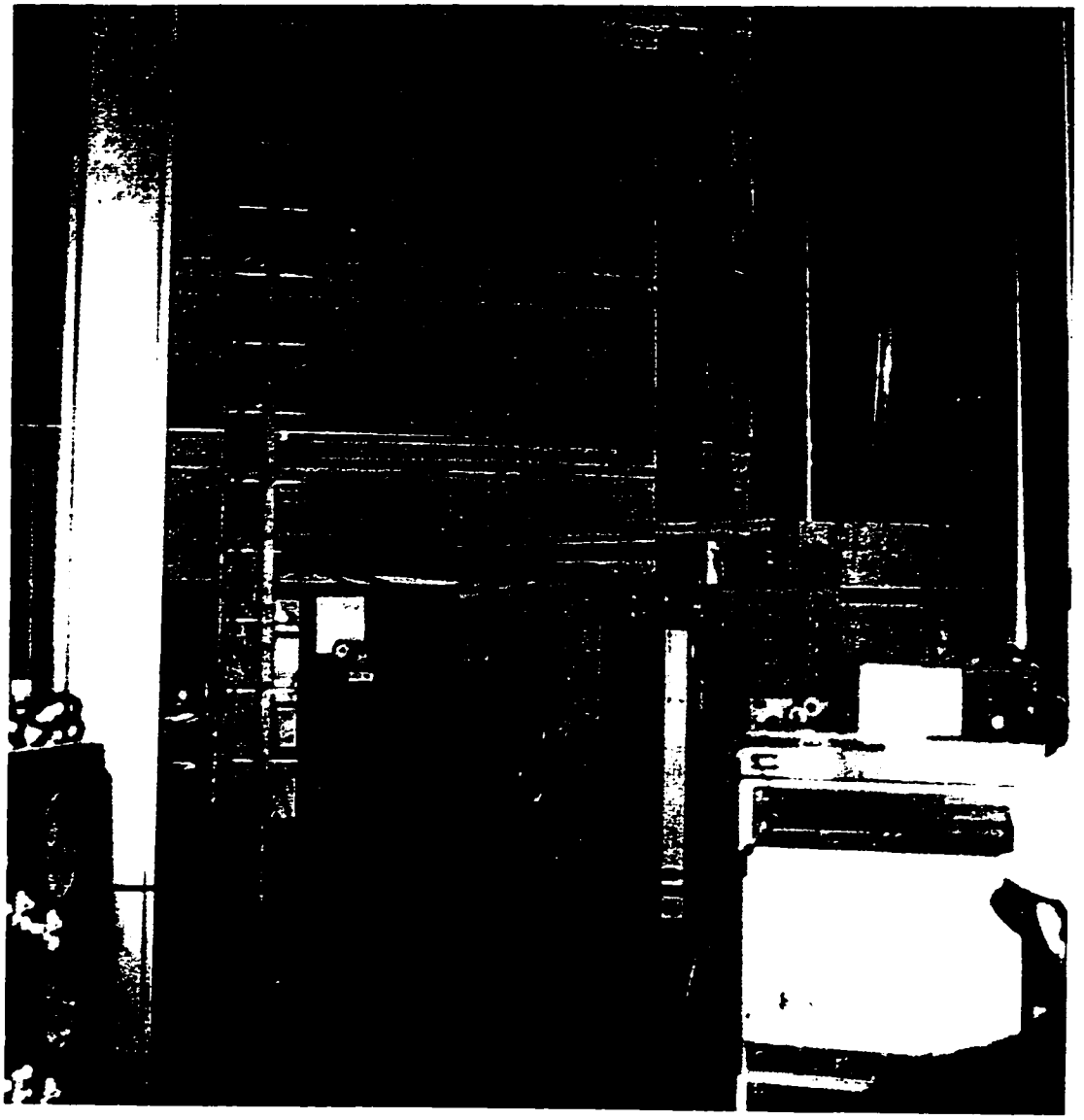

Figure 2.6 LVDT's used for measurement of compression face displacements

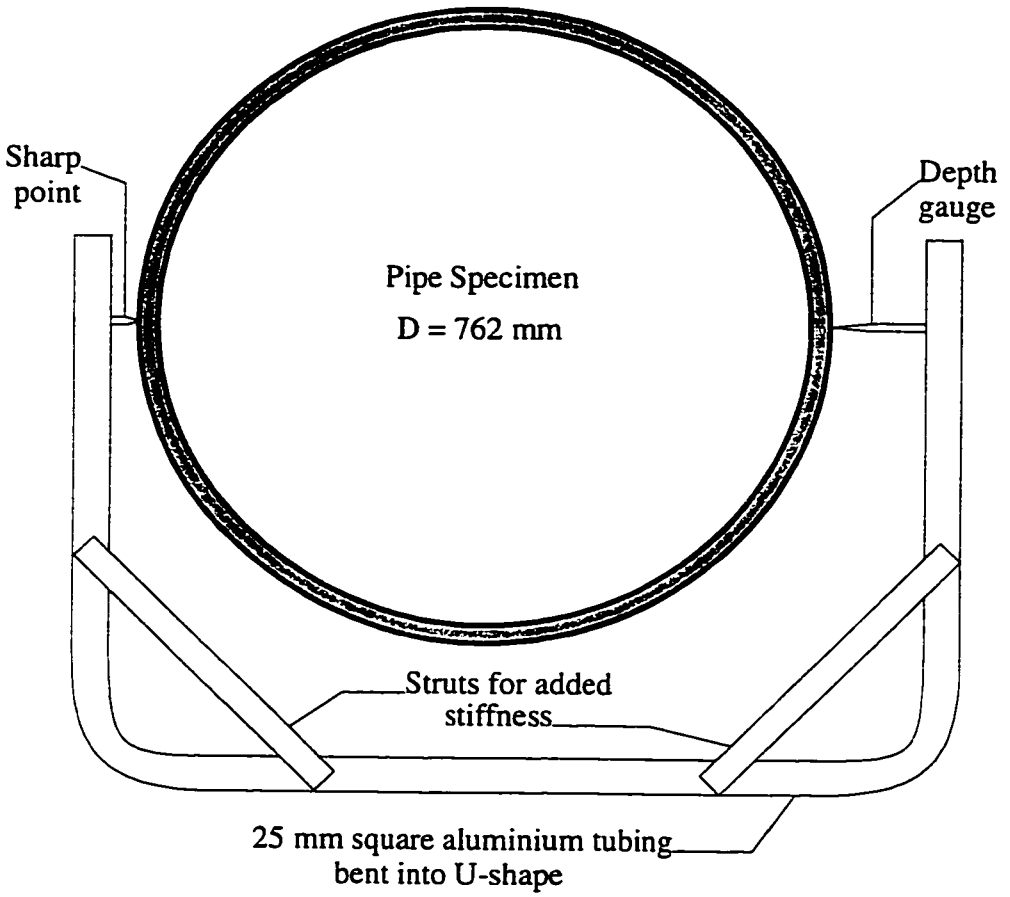

Figure 2.7 Gauge used to measure changes in diameter

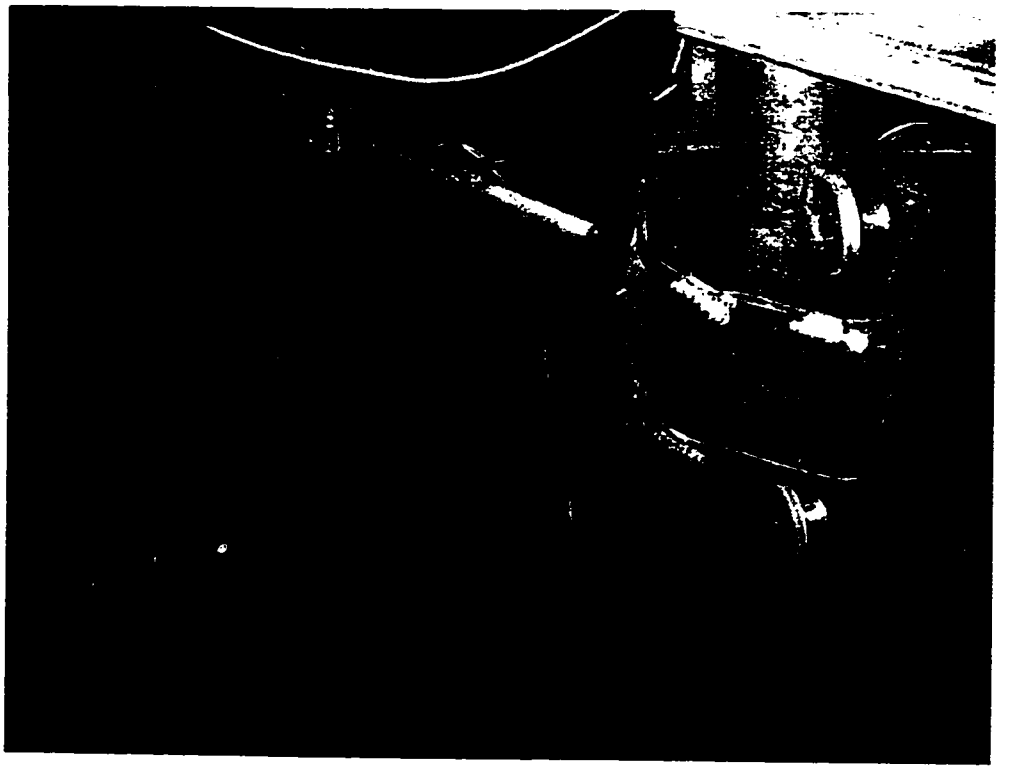

Figure 2.8 Device to measure initial imperfections (showing carriage with LVDT)

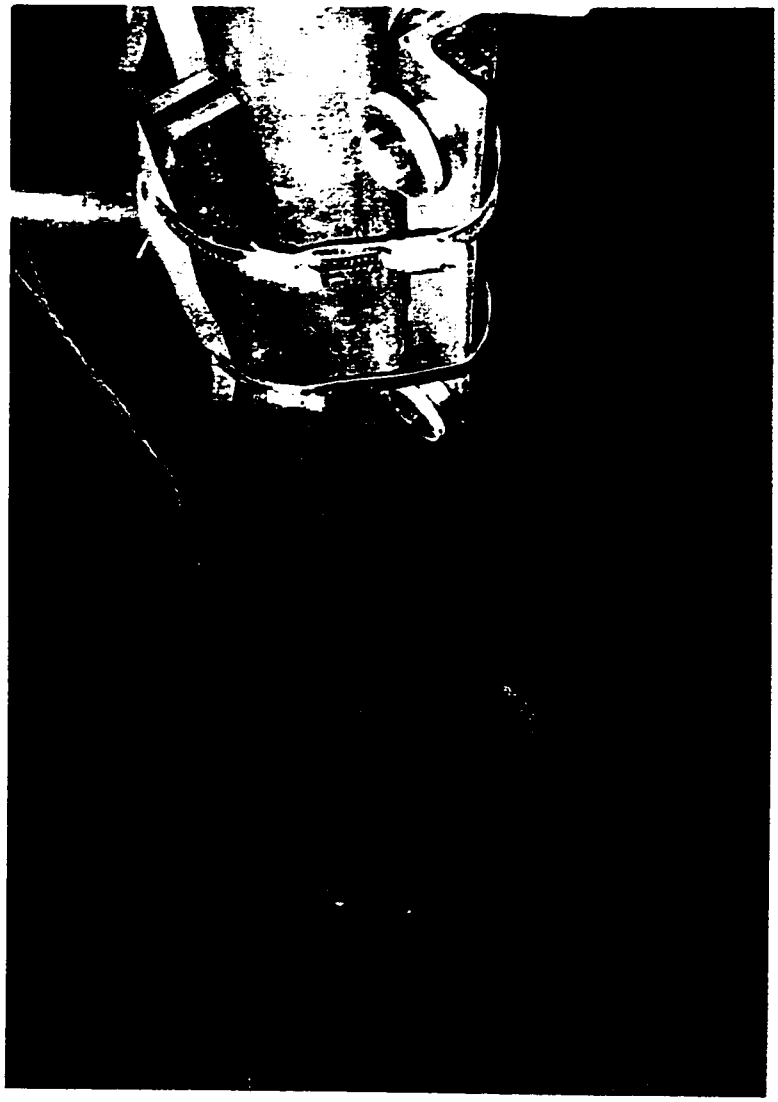

Figure 2.9 Initial imperfection measurement apparatus inside test specimen

3. RESULTS OF EXPERIMENTAL INVESTIGATION

3.1 INTRODUCTION

An experimental investigation on four full-size pipeline segments was conducted to evaluate the effect of combined axial load, internal pressure and increasing curvature. The results of the experimental investigation are presented in the following. Observed moment versus curvature relationships, change in diameter measurements and strain measurements indicating the localization of strains are presented.

3.2 MATERIAL PROPERTIES

Tension coupon specimens were tested to determine actual material properties for inclusion in the numerical analysis. Table 3.1 shows the measured static engineering material properties obtained from these tests. Static properties refer to measurements recorded after a tension coupon test was paused for a few minutes at a constant displacement. Static properties, therefore, do not include any loading rate effects. The table presents values for the three circumferential tension coupons, designated as C-1, C-2 and C-3, as well as the average of the circumferential values, C-Average. Material properties from the three longitudinal tests, L-1, L-2 and L-3, and the average longitudinal properties, L-Average, are also presented. Since the difference between the longitudinal and circumferential properties is small, the average material properties are used as an isotropic material model in the analytical work.

Plots of the resulting static stress versus strain curves are shown in Figures 3.1 and 3.2. The material properties presented in Table 3.1 are: the modulus of elasticity, E, the static engineering stress at the proportional limit, the static engineering stress at 0.2 percent strain, the static engineering stress at 0.5 percent strain, and the ultimate strength. The yield strength, F_y was taken as the stress at 0.5 percent strain. This is in accordance with the method prescribed by API Specification 5L, Specification for Line Pipe, (American Petroleum Institute, 1995). The stress at 0.5 percent strain for the average isotropic material model will be referred to as the measured yield strength, F_y.

The average measured yield strength is 520 MPa in the circumferential direction and 503 MPa in the longitudinal direction. The results show that both circumferential and longitudinal tension coupons gave yield strengths in excess of the specified minimum

yield strength, SMYS, of 483 MPa for X70 Grade steel. The measured ultimate strengths are also greater than the minimum of 565 MPa for grade X70 material.

The average circumferential values exceed the average longitudinal values for all strength properties shown in Table 3.1. The average circumferential values are 1.7, 3.4 and 1.8 percent greater than the average longitudinal values for the stress at 0.2 percent strain, 0.5 percent strain and ultimate strength, respectively. In addition, the proportional limit in the circumferential direction is greater than that in the longitudinal direction. This is consistent with a material that has been work hardened in the circumferential direction due to the pipe forming process (Workman, 1988). Residual strains caused by flattening of the circumferential coupons before testing may also affect the onset of plastic deformations recorded during the tension tests but it is not known to what extent. This effect is assumed to be small.

Following the completion of the research an error was discovered in the calibration of the extensometer used to measure strain in the tension coupon tests. Further tests using two tension coupons from the same steel plate, one prior and one following recalibration, indicated that the strains shown in Table 3.1 should be increased by approximately 8.7 percent. With this adjustment factor, the modulus of elasticity, E, shown in the table become more reasonable. It was assumed that this small discrepancy did not significantly affect the analytical results. The values in the table are therefore used for the remainder the work.

Figure 3.1 shows the complete measured stress versus strain curves for the circumferential and longitudinal directions, as well as the average material properties. The figure indicates the ultimate strength is 17 percent greater than the SMYS value and occurs at a strain of approximately 8 percent.

Figure 3.2 shows the elastic and first yield portion of the measured static engineering material properties in the circumferential and longitudinal directions. Also included in this figure is the average engineering stress versus strain curve that was used for modelling the isotropic material model in Chapter 4. As shown in this figure, the circumferential stress versus strain curve, C-Average, shows a stiffer initial plastic response compared to the longitudinal coupons, L-Average. It should be noted that non-

linearities in the resulting stress versus strain curve begin at a stress of approximately 60 percent of the measure yield stress.

3.3 MEASURED INITIAL IMPERFECTIONS

Initial imperfections, as described in Section 2.7.2, were measured so that they could be incorporated into the numerical analysis. Since the reference line from which initial imperfections were measured did not coincide with the longitudinal axis of the pipe, the data needed to be adjusted accordingly. The longitudinal axis, along which the axial load is applied in the finite element analysis, was taken to be the axis determined by a line of best-fit through the measured data along the length of the specimen. The measured values of the radii were then adjusted using linear transformations of the co-ordinates. Following these transformations, the new reference line for the measurements was aligned with the longitudinal axis of the specimen.

Figures 3.3, 3.4, 3.5, and 3.6 show the developed surfaces of the patterns of adjusted initial imperfections for the four test specimens. In these figures, axis a-a coincides with the extreme fibre on the compression face of the specimen. The location of the seam weld is also identified. The imperfections are amplified by a factor of one hundred to better visualize the pattern. The tension face (the two edges of the developed surface of the pipe) exhibits a jagged surface compared to the compression face. This is attributed to the presence of the seam weld that adversely affects the integrity of the measurements in this area.

The magnitude of an initial imperfection is defined as the deviation of the measured radius from the nominal radius of the pipe. The imperfection can subsequently be expressed as a percentage of the wall thickness. This definition does not differentiate between localized and overall deviations resulting from curvature of the pipe. Table 3.2 summarizes the results of the imperfection measurements. Included in this table are the maximum (a positive imperfection indicates an outward deviation) and minimum (a negative imperfection indicates an inward deviation) measured imperfections as well as the maximum and minimum along the axis a-a for the four test specimens. The values along the axis a-a correspond to the imperfections that are located on the extreme compression fibre during the tests. These compression face initial imperfection values are considered to most affect the behaviour of the specimens. Based on all the measured

values, initial imperfections ranged from –2.41 mm to +1.93 mm. Based on the compression face values, the imperfections ranged from –0.81 mm to +1.08 mm.

3.4 MOMENT VERSUS CURVATURE RELATIONSHIP

A characteristic force-displacement relationship is commonly used to describe the overall behaviour of a structure. These diagrams are particularly suited for problems with limit points because they demonstrate the behaviour of a structure in the pre- and post-buckling ranges and clearly indicate the onset of instability. For problems involving bending, the force parameter is chosen as the bending moment and the displacement parameter is chosen as curvature. The parameters then have to be further defined since the moment is continuously changing along the specimen due to second order effects. Also, for segments not subjected to constant curvature, curvature is dependent on the length over which it is calculated. A reasonable gauge length must be selected that encompasses the area disturbed by a local buckle. A gauge length equal to the pipe diameter, D, was believed to be appropriate. This length is sufficiently long to encompass the majority of the localized deformation effects in all the test specimens. It has also been shown (Yoosef-Ghodsi *et al.* 1994) that this is true for pipes with smaller diameter-to-thickness ratios. The moment versus curvature relationship over length D will henceforth be referred to as the local moment versus curvature relationship. The following sections will also define a global moment versus curvature relationship in which moment and curvature are averaged over the full length of the test specimen.

3.4.1 Calculation of Moment

The calculation of global moments is simplified compared to the local moment calculation. The global moment, M_G, is defined as the average of the moments applied to the end plates, M_i, during the tests. The subscript i can be either t, indicating a value at the top, or b, indicating a value at the bottom of the specimen. The end moment given by Eq. (3.1) was obtained from the free body diagram of the top loading arm as shown in Figure 3.7 with the summation of moments taken about point *O*. The global end moment calculation, therefore, does not include second order effects based on the deformed specimen and is calculated by using the following expression for the top end moment:

$$M_t = F \cdot (e \cdot \cos\theta_t - (d - d') \cdot \sin\theta_t) + P \cdot d \cdot \sin\theta_t - V_t \cdot d \cdot \cos\theta_t \qquad (3.1)$$

This equation is applicable to the top and bottom ends of the pipe, therefore the subscript t can be generalized using a subscript i. In this equation, θ_t is the end rotation as measured by the rotation meters as discussed in Chapter 2, e is the initial eccentricity of the jacks, d is the distance from the pivot point to the end of the specimen and d′ is the vertical distance from the pivot point to the jack force. As stated, the global moment is then defined as the average of the top and bottom end moments.

Since the local moment versus curvature relationship is obtained for a segment of pipe of length D, the moment should be directly related to this length. As for the global moment, the local moment, M_L, is taken as the average of the moments on the ends of a free body diagram of length D.

The moment at the end of a segment D, M_D^i, may be computed considering the free body diagrams of the top and bottom portions of the test set-up. The superscript i can indicate a top value, t, or a bottom value, b. Figure 3.8 shows the free body diagram of the top portion of the test set-up where summation of moments about point *O* results in the following expression:

$$M_D{}^t = F(e\cdot\cos\theta_t - y_t + d'\cdot\sin\theta_t) + P\cdot y_t - V_t\cdot z_t\cos\theta_t \qquad (3.2)$$

where y_t is the horizontal displacement of the centroid and z_t is the distance from the pivot point to the top of segment D. For simplicity, the value of z_t is based on the undeformed configuration. Also, it should be noted that the angle through which the specimen is sliced to produce the free body diagram does not affect Eq. (3.2) due to the choice of the summation point, therefore eliminating geometric complications. In addition, the vertical force denoted as P-F in Figure 3.8 consists of the net axial load in the pipe wall and the resultant of the fluid pressure acting on the sliced plane.

The moment at the bottom of the pipe segment is obtained using Eq. (3.2) where the subscript and superscript t is replaced by b. The local moment, M_L, as stated, is calculated as the average of the moment at the top of segment D, M_D^t, and the moment at the bottom of segment D, M_D^b.

Secondary, or P-δ, moments caused by the deformation of the test specimen are accounted for in the calculation of moments at the ends of the segment D. The horizontal displacement of a cross-section centroid, y_i, were the subscript i may indicated a top value, t, of a bottom value, b, is affected by radial displacement and cross-sectional

distortion of the specimen. Radial displacement measurements were recorded on the compression face of the test specimens using LVDT's spaced at 250 mm intervals. The results of these measurements will be discussed in Section 3.5. In addition, the change in diameter measurements were recorded during the tests, the results of which are also discussed in Section 3.5. From the compression face displacement and the change in diameter measurements of the specimen, the displacement, y, of the centroid of the test specimen can be calculated. To perform this calculation it is assumed that the centroid of the cross-section being considered is located at mid-point between the compression and tension face. A symmetrical distortion where the centroid of the pipe wall coincides with the centre of the area contained by the cross-section is implied. The assumed symmetrical distortion is shown in Figure 3.9. This may be important for the pressurized specimens because the axial load is applied to the centroid of the pipe wall and the resultant of the internal pressure acts at the centroid of the area contained by the cross-section. As discussed previously, a free body diagram of the end portion of the test set-up is considered and moments are summed about its centroid, *O*, eliminating the axial load acting on the pipe cross-section and the resultant of the internal pressure, from the calculation.

The calculation of the local moment in the test specimens necessitated two assumptions regarding the secondary effects. Since the changes in diameter measurements were not recorded at every load increment the values for intermediate load increments had to be obtained by interpolation between the measured values in the same proportion as the global moments. The local moments were then calculated using the interpolated values. It was also assumed that the friction forces in the test set-up are small and negligible. These assumptions are believed to have little effect on the calculated values of the local moment.

3.4.2 Calculation of Curvature

As with moments, two curvatures, global and local, are defined. The global curvature, ϕ_G, can be calculated using:

$$\phi_G = \frac{|\theta_t| + |\theta_b|}{L} \tag{3.5}$$

where θ_t and θ_b are the top and bottom end rotations, respectively, in radians and L is the specimen length. This curvature includes the end portions of the specimen, which were restrained with collars and therefore stiffer.

A local gauge length equal to the pipe diameter, D, was selected as a suitable gauge length over which a local curvature can be defined. From the experimental data, the curvature may be calculated using the strain readings from the electrical resistance gauges or using the strains calculated from the Demec gauge measurements. In both cases, curvature is defined as the change in angle between two cross-sections divided by the distance between the cross-sections. Figure 3.10 shows a diagram of the segment of pipe D and Eq. (3.6) shows the general formulation to calculate local curvature, ϕ_L, over a segment of length D.

$$\phi_L = \frac{\int_0^D \varepsilon_t dl - \int_0^D \varepsilon_c \cdot dl}{D^2} \tag{3.6}$$

where ε_t and ε_c are the strain on the tension and compression faces respectively and *dl* is an infinitesimal increment along the length of the pipe. For the determination of the experimental local curvature the integrations are replaced by summations because of the discrete nature of strain gauge and Demec gauge measurements.

Local buckling of the pressurized specimens occurred near the end collars. The local buckles occurred partially outside the instrumented test region and a segment of length D, therefore, could not encompass the local deformations. It will be shown in subsequent sections that prior to local buckle formation, the entire specimen length shows regular waves on the compression face. The presence of these deformations indicates that in the pre-buckling range, the location of interval D is not critical and does not significantly affect the result. For this reason, the region of length D was chosen to be located about the centreline of the specimen. Calculations of local moment about the centreline also reflect the most severe second order effects, resulting in a more representative description of the moment capacity of the specimen. For the above reasons the local moment and curvature calculations were performed for the pre-buckling range over a region centred about mid-length of the specimens. Strain gauge measurements were used for the calculation of the local curvature because more data

points were available. As will be shown, the strain measured using strain gauges and Demecs are in good agreement in the pre-buckled range.

Calculation of a local moment versus curvature curve was not feasible for the post-buckling range of the specimens because strain measurements, electric resistance gauges and Demecs, became erratic due to strain localization. A meaningful local curvature, therefore, could not be obtained.

3.5 RESULTS FROM EXPERIMENTS

The following sections describe the experimental results for the four test specimens. Included for each specimen are the following figures:

1) Global moment versus curvature diagram, as described in Section 3.4, superimposed on a plot of percentage of the target axial load and percentage of the yield pressure;
2) A comparison of the local moment versus curvature diagram with the global moment versus curvature diagram as described in Section 3.4;
3) Plots of the buckled configurations;
4) Compression face displacement diagrams;
5) Plots showing the progression of compression face deformations;
6) Change-in-diameter measurements;
7) Extreme fibre strains from strain and Demec gauges; and
8) Determination of the softening strains.

3.5.1 Results from Specimen C45P00

Experimental results for the non-pressurized specimen C45P00 are presented in Figures 3.11 to 3.27.

3.5.1.1 C45P00 – Moment Versus Curvature

The global moment versus curvature diagram, Figure 3.11, shows the overall behaviour of the specimen in the pre- and post-buckling ranges. Plots of global moment, and axial load expressed as a percentage of the target axial load, indicate that the peak moment was reached just before a sudden loss of capacity corresponding to the formation of a local buckle. The peak global moment for this specimen was 1889 kN·m with a corresponding global limit point curvature of 7.6×10^{-6} mm^{-1}. The post-buckling portion

of the moment versus curvature curve is characterized by a sharp descending branch and is accompanied by a sudden drop in axial load. This is a direct consequence of the sudden deformation of the pipe as the local wrinkle formed, resulting in axial shortening of the specimen. Since the MTS Universal Testing Machine was operated under displacement control, deformations of the test specimen resulted in a reduction of the concentric load, P and the axial load in the specimen. The portion of the moment versus curvature diagram affected by the reduced axial load is shown in Figure 3.11 as discontinuous. The global moment values plotted in this region consist of axial loads less than the target values and are therefore not part of the desired equilibrium path. This phenomenon was also encountered by Zimmerman *et al.* (1995), during the testing of a non-pressurized pipe with a D/t of 87 subjected to bending.

A comparison between the global and local moment versus curvature is shown in Figure 3.12. The local moments are only slightly higher than the global moments with a 1.2 percent increase at the peak moment. However, the difference is particularly small in this non-pressurized case because bending deflections, and hence P-δ moments before local buckling, are small. Also, the addition of end collars to stiffen the test specimen near the end plates decreases the global limit point curvature. Local curvatures are less affected by the above effects.

3.5.1.2 C45P00 - Deformations

The deformed configuration for the non-pressurized specimen exhibits a "diamond shape" local buckle with a main depression centred along the bending plane on the extreme compression face and two smaller depressions located on either side of the bending plane. Figure 3.13 shows the compression face of the local buckled and Figure 3.14 shows the profile. This configuration is consistent with the results of previous researchers for non-pressurized specimens (Bouwkamp *et al.* 1973; Mohareb *et al.* 1994; Yoosef-Ghodsi *et al.* 1994, Zimmerman *et al.* 1995). The main depression was located approximately 130 mm below the mid-length of the test specimen with end rotations nearly symmetrical prior to the peak moment.

Figures 3.15 and 3.16 show the history of the compression face displacements measured with LVDT's. Figure 3.15 presents the results for the initial loading stages. Figure 3.16 shows pre- and early post-buckling compression face displacements

including the localization of deformations following local buckle formation. The curves corresponding to a global moment of 1831 kN·m and 1415 kN·m indicate the accelerated deformations that occurred in the post-buckling range. Note that the peak moment configuration is shown by a heavy solid line, pre-buckling configurations are shown by solid lines and post-buckling configurations are shown by dotted lines. This system is followed in the remainder of this chapter. These figures show that there is a distinct pattern of compression face displacements throughout the load history. Figure 3.17 presents the compression face displacements for various global moments. The curves are plotted individually with a vertical axis scaled such that the amplitudes of the different displacements are similar. In Figures 3.15 to 3.17, a positive displacement is a displacement of the compression face towards the tension face of the specimen, (away from the column of LVDT's). This measurement includes the displacement due to overall curvature of the specimen and any local deformations occurring on the compression face.

Figure 3.17 clearly shows that the displaced configuration adopted by the specimen during the application of the axial load is maintained as the applied moment and curvatures are increased. At the peak moment of 1889 kN·m, the shape corresponds to an amplification of the initial displacements. This pattern of deformations is believed to result from the amplification of initial imperfections and non-linearities due to boundary conditions arising from the application of external load. It is evident that these effects are present from the introduction of loading and are not confined to buckling in the vicinity of the limit point. Researchers have previously noted this phenomenon (Kyriakides and Ju, 1992; Kim and Valesco, 1988). As with the axial load tests described by Mohareb *et al.* (1993), the softening, or reduction in the capacity, of the specimen following the limit point is caused by the increased magnitude of the local buckle creating a configuration that is less able to resist the applied load. As stated, the deformations consist of two components: the overall curvature of the specimen and the increased magnitude of the local deviations.

Changes in diameter measurements were recorded as described in Section 2.6.5. The results of these measurements may be subsequently used to calculate out-of-roundness of the specimen based on any of the many proposed equations (Zhou and

Murray, 1994). A positive change is considered to be an increase in diameter, or an outward displacement. The measured cross-sectional distortions in C45P00 are shown in Figure 3.18. Pre-buckled measurements are shown with solid lines and post-buckled measurements are shown with dashed lines. Consequently, increasing distortions are associated with decreasing moments. The figure is further separated in to part a) and b) showing the in-plane and the out-of-plane change in diameter, respectively.

The data suggests that in the pre-buckling range and in regions not directly subjected to local buckling, the decrease of the in-plane diameter is roughly equal to the increase of the out-of-plane diameter. This implies a symmetrical distortion termed ovalization (Brazier, 1927).

Since the data were recorded manually a complete history was not obtained. Only the deformations in the vicinity of the local buckle and the most severe deformations were recorded resulting in the incomplete curves at moments of 878 kN·m and 676 kN·m.

3.5.1.3 C45P00 - Strains

Strains obtained from electric resistance strain gauges are shown in Figures 3.19 to 3.22. Figure 3.19 shows the compression face strains for the initial loading stage. This figure shows that there are slight increases of compression strain at 450 mm, 1250 mm, and 2250 mm from the bottom of the specimen. These stations correspond to locations on the compression face profile shown in Figure 3.17 where inward depressions, relative to the deformed configuration of the pipe, were recorded. These inward local deformations result in increased compressive strains on the surface of the pipe wall. Figure 3.20 shows the compression face strains where the localized increases become more prominent as loading progresses. Strain localization at the local buckle is present on the compression face with strain values greater than 100 000 micro strain recorded using strain gauges for this specimen. However, the scale in Figure 3.20 does not show these points because it would inhibit observation of the behaviour prior to local buckling. Following local buckle formation, strains in the localized region continue to increase while strains in the vicinity of the local deformations decrease with the associated decrease in global moment. This observation is consistent with the mechanism by which softening occurs as described by Murray (1997).

Figure 3.21 shows that the tension face strains for the initial loading stage exhibit the same pattern as on the compression face (Figure 3.19). Increased tension strains are observed at the same locations as on the compression face, namely, at 450, 1250 and 2250 mm from the bottom of the specimen. This is believed to be the result of the slight decrease in diameter due to the local deformations at these points. Figure 3.22 presents the strain history for the extreme tension fibre showing the increased tension at the ends as the specimen approaches the peak moment. Unloading of the tension face is observed in the post-buckling range.

Figures 3.23 to 3.26 show the strains obtained from the Demec gauge measurements on the extreme compression and tension fibres. The Demec strain values are in good agreement with strains obtained from strain gauges. These measurements, however, do not show the additional strains as the strain gauges did for the initial loading stage. Demec measurements were found to sometimes suffer in accuracy when recording low values of strain as shown from the results at 2000 mm from the bottom of the specimen in Figure 3.23. As shown in Figure 3.24, the Demec gauge measurements also indicate strain reversal in the vicinity of the main depression following strain localization. Strains in excess of 160 000 micro strain were recorded using the Demec gauge. Tension face Demec strains for the initial loading stage are presented in Figure 3.25 and the pre- and early post-buckling Demec strains are presented in Figure 3.26. Figures 3.24 and 3.26 clearly demonstrate the increased strain values near the ends of the specimen as the peak moment is approached and confirm the strain gauge results. Since these measurements were recorded manually no data was obtained at or near the peak moment.

Compression face strains are also used to determine critical longitudinal strain values at which local buckling initiates in a pipeline. This strain may be used for the design and maintenance of pipelines if adopted as a limit state. To determine these critical strain values, a comparison of strains based on a gauge length of 2032 mm, i.e. global strain, and strains based on a gauge length of one pipe diameter, i.e. local strain, is used. The length of one pipe diameter was located on the pipe so that it would produce the greatest average local strain value. Figure 3.27 shows the comparison between global and local strains on the compression face of this specimen. The global strain represents average strain over the entire instrumented region of the specimen. The global and local

strains were calculated independently for both strain gauge values and Demec measurements.

The curves plotted in Figure 3.27 for the strain gauge and Demec values show an initial linear relationship with a slope of approximately 45 degrees indicating that the global strains and local strains are almost identical. Strain localization, which coincides with the development of a local buckle, is defined as the point where the curves deviate significantly from the initial linear behaviour. A *softening point* has been defined by Yoosef-Ghodsi *et al.* (1995) as the point on the moment versus curvature response at which the end moments begin a rapid descent. However, the average strain over D at the point of deviation is considered to be the critical strain at which a wrinkle begins to develop. The critical longitudinal compressive strain over a local gauge of one diameter, D, for this specimen is 5200 με based on the strain gauge results. The Demec gauge results indicate that the critical strain is somewhat lower at 3800 με in Figure 3.27. This diagram also demonstrates the excellent agreement between the Demec strain values and strain gauge values in the pre-buckling range.

3.5.2 Results from Specimen C45P20

Experimental results for specimen C45P20 are presented in Figures 3.28 to 3.44.

3.5.2.1 C45P20 – Moment Versus Curvature

The global moment, axial load and internal pressure versus curvature curves are presented in Figure 3.28. A comparison with Figure 3.11 indicates that low internal pressure has the effect of stabilizing the descending branch of the moment versus curvature diagram. The peak global moment for this specimen was 1955 kN·m with a corresponding global limit point curvature of 8.9×10^{-6} mm^{-1}. The latter shows an increase of 17 percent over the results of C45P00. This figure also shows that the percentage of the target axial load was maintained at the desired level throughout the experiment. No loss of axial load following the limit point occurred during this test due to the application of smaller displacement increments near the peak and the more stable behaviour exhibited by the specimen in the post-buckling range.

As shown by the plot of internal pressure the specimen was depressurized, with the axial load and curvature kept constant, when the applied moment was approximately

65 percent of the peak moment. No significant change of the displaced configuration or strains was observed as a result of the depressurization. Control of the load parameters throughout the test was maintained without difficulty with only a marginal increase in internal pressure in the post-buckling region.

A comparison between the global and local moment versus curvature diagrams before local buckling, shown in Figure 3.29, demonstrates that the differences in moments and curvatures are small. The pre-buckling deformations for this specimen were small resulting in little additional moment from second order effects. The maximum difference is approximately 1.7 percent of the global moment at the peak. The results show local moments and curvatures that are higher than the global values for the equivalent load steps.

3.5.2.3 C45P20 – Deformations

The buckled configuration for this specimen consisted of a single outward bulge near the bottom of the specimen. Figure 3.30 shows the buckled configuration of the compression face and Figure 3.31 shows the profile of the bulge. The crest of the bulge occurred at a distance of 350 mm from the bottom of the specimen and 125 mm above the confining collar. This buckling mode is consistent with previous experience for pressurized specimens (Bouwkamp *et al.* 1973; Mohareb *et al.* 1994).

Figure 3.32 shows the compression face displacements for the initial loading stage. The curve denoted "Pressure" shows radial expansion of the specimen due to the internal pressure. The curve "Pressure+Axial" indicates that the desired level of internal pressure and axial load have been applied to the specimen without any moment. The curves denoted "Pressure+Axial", "224 kN·m" and "422 kN·m" show that the specimen was slightly misaligned. This is evidenced by the larger displacements at the top of the specimen than at the bottom. Figure 3.33 shows the compression face displacements in the pre-buckling and early post-buckling ranges. The displacements at the bottom of the specimen clearly demonstrate the development of an outward bulge relative to the deformed specimen. Since an LVDT was located within only a few millimetres of the crest of the bulge, the magnitude of the bulge was fully captured.

As with the non-pressurized specimen C45P00, a distinct pattern of compression face deformations is prominent at all stages of loading. Figure 3.34 shows the

compression face displacements for various applied moments. This figure shows the formation of a series of waves along the pipe. The curve "Axial+Pressure" in this figure shows the formation of outward deformations or bulges, relative to the rest of the pipe, close to the ends of the specimens due to the application of internal pressure and the desired axial load. Since the axis of the pipe was not perfectly vertical during the test, a linear regression line was added to the curve (b) to emphasize the end bulges relative to the rest of the pipe. This suggests that the boundary conditions used during the test produce a significant disturbance near the ends of the specimen. This boundary disturbance is a known phenomenon and is caused by the restraints at the ends of the test specimens. This restraint results in local curvature of the pipe wall in order to maintain compatibility between the restrained edge and the pipe wall that expands under internal pressure. The occurrence of these boundary disturbances is further explained by Timoshenko and Gere (1961).

The presence of significant compression face deformations, discussed for Figure 3.34, suggests that local buckling could be triggered at any one of these deformations along the length of the specimen. However, local buckling will occur at the most critical section. The additional deformations in the pipe wall observed at the ends of the specimen due to the boundary disturbances produces the most critical section. Local buckle formation in this test was, therefore, predisposed to occur at one of the ends. It is believed that, with all else being equal, the conditions at the bottom end are slightly more severe than the top end due to the hydrostatic pressure in the pipe and the self-weight of the test set-up, prompting failure at this location.

Figure 3.35 presents the change in diameter measurements for this specimen. For this specimen, only the in-plane change in diameter measurements were recorded resulting in the single figure. This figure demonstrates that the magnitude of the change in diameter does not increase significantly as the load is increased as shown by curves 1342 kN·m and 1444 kN·m. It is believed that the internal pressure stabilizes the pipe wall against decreases in diameter. Following local buckle formation, and hence localization of the deformations into a single outward bulge, cross-sectional deformations are increased significantly at the location where local buckling takes place. After localization, only one reading of the maximum deformations was recorded for this test.

3.5.2.3 C45P20 - Strains

Strains based on electrical resistance gauges yielded the results shown in Figures 3.36 to 3.39. Figure 3.36 and Figure 3.38 present strains on the compression and tension face, respectively, for the initial loading stage. The curve denoted "Pressure" indicates tensile strains in the specimen upon pressurization corresponding to the longitudinal expansion of the specimen due to the pressure acting on the end plates. In addition, both curves exhibit increased tensile strains toward each end of the specimen with good agreement between the tension and compression sides. The occurrence of higher tensile strains at the end strain gauges upon pressurization is consistent for all pressurized specimens. This additional strain is attributed to local bending in the pipe wall due to the formation of the end bulges caused by the boundary restraints. Figure 3.37 and Figure 3.39 show the pre- and post-buckling strain distributions along the specimen. Increased strain on the compression face due to strain localization is not apparent from these measurements because the bulge occurred outside the portion of the pipe instrumented with electrical resistance gauges. Figure 3.30 shows the buckle located below the first strain gauge along the length of the specimen.

Strains obtained from Demec readings are in good agreement with those obtained from the strain gauges throughout the load increments. The initial load stage is shown in Figure 3.40 for the compression face and in Figure 3.42 for the tension face. Demec data was not recorded for the pressurization stage during this test. Figure 3.41 and Figure 3.43 for the compression and tension faces, respectively, show the pre- and early post-buckling strains recorded by Demecs. A Demec point located on the crest of the buckle captures a portion of the strain localization as shown in Figure 3.41. Strains in excess of 65 000 micro strain were recorded using the Demec gauge.

Figure 3.44 represents the comparison between the average strain over 2032 mm and average strain over D for specimen C45P20. The critical compressive strain over a local gauge of one diameter, D, is 5100 $\mu\varepsilon$ based on strain gauge measurements. In this case, no localization was observed due to the location of the local buckle with respect to the strain gauges. The point where strains begin to reverse was therefore considered to coincide with localization of strains in the local buckle. The Demecs, with the local gauge placed as near to the local buckle as possible, show the critical strain at 4400 $\mu\varepsilon$

and demonstrates the good agreement between the two measurement techniques in the pre-buckling region.

3.5.3 Results from Specimen C45P40

Experimental results for specimen C45P40 are presented in Figures 3.45 to 3.61.

3.5.3.1 C45P40 – Moment Versus Curvature

The global moment, axial load and internal pressure versus global curvature curves, shown in Figure 3.45, indicate that internal pressure at this level does not affect the moment capacity compared to the curves in Figures 3.11 and 3.28. The stabilizing effect of internal pressure is also demonstrated with a more gradual loss in capacity in the post-buckling range compared to specimens C45P00 and C45P20 shown in Figures 3.11 and 3.28, respectively. The peak global moment for this specimen was 1952 kN·m with a corresponding global limit point curvature of 11.1×10^{-6} mm^{-1}. The former represents an increase of 3 percent, and the latter represents an increase of 46 percent over the results of C45P00. Also shown in this figure is the axial load that was maintained at the desired level except for a brief period near the end of the test. The corresponding point on the moment versus curvature curve is plotted as discontinuous. The internal pressure curve shows two depressurizations at 70 and 88 percent of the peak moment. The depressurizations did not have a significant effect on the strains or displacements measured during the test.

A comparison between the global and local moment versus curvature diagrams prior to local buckling, shown in Figure 3.46, demonstrates that the second order moment is small, approximately 2 percent of the global moment at the peak moment. However, the difference between local and global curvatures at a given moment is larger than that observed in the specimens having lower pressures.

3.5.3.2 C45P40 - Deformations

The buckled configuration for this specimen consisted of a single outward bulge near the bottom of the specimen. Figure 3.47 shows the buckled configuration of the compression face and Figure 3.48 shows the profile of the bulge. The crest of the bulge occurred at 400 mm from the bottom of the specimen and 175 mm above the confining collar.

Figure 3.49 presents the compression face displacements for the initial load increments. The curve denoted "Pressure" shows radial expansion of the specimen due to the internal pressure acting alone. Figure 3.50 shows the compression face displacements for the pre- and early post-buckling ranges. The measured displacements at the bottom of the specimen demonstrate the development of the outward bulge relative to the deformed pipe. The full magnitude of the buckle was not captured, however, because the peak displacement occurred between the two bottom measurement points. Note also that the curves for 328 kN·m and 905 kN·m overlap near the top of the specimen. This was caused by an inadvertent interruption of the test resulting in unloading of the test specimen. As the test was resumed, it is believed that the specimen shifted a few millimetres causing the curves to overlap. The progression of the compression face deformations is presented in Figure 3.51. The compression face pattern is shown to initiate during the application of the axial load and to fully develop with a small moment. A regression line was added to the "Pressure+Axial" curve in Figure (b) to demonstrate the occurrence of the end bulges, relative to the rest of the pipe, caused by the boundary restraints. Compared to C45P20, the end bulges do not appear to be as prominent for this specimen. This may be due to the interval and location of the LVDT measurements. As will be shown in the following sections, strain measurements at the ends of the specimen indicate significant bulging.

Measurements of the change in diameter are presented in Figure 3.52. These measurements indicate that ovalization of the cross-section does occur when the specimen is subjected to bending. However, the magnitude of these distortions in-plane is less than the magnitude out-of-plane. After local buckling, the deformations localize into a single outward bulge increasing cross-sectional deformations significantly both in the in-plane and out-of-plane directions. The maximum increase in diameter occurs in the out-of-plane direction.

3.5.3.3 C45P40 - Strains

Strains based on electrical resistance gauges are presented in Figure 3.53 to Figure 3.56. Figures 3.53 and 3.55 show the strain distribution for the initial loading stage on the compression and tension faces, respectively. The curves denoted "Pressure" indicate tensile strains in the specimen due to pressurization. The compression face and

tension face gauge values are also in good agreement with each other. As observed in previous test specimens, both extreme fibres exhibit the higher tensile strains toward each end of the specimen indicating the presence of end bulges as discussed previously. Figure 3.54 and Figure 3.56 show the pre- and early post-buckling strain distributions for this specimen. The strain distribution is less uniform on the compression face due to significant local deformations prior to local buckling. The increased compression strains measured at 1500 mm from the bottom of the specimen agree well with the deformations presented in Figure 3.51 and can be attributed to bending of the pipe wall. As with specimen C45P20, the local bulges detected near the ends of the test specimen are the most critical section causing local buckle formation near the disturbed boundary conditions.

As for the previous specimens, the Demec strain values are in good agreement with the strain gauge readings for all loading stages. The initial loading stage is shown in Figure 3.57 and Figure 3.59 for the compression and tension faces, respectively. At the time that the Demec readings were taken under full internal pressure, some of the axial load was applied to the specimen to compensate for the internal pressure acting on the end plates. These figures, therefore, do not show tensile strains for the "Pressure*" step. Figures 3.58 and 3.60 show the strain distributions for the pre- and early post-buckling range. Strain localization is shown to occur at the bottom of the specimen on the compression face. Figure 3.60 shows curves with discontinuities on the tension face due to the loss of a Demec point during the test.

Figure 3.61 presents a comparison between global and local strains for specimen C45P40. The critical compressive strain from strain gauge measurements averaged over a local gauge of one diameter, D, is 7100 $\mu\varepsilon$. This figure shows both Demec strain values and strain gauge values and demonstrates the good agreement between the two measurement techniques in the pre-buckled region. A representative critical compressive strain based on Demec measurements could not be obtained due to erratic strains measured across the bulge following local buckle formation. A linear relationship, therefore, could not be established in the post-buckling region to properly determine the point of localization. The value indicated in the Figure 3.61, 4600 $\mu\varepsilon$, was used as a conservative estimate of the critical strain based on Demecs for this specimen.

3.5.4 Results from Specimen C45P80

Experimental results for specimen C45P80 are summarized in Figure 3.62 to Figure 3.78.

3.5.4.1 C45P80 – Moment Versus Curvature

The global moment, axial load and internal pressure versus curvature curves are presented in Figure 3.62. A significant change in the overall moment carrying behaviour of the specimen is seen compared to the previous loading conditions of C45P00, C45P20 and C45P40 in Figures 3.11, 3.28 and 3.45, respectively. High internal pressure, $0.8p_y$, reduces the moment carrying capacity of the specimen by 19 percent compared to the non-pressurized specimen, C45P00. However, the stabilizing effect of internal pressure is further demonstrated with the gradual and stable loss of capacity following local buckle formation. The curvatures, and hence deformations, are significantly increased at all load levels compared to specimens subjected to lower internal pressure. The peak global moment for this specimen was 1525 kN·m with a corresponding global limit point curvature of 17.0×10^{-6} mm^{-1}. The latter represents an increase of 124 percent over the results of C45P00. The internal pressure shows three depressurization cycles at 77, 84 and 97 percent of the peak moment. The third depressurization was conducted at a curvature 101 percent greater than the limit point curvature for specimen C45P00 resulting in no significant change in strains or displacements other than the small dip observed in the moment versus curvature curve shown in Figure 3.62.

A comparison between the global and local moment versus curvature diagrams, presented in Figure 3.63, shows no significant difference between the moments at this level of internal pressure. The internal pressure stabilizes the specimen to enable large deformations to occur prior to local buckling, resulting in slightly higher second order moments. At the peak moment, the second order moment increases the global moment by 7 percent.

3.5.4.2 C45P80 - Deformations

The buckled configuration for this specimen consisted of a single outward bulge at the bottom end of the specimen. Figure 3.64 shows the configuration of the compression face and Figure 3.65 shows the profile. The crest of the bulge occurred at 430 mm from the bottom of the specimen and 205 mm above the confining collar.

Figure 3.66 shows the compression face displacements during the initial loading stage. The difference between the end displacements during the initial increments is believed to be the result of a small misalignment causing the top of the specimen to shift outward as load was applied. This is not considered to adversely affect the validity of these measurements. Figure 3.67 shows the compression face displacements for the pre- and early post-buckling ranges. The measurements at the bottom of the specimen demonstrate the development of the outward bulge but do not capture the full magnitude of the buckle because the peak displacement occurred between the two bottom measurement points as indicated.

From Figure 3.68 it is apparent that the deformed configuration adopted with the application of internal pressure and axial load is maintained with increasing moment. The curve designated "Pressure+Axial" shows the end bulges (less displacement relative to the rest of the pipe) resulting from the boundary disturbances. As with the other pressurized specimens, the most critical section occurred at the bottom end of the specimen resulting in local buckle formation at that point.

Change in diameter measurements for specimen C45P80 are presented in Figure 3.69 and are similar to the results for C45P20 and C45P40. No ovalization of the cross-section is shown to occur; however the magnitude of the out-of-plane distortion increases gradually until the limit point is reached. The in-plane measurements are essentially zero until the post-buckling range. Once deformations localize, the specimen exhibits a prominent outward bulge in both the in-plane and out-of-plane directions as shown in figure (a) and (b), respectively. The maximum increase in diameter is in the out-of-plane direction. Figure (a) also shows a wavy deformation along the specimen in the curve denoted "1275 kN·m".

3.5.4.3 C45P80 - Strains

Strains based on electrical resistance gauges are presented in Figures 3.70 to 3.73. Figures 3.70 and 3.72, show the compression and tension face strain distributions, respectively, for the initial loading stage. The curves denoted "Pressure" indicate small strains in the specimen because this increment includes the portion of the axial load to compensate for pressure effects. The compression face and tension face gauge values are also in good agreement with each other. As observed in the previous test specimens, both

curves exhibit increased tensile strains towards each end of the specimen. This indicates the presence of end bulges due to the boundary disturbances. Figure 3.71 and Figure 3.73 show the pre- and early post-buckling strain distributions for this specimen. The strain distribution is less uniform on the compression face due to significant deformations prior to local buckling.

Demec strain values are in good agreement with the strain gauge readings throughout the load increments. As expected, deviations become more notable once local deformations occur. Figures 3.74 and 3.76 show the initial loading stage for the compression and tension face, respectively. At the time that the Demec readings were taken for the "Pressure" increment, some axial load was already applied to the specimen to compensate for pressure effects. Figures 3.75 and 3.77 show the strain distributions for the remainder of the test. Strain localization on the compression face is shown to occur at the bottom of the specimen. The strain distribution just prior to the peak moment for this specimen is erratic because of large local deformations that occurred on the compression face.

Figure 3.78 presents a comparison between global and local strains for specimen C45P80. The figure does not show a distinct point of localization for this specimen. The figure therefore includes the comparison of the highest compressive strain gauge or Demec measurement as the local measure versus the global strain. Distinct points of localization are then determined. Following, the corresponding critical compressive strain averaged over a local gauge of one diameter, D, is 13100 $\mu\varepsilon$ based on electrical resistance gauges. Demec measurements yield a critical strain of 12700 $\mu\varepsilon$. Also, these diagrams demonstrate the good agreement between the two measurement techniques in the pre-buckled range even with the presence significant of local deformations.

3.5.5 General Results

The global moment versus curvature relationships for the four test specimens are presented in Figure 3.79. This figure shows the effect of increasing internal pressure on the response of pipe subjected to combined loads. Increasing internal pressure stabilizes the pipe wall and delays local buckling until greater values of curvature are attained. Also, increasing internal pressure produces a post-buckling behaviour that is more stable resulting in a reduction of the overall loss of capacity following local buckle formation.

In addition, the figure demonstrates that at the third depressurization of specimen C45P80, as indicated by an arrow, the curvature is significantly higher than the limit point curvature of the specimen with no internal pressure. The conclusion can be drawn that pressure reductions at an imposed level of curvature do not trigger buckling of the pipe when subjected to these test conditions.

The relationship between the level of internal pressure and the peak moment is shown in Figure 3.80 for the global and local moments. Cubic polynomial regression lines are included to show a possible relationship between the internal pressure and peak moment.

Figure 3.81 shows the limit point curvature as a function of the internal pressure of the specimen. Global and local values are included in this figure with curves showing possible relationships based on quadratic polynomials. It can be seen that the difference between the local and the global values for a given pressure is roughly constant.

Figure 3.82 shows the critical longitudinal compressive strains as a function of the level of internal pressure. Strain gauge and Demec results from the tests are shown and are based on the average strain over a gauge length D as described previously. Quadratic polynomials are included to show a possible relationship between the parameters. The values are the strains determined from Figures 3.27, 3.44, 3.61 and 3.78.

Table 3.3 summarizes the results of the preceding figures. Included for each specimen are the peak global and local moments; global and local limit point curvature; and critical compressive strains determined from strain gauge and Demec measurements. In addition, the post-buckling configuration is noted.

Table 3.1
Measured Static Engineering Material Properties from Tension Coupon Tests

Material Test	E MPa	Proportional Limit MPa	Stress@ 0.2% Strain MPa	Stress@ 0.5% Strain MPa	Ultimate Strength MPa
Circumferential Coupons					
C-1	235700	305	412	526	614
C-2	221900	298	401	519	607
C-3	234200	302	409	516	600
C-Average	**230600**	**302**	**407**	**520**	**607**
Longitudinal Coupons					
L-1	207000	294	404	507	599
L-2	222700	298	402	502	593
L-3	232700	288	393	500	595
L-Average	**220800**	**293**	**400**	**503**	**596**
Average Material Properties					
	225700	**298**	**404**	**512**	**601**

Table 3.2
Magnitude of Measured Initial Imperfections

Specimen	Maximum (mm)	Compression Face Maximum (mm)	Minimum (mm)	Compression Face Minimum (mm)
C45P00	1.74	0.24	-1.54	-0.75
C45P20	1.93	1.08	-2.41	-1.01
C45P40	1.47	0.84	-1.62	-0.81
C45P80	1.46	0.73	-1.76	-0.01

Table 3.3
Summary of Experimental Results

Specimen	Peak Global Moment (Local) in kN·m	Global Limit Point Curvature (Local) in $x10^{-6}$ mm^{-1}	Critical Strains Strain Gauges (Demecs) in με	Buckle Shape
C45P00	1889 (1912)	7.6 (9.7)	5200 (3800)	Diamond
C45P20	1955 (1987)	8.9 (9.1)	5100 (4400)	Bulge
C45P40	1952 (1995)	11.1 (12.8)	7100 (4600*)	Bulge
C45P80	1525 (1634)	17.0 (19.1)	13100 (12700)	Bulge

* Critical strain based on Demecs for specimen C45P40 was not defined properly. See Section 3.5.3

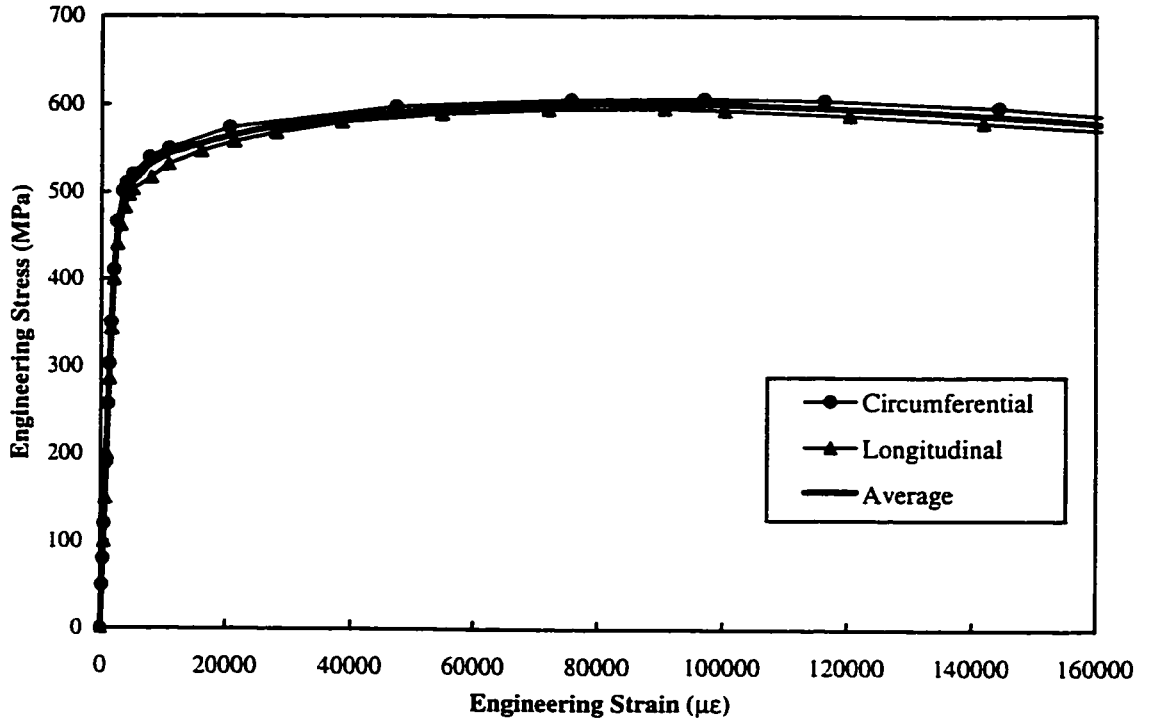

Figure 3.1 Static engineering material properties from tension coupon tests

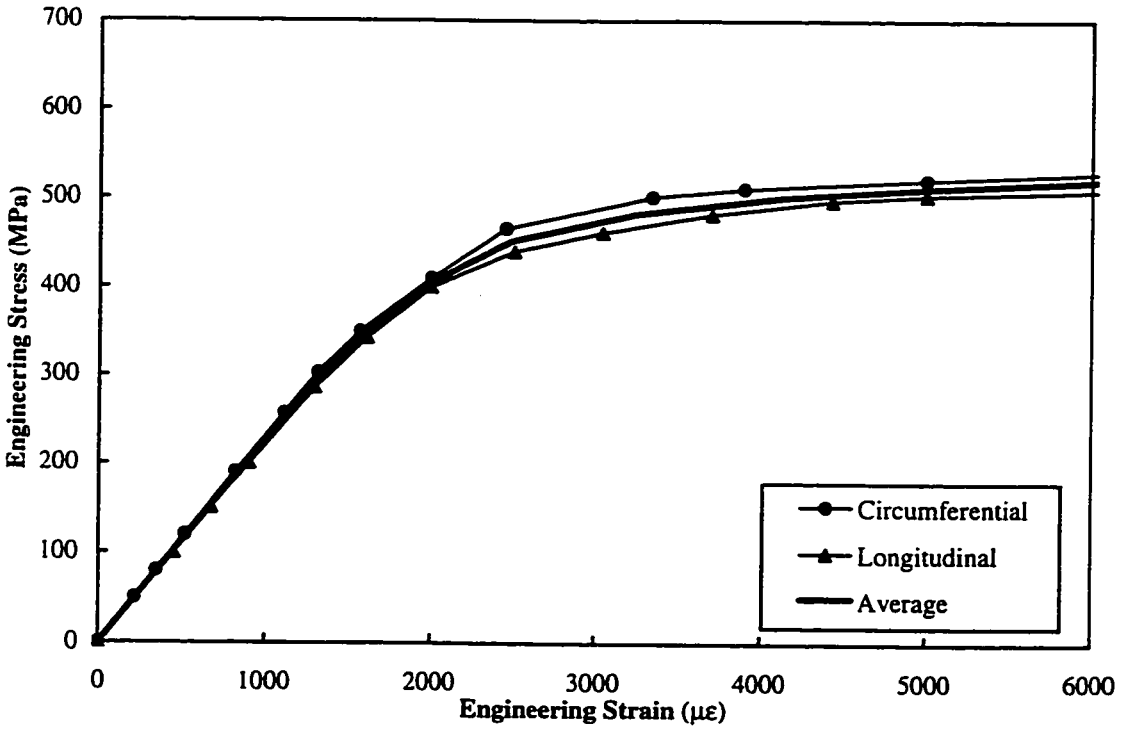

Figure 3.2 Elastic and first yield static engineering material properties from tension coupon tests

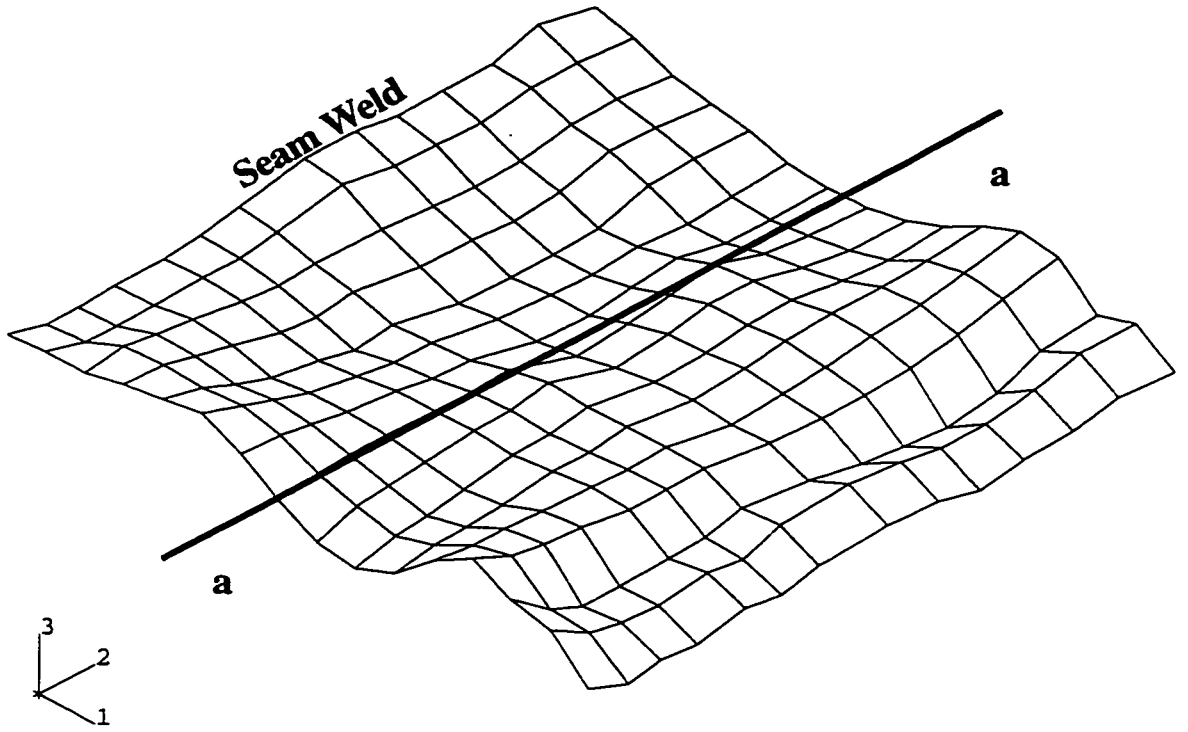

Figure 3.3 Measured initial imperfection pattern for specimen C45P00

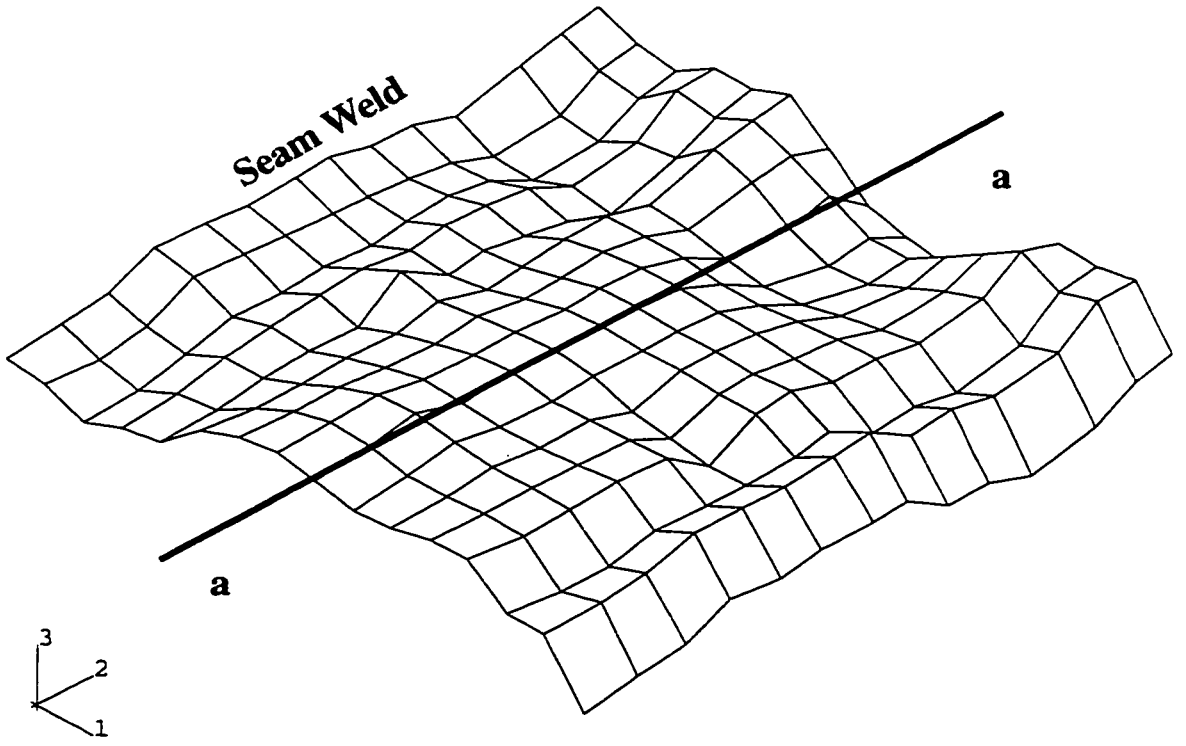

Figure 3.4 Measured initial imperfection pattern for specimen C45P20

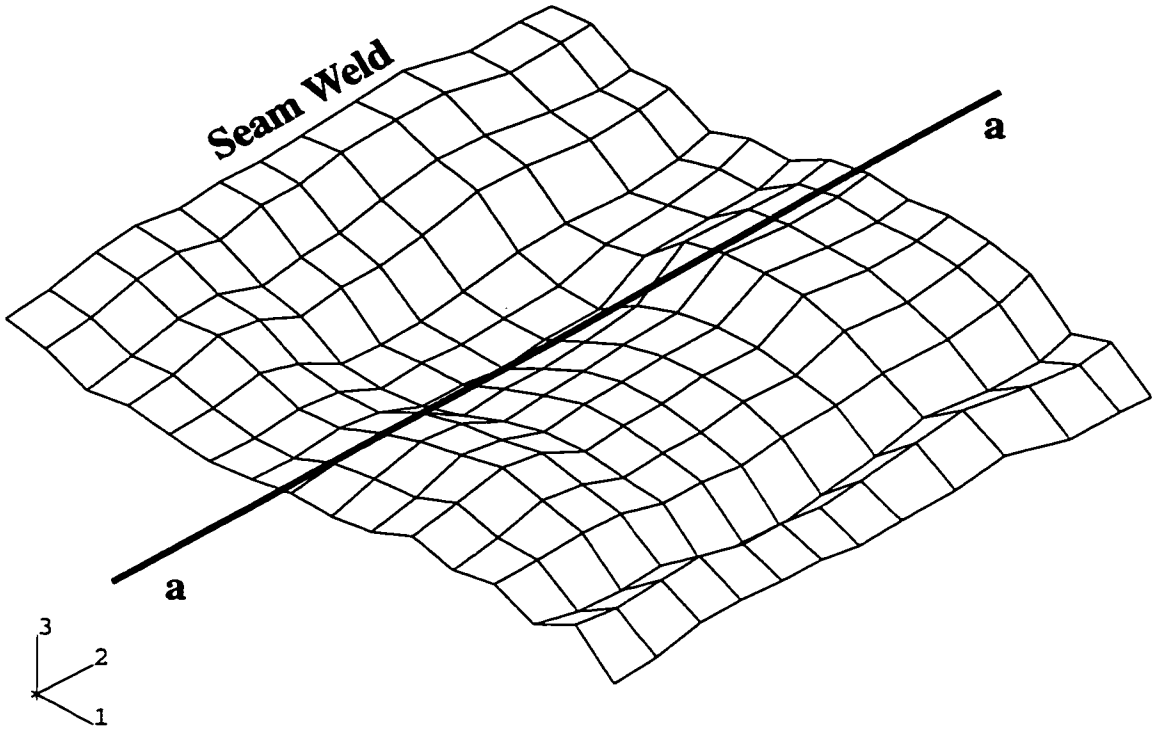

Figure 3.5 Measured initial imperfection pattern for specimen C45P40

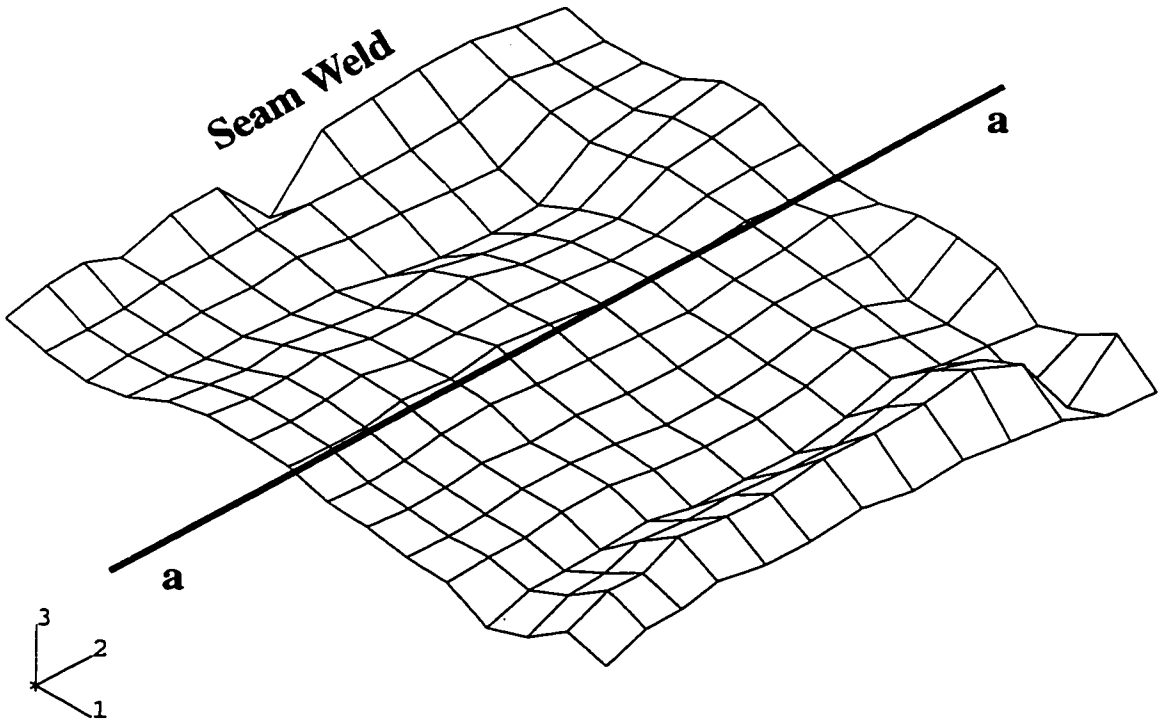

Figure 3.6 Measured initial imperfection pattern for specimen C45P80

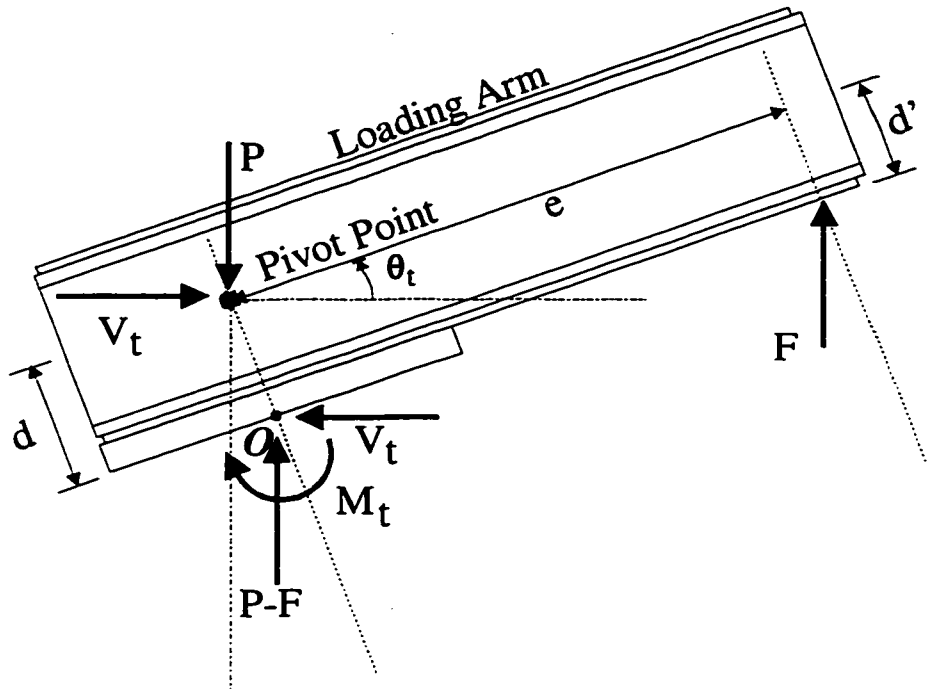

Figure 3.7 Free body diagram of top loading arm for calculation of top end moment

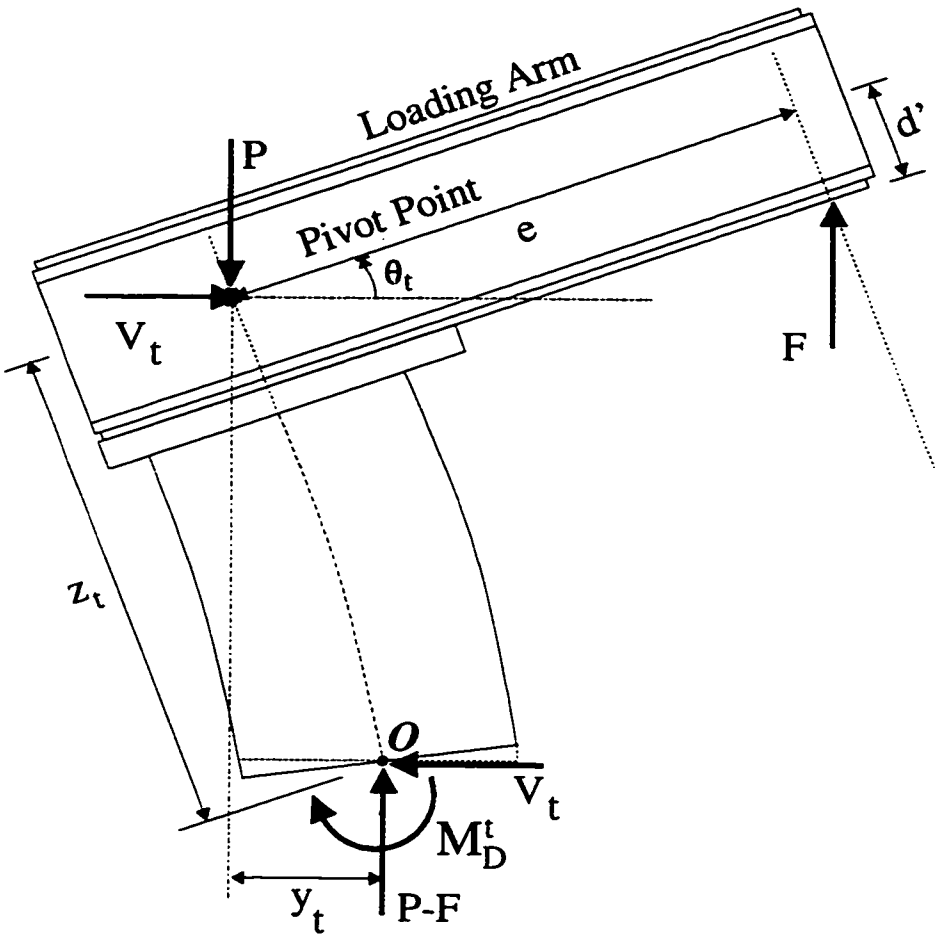

Figure 3.8 Free body diagram used for calculation of moment at the top end of segment D

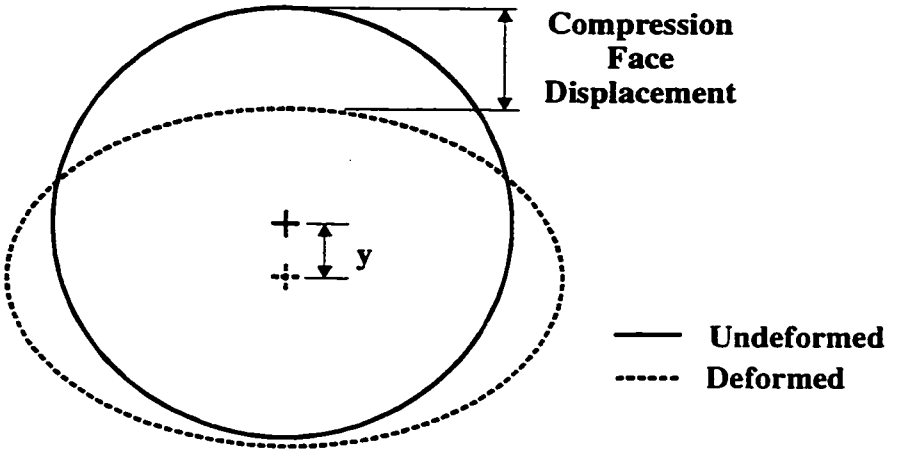

Figure 3.9 Symmetric cross-section distortion

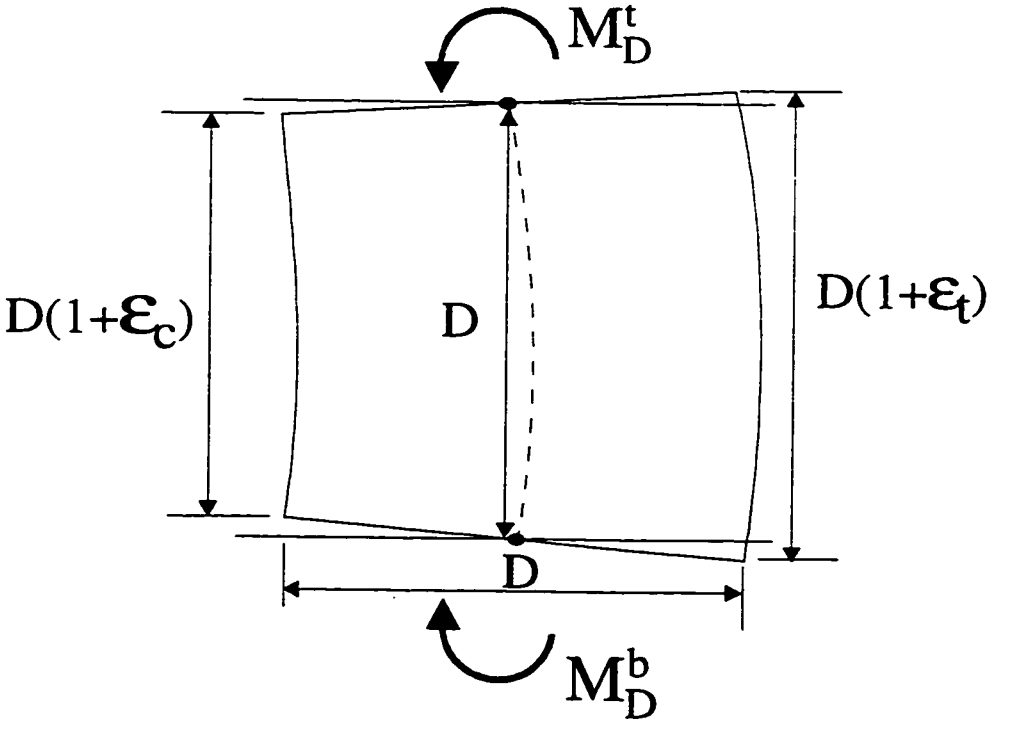

Figure 3.10 Pipe segment of length D used to define local curvature

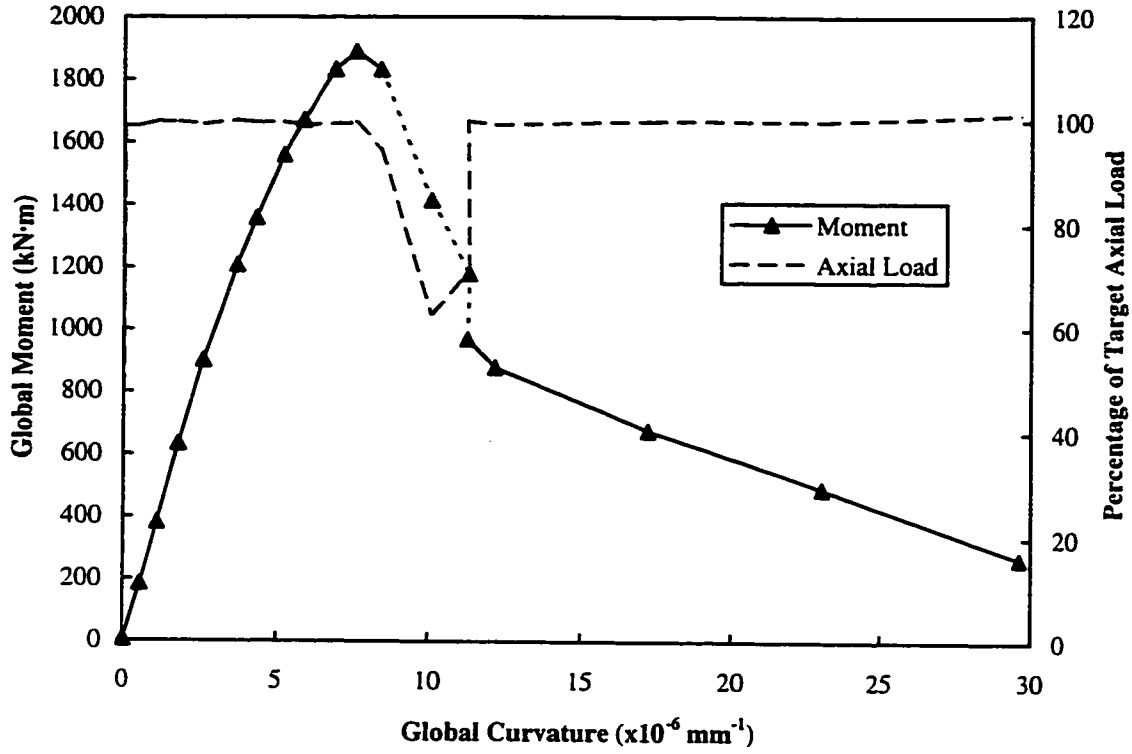

Figure 3.11 C45P00 – Global moment and axial load versus curvature diagram

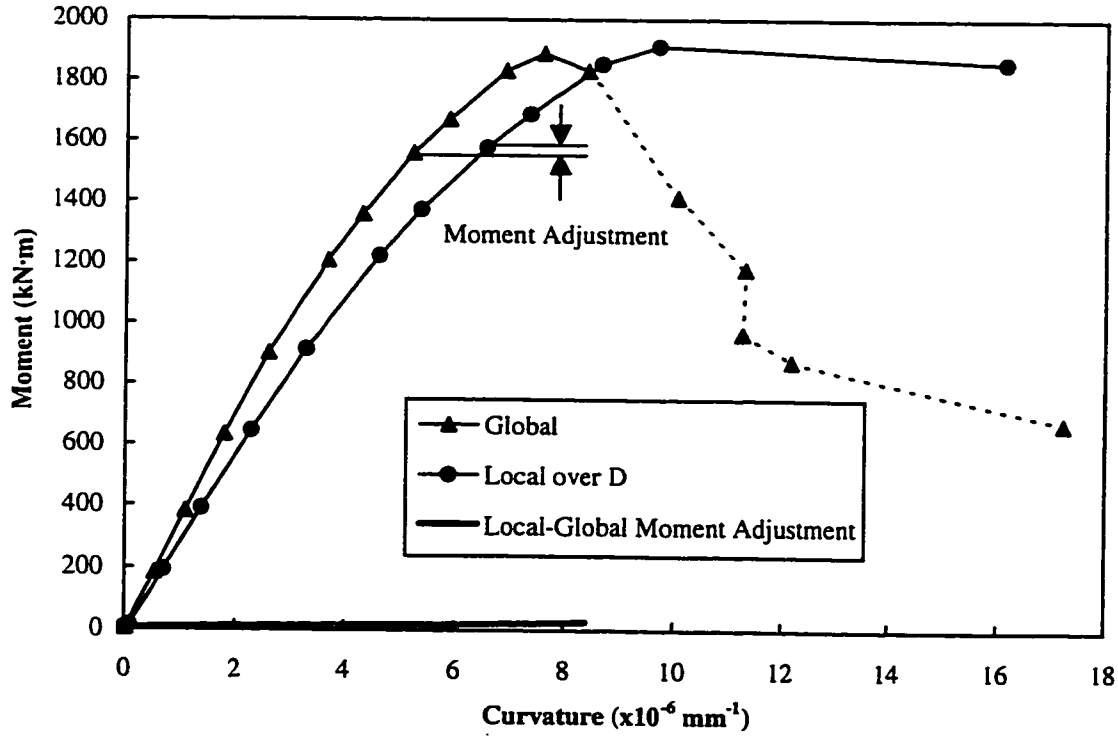

Figure 3.12 C45P00 – Comparison of global and local moment versus curvature

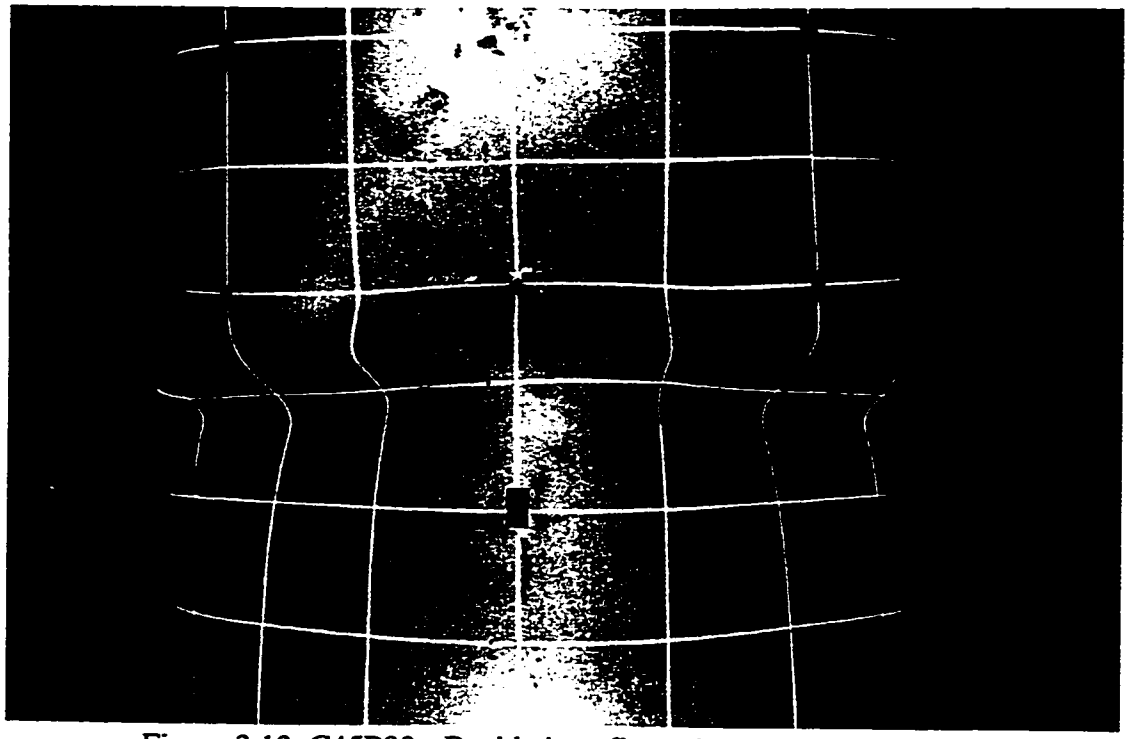

Figure 3.13 C45P00 - Buckled configuration, compression face

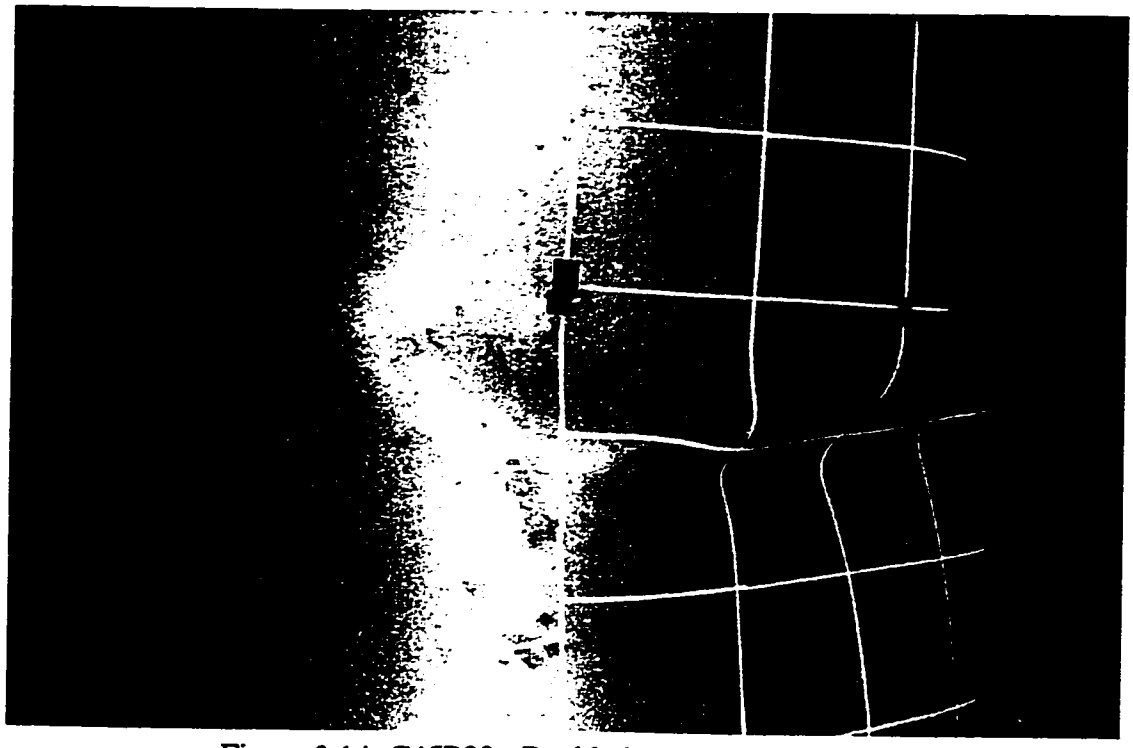

Figure 3.14 C45P00 - Buckled configuration, profile

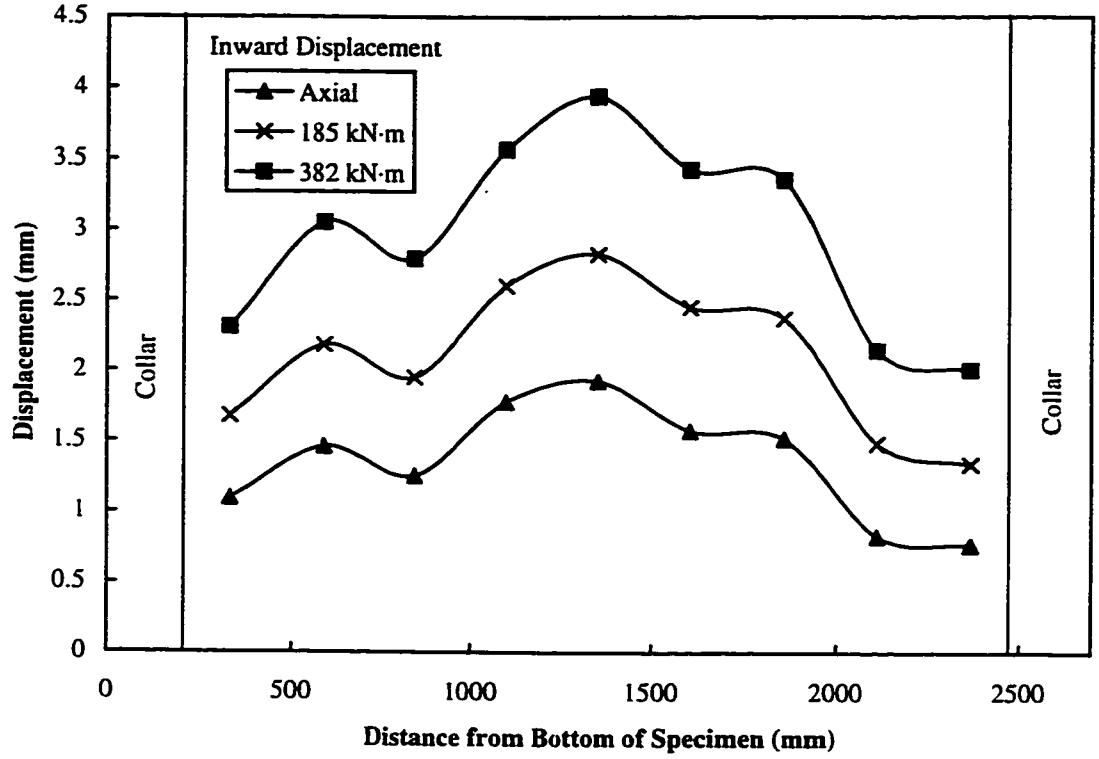

Figure 3.15 C45P00 – Compression face displacements: initial loading stage

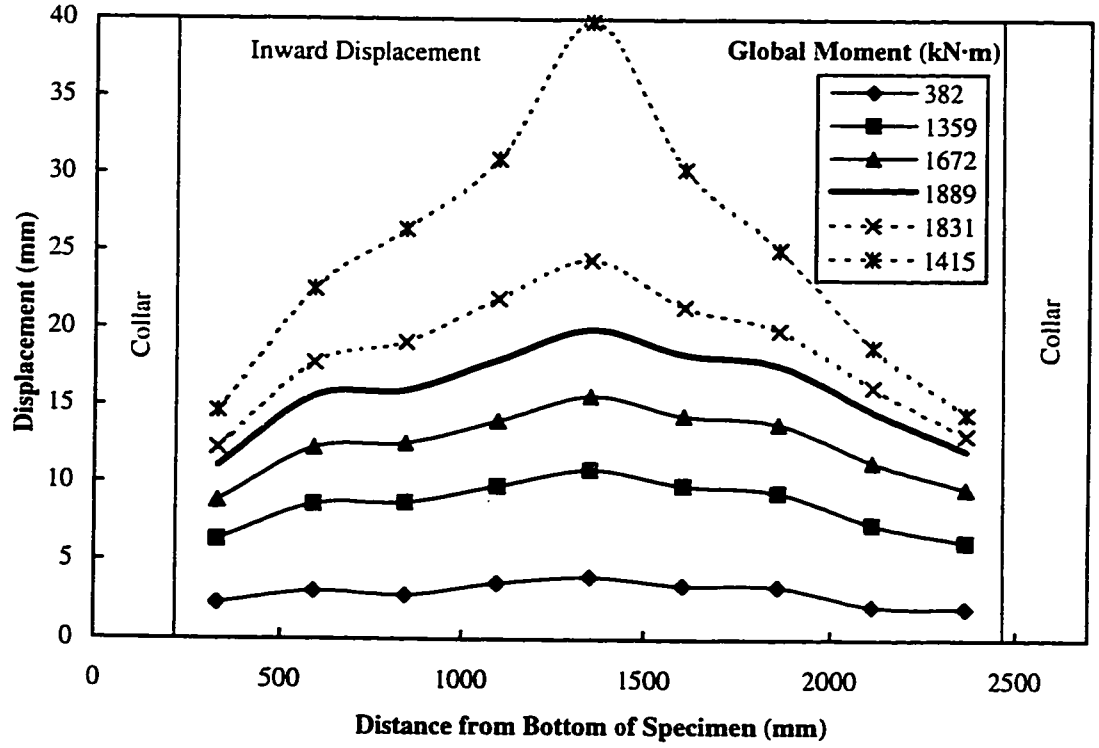

Figure 3.16 C45P00 – Compression face displacements

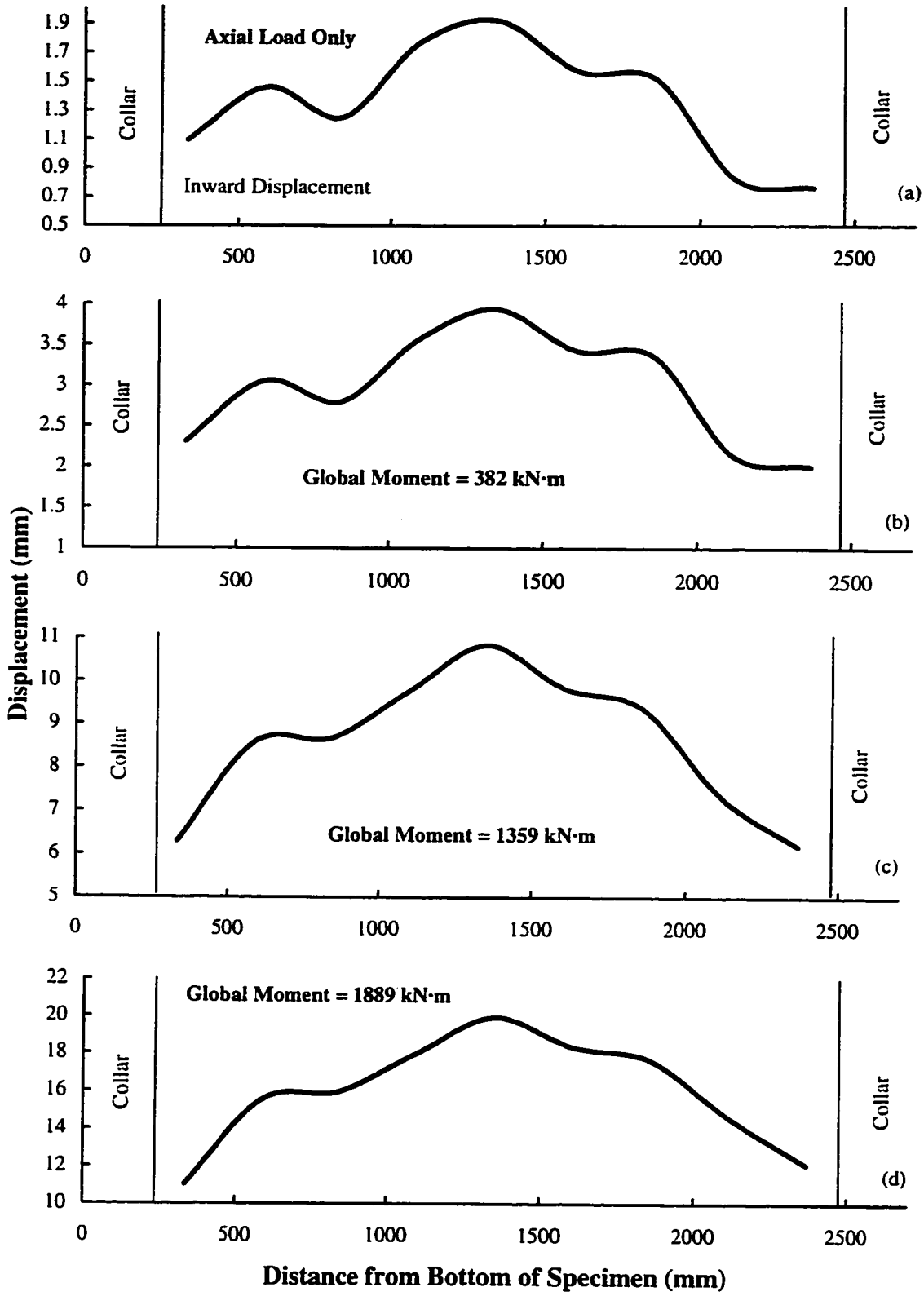

Figure 3.17 C45P00 - Progression of compression face displacements

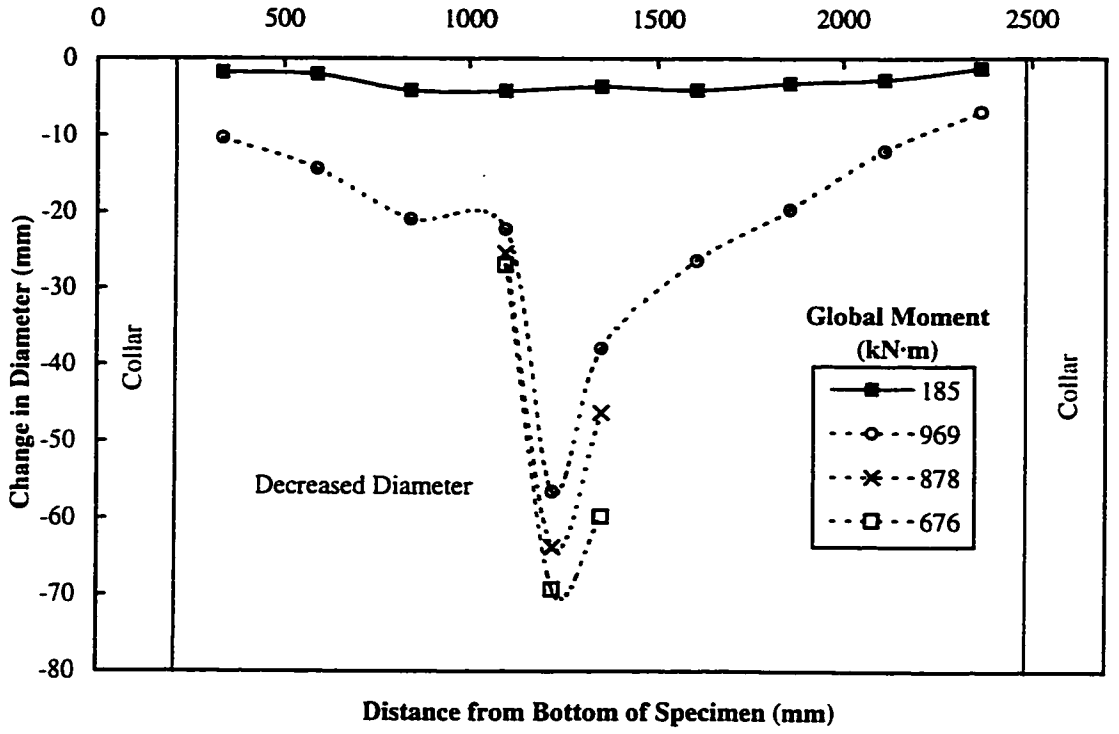

a) In-Plane Change In Diameter

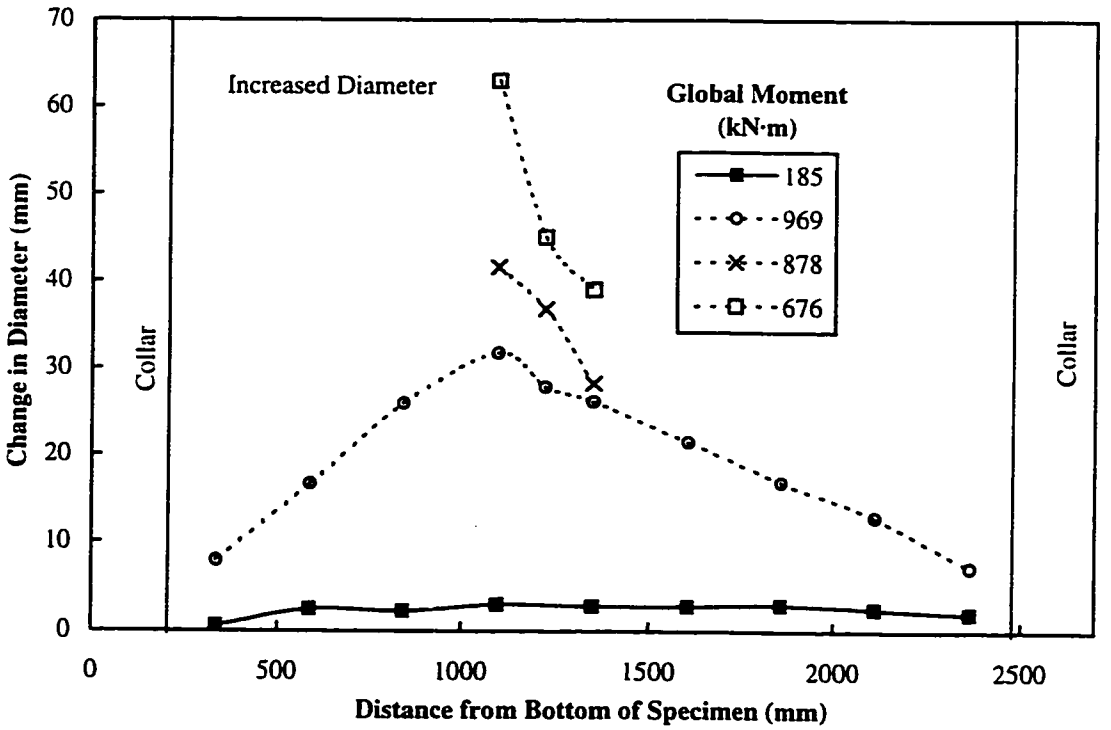

b) Out-of-Plane Change in Diameter

Figure 3.18 C45P00 – Measured changes in diameter

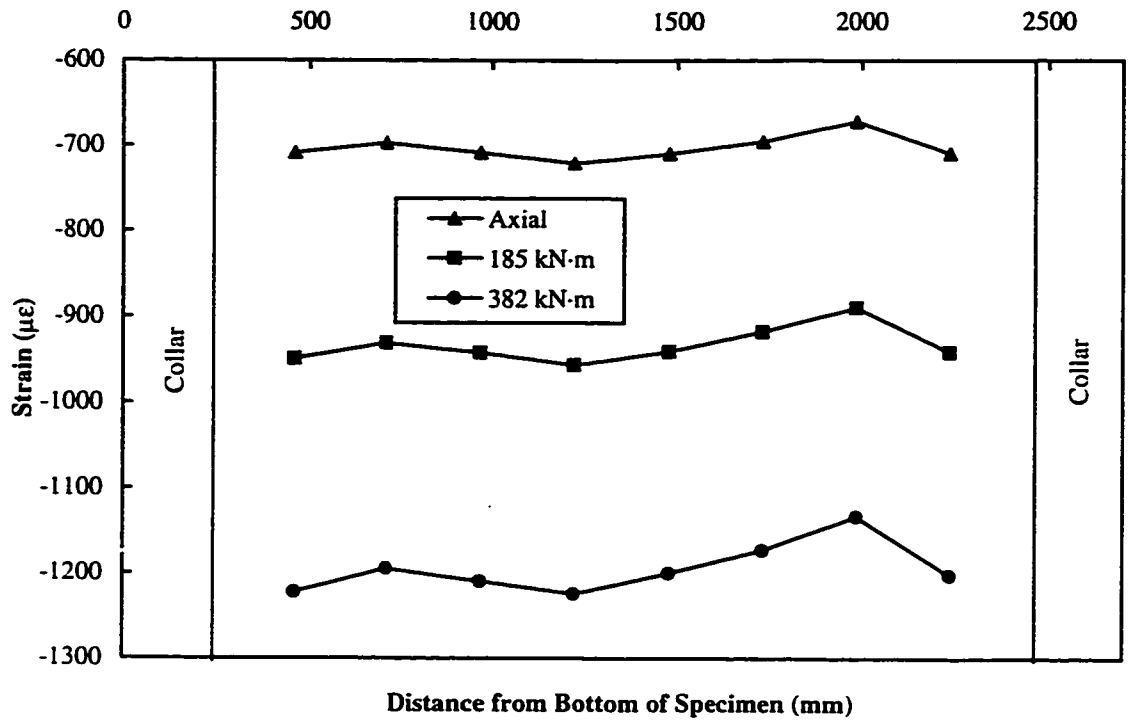

Figure 3.19 C45P00 – Compression face strain gauge measurements: initial loading stage

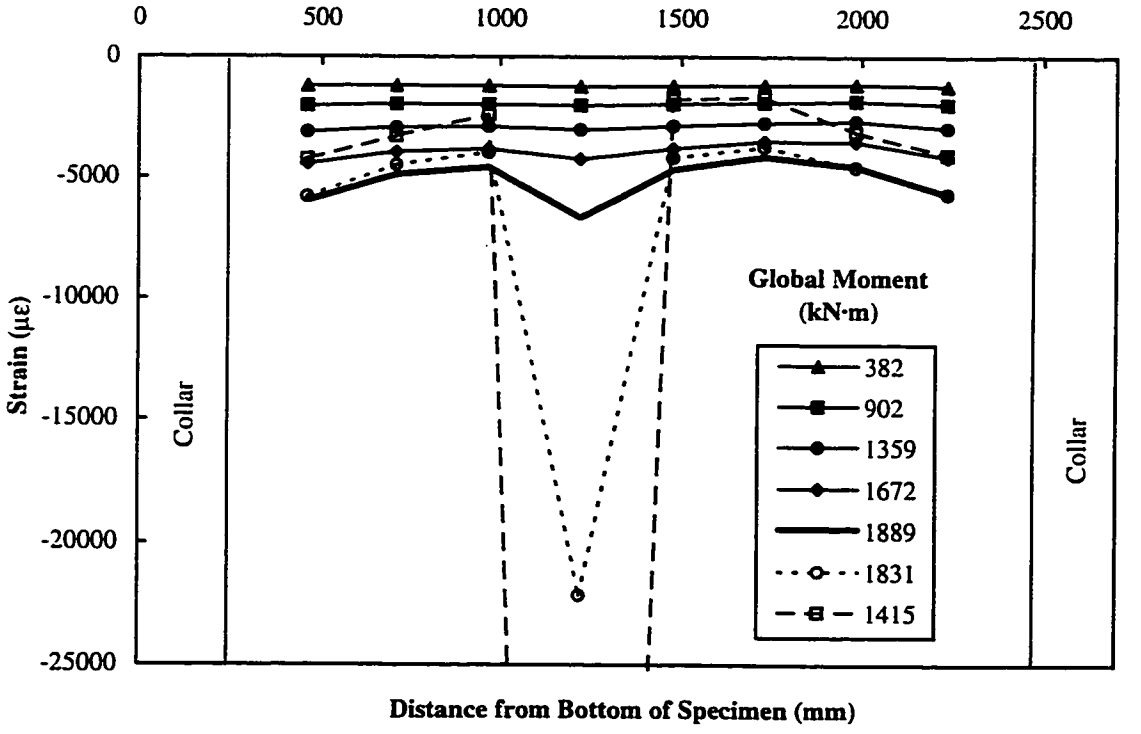

Figure 3.20 C45P00 – Compression face strain gauge measurements: pre- and post-buckling

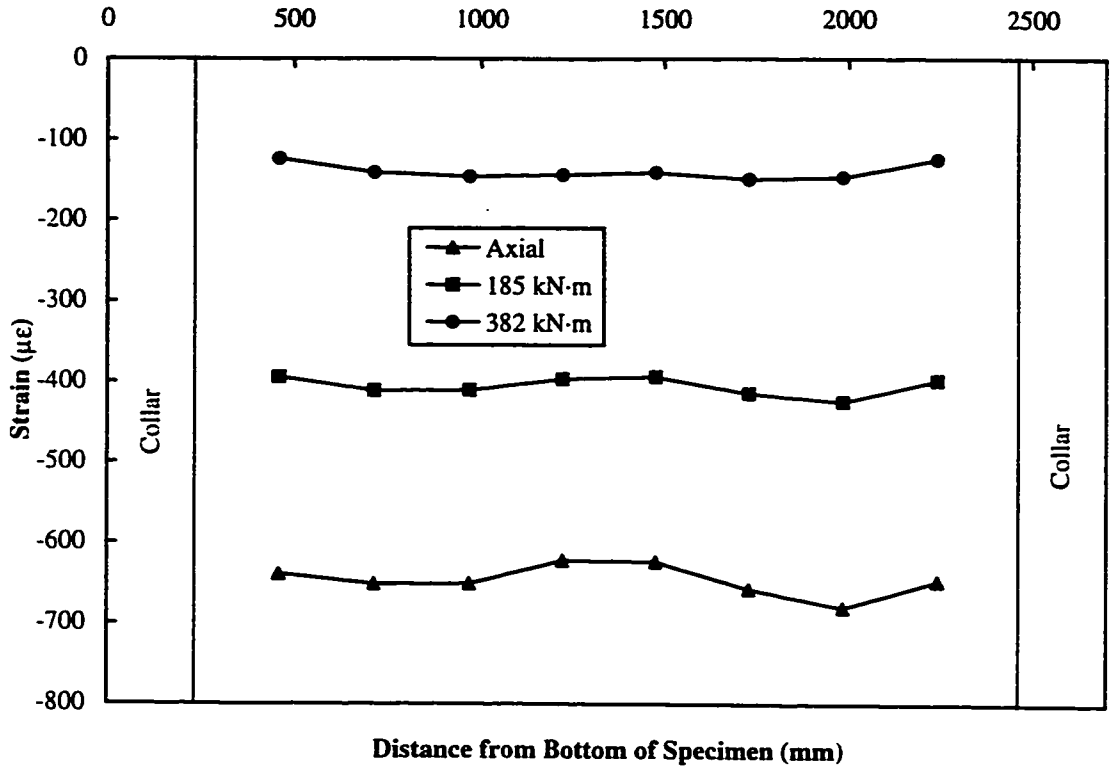

Figure 3.21 C45P00 – Tension face strain gauge measurments: initial loading stage

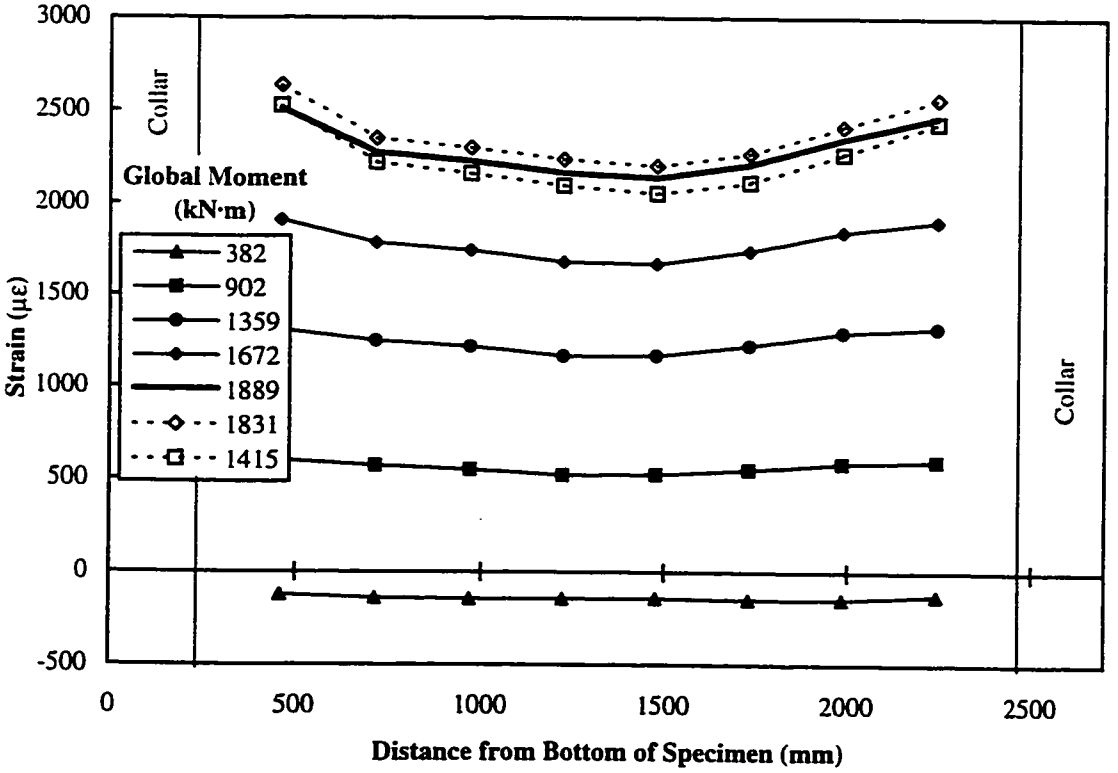

Figure 3.22 C45P00 – Tension face strain gauge measurements: pre- and post-buckling

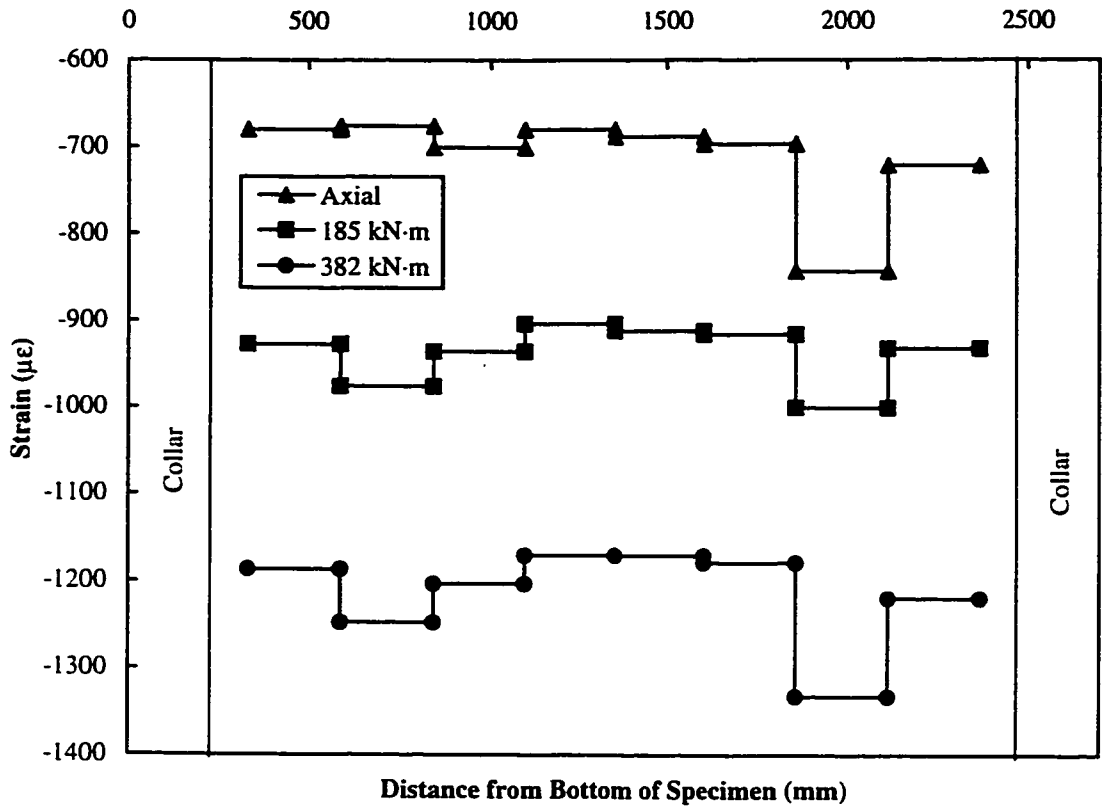

Figure 3.23 C45P00 – Compression face Demec measurements: initial loading stage

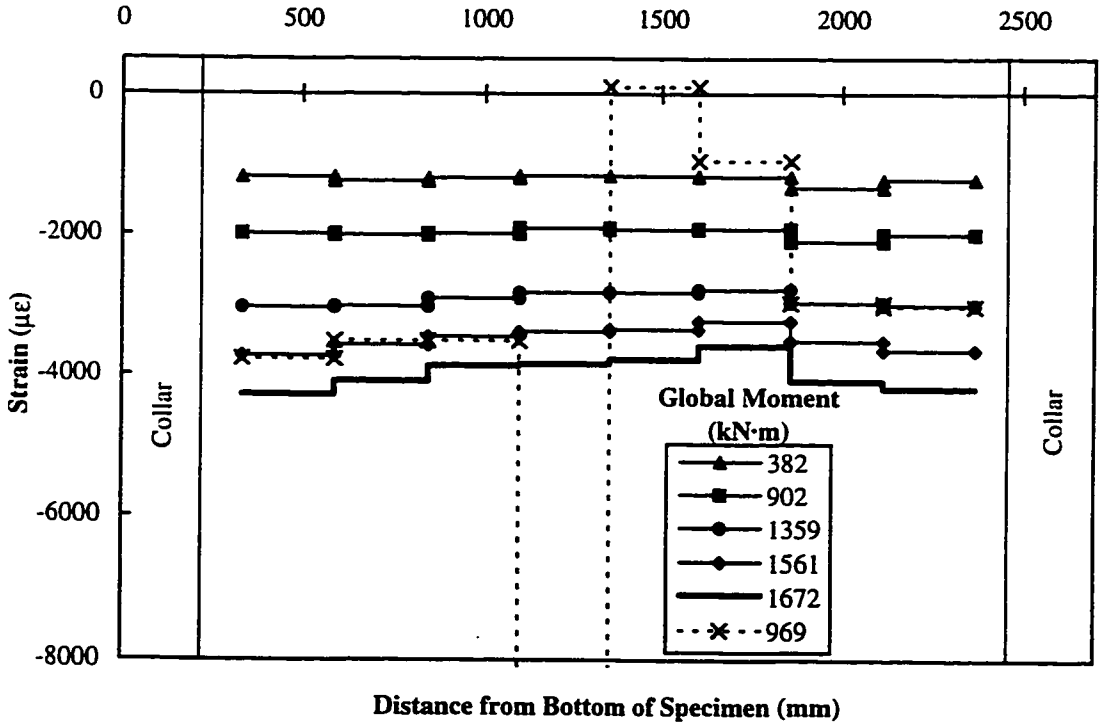

Figure 3.24 C45P00 – Compression face Demec measurements: pre- and post-buckling

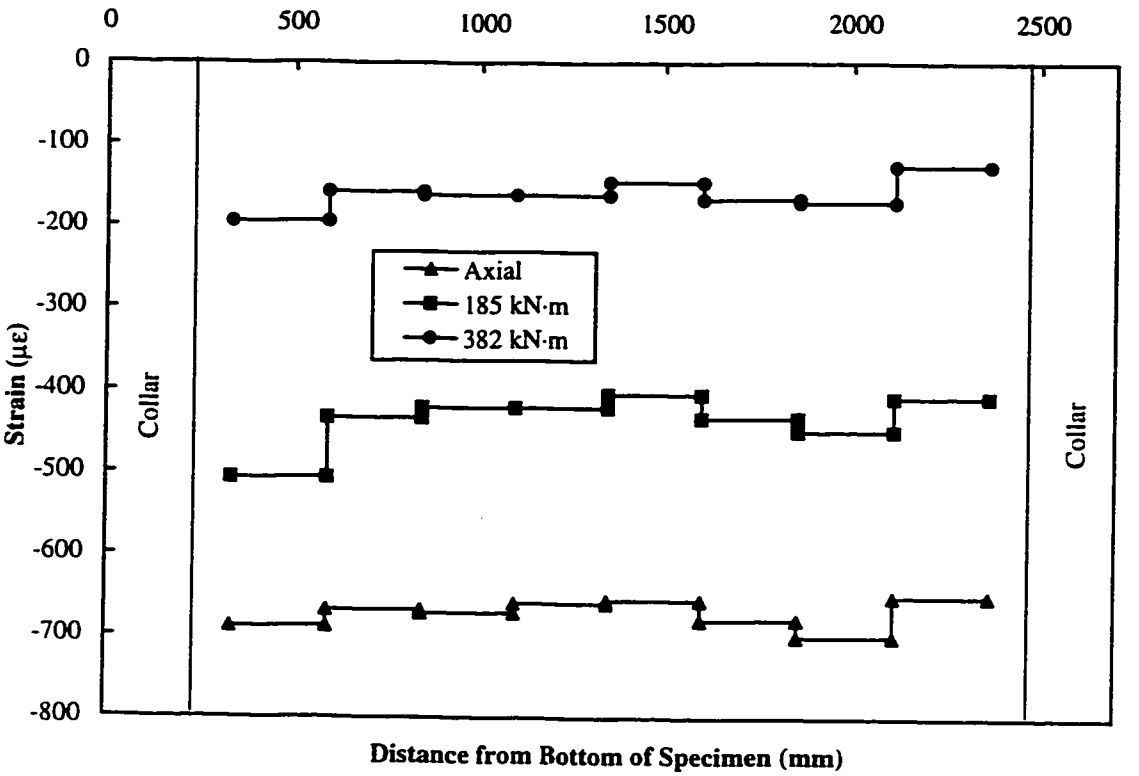

Figure 3.25 C45P00 – Tension face Demec measurements: initial loading stage

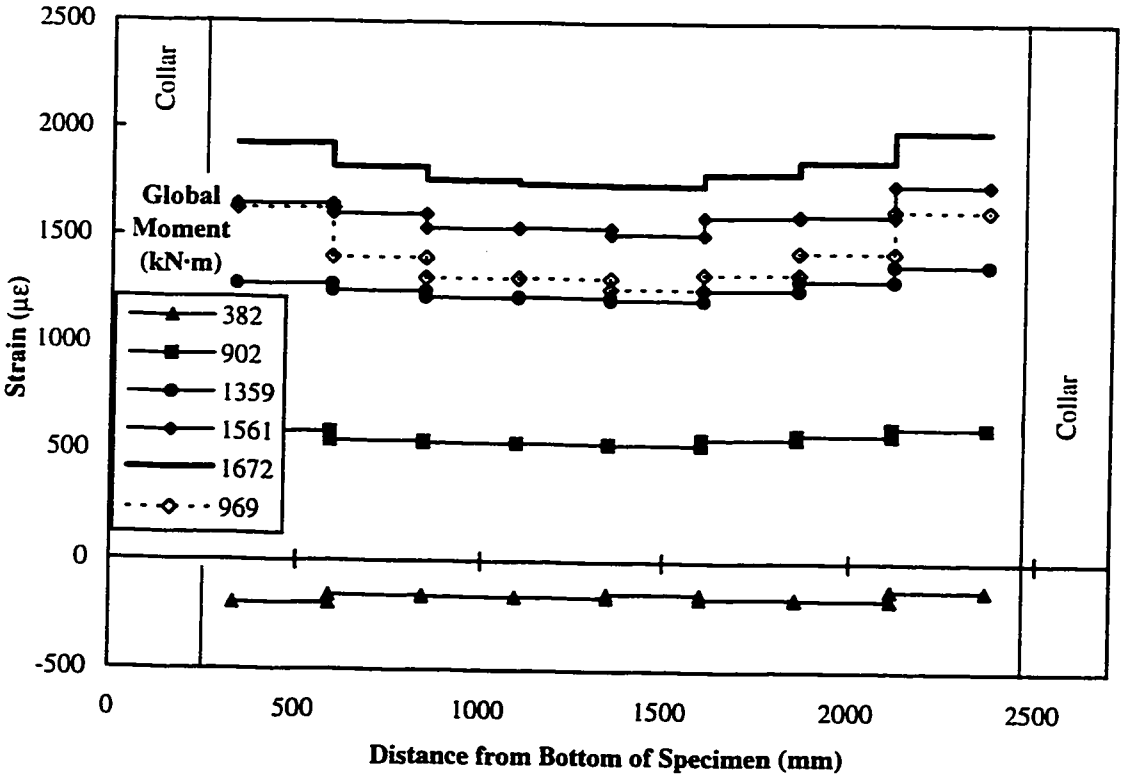

Figure 3.26 C45P00 – Tension face Demec measurements: pre- and post-buckling

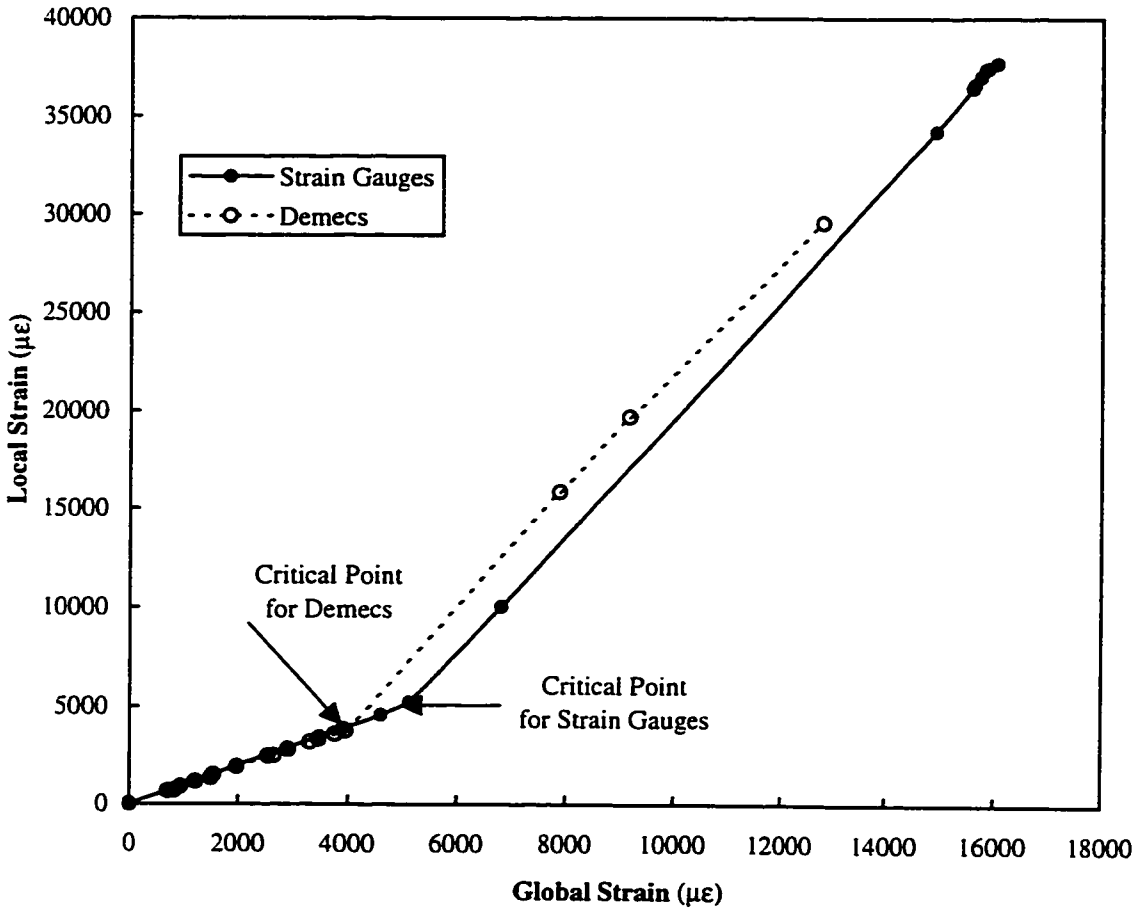

Figure 3.27 C45P00 – Determination of critical longitudinal compressive strain

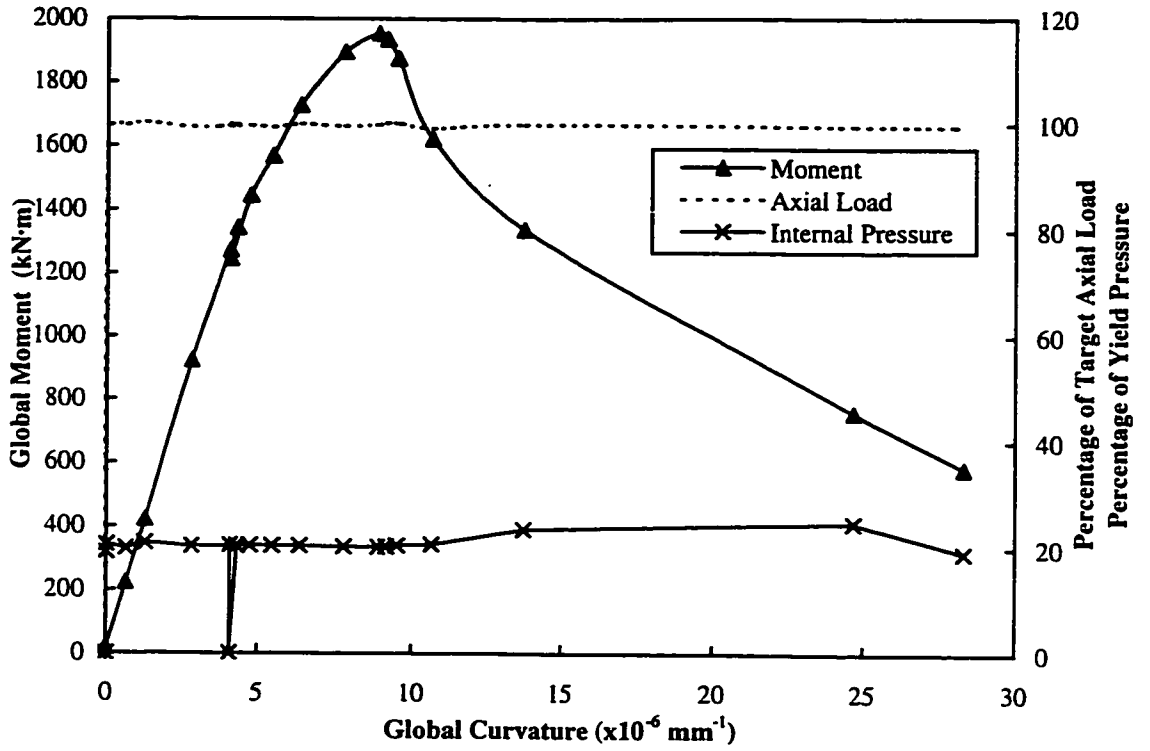

Figure 3.28 C45P20 – Global moment, axial load and pressure versus curvature diagram

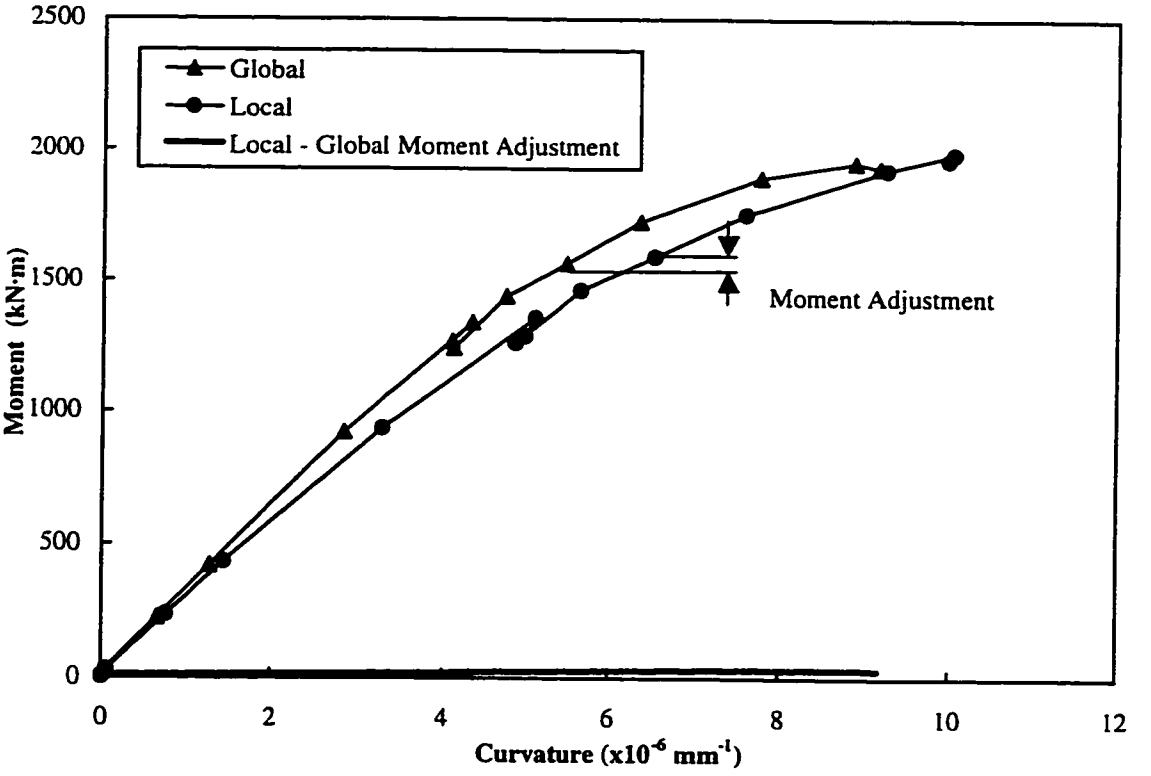

Figure 3.29 C45P20 – Comparison of global and local moment versus curvature

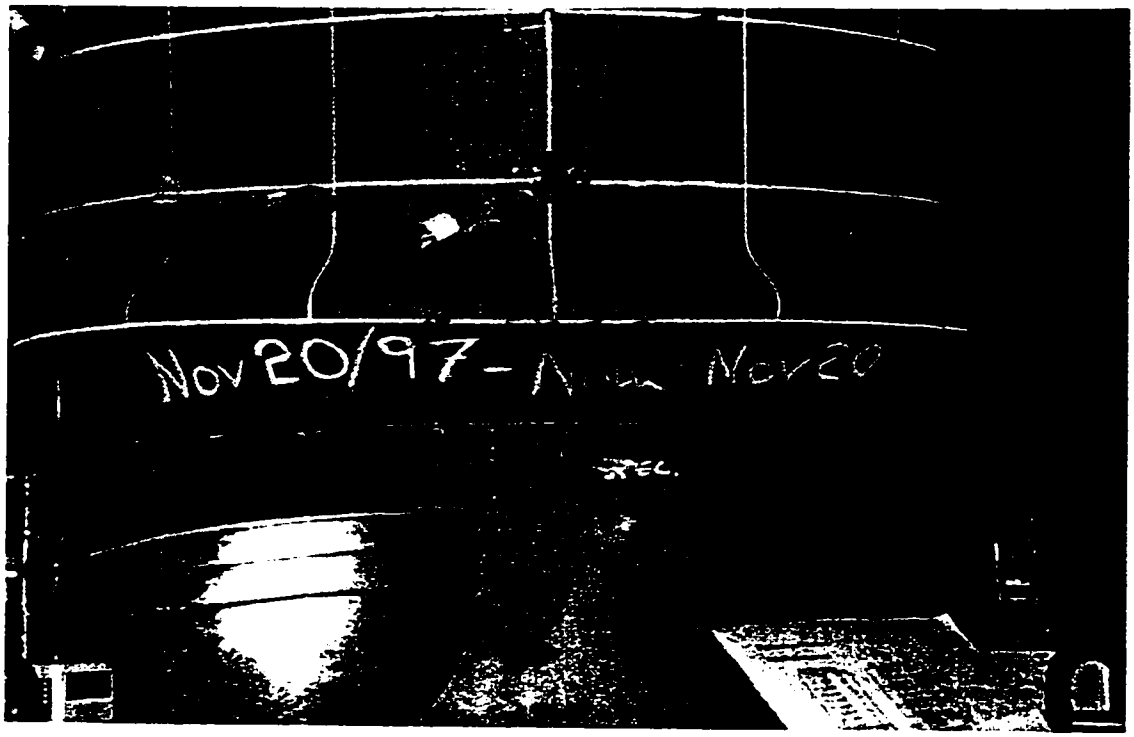

Figure 3.30 C45P20 – Buckled configuration, compression face

Figure 3.31 C45P20 – Buckled configuration, profile

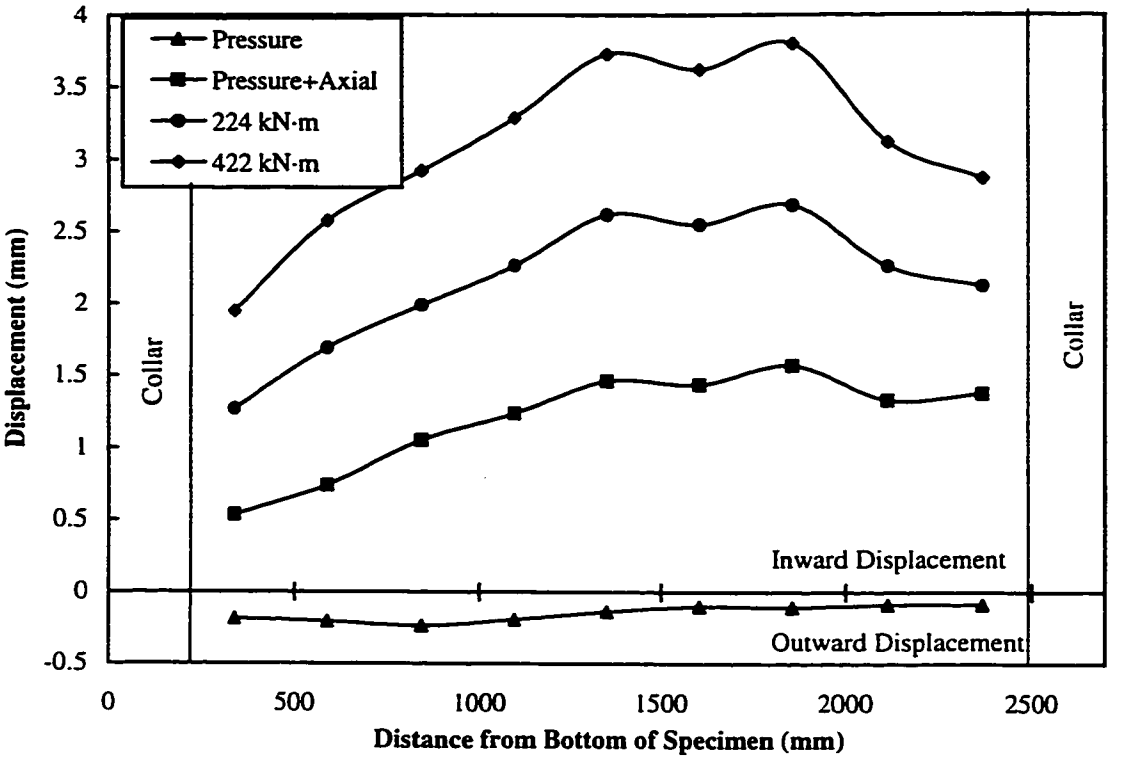

Figure 3.32 C45P20 – Compression face displacements: initial loading stage

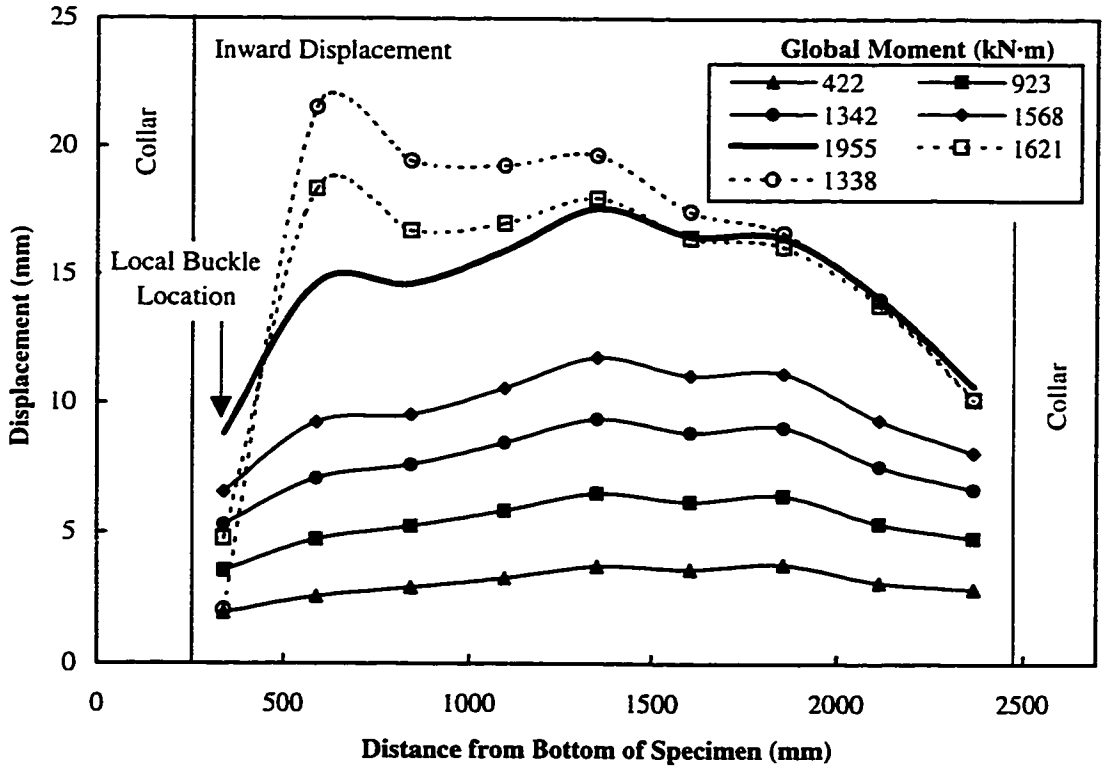

Figure 3.33 C45P20 – Compression face displacements

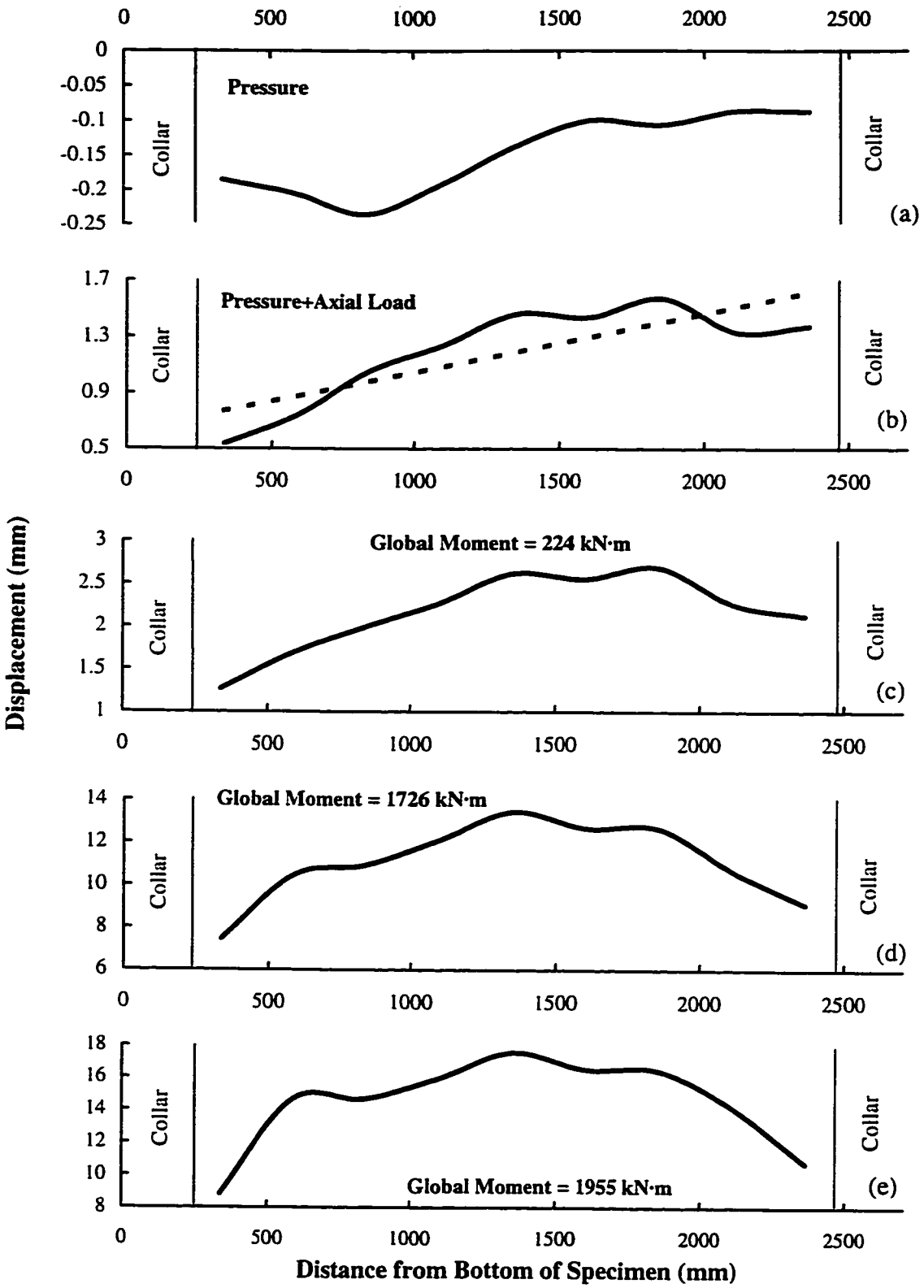

Figure 3.34 C45P20 - Progression of compression face displacements

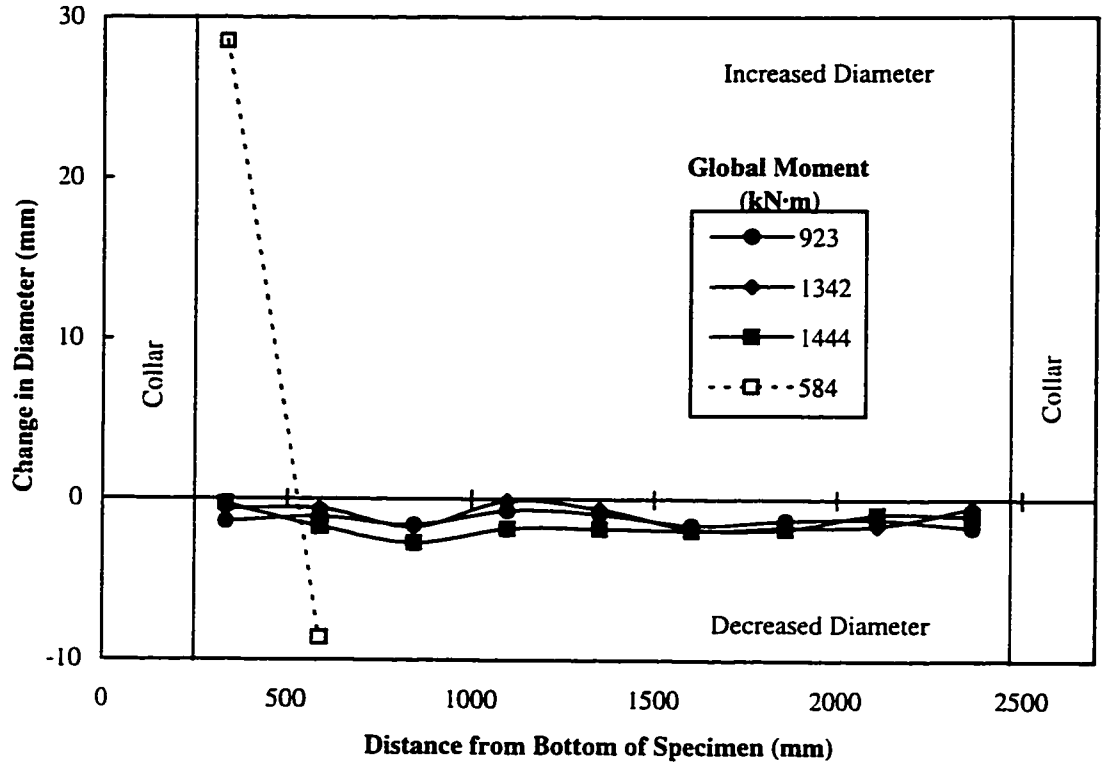

Note: Only in-plane measurements were recorded for this specimen

Figure 3.35 C45P20 – Measured changes in diameter

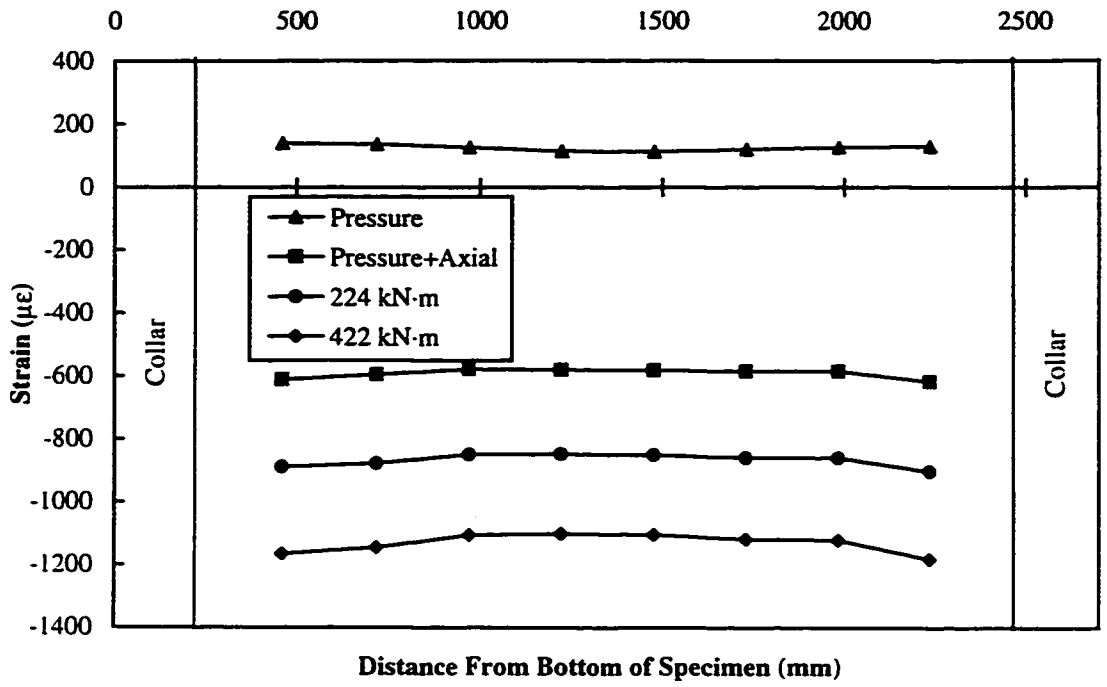

Figure 3.36 C45P20 – Compression face strain gauge measurements: initial loading stage

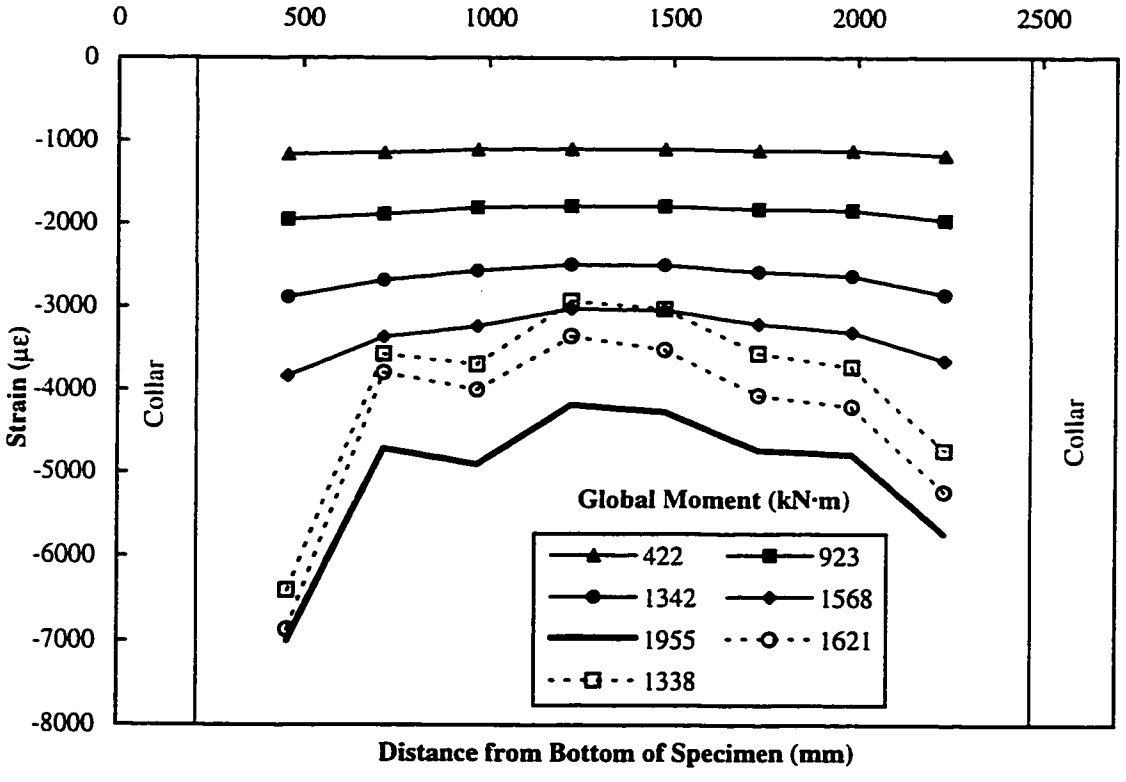

Figure 3.37 C45P20 – Compression face strain gauge measurements: pre- and post-buckling

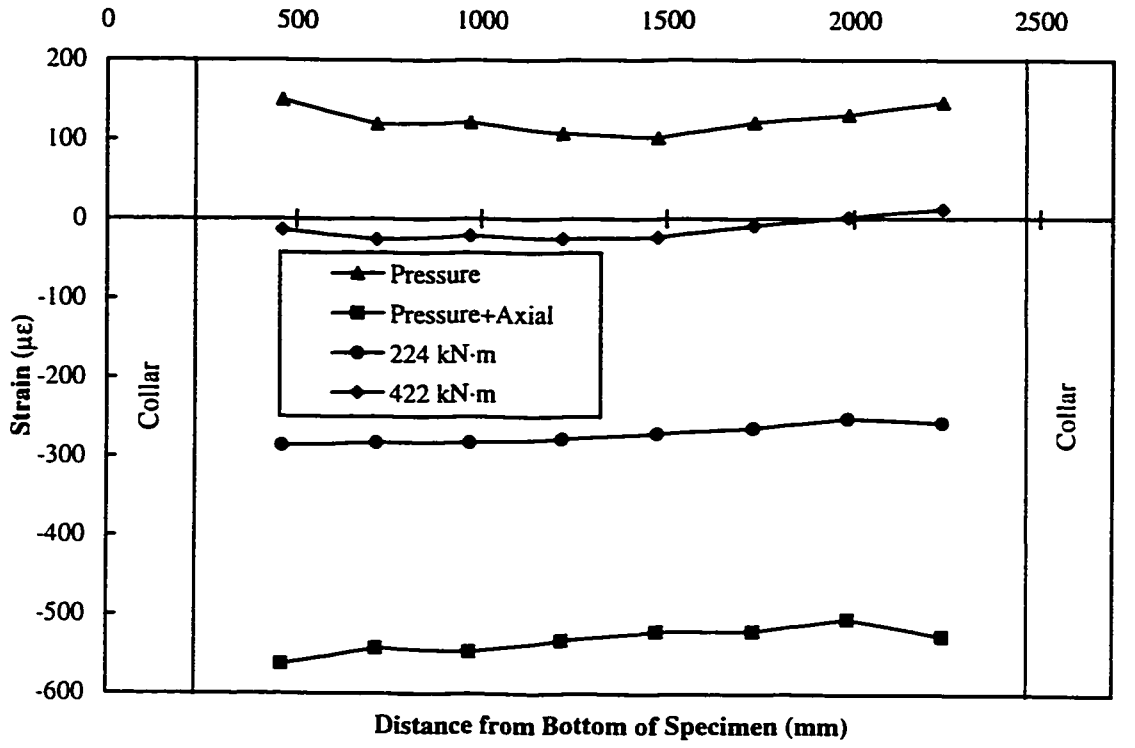

Figure 3.38 C45P20 – Tension face strain gauge measurements: initial loading stage

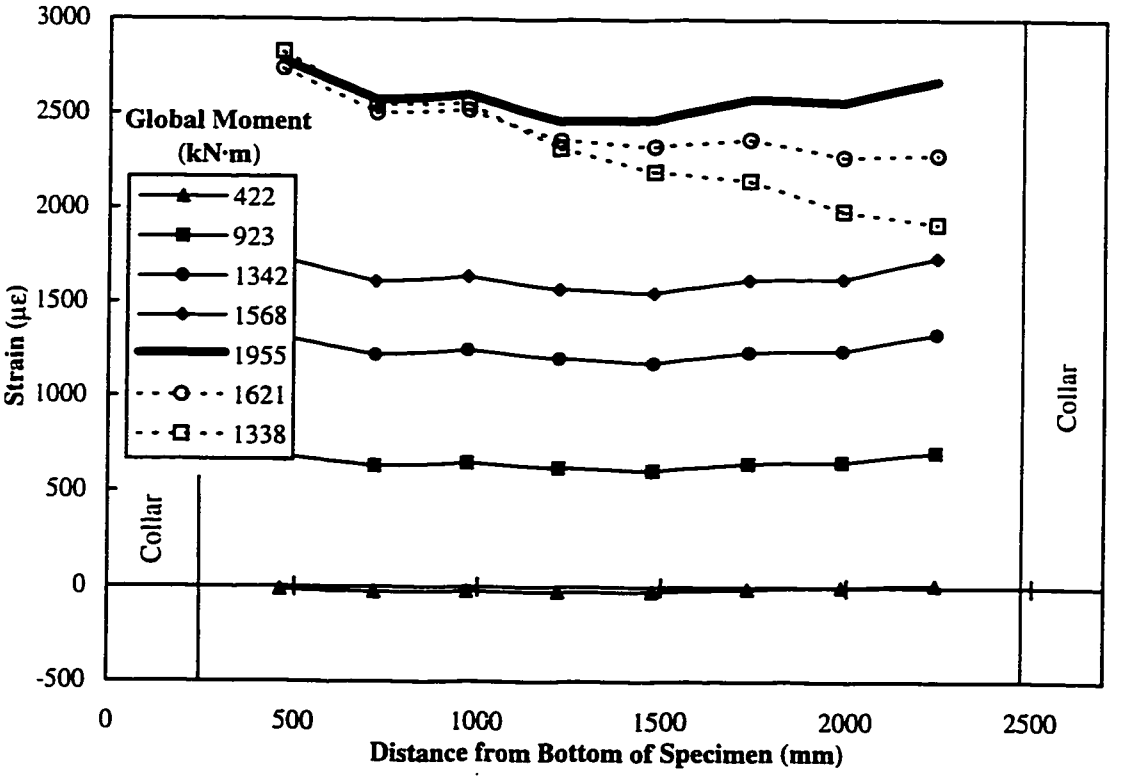

Figure 3.39 C45P20 – Tension face strain gauge measurements: pre- and post-buckling

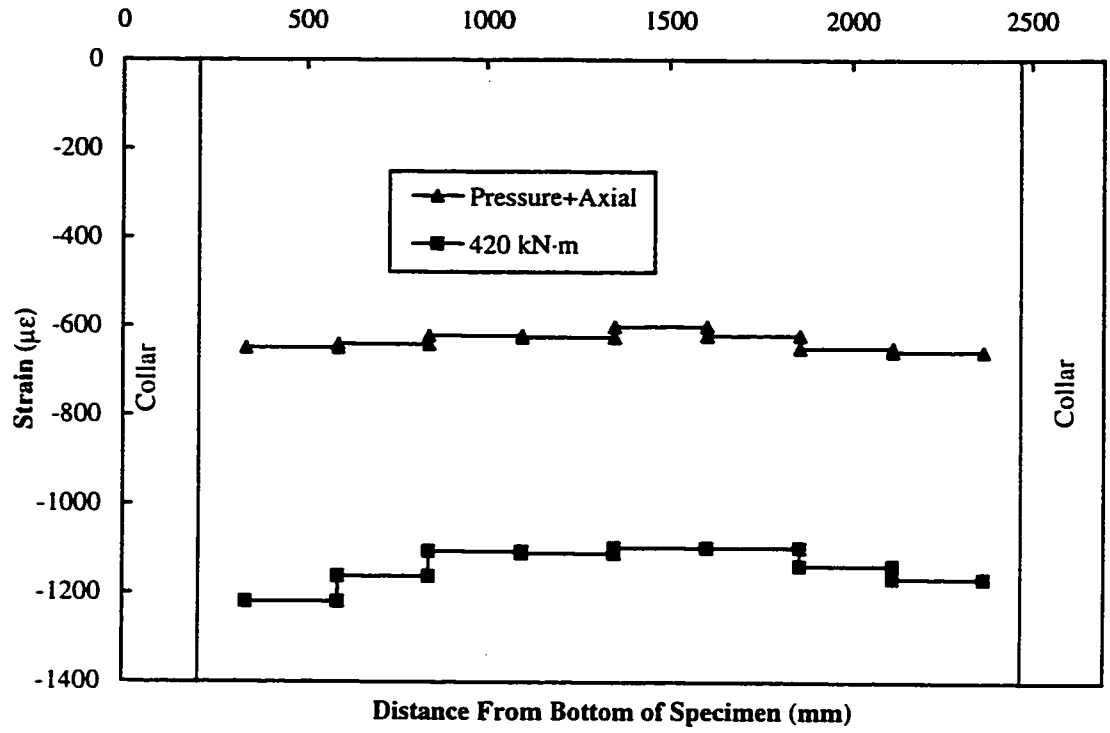

Figure 3.40 C45P20 – Compression face Demec measurments: initial loading stage

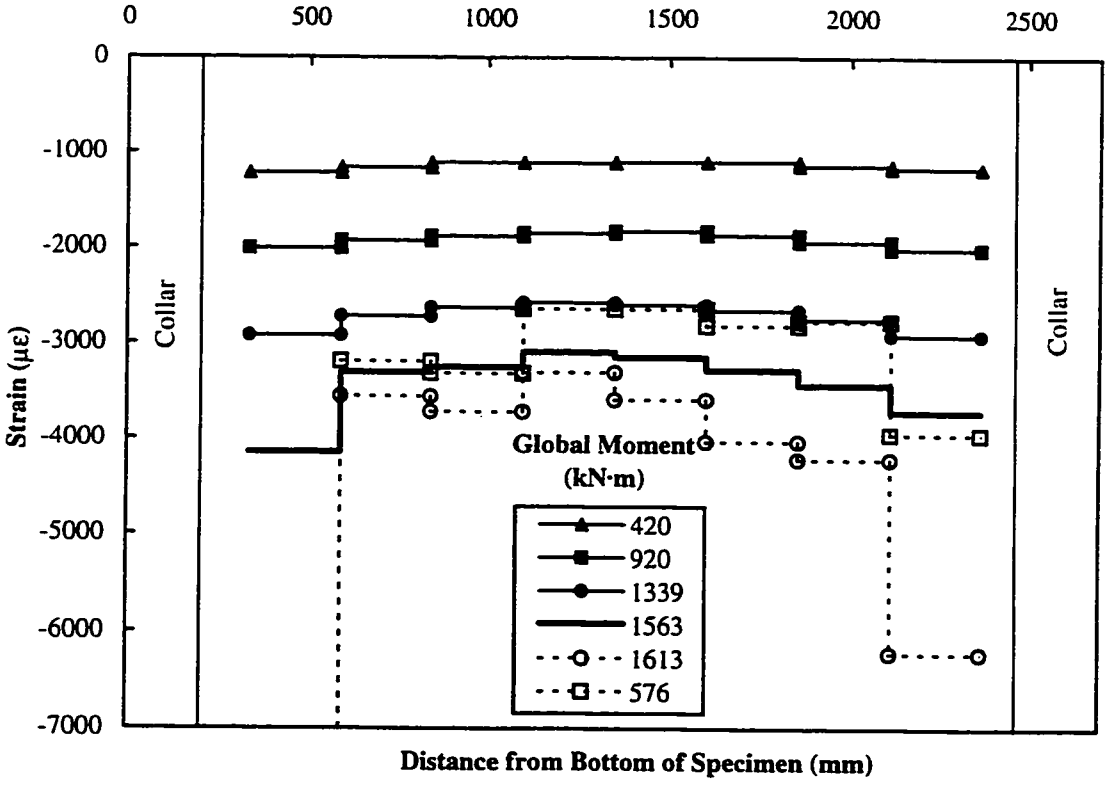

Figure 3.41 C45P20 – Compression face Demec measurements: pre- and post-buckling

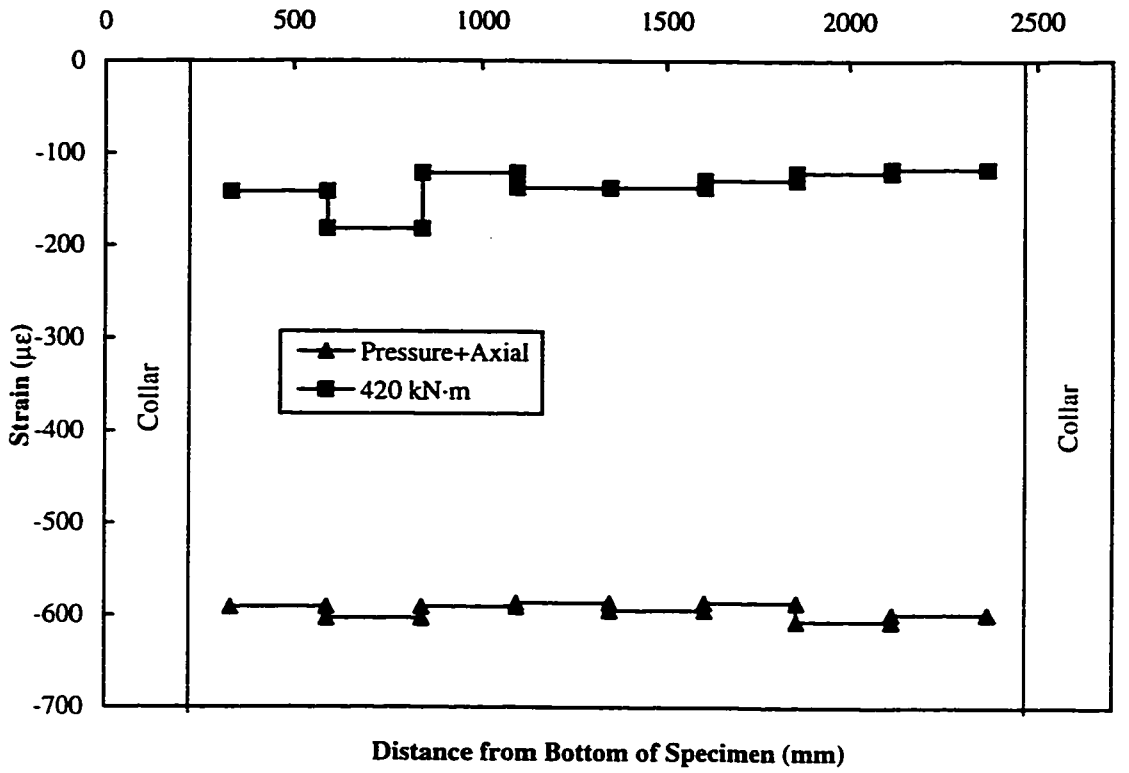

Figure 3.42 C45P20 – Tension face Demec measurements: initial loading stage

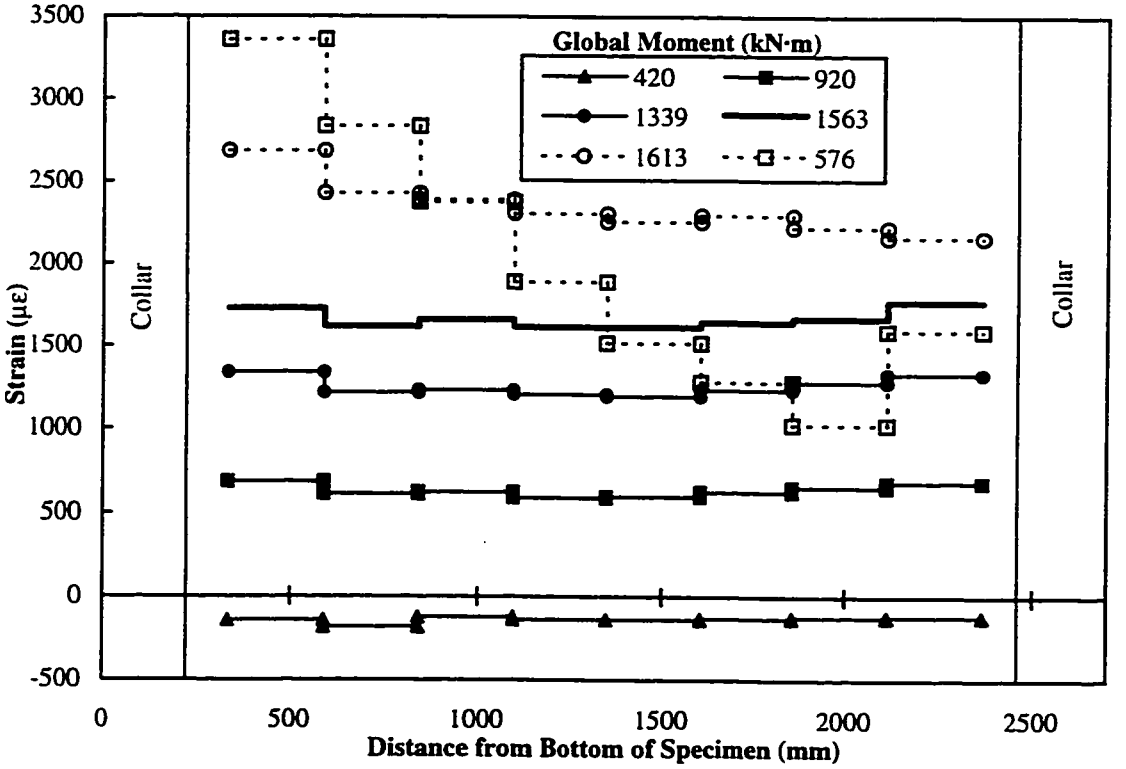

Figure 3.43 C45P20 – Tension face Demec measurments: pre- and post-buckling

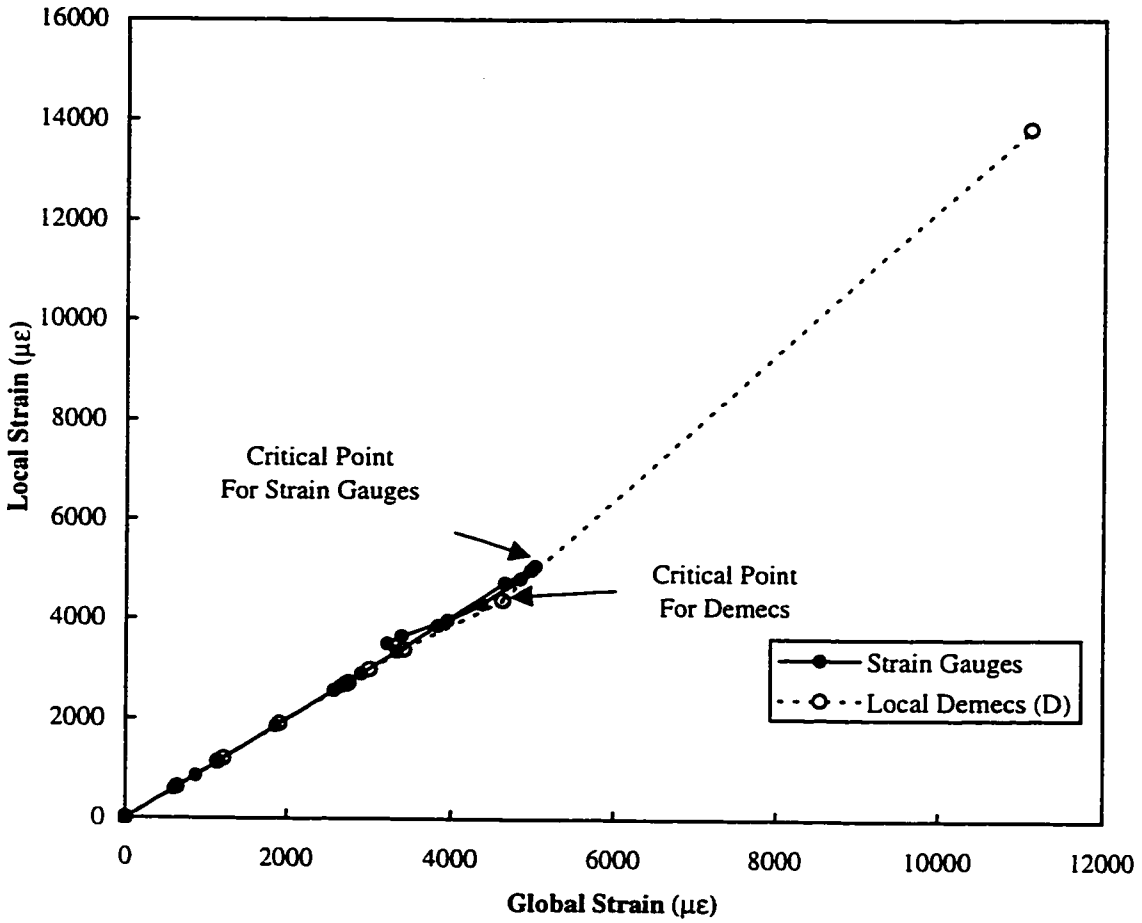

Figure 3.44 C45P20 – Determination of critical longitudinal compressive strain

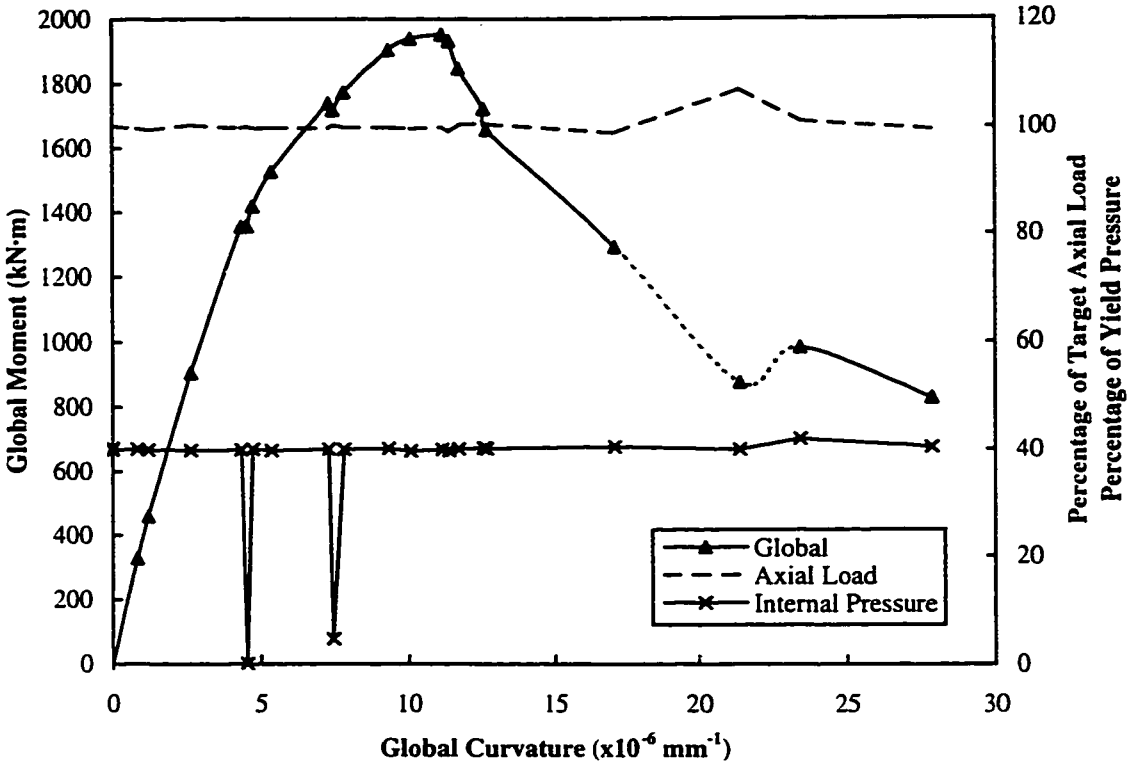

Figure 3.45 C45P40 – Global moment, axial load and pressure versus curvature diagram

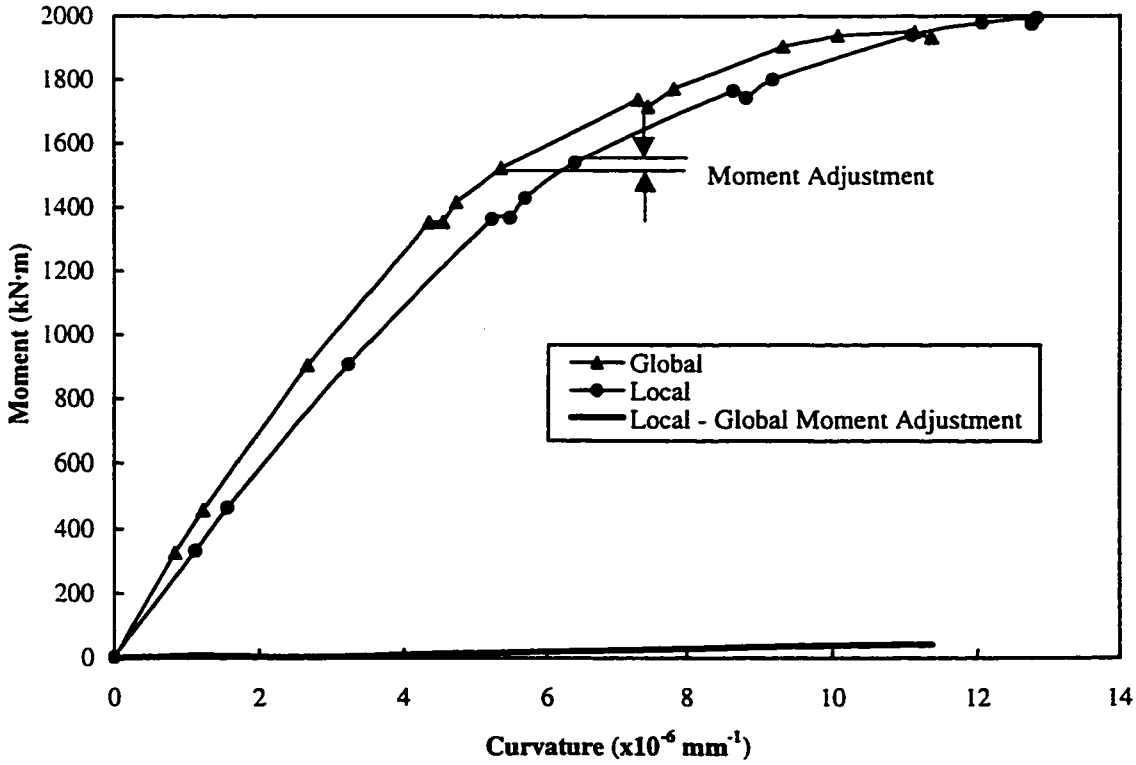

Figure 3.46 C45P40 – Comparison of global and local moment versus curvature

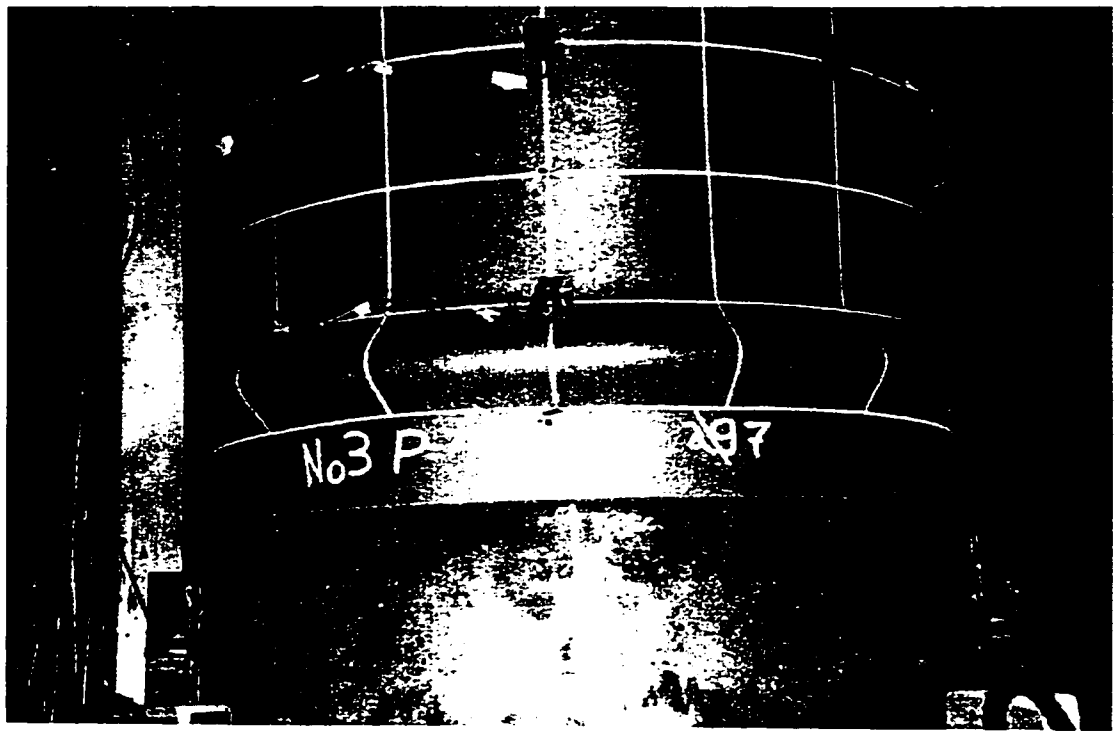

Figure 3.47 C45P40 – Buckled configuration, compression face

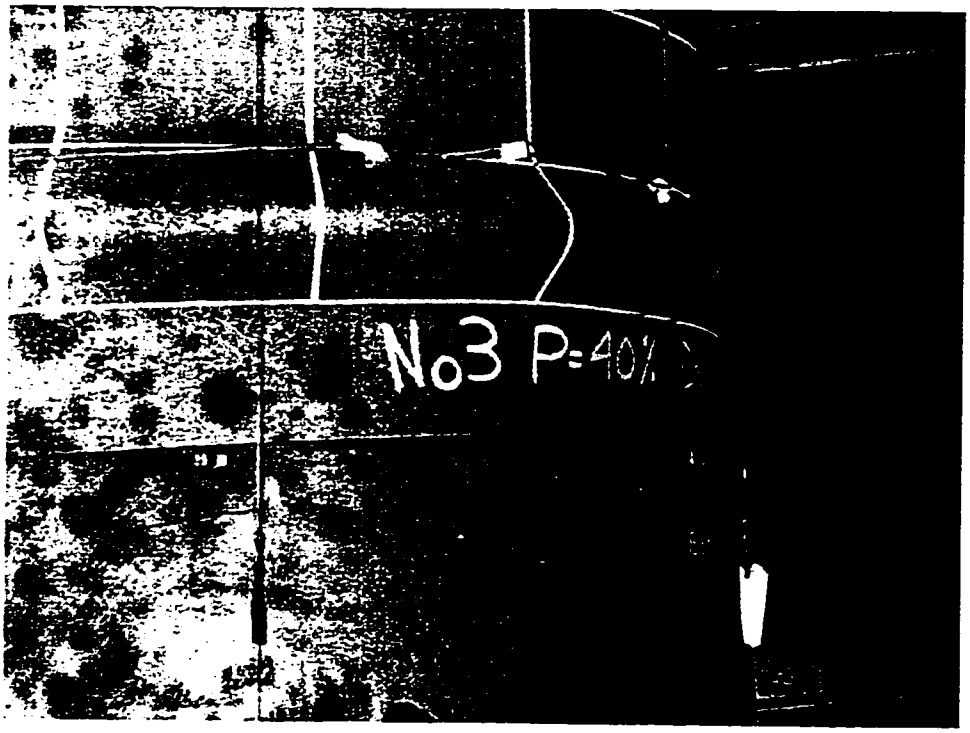

Figure 3.48 C45P40 – Buckled configuration, profile

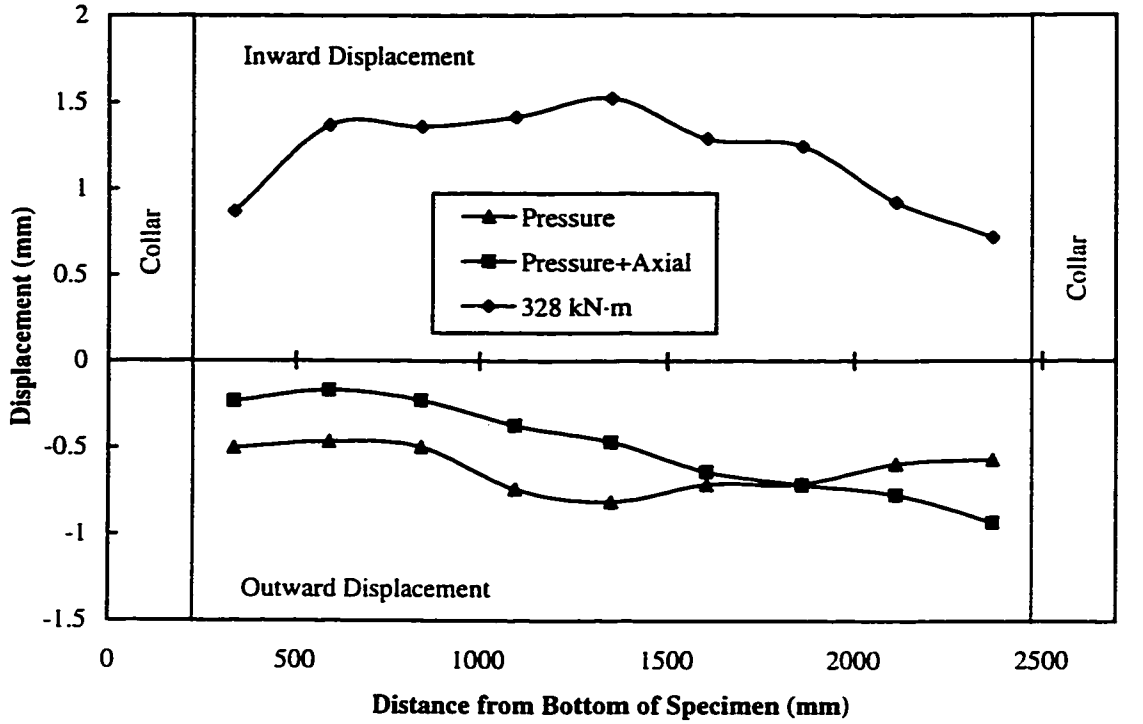

Figure 3.49 C45P40 – Compression face displacements: initial loading stage

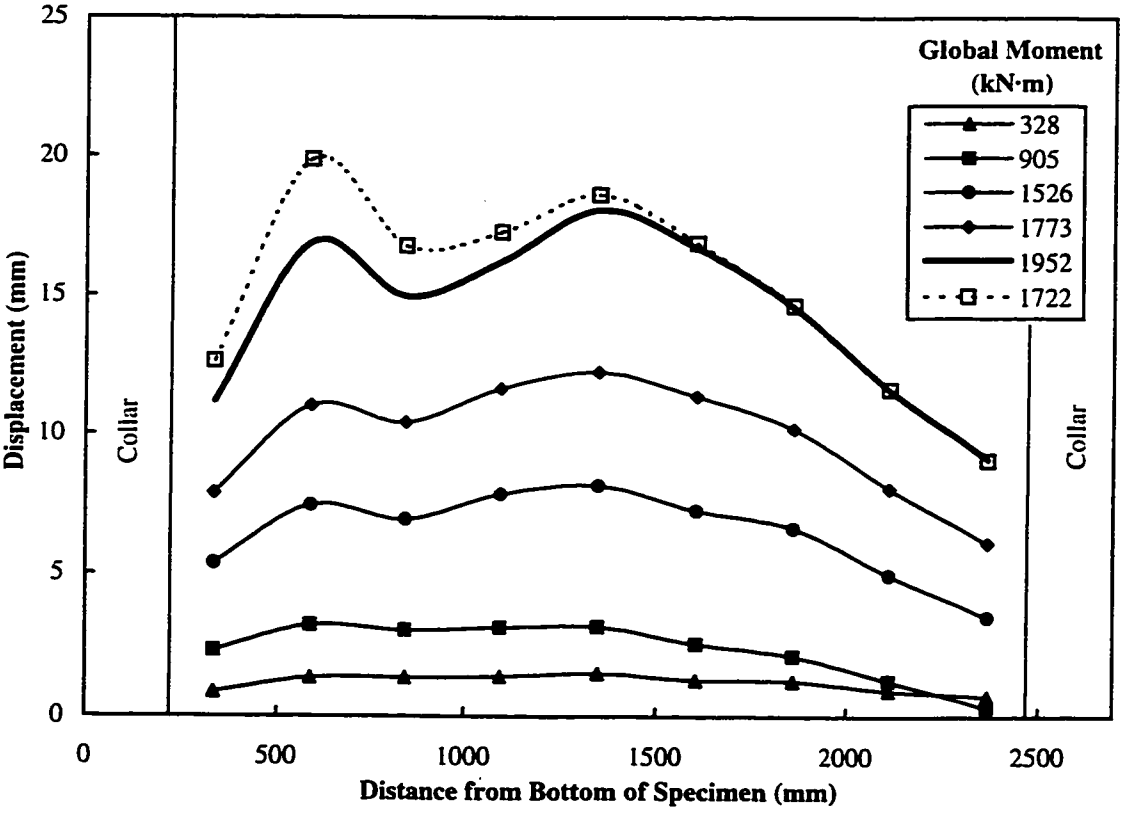

Figure 3.50 C45P40 – Compression face displacements

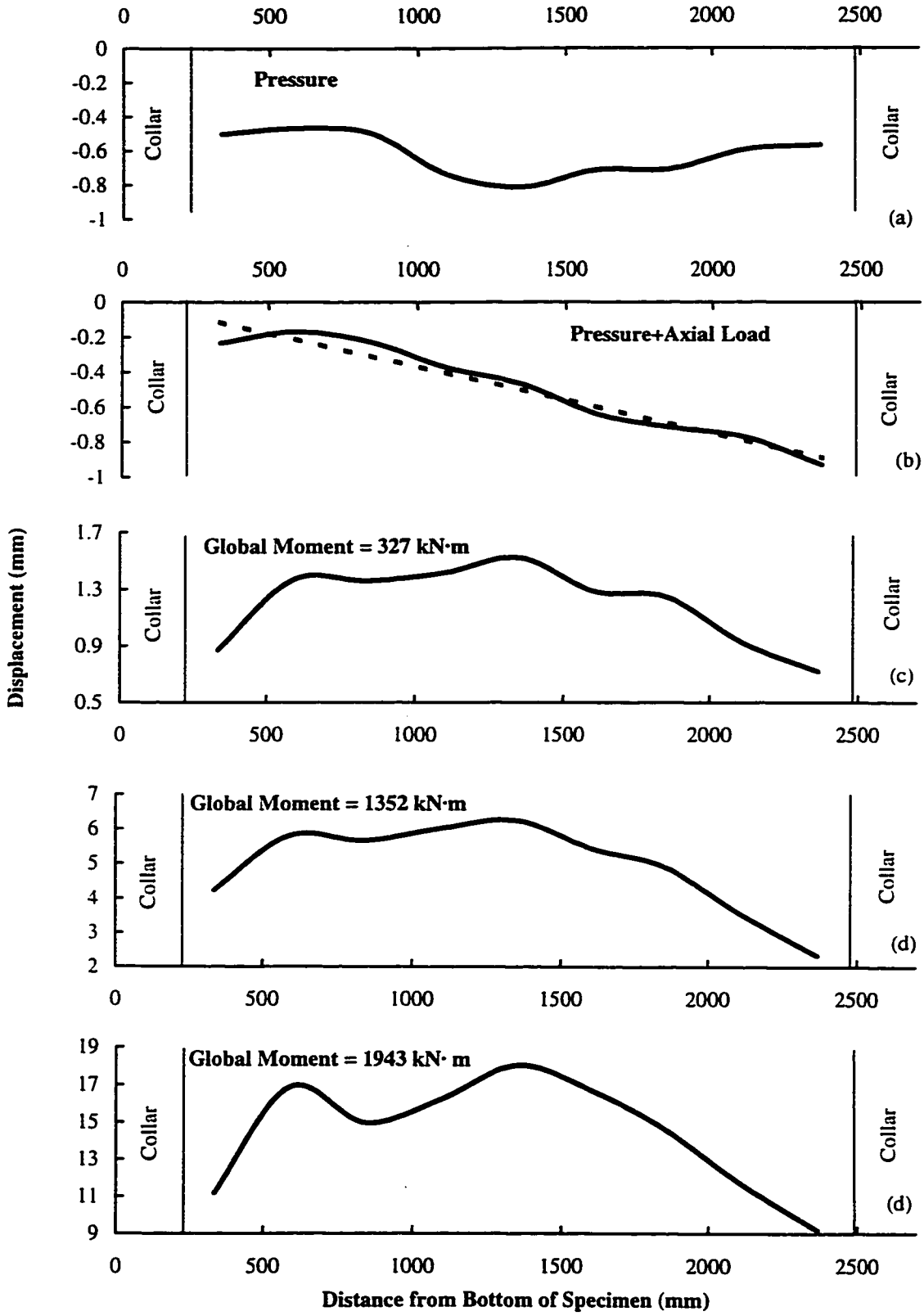

Figure 3.51 C45P40 - Progression of compression face displacements

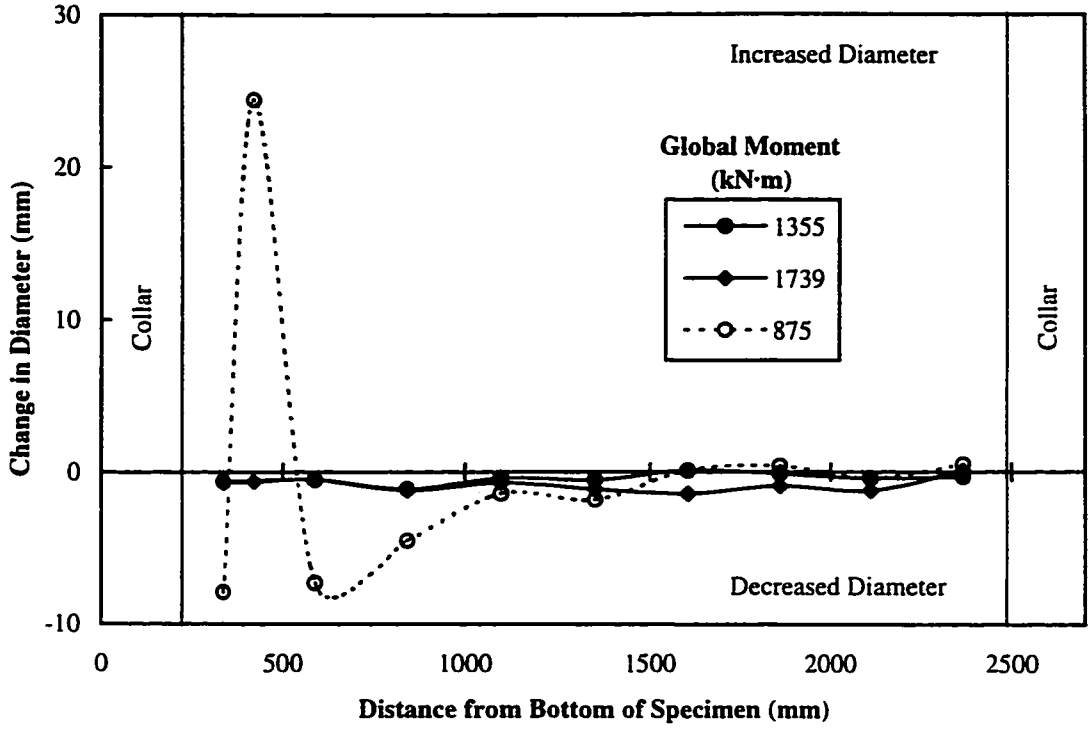

a) In-Plane Change in Diameter

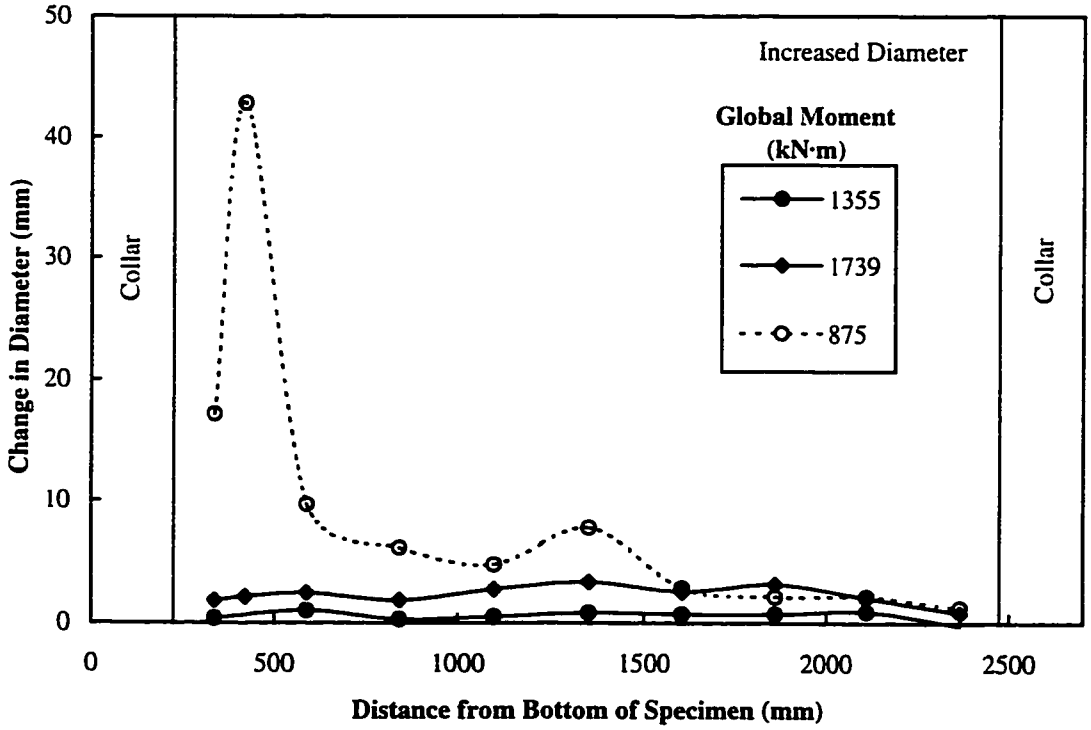

b) Out-of-Plane Change in Diameter

Figure 3.52 C45P40 – Measured changes in diameter

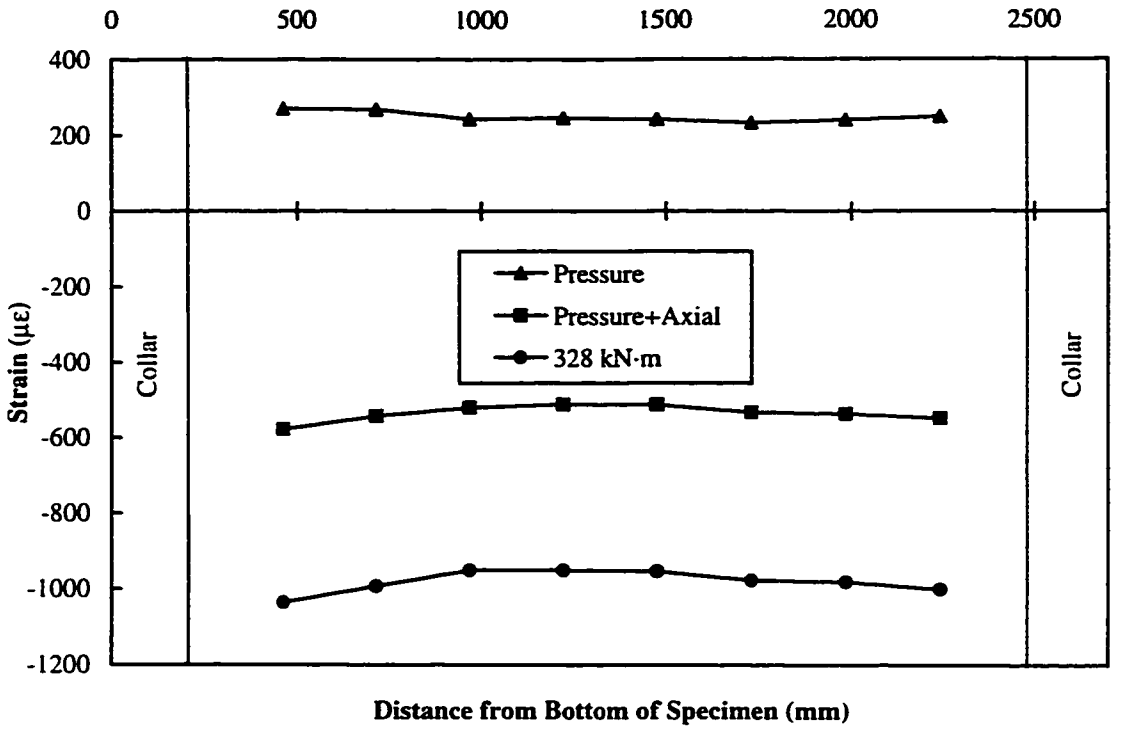

Figure 3.53 C45P40 – Compression face strain gauge measurements: initial loading stage

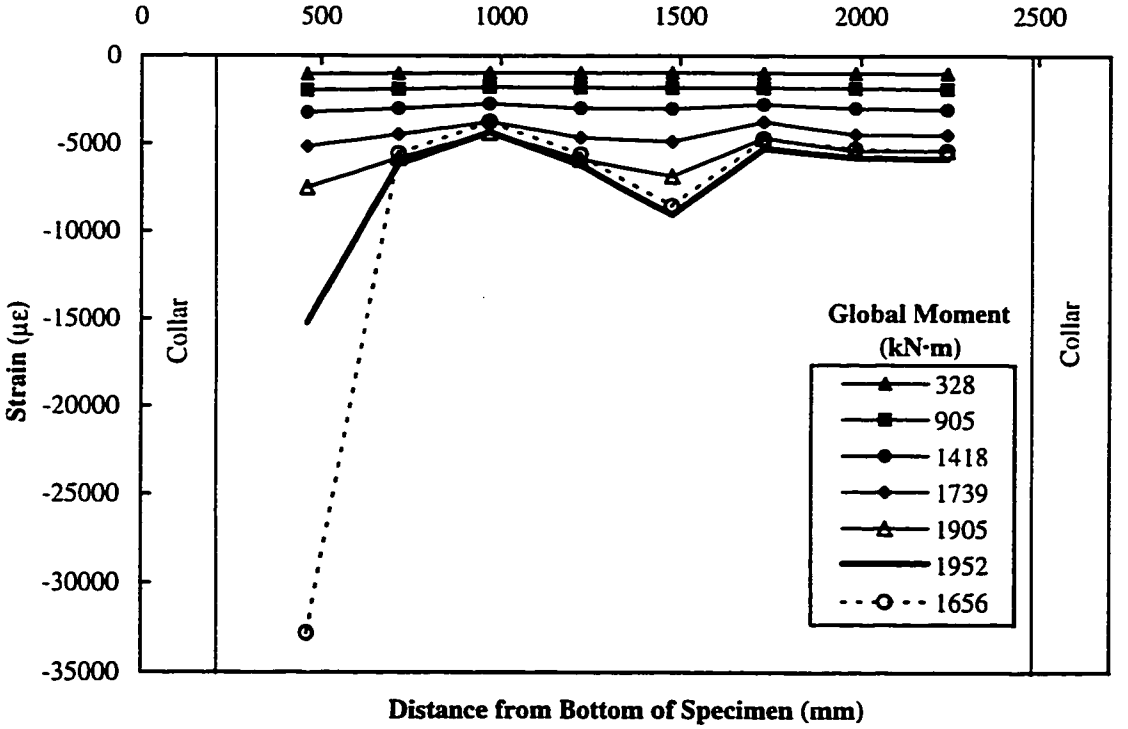

Figure 3.54 C45P40 – Compression face strain gauge measurements: pre- and post-buckling

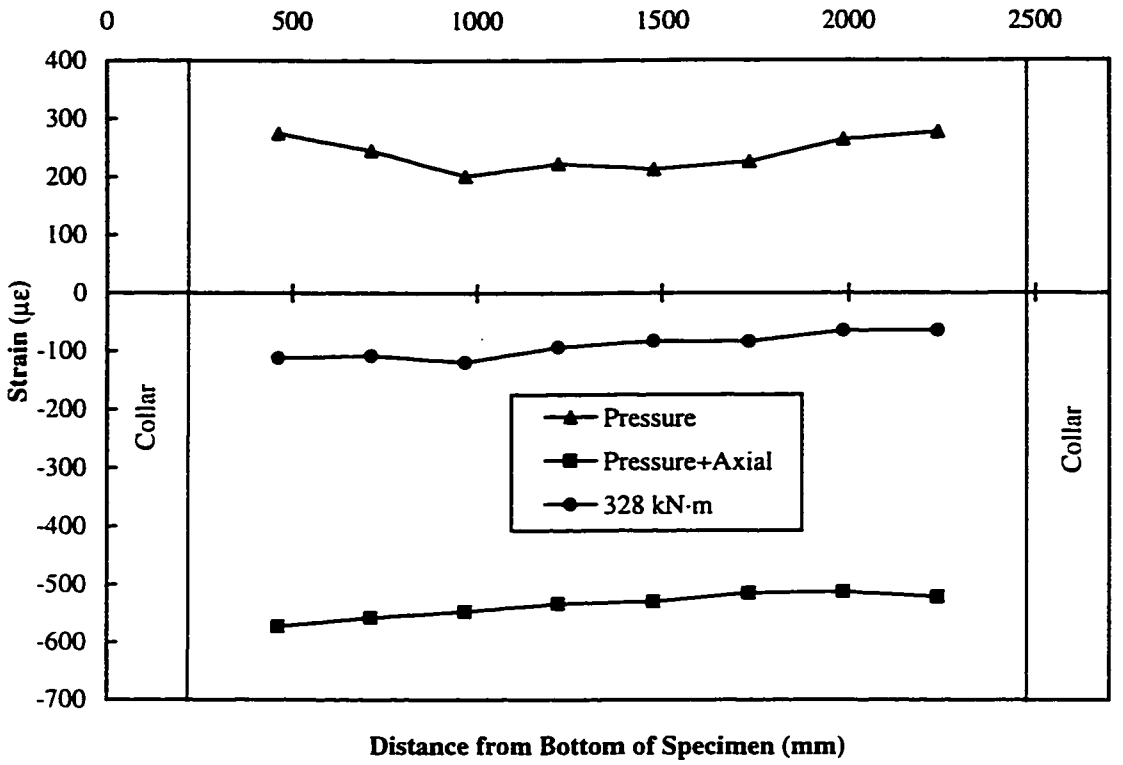

Figure 3.55 C45P40 – Tension face strain gauge measurements: initial loading stage

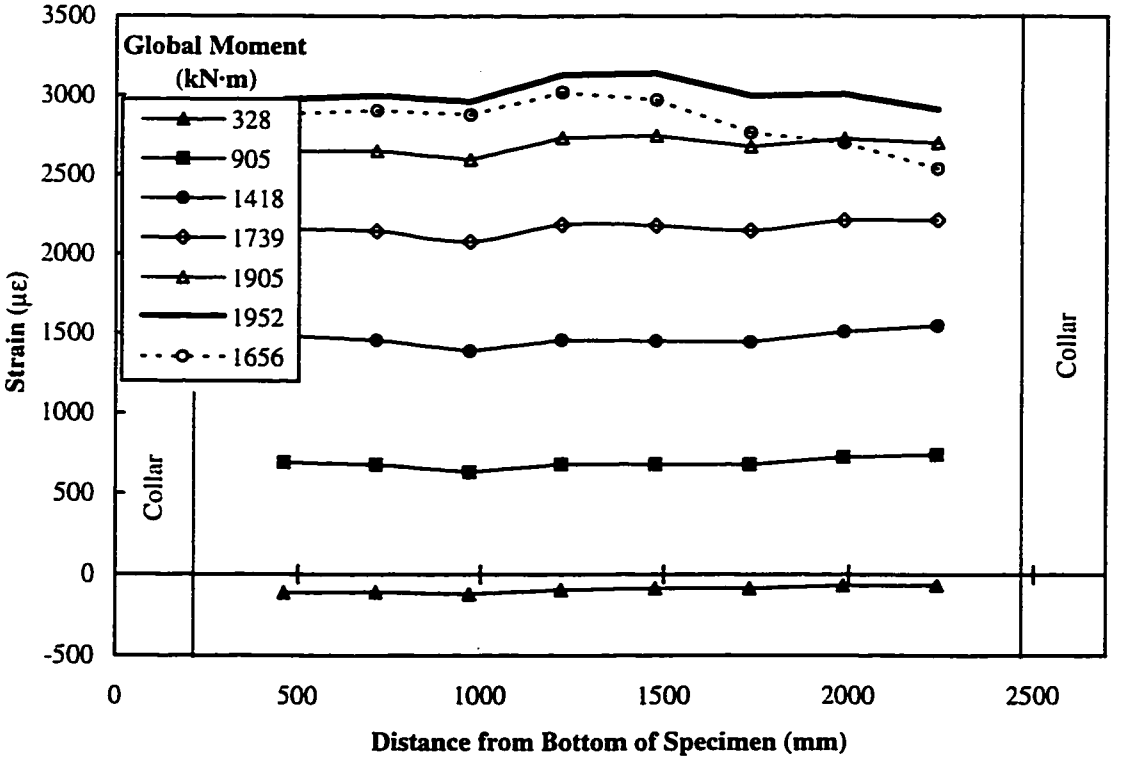

Figure 3.56 C45P40 – Tension face strain gauge measurements: pre- and post-buckling

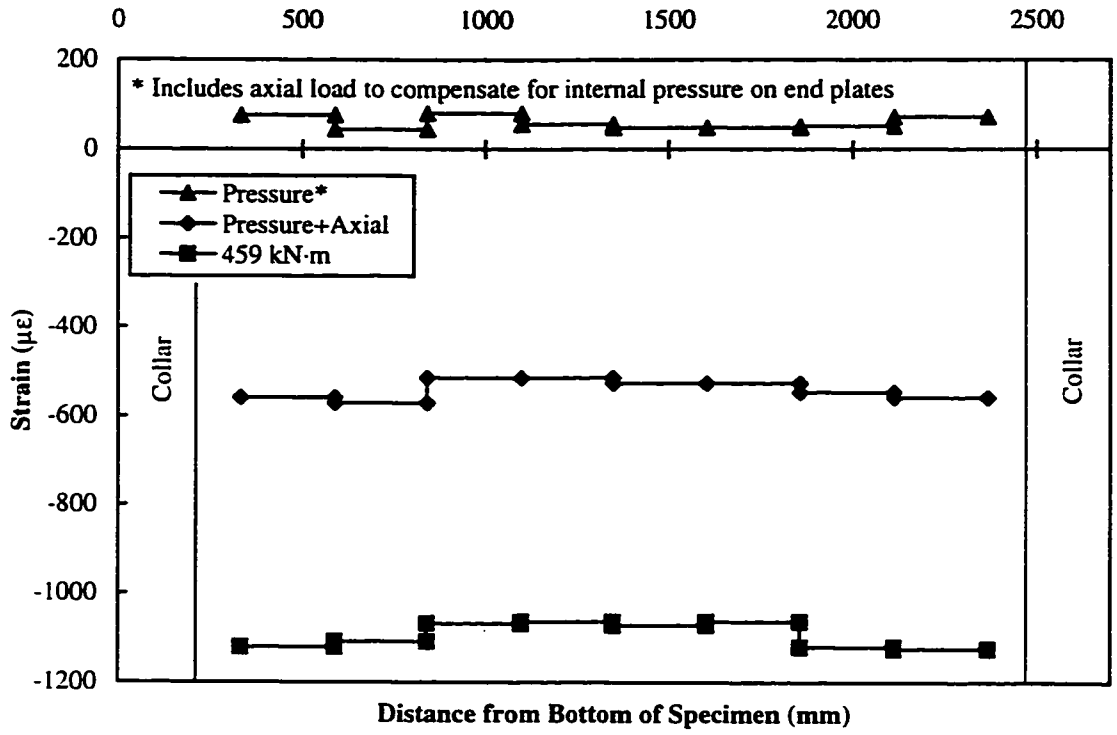

Figure 3.57 C45P40 – Compression face Demec measurements: initial loading stage

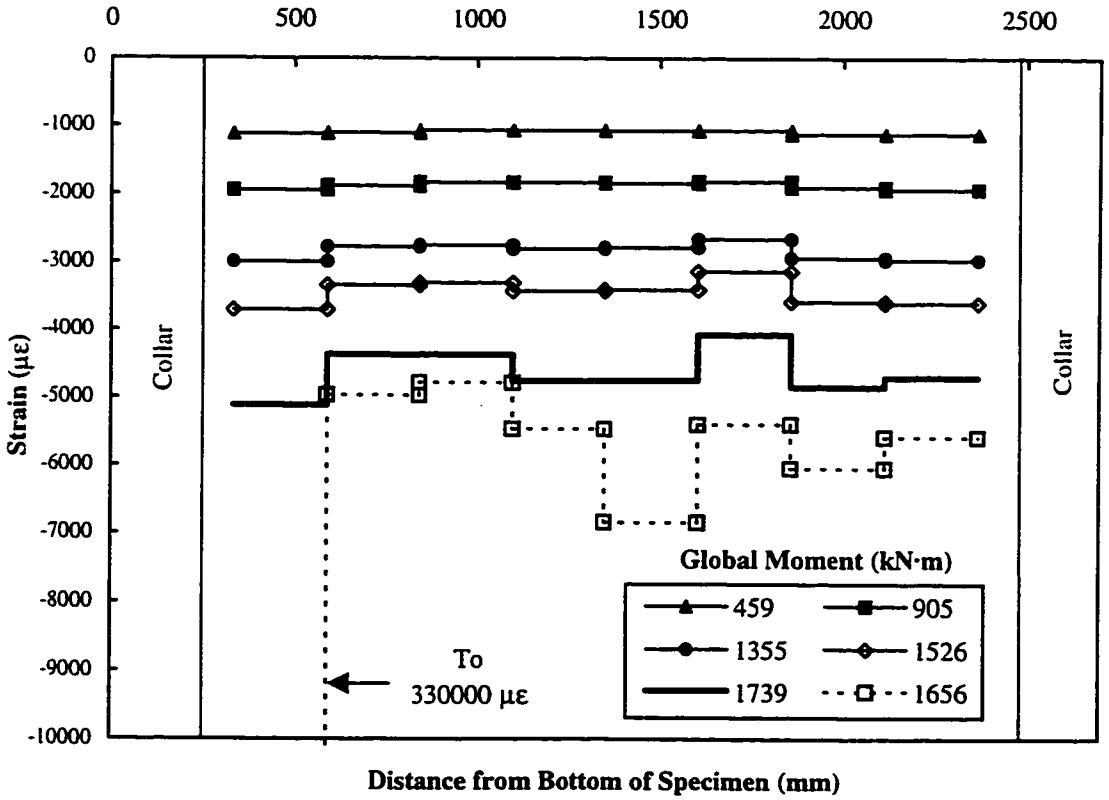

Figure 3.58 C45P40 – Compression face Demec measurements: pre- and post-buckling

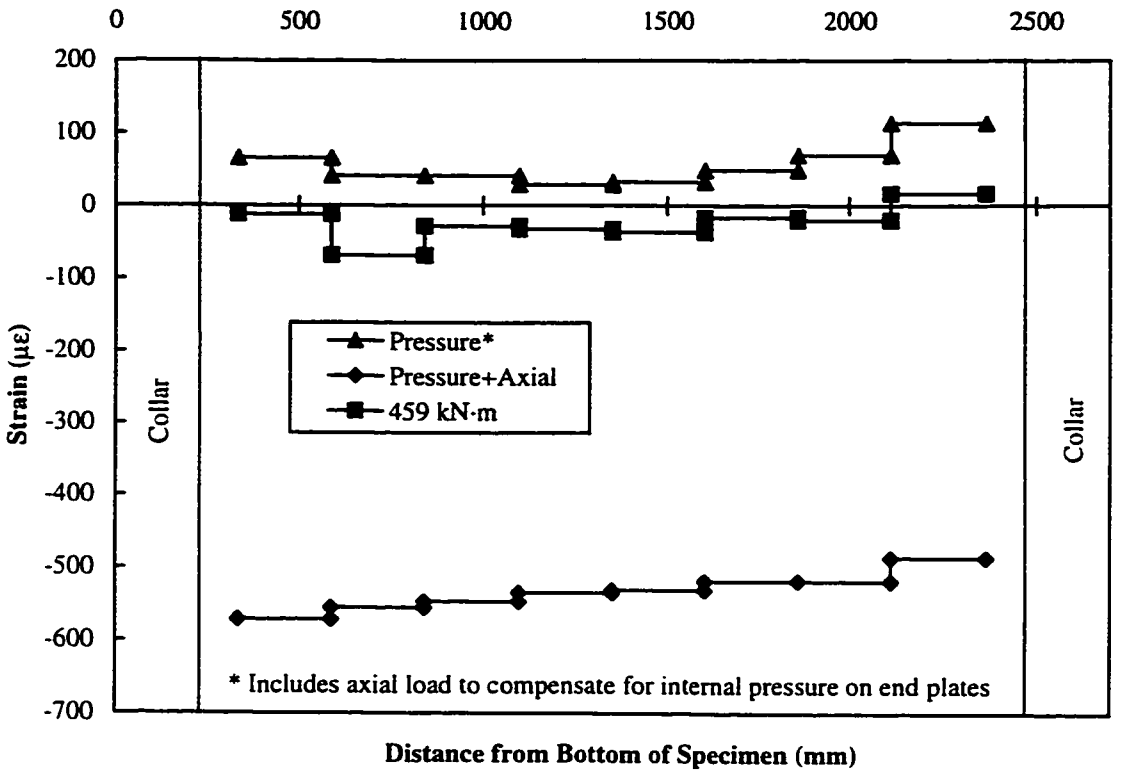

Figure 3.59 C45P40 – Tension face Demec measurements: initial loading stage

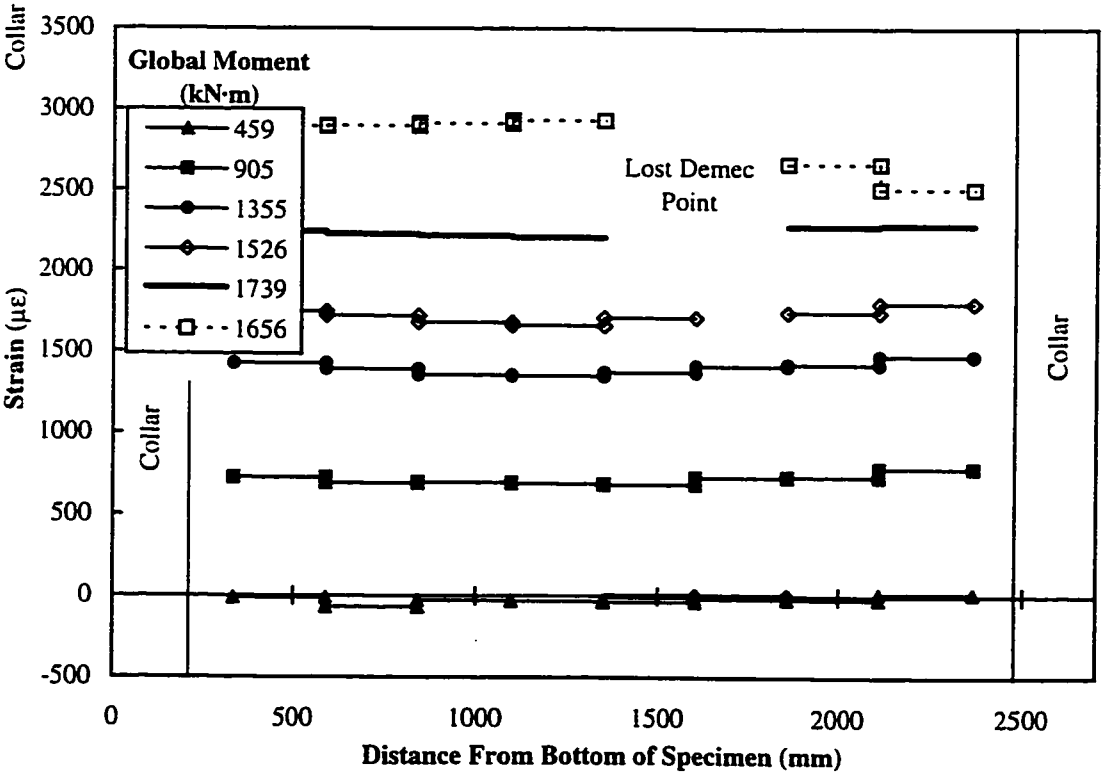

Figure 3.60 C45P40 – Tension face Demecs measurements: pre- and post-buckling

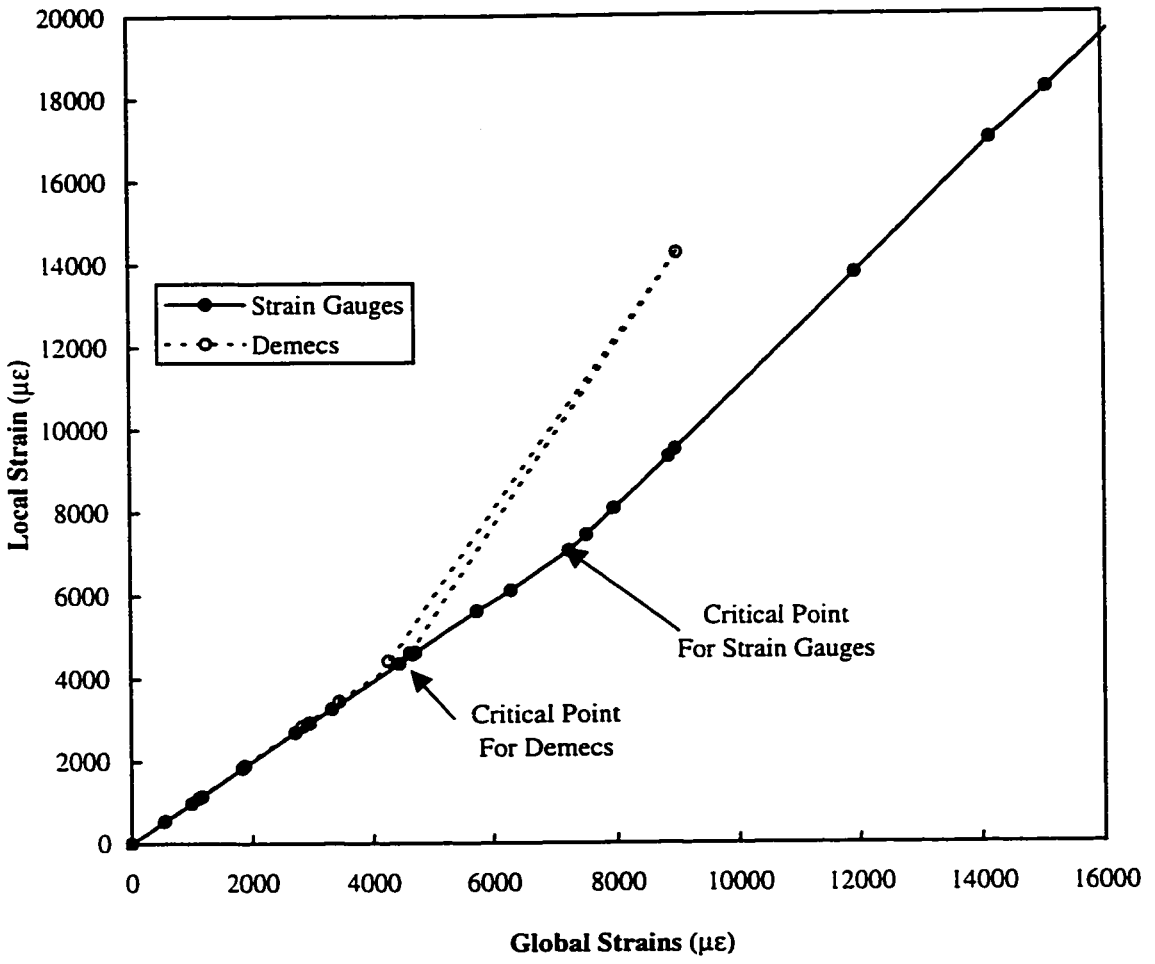

Figure 3.61 C45P40 – Determination of critical longitudinal compressive strain

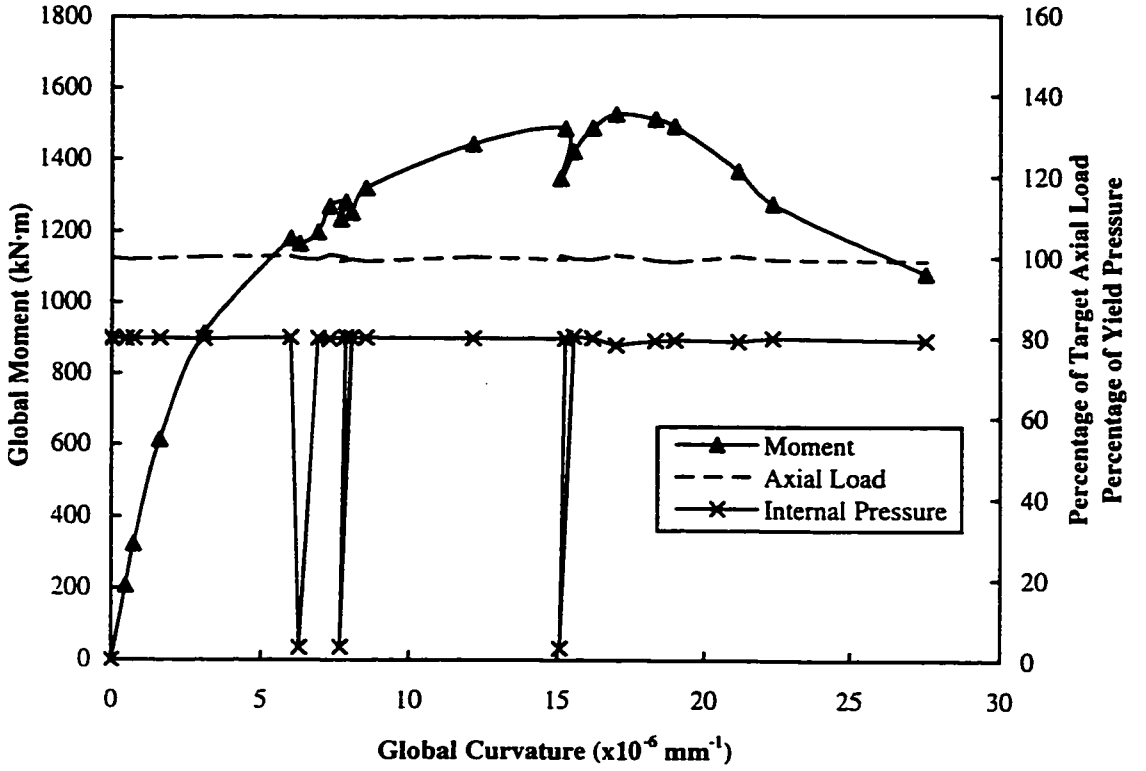

Figure 3.62 C45P80 – Global moment, axial load and pressure versus curvature diagram

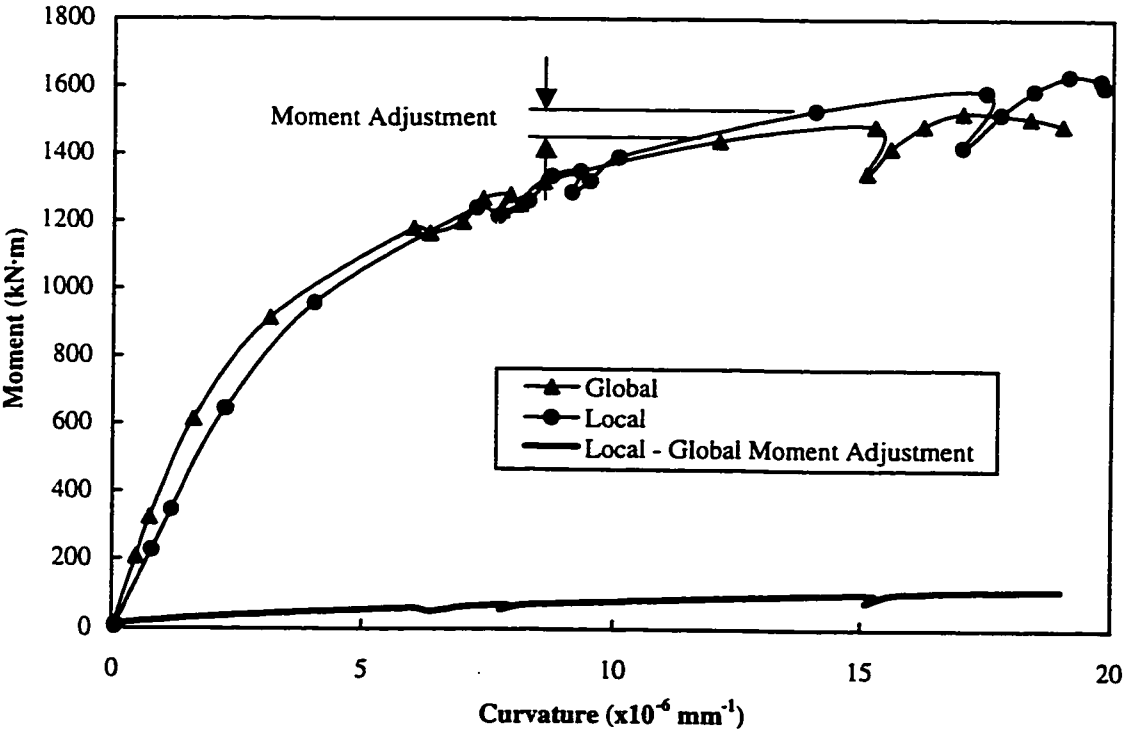

Figure 3.63 C45P80 – Comparison of global and local moment-curvature

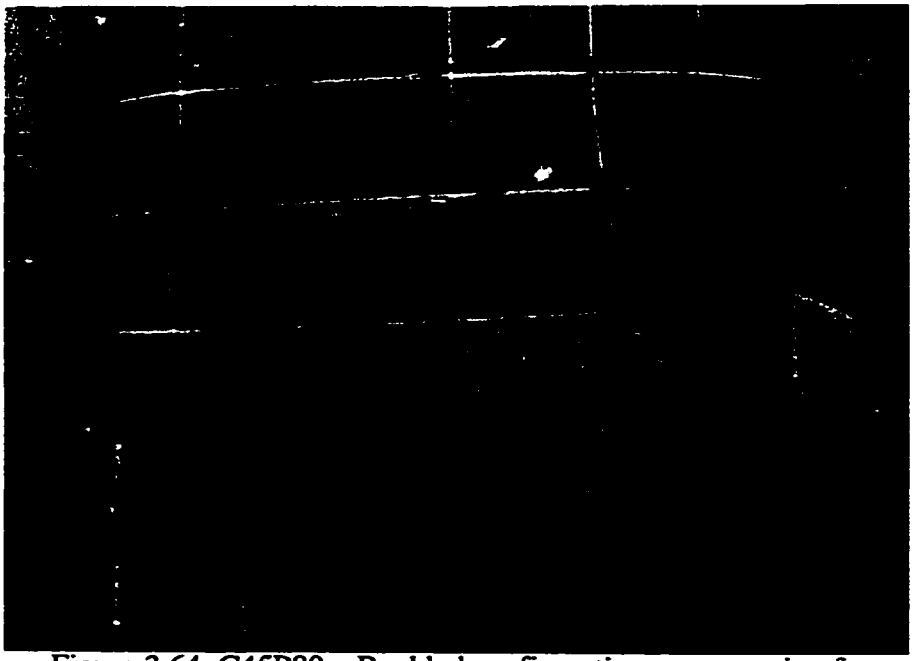

Figure 3.64 C45P80 – Buckled configuration, compression face

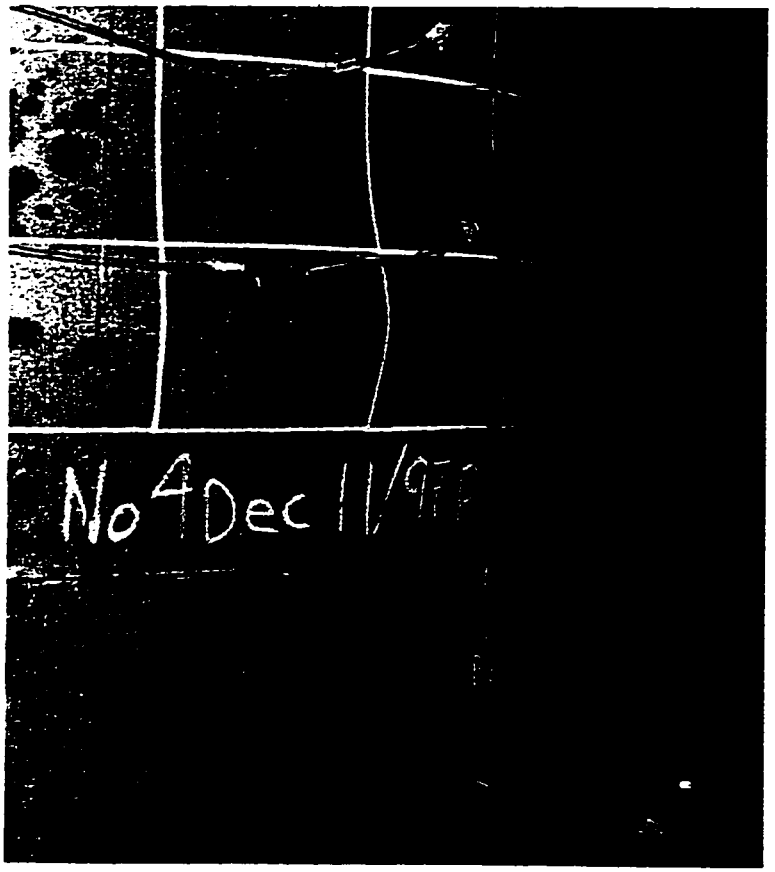

Figure 3.65 C45P80 – Buckled configuration, profile

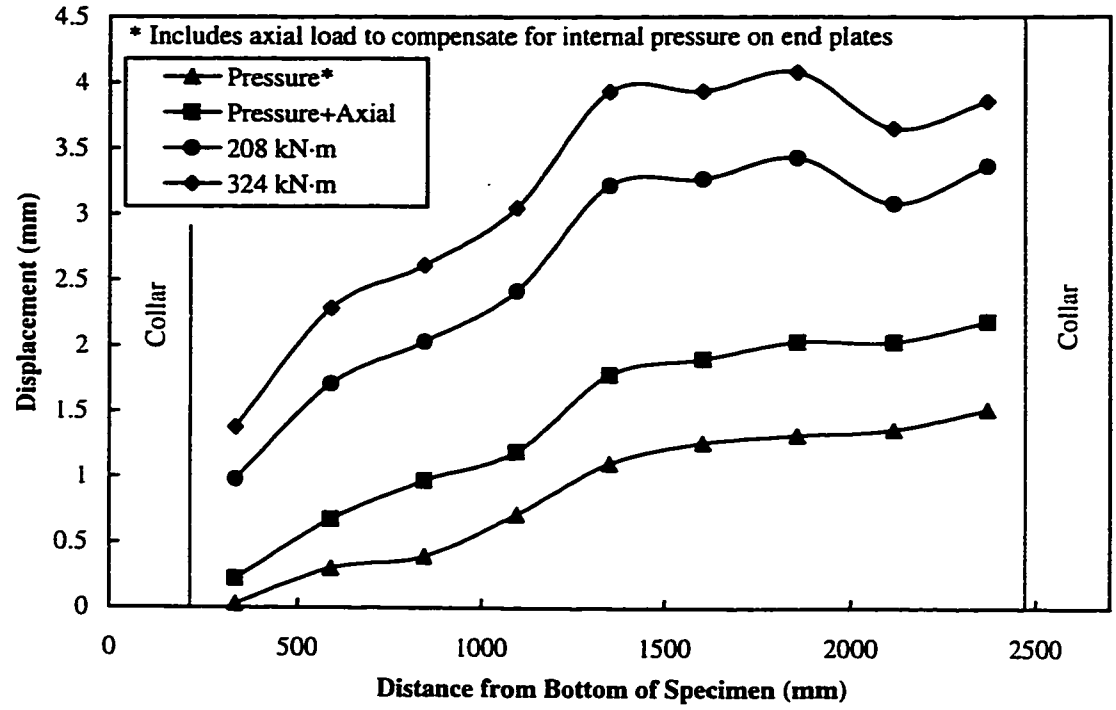

Figure 3.66 C45P80 – Compression face displacements: initial loading stage

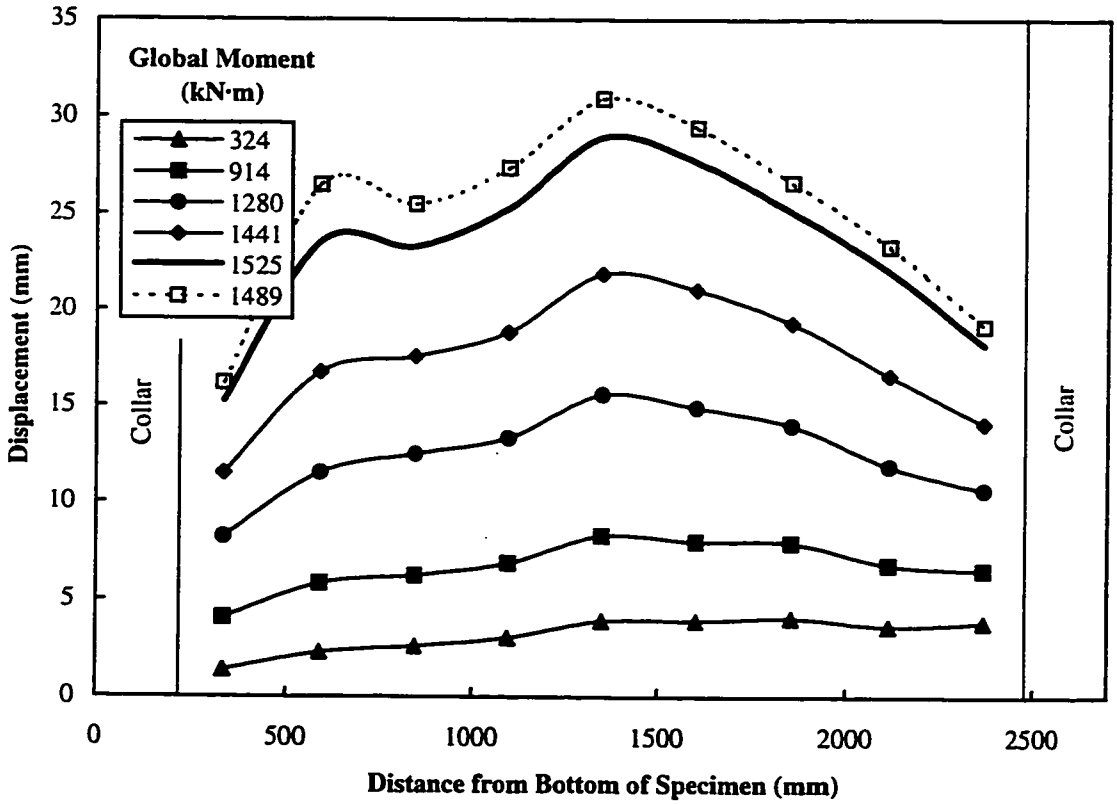

Figure 3.67 C45P80 – Compression face displacements

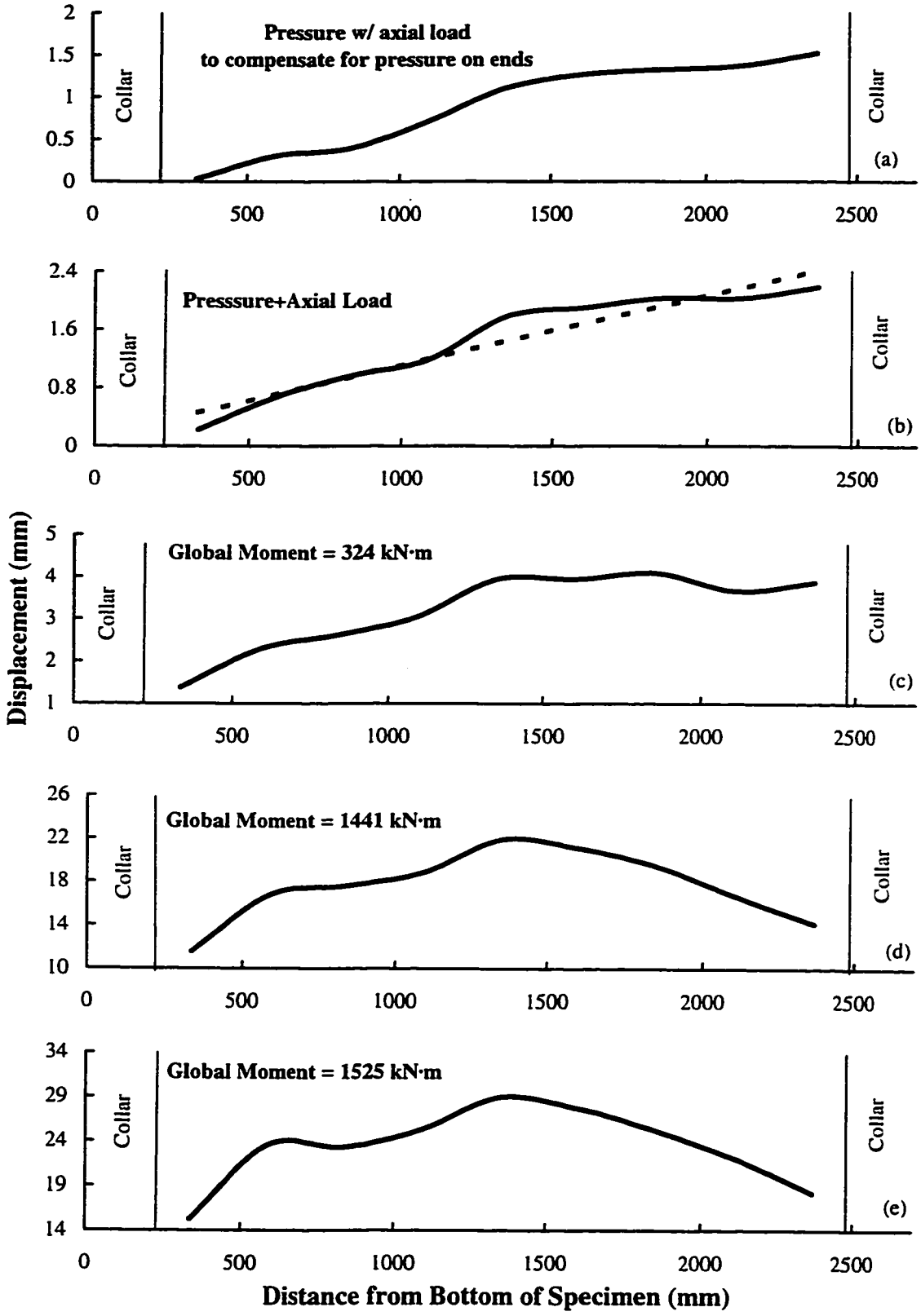

Figure 3.68 C45P80 - Progression of compression face displacements

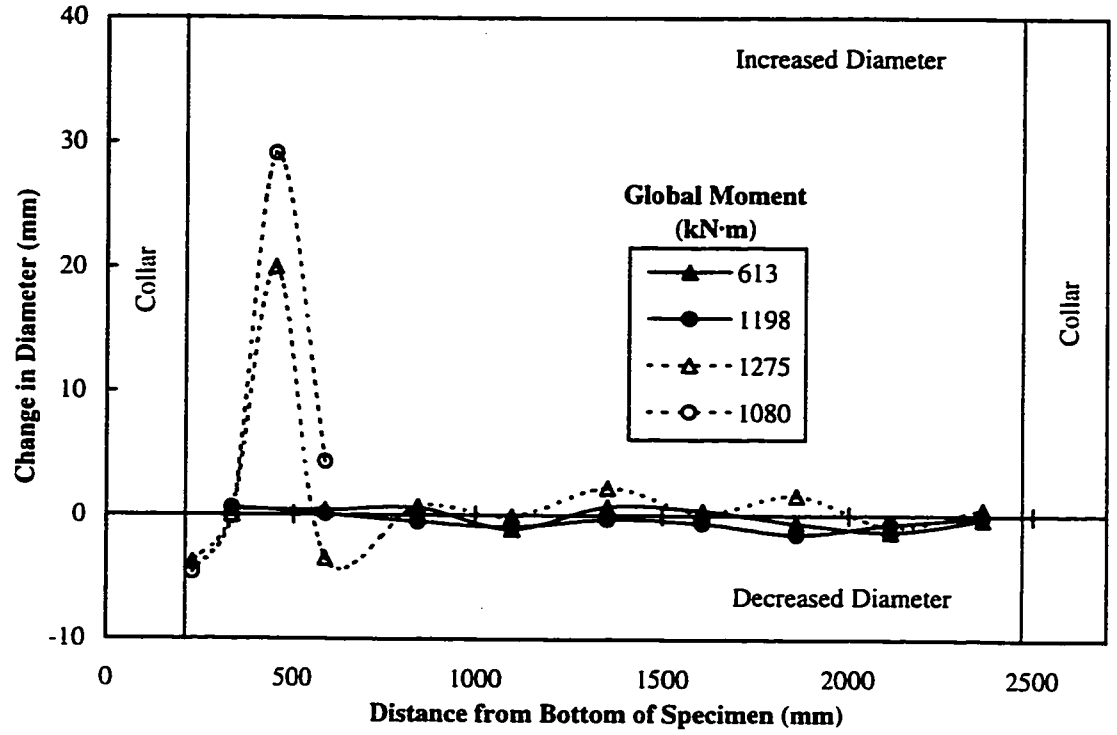

a) In-Plane Change in Diameter

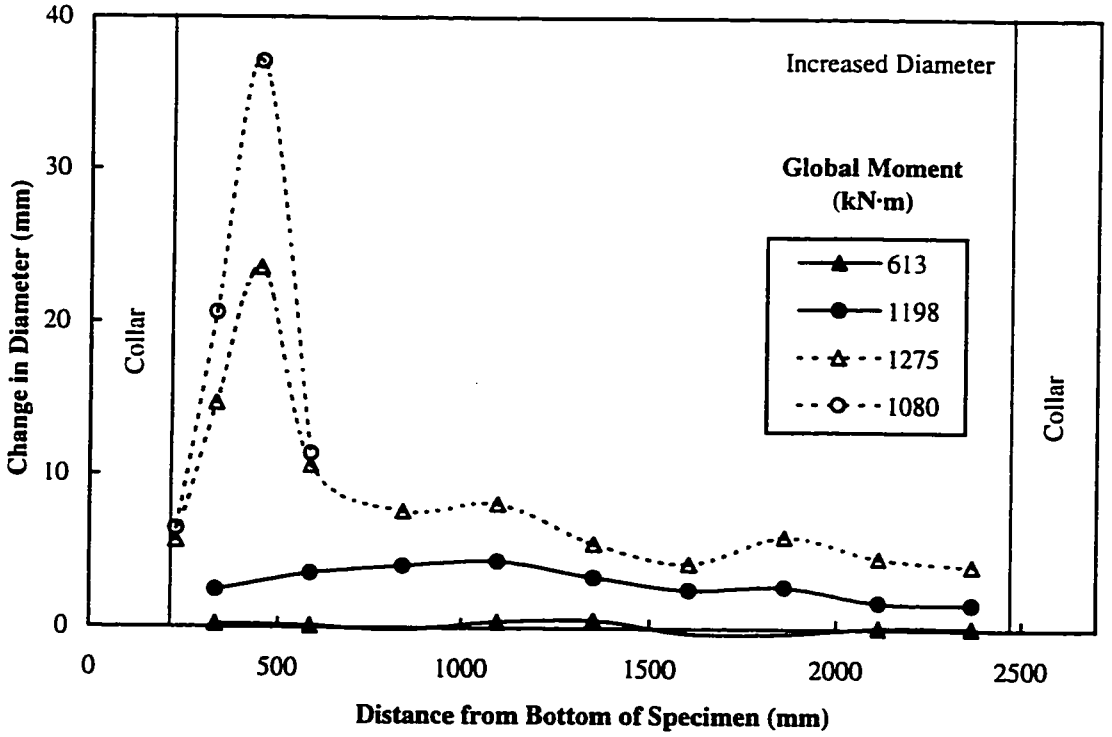

b) Out-of-Plane Change in Diameter

Figure 3.69 C45P80 – Measured changes in diameter

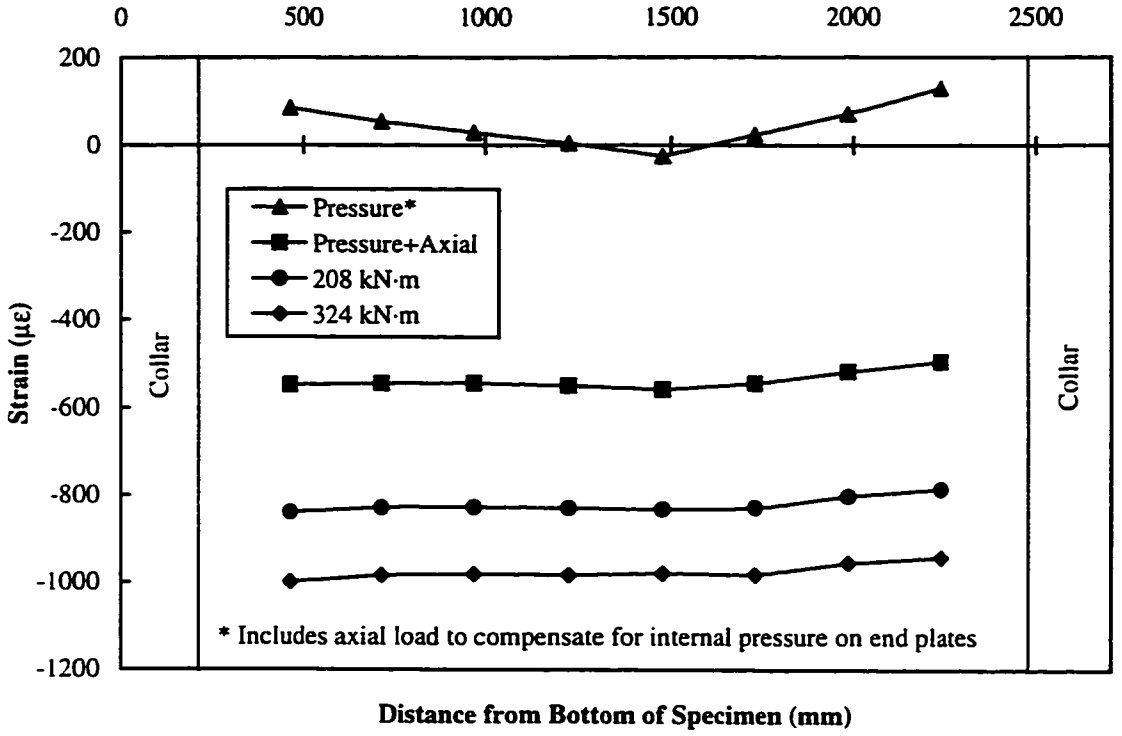

Figure 3.70 C45P80 – Compression face strain gauge measurements: initial loading stage

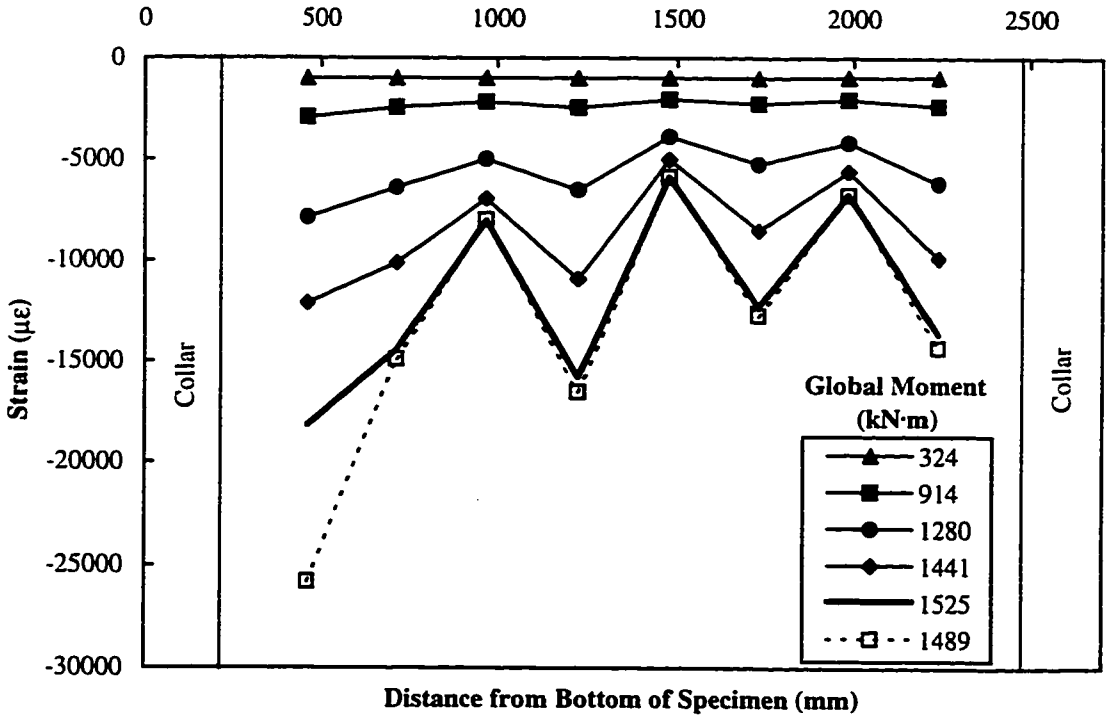

Figure 3.71 C45P80 – Compression face strain gauge measurements: pre- and post-buckling

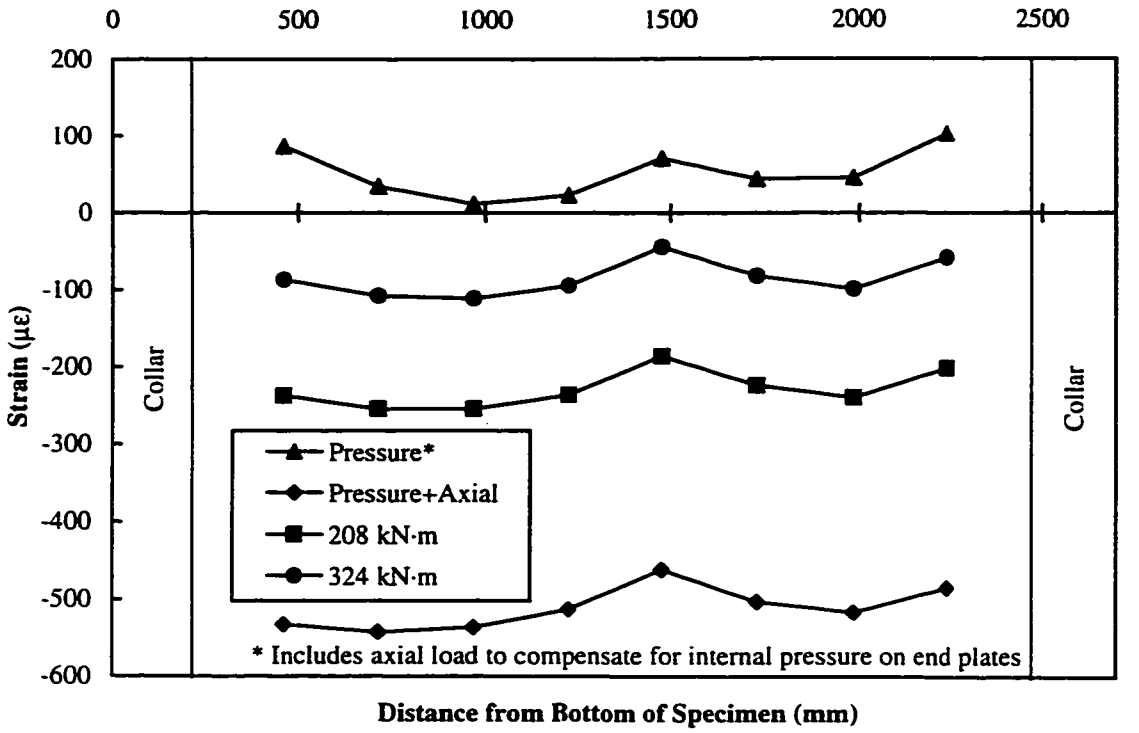

Figure 3.72 C45P80 – Tension face strain gauge measurements: initial loading stage

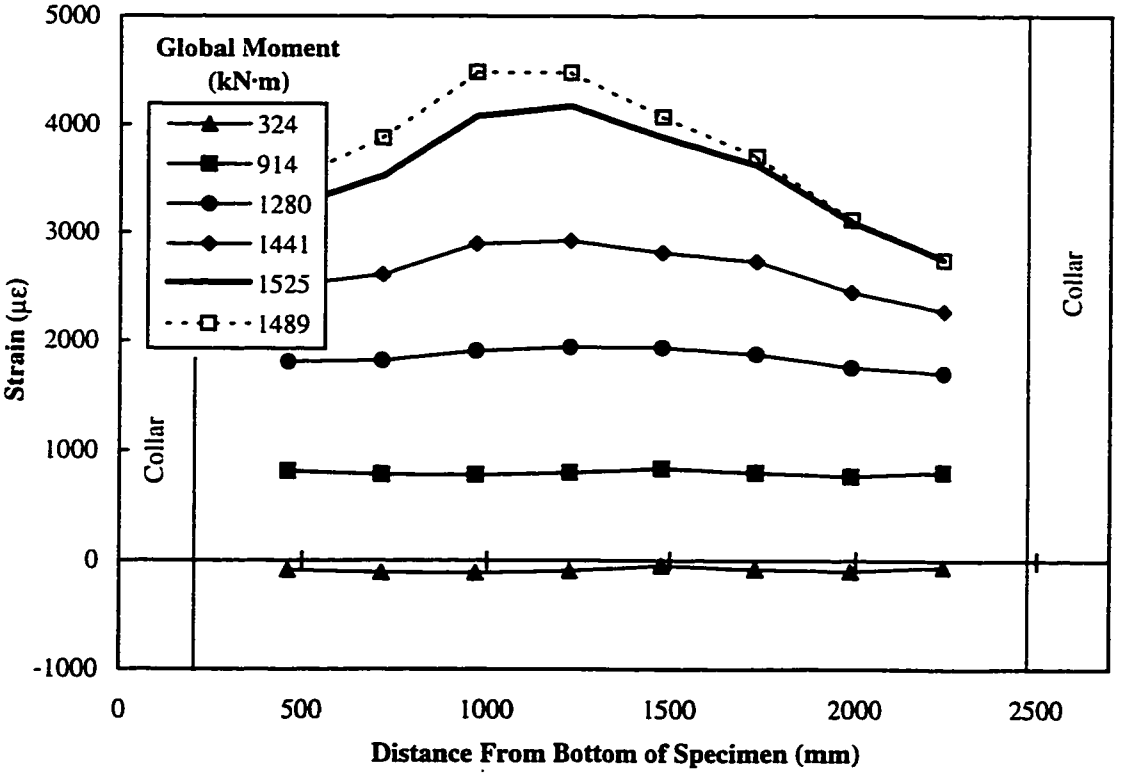

Figure 3.73 C45P80 – Tension face strain gauge measurements: pre- and post-buckling

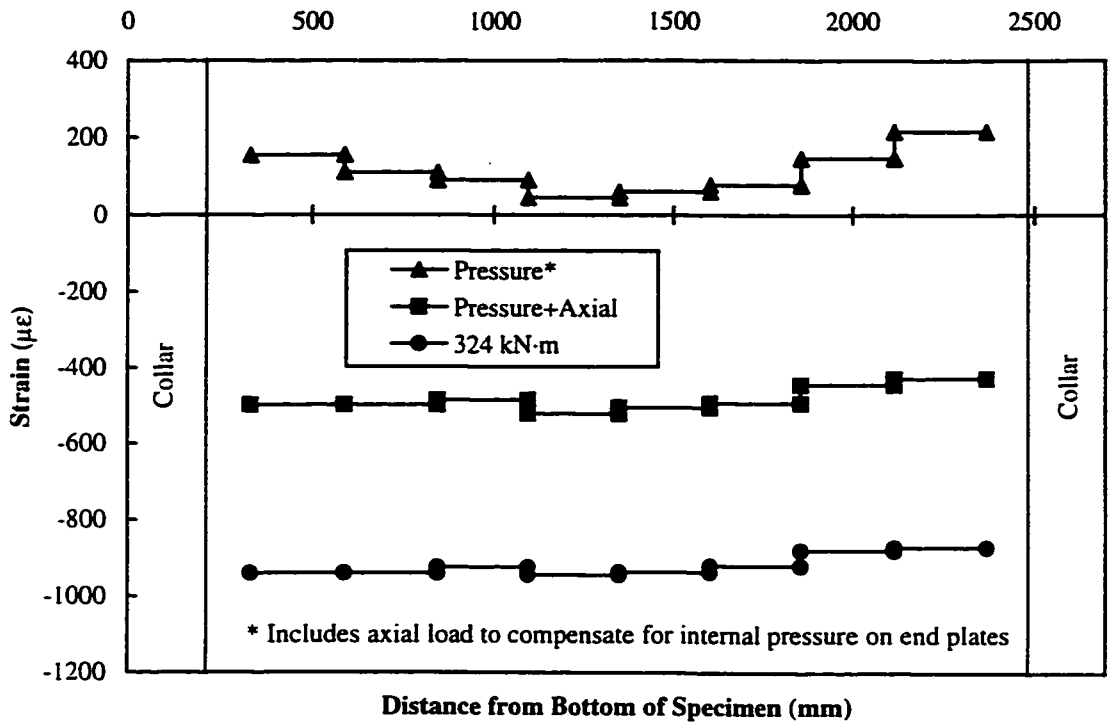

Figure 3.74 C45P80 – Compression face Demec measurements: initial loading stage

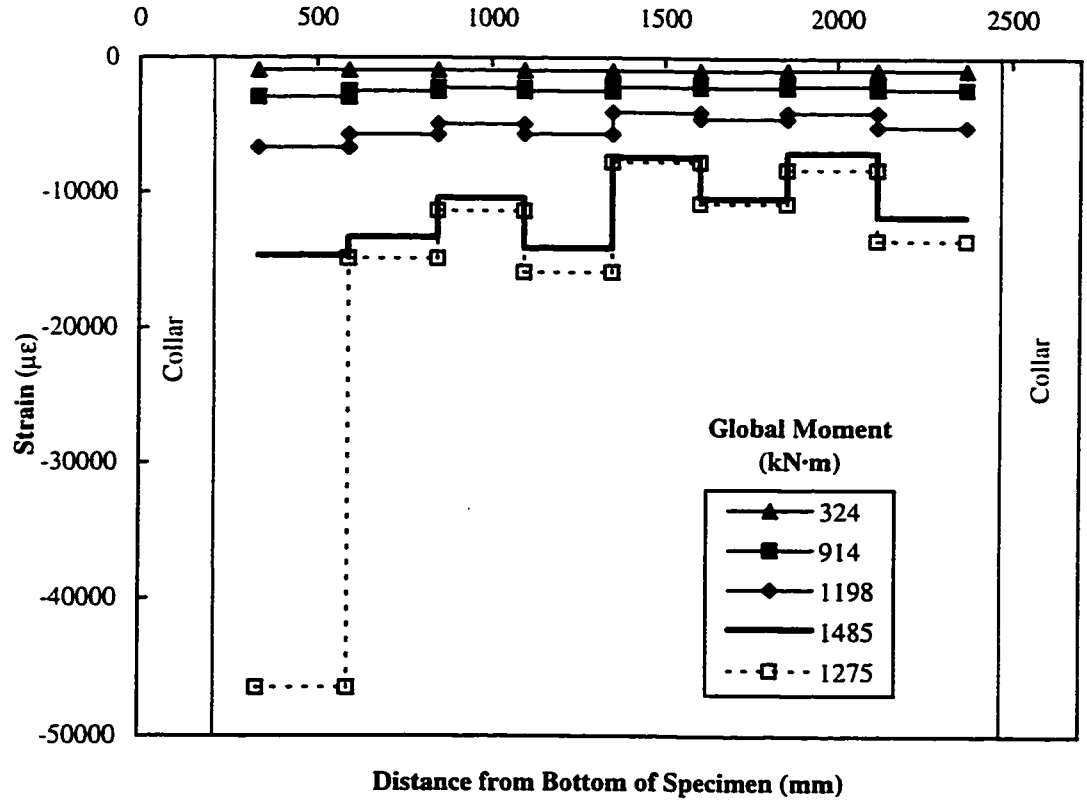

Figure 3.75 C45P80 – Compression face Demec measurements: pre- and post-buckling

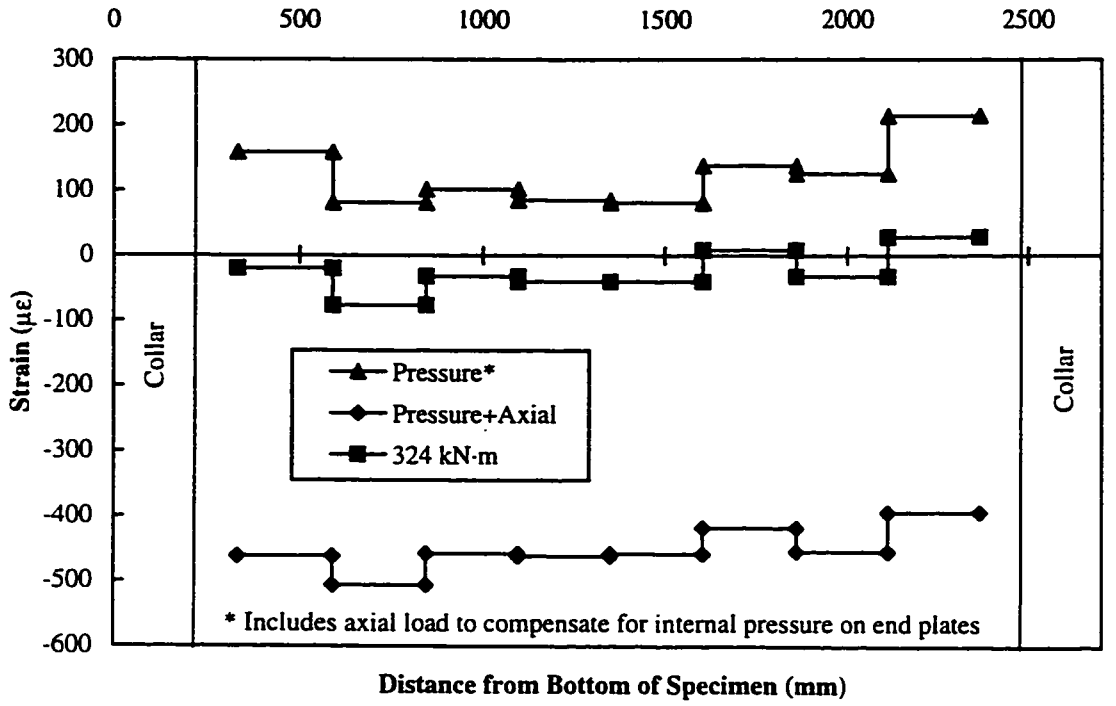

Figure 3.76 C45P80 – Tension face Demec measurements: initial loading stage

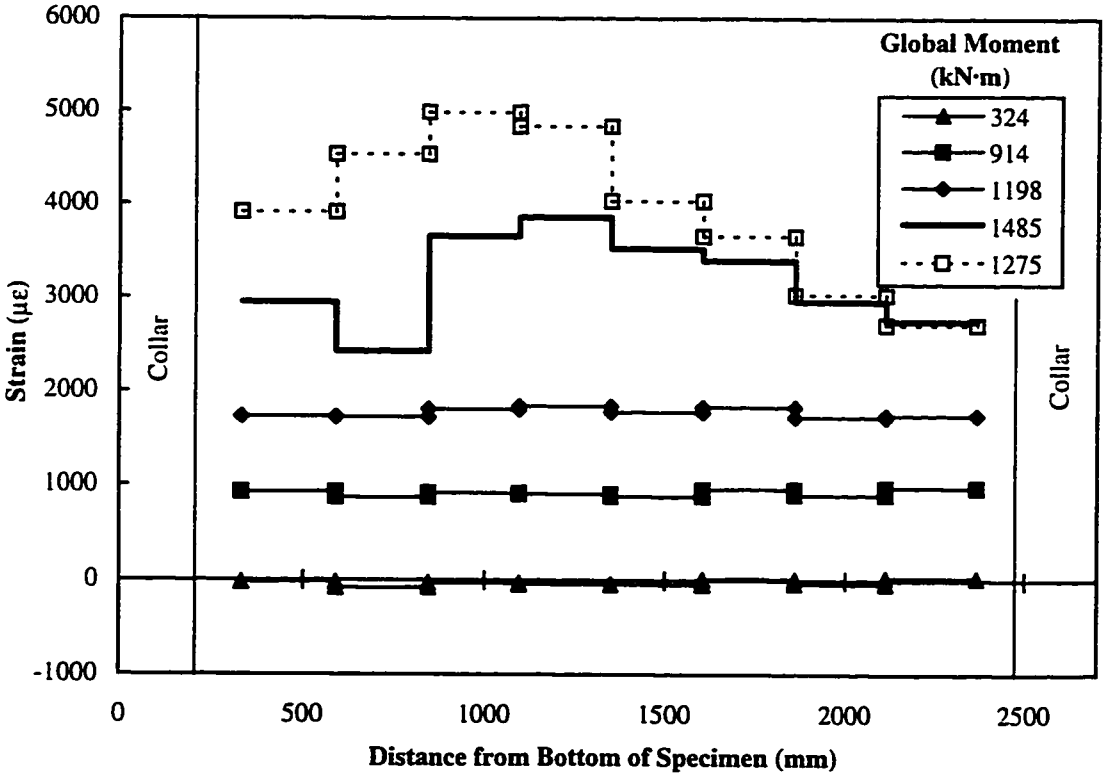

Figure 3.77 C45P80 – Tension face Demec measurements: pre- and post-buckling

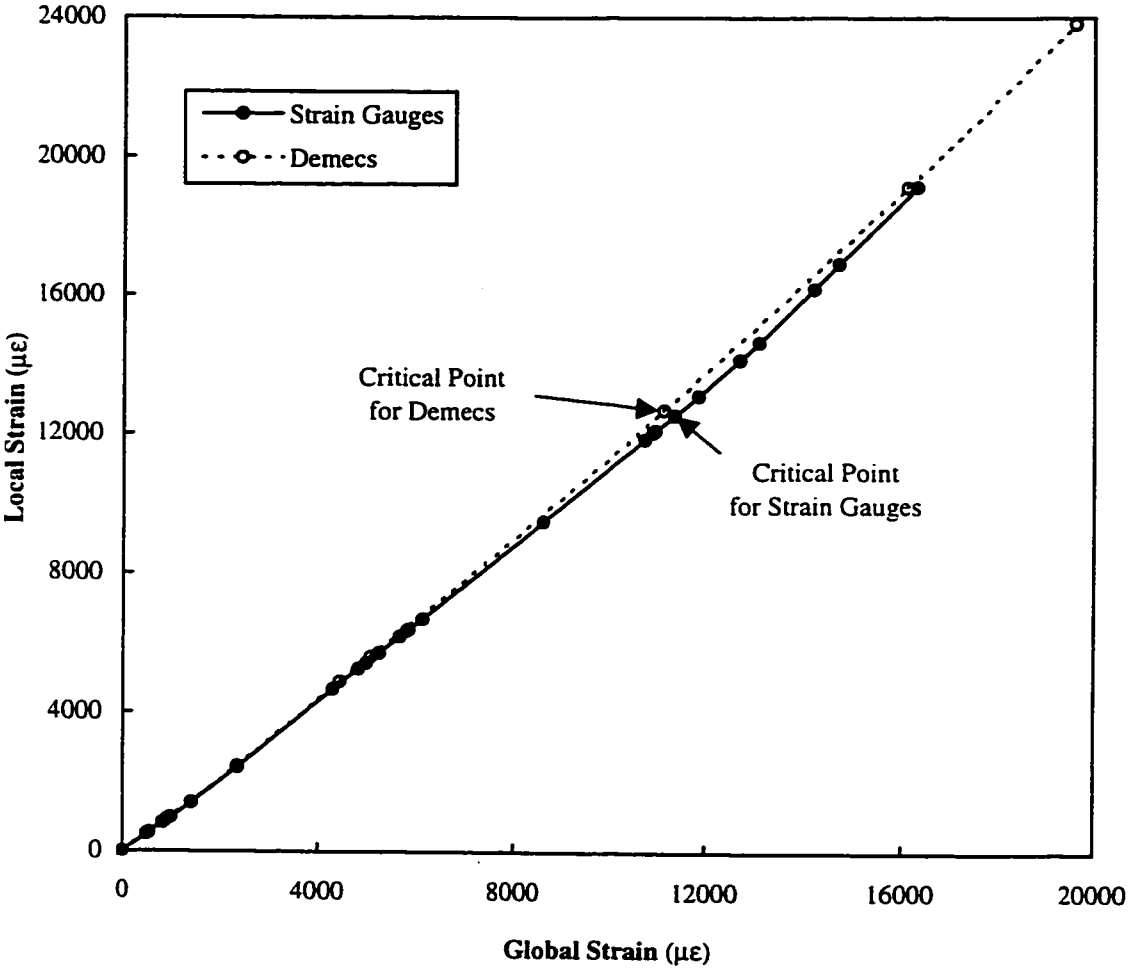

Figure 3.78 C45P80 – Determination of critical longitudinal compressive strain

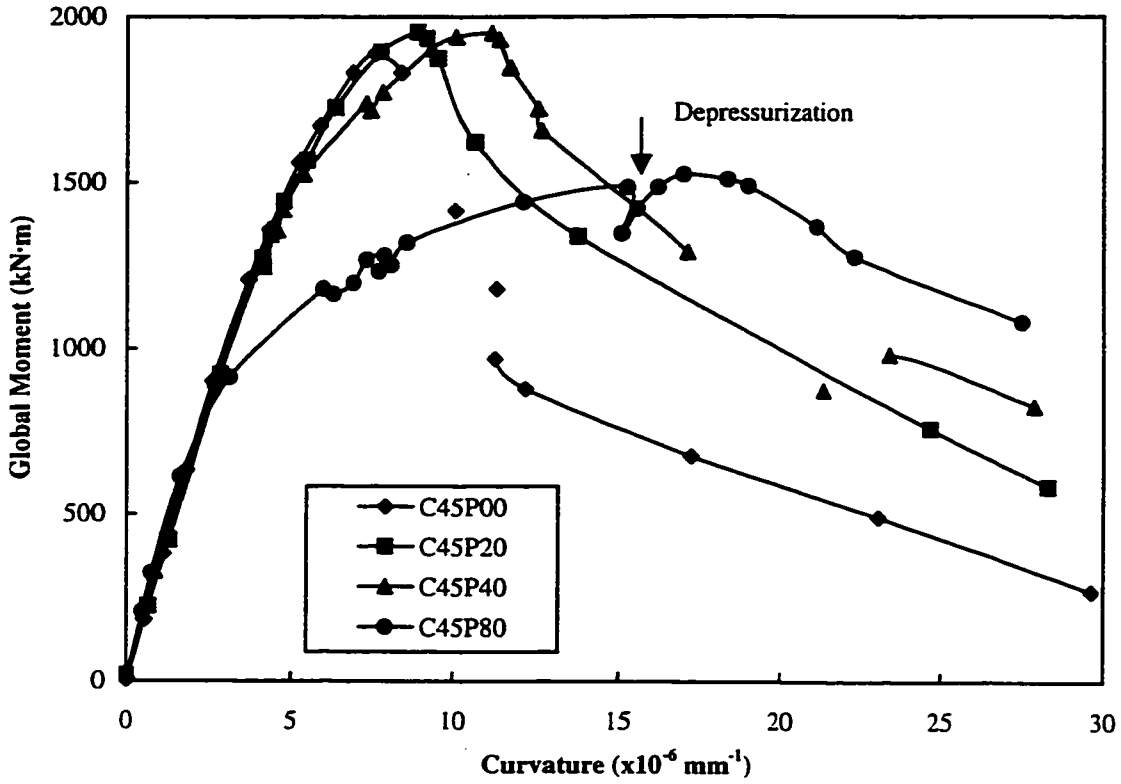

Figure 3.79 Comparison of Global moment versus curvature for all tests

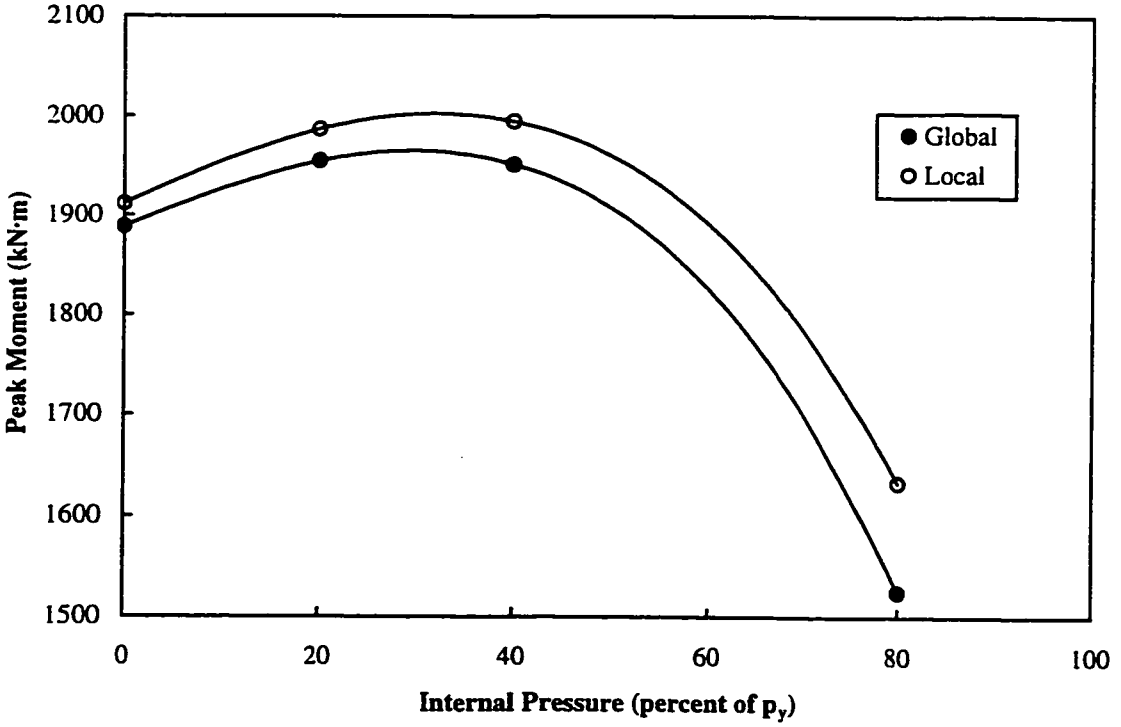

Figure 3.80 Peak moment as a function of internal pressure

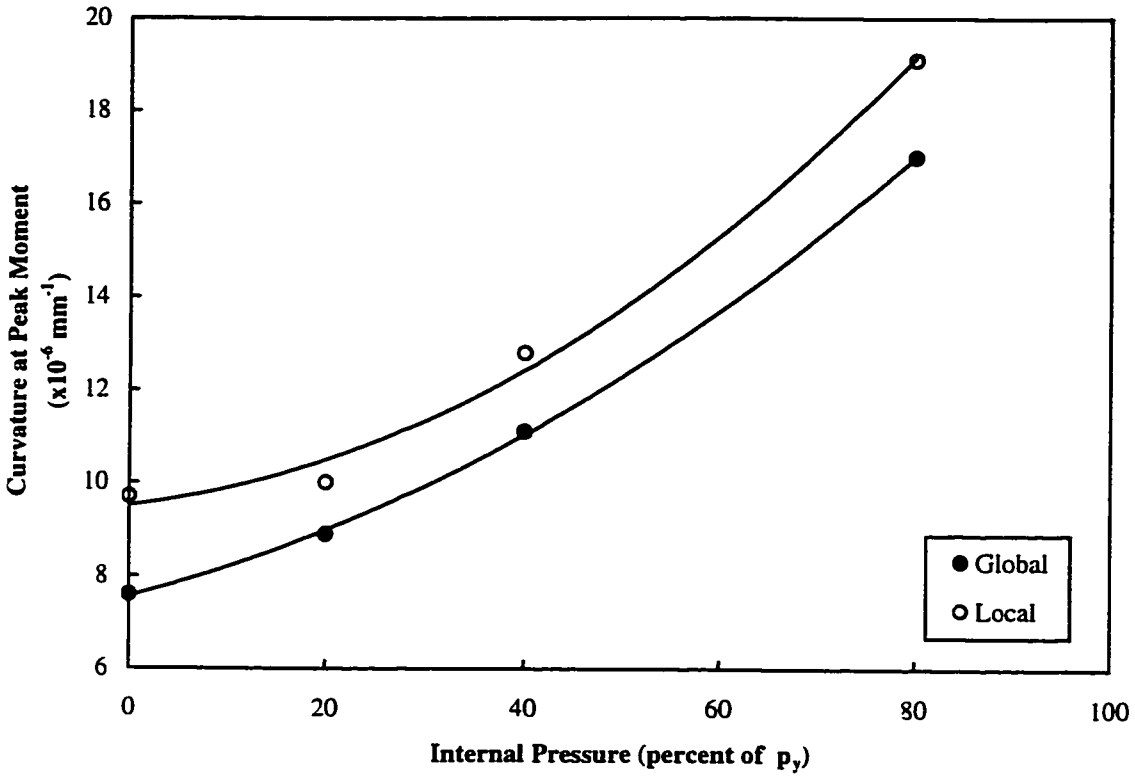

Figure 3.81 Curvature at peak moment as a function of internal pressure

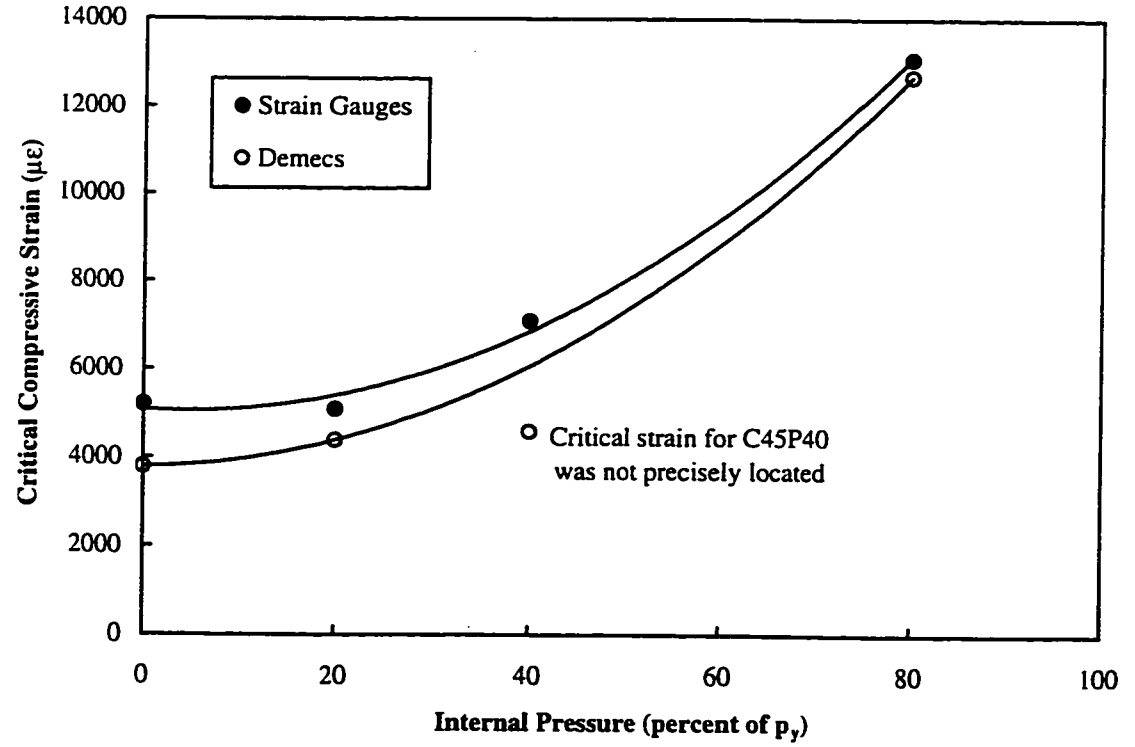

Figure 3.82 Critical longitudinal compressive strain as a function of internal pressure

4. FINITE ELEMENT ANALYSIS

The purpose of the second part of this research is to determine how the strength and behaviour of pipelines subjected to combined loading can be reliably modelled and therefore predicted using the finite element method. By comparing the results of an analytical model to the results obtained in the experimental study, one may determine the validity of such a model. The finite element analysis was limited primarily to modelling the tests that were performed as described in Chapter 2. A parametric study of the effects of element size and magnitude of initial imperfections is also included.

4.1 MODELLING OF TEST SPECIMENS

The analysis described herein was performed using ABAQUS 5.6 finite element software. This analytical tool is commercially available and was licensed to the University of Alberta at the time of the work. ABAQUS was chosen because its extensive use at the University of Alberta on various structures has shown excellent correlation between predicted structural response and test results. The software was used successfully for the analysis of pipelines by Mohareb *et al.* (1994), and Souza and Murray (1994). The shell element S4R from the ABAQUS element library was used. The S4R element is a four-node shell element formulated for large displacement, finite membrane strain problems (Hibbit *et al.* 1995). A mesh study was performed, as discussed further in Section 4.2, and it was found that 40 elements around the circumference and 78 elements along the length provided acceptable resolution to interpolate the displacement fields encountered. The aspect ratio of the elements in this arrangement is 1.73. Mohareb *et al.* (1994) used 18 elements around half a circumference (symmetry was assumed) and 60 elements along the length of the model. Also, the effect of initial imperfections was investigated, as described in Section 4.3, and incorporated into the model.

4.1.1 Symmetry of Model

For perfectly cylindrical specimens the use of a half model, symmetric with respect to the plane of bending, can reduce the number of degrees of freedom and, therefore, the computational time required to obtain a numerical solution. However, the study described herein includes the effect of the initial imperfections measured on the test

specimens. Since the measured geometry of the pipe does not have a plane of symmetry a full model of the pipe was used.

4.1.2 Boundary Conditions

To simulate the test conditions in the finite element model, the boundary conditions described in Chapter 2 had to be considered carefully. The ends of the test specimens were welded to 76 mm thick steel plates that rotated about pivot points as shown in Figure 2.1. For modelling purposes, these end plates are considered rigid bodies. Another important consideration for modelling the end displacement boundary conditions is the fact that the internal pressure during the test will always act normal to the surface of the end plates. The resulting force is, therefore, a follower force and acts on the deformed geometry of the model. In order to model these conditions at the ends of the pipe, 3-node rigid elements, 3RB from ABAQUS, were used to connect points on the end of the pipe to a single node placed in the position of the pivot point of the experimental set-up. These elements formed a closed, rigid cone on each end of the pipe keeping the ends of the specimen undeformed. The forces resulting from the internal pressure acting on the sloped surfaces of the cone cancel one another in all but the direction perpendicular to the plane that defines the end of the specimen. In effect, the resulting pressure follower force is as if the end plates were flat.

The pivot points at the top and bottom of the specimen were restrained to model the boundary conditions used in the test set-up. The top point was restrained in the direction of the two horizontal translational degrees of freedom and free to translate in the longitudinal direction. This pivot was also prevented from rotating about the torsional degree of freedom. The bottom pivot was restrained in all translational degrees of freedom as well as the out-of-plane rotational and torsional degrees of freedom.

Confining collars were placed around the ends of the test specimens to prevent buckling in the region of the pipe disturbed by the end conditions. The confining collars in this study were modelled using an effective wall thickness for the end elements in the regions supported by the confining collars. The effective wall thickness used in the model provides the same wall bending stiffness as the combined pipe wall and collar thickness, assuming no significant friction between the collar and pipe. The end elements

corresponding to the end collars and affected by the modified thickness used the same elastic-plastic material property as the remainder of the pipe.

4.1.3 Residual Stresses

Although Chen and Ross (1977) have showed that residual stresses in line pipe due to the forming and seam welding processes are present to some degree; no measurements of these stresses were included in the experimental program. Also, as stated in Chapter 2, the seam welds in the experimental program were intentionally placed on the tension face of the specimens in order to minimize their effect on the specimen behaviour. Karamanos and Tassoulas (1996a) have also demonstrated that the effect of residual stresses is not significant for combinations of low levels of axial load and bending. The effect of residual stresses on the overall behaviour was therefore deemed to be small and was not included in the numerical analysis.

4.1.4 Material Properties

The material properties used in the analysis were based on the results of the tension coupon tests described in Chapter 3. Since the longitudinal and circumferential material properties were very close, an isotropic material model, based on the average of the longitudinal and circumferential properties, was used in the numerical analysis. Also, an isotropic hardening rule was used for this study. Previous analysis by Mohareb *et al.* (1994) and Zhou and Murray (1993), assumed an isotropic material model with an isotropic hardening rule and good correlation between experimental and analytical results was found.

Measured engineering stress versus strain properties were transformed into the true (Cauchy) stress, σ_T, and true strain, ε_T, for use in the analytical model. The transformations were made using the following:

$$\sigma_T = \sigma_e \cdot \frac{l_d}{l_0} \tag{4.1}$$

$$\varepsilon_T = \ln(1 + \varepsilon_e) \tag{4.2}$$

Eq. (4.1) applies to stress and Eq. (4.2) to strain where l_d is the deformed gauge length and l_0 is the initial gauge length.

Figure 4.1 shows the engineering isotropic material model as well as the transformed, true material properties used for the analysis. Significant strain hardening of the material can be observed. Table 4.1 shows the values for the piecewise, non-linear, isotropic material properties included in the finite element model taken from the plot in Figure 4.1.

The compressive properties of the material were not determined during the experimental investigation. Although the true stress versus strain properties in compression may not be the same as in tension due to work hardening of the material during pipe fabrication and the Bauschinger effect, the tension and compression material properties were assumed to be the same in this analysis.

4.1.5 Loading

The test specimens were subject to various combinations of axial load, internal pressure and monotonically increasing curvatures as described in Section 2.3. In the finite element model, as in the tests, the axial load was applied to the top pivot point in the direction of the longitudinal degree of freedom. This load consisted of components that account for the axial loads due to temperature, Poisson's ratio effect and pressure acting on the end plates. Also, the use of shell elements S4R for the pipe and 3RB for the end cones allows for a distributed pressure to be applied perpendicular to the surface of these elements to simulate internal pressure. The loading sequence adopted for the analysis closely followed the loading sequence used during the tests. The internal pressure was applied in the first step, the axial load was applied in the second step and equal and opposite end moments were applied in the following load steps. The end moments were applied at the pivot points to simulate the loading method used during testing. The non-linear solution strategy adopted for this analysis was the arc-length control method (Riks' algorithm) to adjust the load increments, (Hibbitt *et al.* 1995).

4.2 FINITE ELEMENT MESH SIZE STUDY

To determine an appropriate mesh size, three models were constructed using element meshes of 24x46, 36x70 and 40x78. The first value used in this designation is the number of elements in the circumferential direction and the second value is the number of elements in the longitudinal direction. Also, initial imperfections were not considered at

this stage. It was decided that the load case with no internal pressure, corresponding to specimen C45P00 as described in Table 2.1, would govern the mesh needs of the finite element model. As observed in the test, the post-buckling configuration of specimen C45P00 consisted of the most complex displacement field. It is therefore expected that a finite element mesh suitable for this displacement field would also be suitable for the other local buckling configurations observed in the tests.

4.2.1 Results and Discussion of Mesh Size Study

Three behavioural characteristics where used to select the most appropriate mesh size for use in the finite element model. These included: the peak moment, the shape of the descending branch of the global moment versus curvature curve, and the post-buckling configuration. These characteristics were compared for the three mesh sizes to determine a suitable mesh size for the finite element analyses of the test specimens.

A plot of global moment versus curvature, shown in Figure 4.2, shows that the peak moment is essentially the same for the three mesh models. Also, it can be seen that the descending branch for the coarse mesh (24x46) is significantly different from the other two meshes. As expected, the descending branch of the 40x78 mesh begins at a smaller end rotation than that of the 36x70 mesh because the finer mesh is less stiff and better adapted to interpolate the displacement field in the buckled region.

Figure 4.3 to Figure 4.5 show the buckled shapes obtained for the different mesh sizes. Figure 4.3 shows clearly that the 24x46 mesh is not converging to the same buckling mode as the two other finer meshes and reverts to a mode consisting of an outward bulge at the centreline of the specimen. The buckling mode obtained using the 36x70 and 40x78 meshes, shown in Figures 4.4 and 4.5, respectively, consisted of a major depression along the centreline of the specimen with a set of two smaller depressions positioned on each side of the bending plane. Because the predictions based on these two meshes were similar in all respects, it was considered that the 40x78 mesh had converged to a sufficiently accurate solution.

The buckled configurations using the two finer meshes are doubly symmetric. During the test, a mode that consisted of only three depressions, referred to as the "diamond shape" mode, was observed as shown in Figures 3.13 and 3.14. The finite element models converged to a solution for a perfectly symmetrical model and this mode

could not be expected to occur in a laboratory setting because of imperfections in geometry and loading. Regardless, it was concluded that a mesh that can represent this symmetric "diamond shape" mode could be expected to accurately represent the mode encountered during the test. For the three mesh sizes, the computation time was not prohibitive. A complete solution could be generated for the 40x78 mesh in 3 to 12 hours depending on the availability of computer resources. Therefore, based on these observations, the 40x78 mesh was used throughout the remainder of this study for the finite element work.

4.3 INITIAL IMPERFECTIONS

It is generally accepted that initial imperfections have a significant effect on stability problems such as local buckling. It is not, however, understood how initial imperfections affect line pipe subjected to the load combinations of the tests described herein. It is anticipated that the greater the D/t ratio, the greater will be the effect of imperfections on the response of the pipe. Initial imperfections were, therefore, measured on the test specimens and presented in Section 3.3. These measured imperfections were subsequently introduced into the numerical model.

4.3.1 Study of Model Sensitivity to Initial Imperfections

Before the initial imperfections were measured on the test specimens, a series of analyses was performed to determine the sensitivity of the pipe behaviour to initial imperfections. It was decided that, as with the determination of the mesh size, the loading parameters of specimen C45P00 would show the greatest sensitivity to changes in the initial imperfections. This is due to the absence of the stabilizing effect of internal pressure. As described below, the model was seeded with an assumed initial imperfection pattern considered representative of imperfections encountered in a segment of pipe.

4.3.2 Pattern of Assumed Initial Imperfections

The assumed pattern of the initial imperfections used for this study is shown on a developed surface in Figure 4.6. In this figure, the magnitude of imperfection has been amplified by a factor of 100 for easier visualization and line a-a is located at the extreme compression fibre. Figure 4.6 shows that there is a prominent depression on the

compression face at the position indicated by an arrow. Figure 4.7 shows the profile of the initial imperfections along the compression face of the assumed model. The depression mentioned above is clearly visible at approximately 1000 mm from the bottom of the pipe. The magnitude of the localized depression is 1.28 mm or 15.4 percent of the wall thickness.

4.3.3 Analysis of Initial Imperfections

Three analyses were performed to determine the sensitivity of the model to initial imperfections. The analyses were conducted with initial imperfections of 100%, 50% and 10% of the magnitude of the assumed imperfections which yielded maximum magnitudes of imperfection equal to 15.4, 7.7 and 1.5 percent of the wall thickness, t, respectively. The analysis was performed with imposed equal and opposite end moments. The resulting moment versus curvature diagrams for the three magnitudes of initial imperfections are plotted in Figure 4.8 with the corresponding response of the perfect pipe. In this section, due to the imposition of equal end moments and the unsymmetrical buckling mode, the rotations at the top and bottom of the pipe are generally unequal. For simplicity, global curvature was used as the displacement parameter. In Figure 4.8 the moments have been normalized in terms of the peak moment obtained from the pipe with no imperfections.

As can be seen from Figure 4.8, imperfections do not affect the initial load response. However, with imperfections local buckling occurs at a lower moment capacity than the perfect cylinder for all magnitudes of initial imperfections. The moment capacity for a pipe with 100% of the assumed imperfections was 91 percent of the peak moment for the perfect pipe. The moment capacity for a pipe with 10% of the assumed imperfections was 97 percent of the peak moment for the perfect pipe. The shape of the descending branches for the response including initial imperfections also shows a more gradual loss of capacity when compared to the perfect pipe.

Figure 4.9 shows a plot of the percentage of the perfect pipe capacity versus the magnitude of initial imperfections, expressed as a percentage of the assumed initial imperfection. The figure shows that the initial reduction in moment capacity and limit point curvature for small imperfections is important. As the magnitude of the initial imperfections is increased, the sensitivity to an increase in initial imperfection magnitude

becomes less significant. This indicates that for imperfections of the magnitude shown in the assumed pattern, the effect of small deviations in this magnitude does not result in large variations in the analytical solution. The assumed imperfection of 1.28 mm along the compression face is approximately equal to the magnitude of imperfections measured experimentally as shown in Section 3.3. Therefore, small errors in the measured imperfection values do not significantly affect the analytical results.

Figures 4.10 to 4.12 show the buckled configurations for the various magnitudes of initial imperfections. Figure 4.10 shows the buckled pipe with 100% of the assumed initial imperfection. Figure 4.11 shows the buckled pipe with 50% of the assumed initial imperfection. For these cases, it can be seen that the configurations, as well as the location of the local buckle, are nearly identical and located at approximately 1000 mm, from the bottom of the pipe, shown as the left end in the figures. Clearly the depression in the assumed imperfection, described previously, triggers local buckling in this region. As the magnitude of the initial imperfections is reduced to 10% of the assumed initial imperfections, the local buckle occurs slightly above the centreline of the specimen, as shown in Figure 4.12. In this case, the secondary or P-δ moments are a more influential factor in determining the location of the local buckle than the depression in the pipe wall identified earlier, drawing the local buckle toward the centreline where these effects are greatest. The corresponding descending branch for this level of initial imperfection is slightly different as shown in Figure 4.8. This difference is attributed to the different local buckle location. In all cases the buckled configuration was a "diamond shape" as in the test, shown in Figures 3.13 and 3.14.

The above analytical study indicated that initial imperfections significantly affect the response of the finite element model. It was demonstrated that:

1) A localized depression along the compression face can trigger local buckling depending on the magnitude of this imperfection.

2) Small levels of initial imperfections, approximately 15 percent of the wall thickness, reduced the moment capacity up to 10 percent, as well as provided a more gradual loss of capacity than occurs for a perfect pipe.

3) The sensitivity to increases in the magnitude of initial imperfection, decreases rapidly beyond an imperfection of approximately 2 percent of the wall thickness.

4) Any imperfection in the model induces a "diamond shape" buckled configuration, as opposed to the symmetric "diamond shape" observed in Figure 4.5 for the perfect pipe.

4.3.4 Measured Initial Imperfections

As described in Chapter 2, the initial imperfections were measured on a coarse grid. To incorporate the initial imperfections in the finite element model, the measured values, discussed in Section 3.3, were mapped on the finite element mesh. A contour mapping program, MacGridzo (RockWare Inc., 1988) was well suited for this application. The output from MacGridzo consisted of the finite element grid points, on a user-defined grid, calculated by interpolating between measured points on the coarse grid. The program uses an inverse-distance type of interpolation based on the five closest points and a power exponent of two. Also included was the option of forcing the measured points to remain on the mapped surface.

Figures 4.13, 4.15, 4.17, and 4.19 show the developed surfaces of the mapped initial imperfections for the test specimens. The centreline a-a coincides with the extreme compression fibre of the test specimens and the location of the seam weld is identified. The imperfections were amplified by a factor of one hundred in the plots to better visualize the pattern. The tension face (the two edges of the developed pipe surface) exhibits a jagged surface compared to the compression face. This is attributed to the presence of the seam weld that adversely affected the integrity of the initial imperfection measurements in this area. The imperfections along the tension face are not considered to affect the buckling of the compression face or the overall stability of the pipe. Figures 4.14, 4.16, 4.18 and 4.20 present plots of the imperfections along the length of the compression face of each test specimen to show the distribution of imperfections that will most likely affect the behaviour of the specimens. As can be seen from these plots, the maximum amplitude of initial imperfection along the compression face of all test specimens was approximately $\pm$ 1mm.

Table 4.1

Piecewise Material Property Definition Used in Finite Element Analysis

Stress σ_T (MPa)	Strain ε_T ($\mu\varepsilon$)
0	0
298	1320
353	1620
406	2000
453	2490
484	3230
502	4080
514	4990
535	7470
551	10800
570	17800
586	24700
611	39200
634	58300
649	76200
661	96000
671	125000
672	143000
665	166000

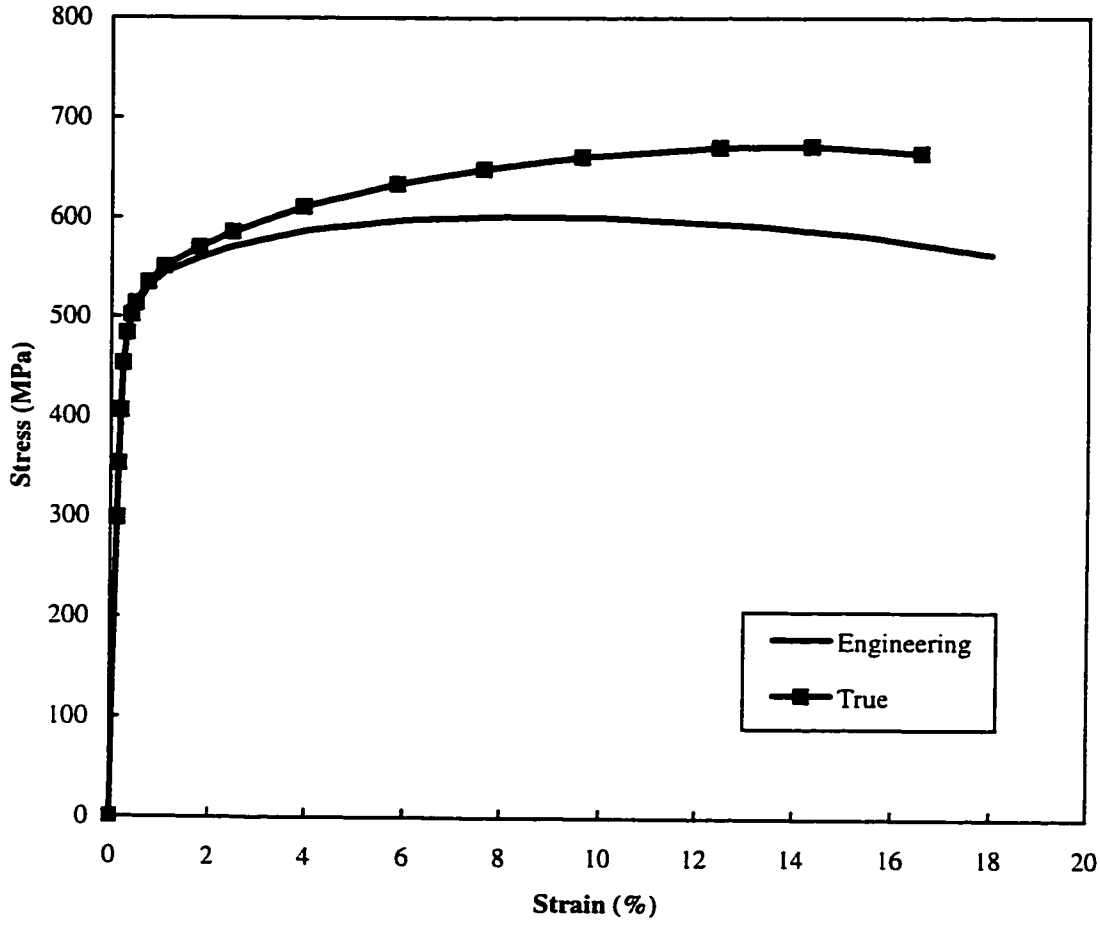

Figure 4.1 Material properties used in the finite element model

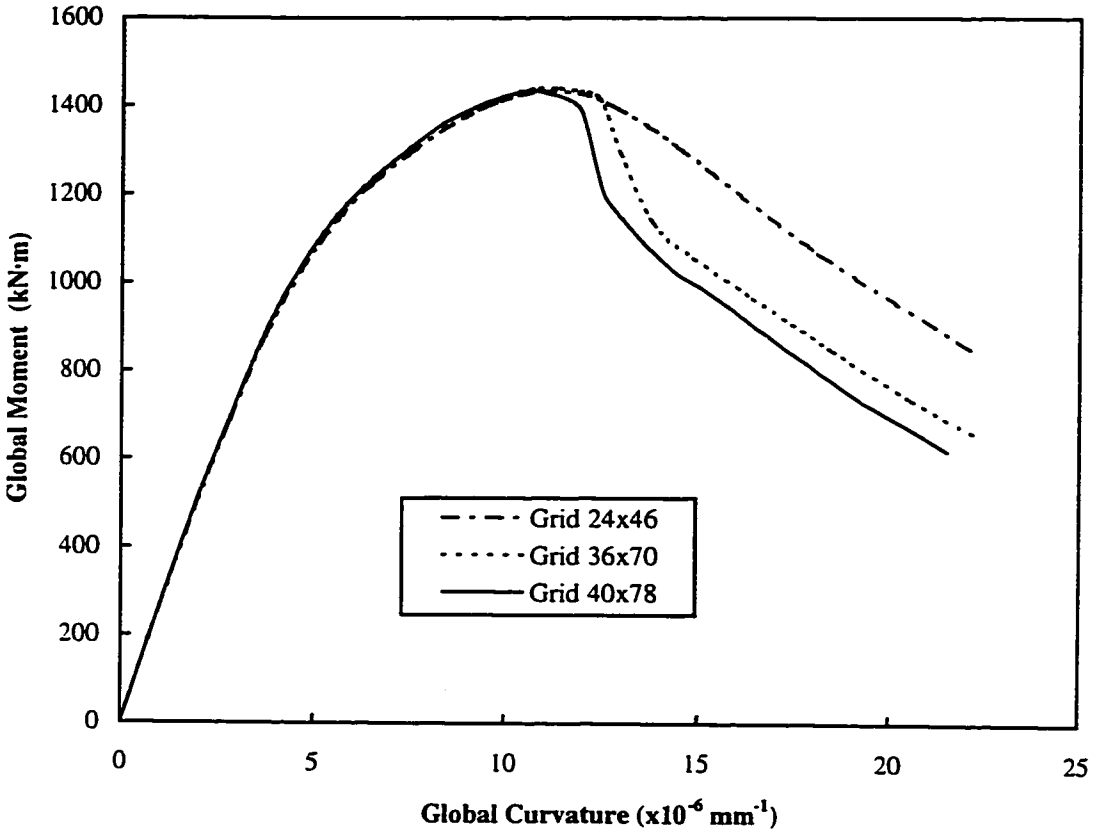

Figure 4.2 Moment versus curvature relationship from mesh size study

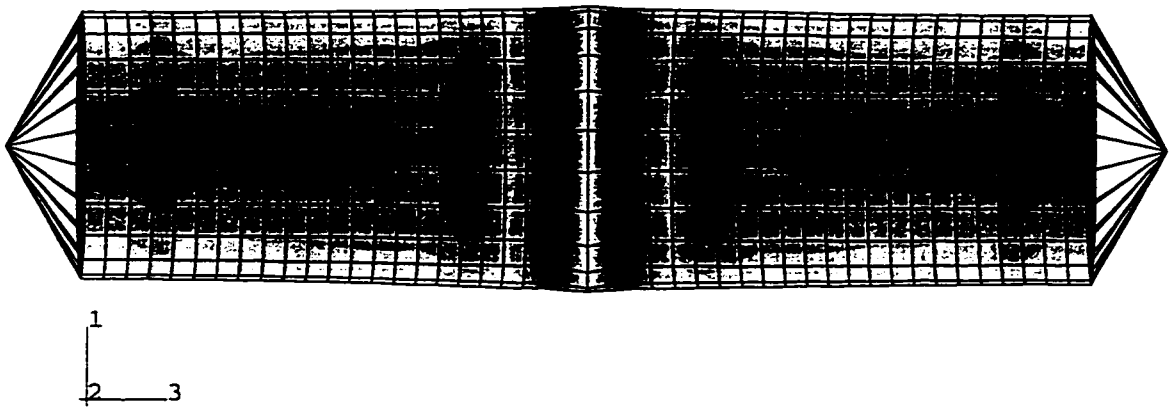

a) Compression Face

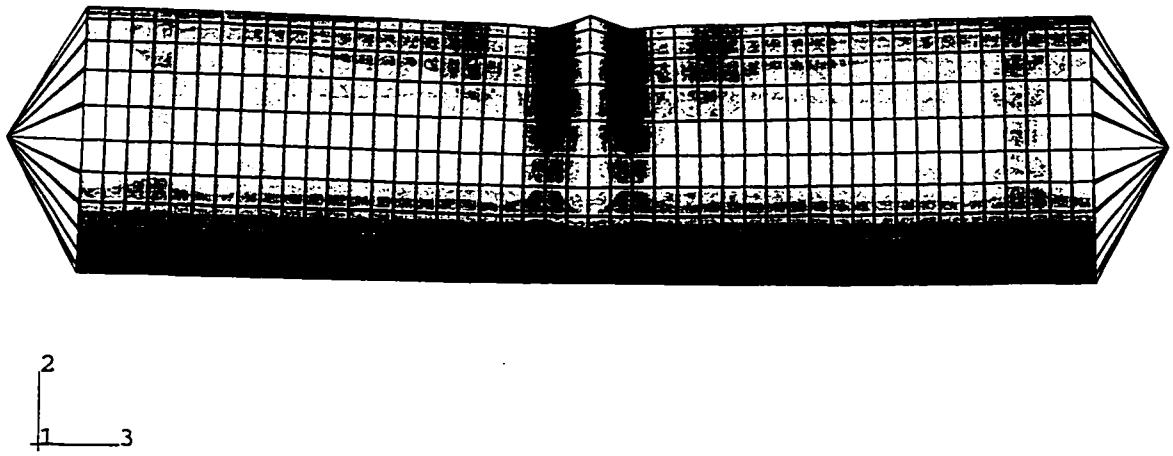

b) Profile

Figure 4.3 Buckled configuration for Grid 24x46

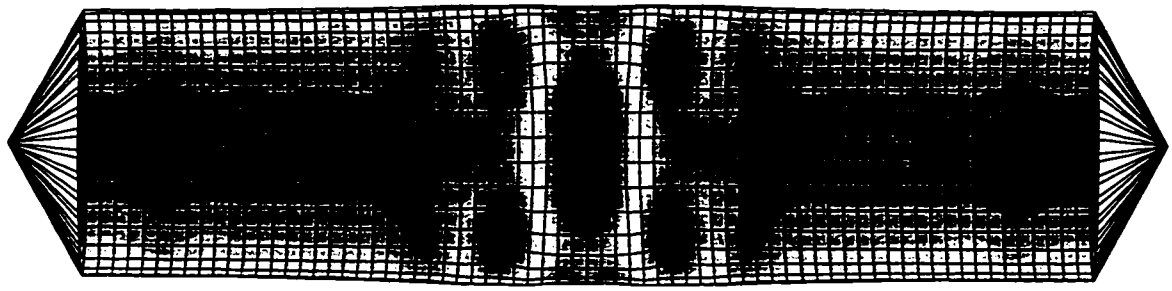

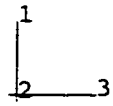

a) Compression Face

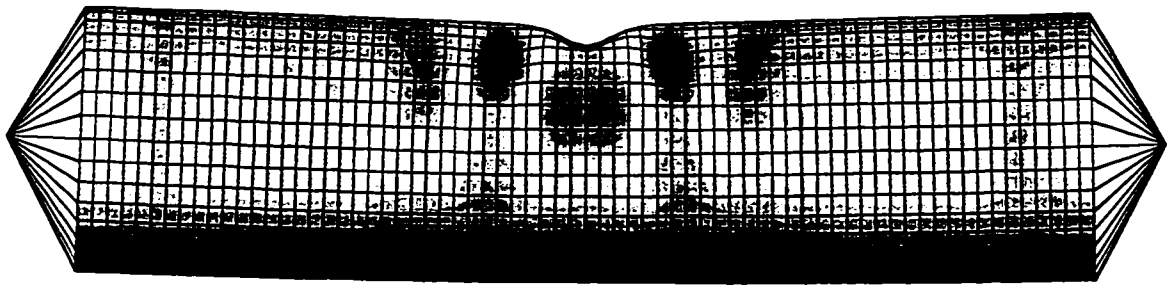

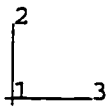

b) Profile

Figure 4.4 Buckled configuration for Grid 36x70

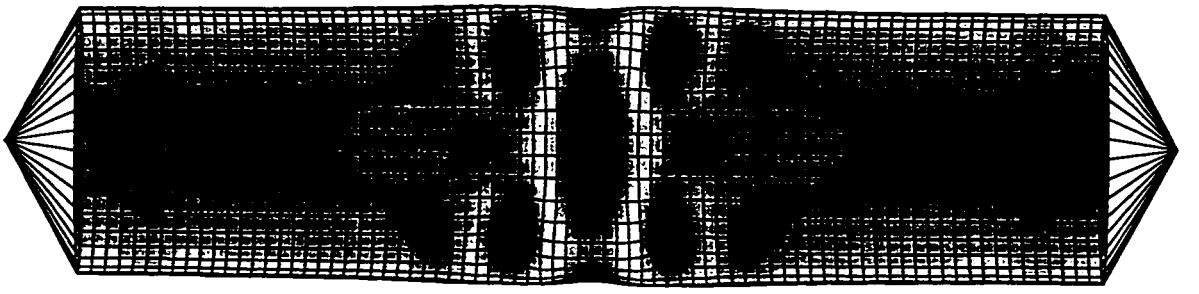

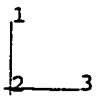

a) Compression Face

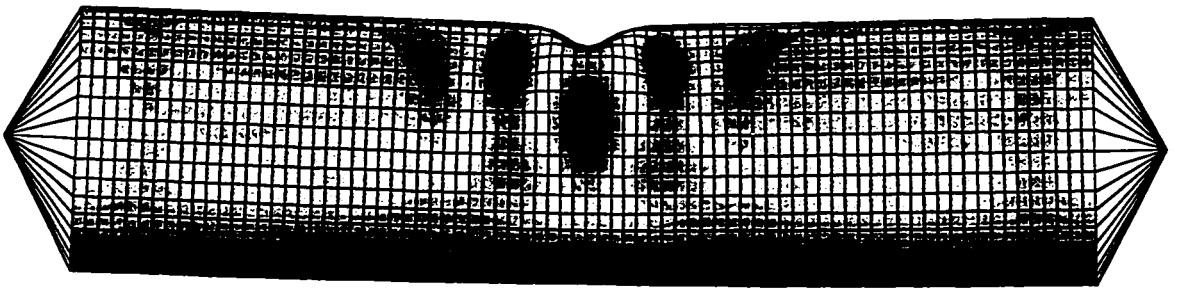

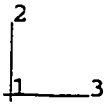

b) Profile

Figure 4.5 Buckled configuration for Grid 40x78

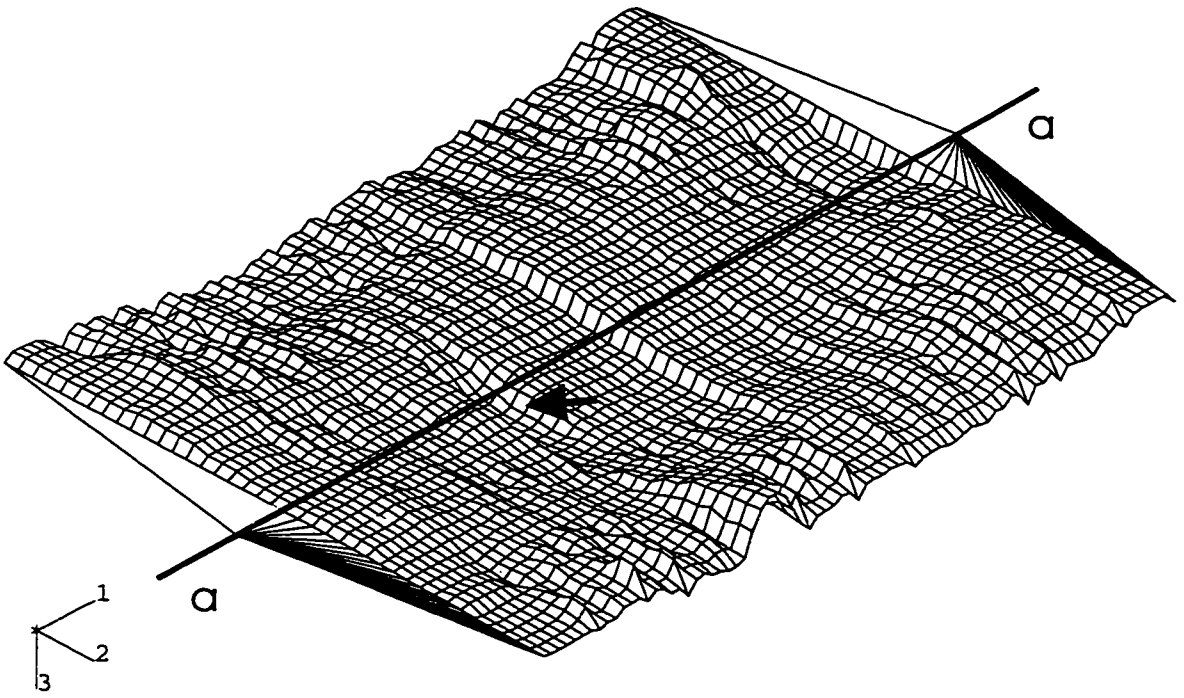

Figure 4.6 Assumed initial imperfection pattern

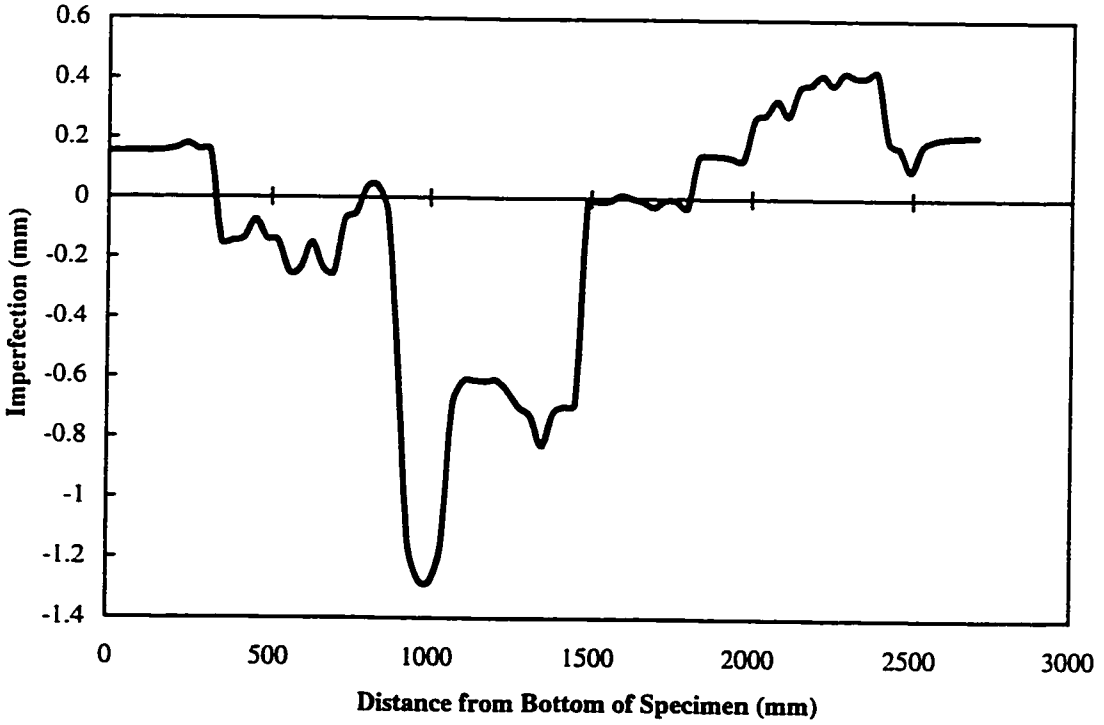

Figure 4.7 Imperfections along compression face of assumed pattern

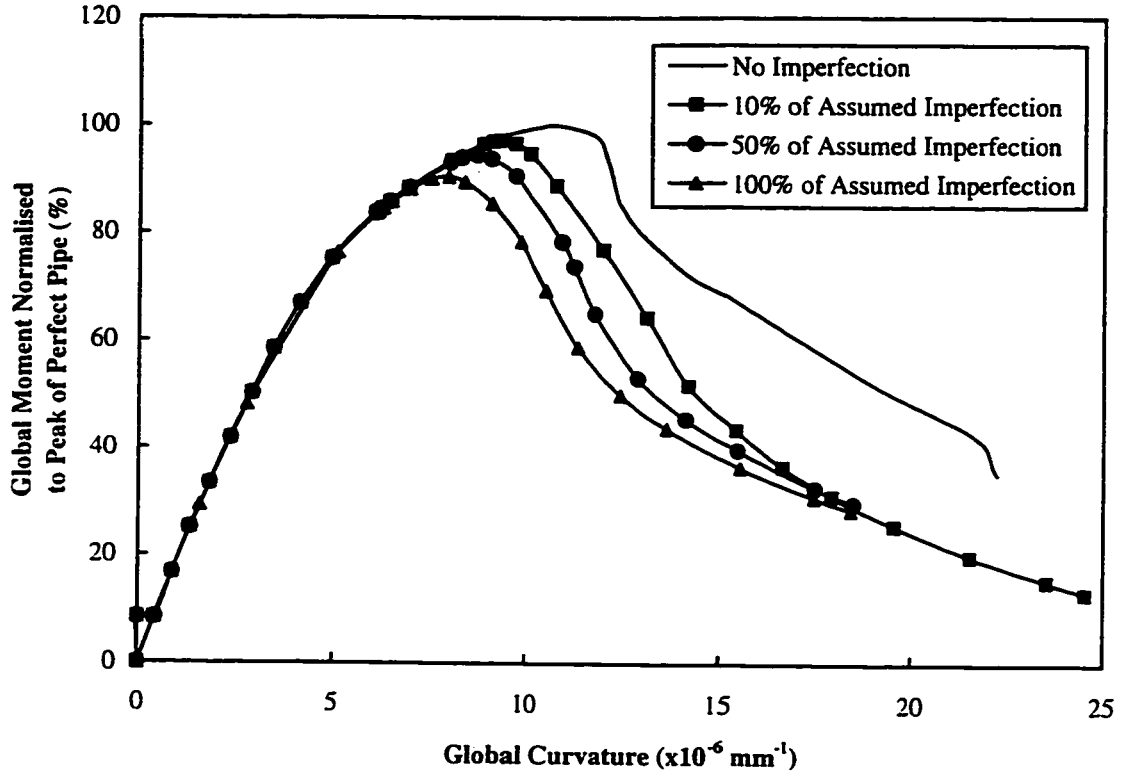

Figure 4.8 Effect of initial imperfections on moment versus curvature response

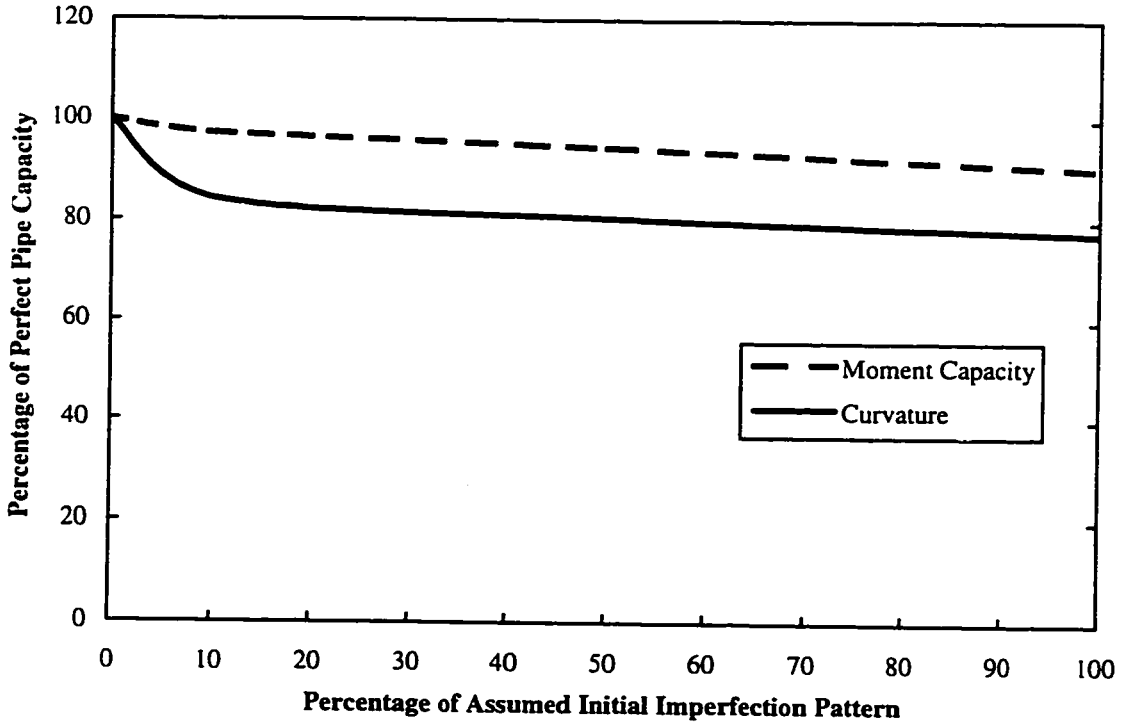

Figure 4.9 Effect of magnitude of initial imperfections on moment capacity and limit point curvature

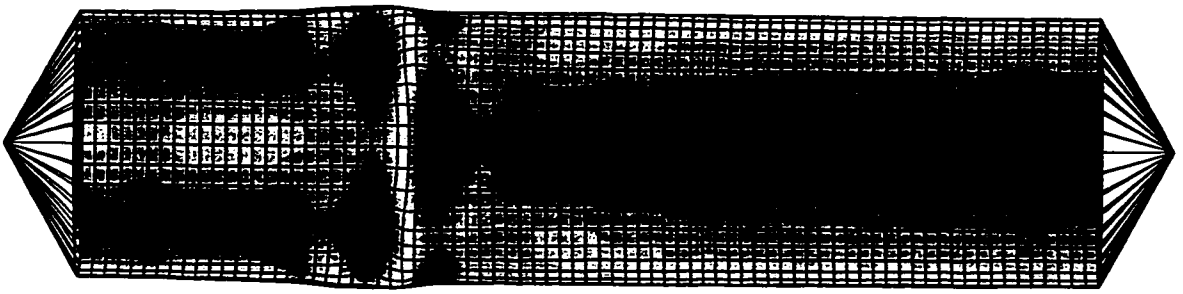

a) Compression Face

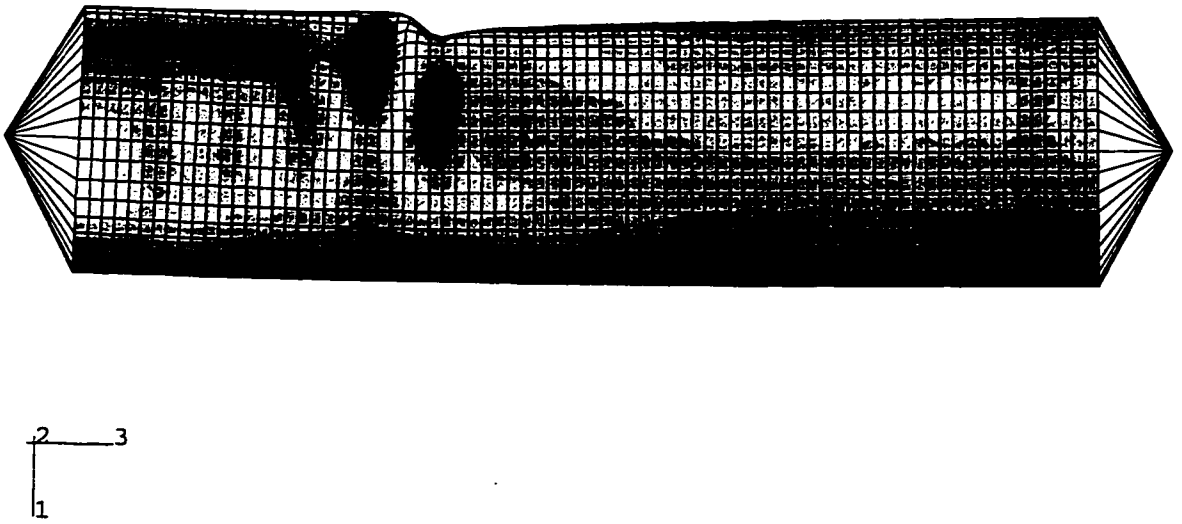

b) Profile

Figure 4.10 Buckled configuration for 100% of assumed initial imperfections

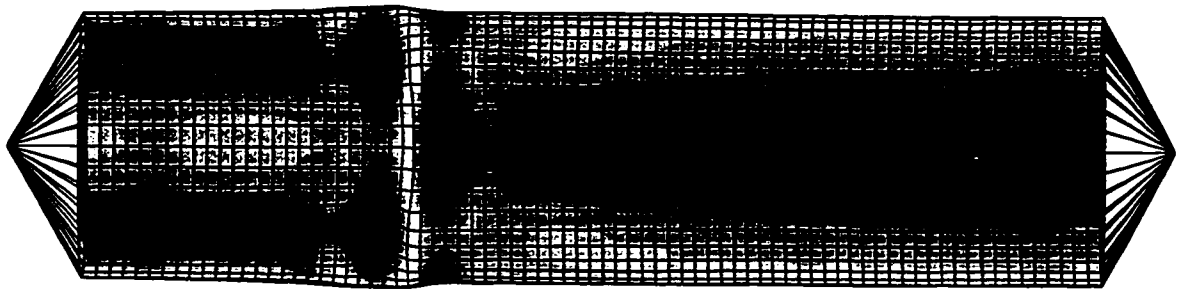

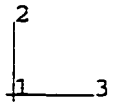

a) Compression Face

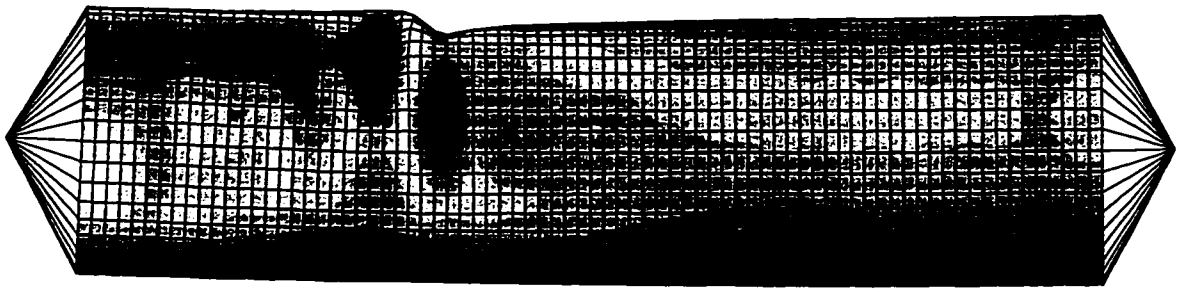

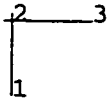

b) Profile

Figure 4.11 Buckled configuration for 50% of assumed initial imperfections

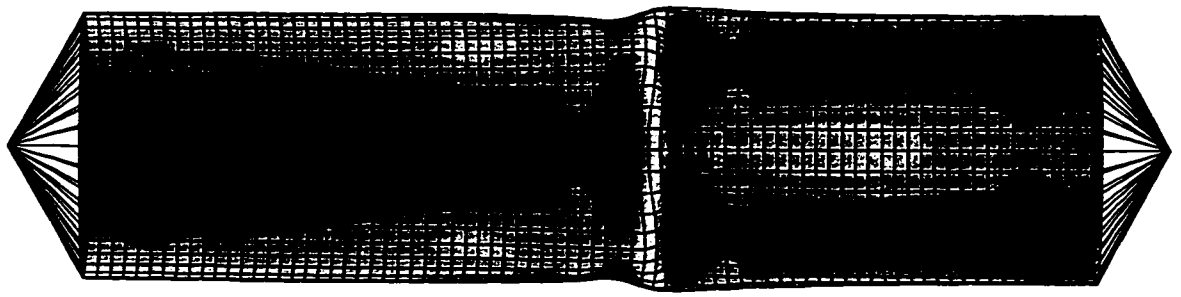

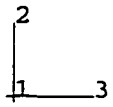

a) Compression Face

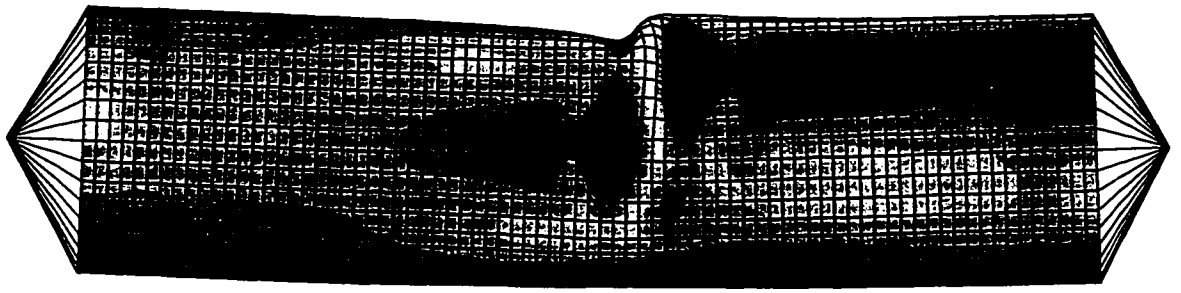

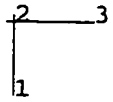

b) Profile

Figure 4.12 Buckled configuration for 10% of assumed initial imperfections

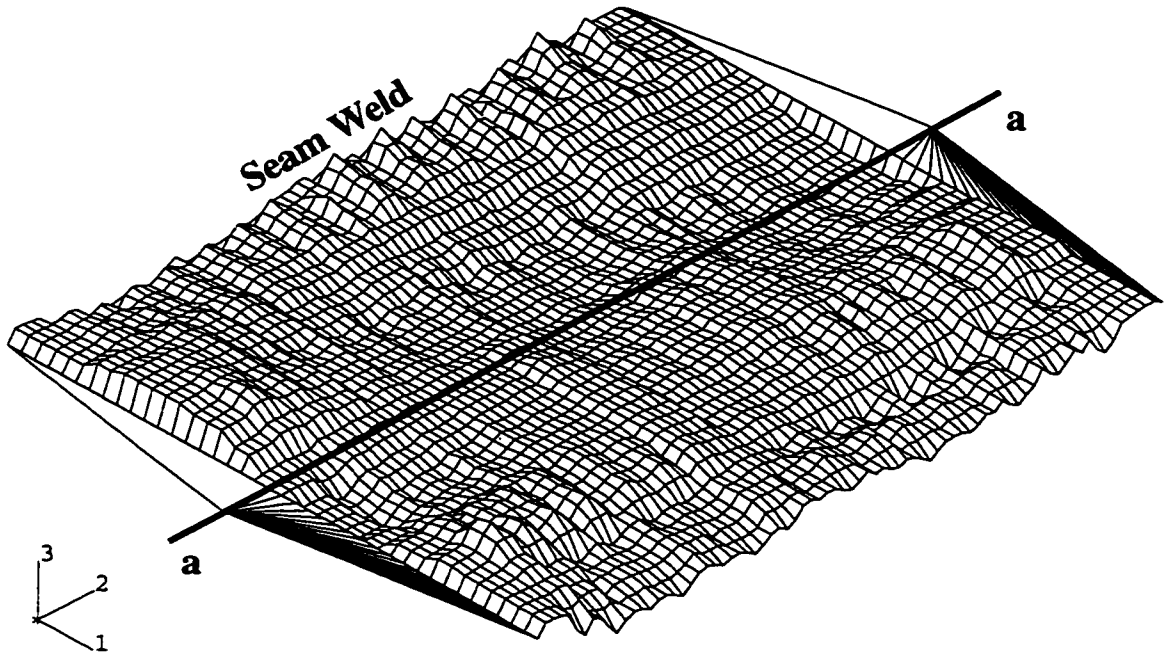

Figure 4.13 Mapped initial imperfection pattern for specimen C45P00

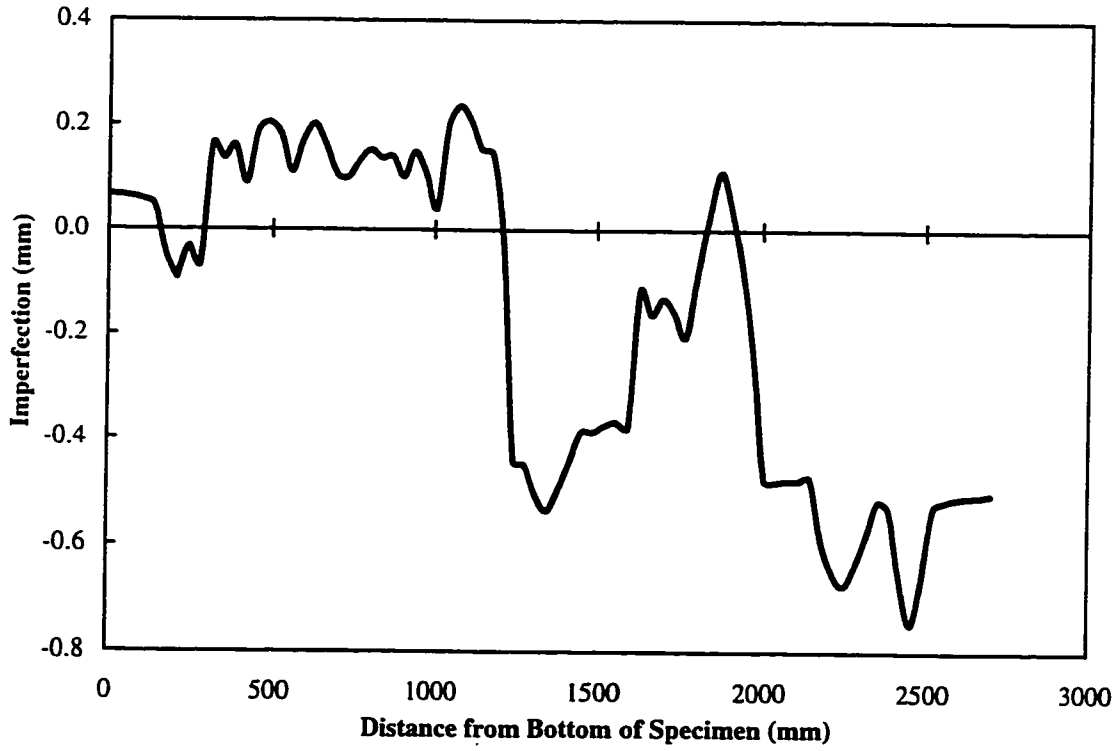

Figure 4.14 Mapped initial imperfections along compression face of C45P00

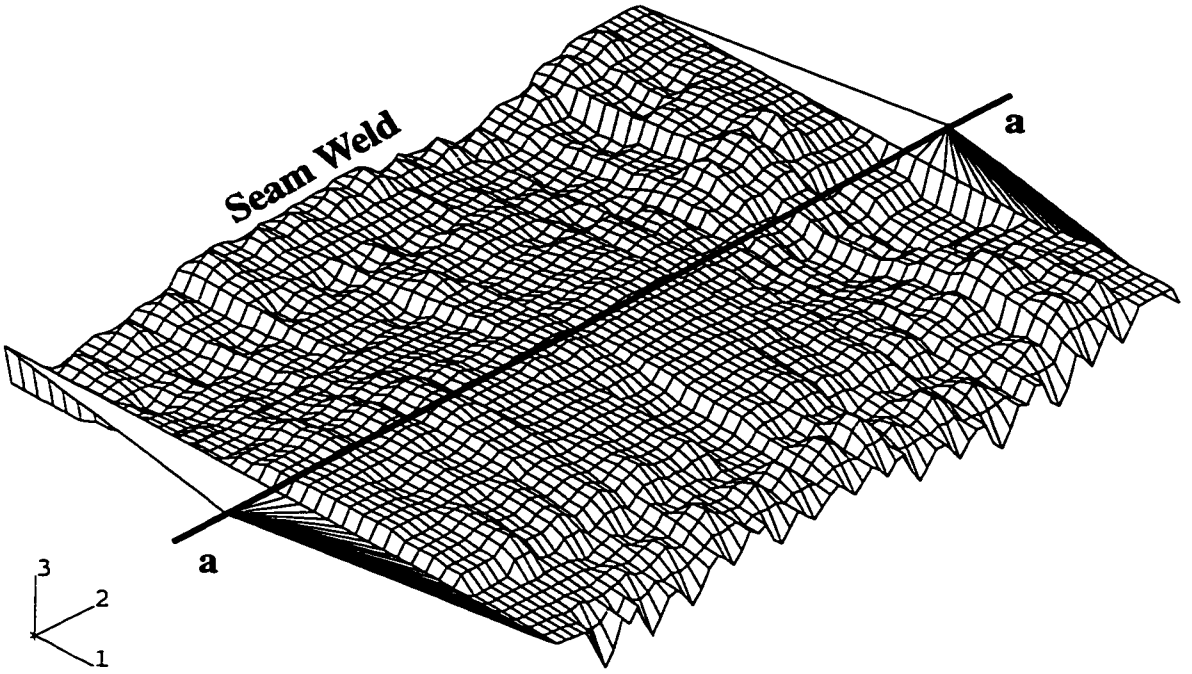

Figure 4.15 Mapped initial imperfection pattern for specimen C45P20

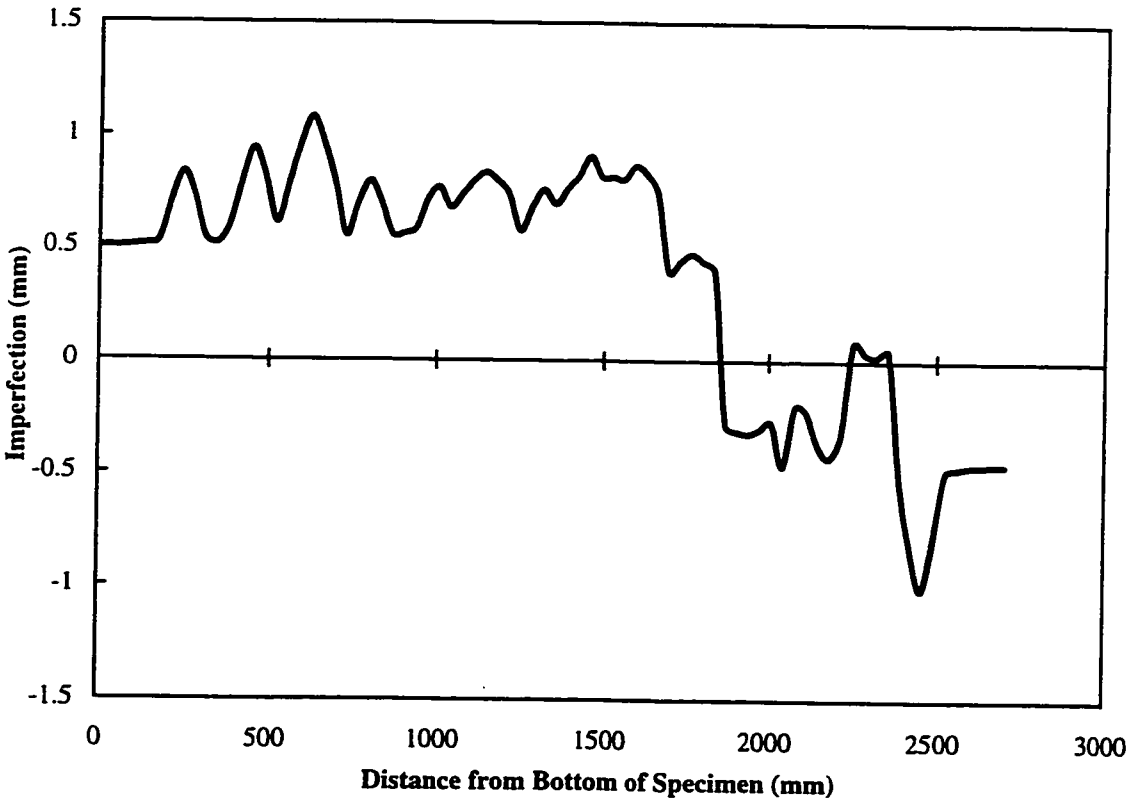

Figure 4.16 Mapped initial imperfections along compression face of C45P20

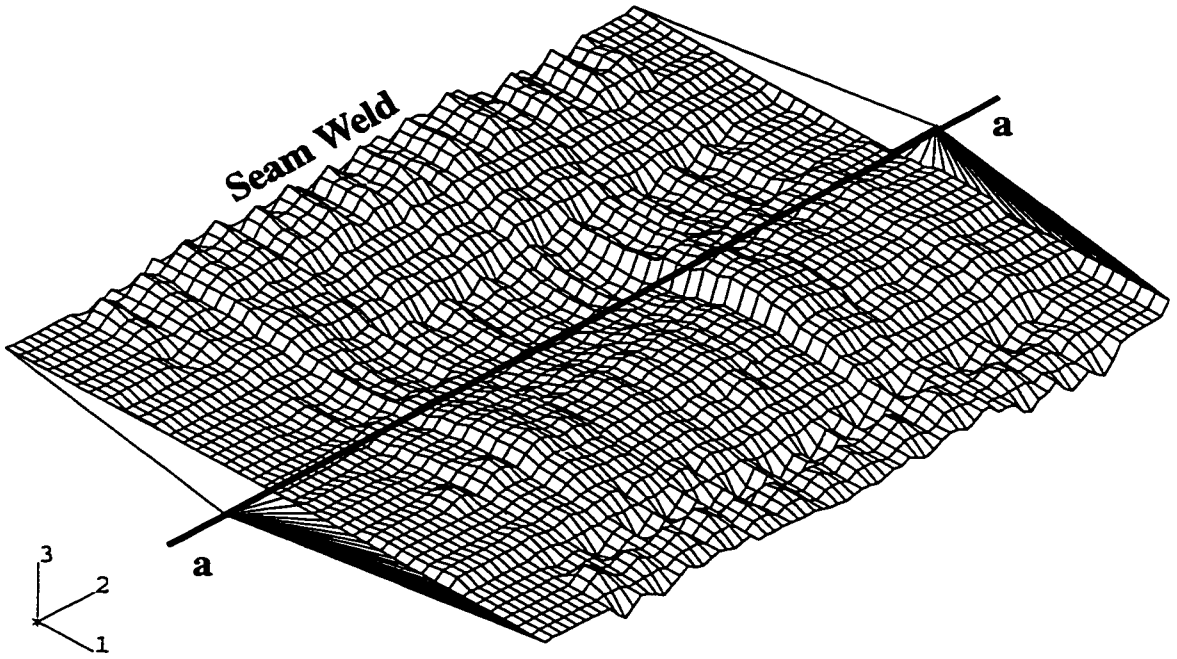

Figure 4.17 Mapped initial imperfection pattern for specimen C45P40

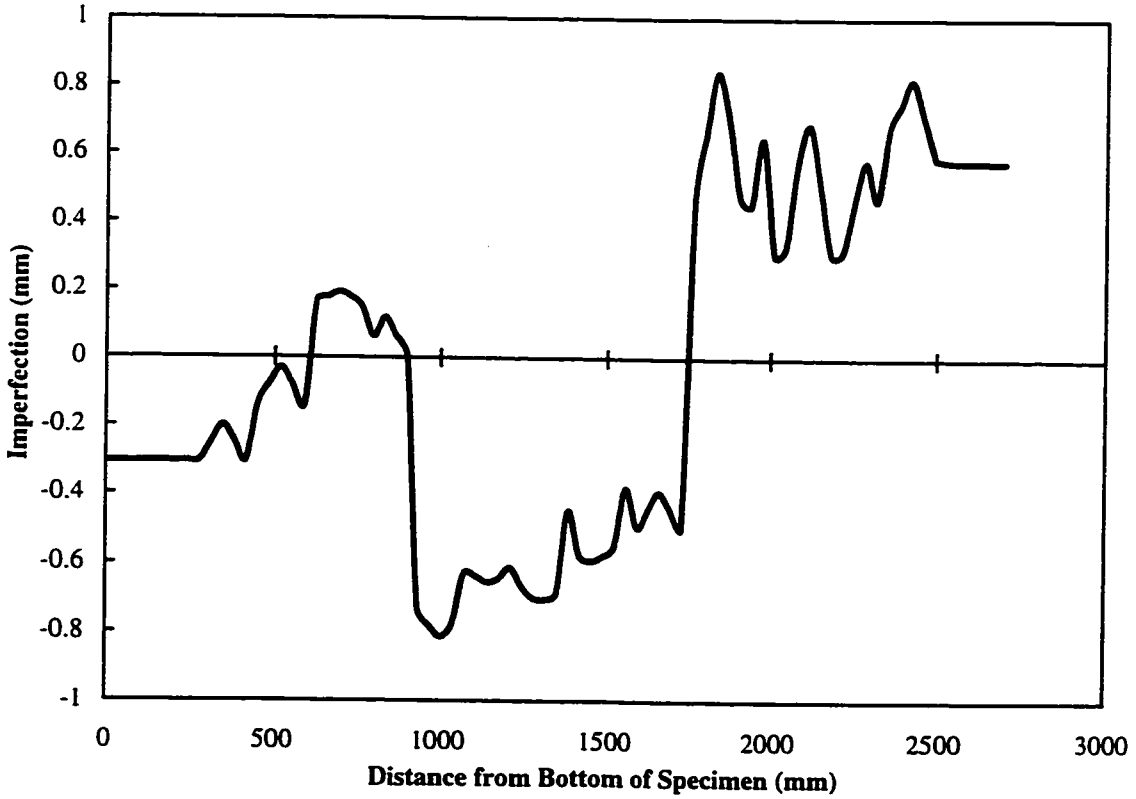

Figure 4.18 Mapped initial imperfections along compression face of C45P40

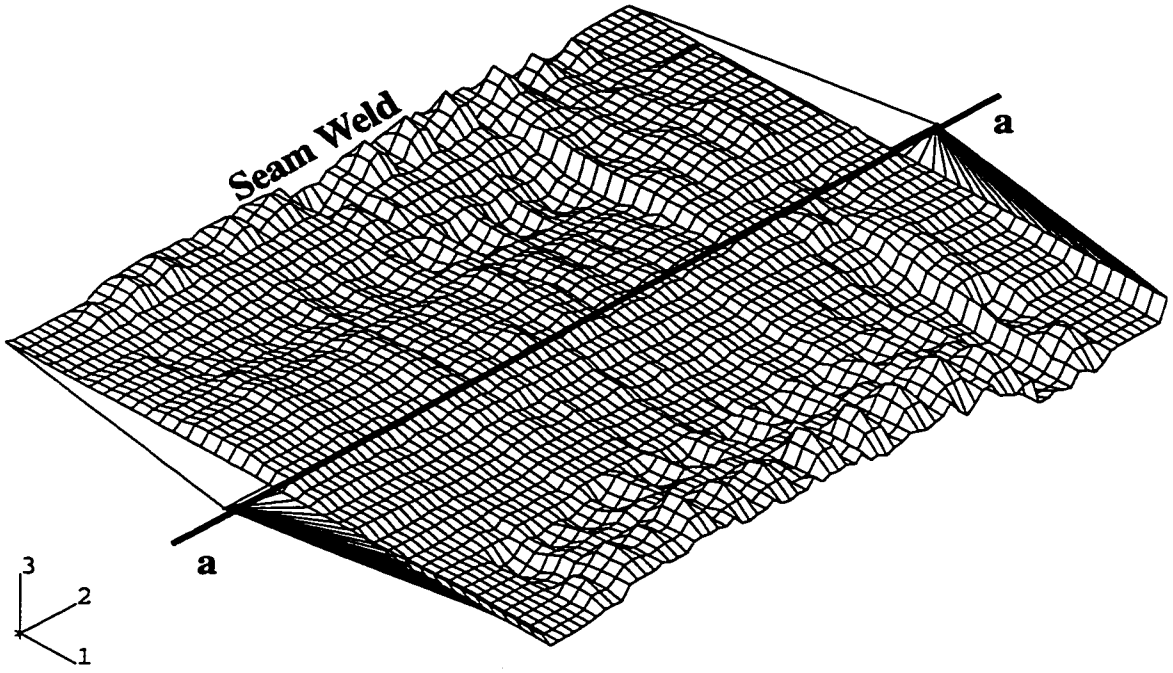

Figure 4.19 Mapped initial imperfection pattern for specimen C45P80

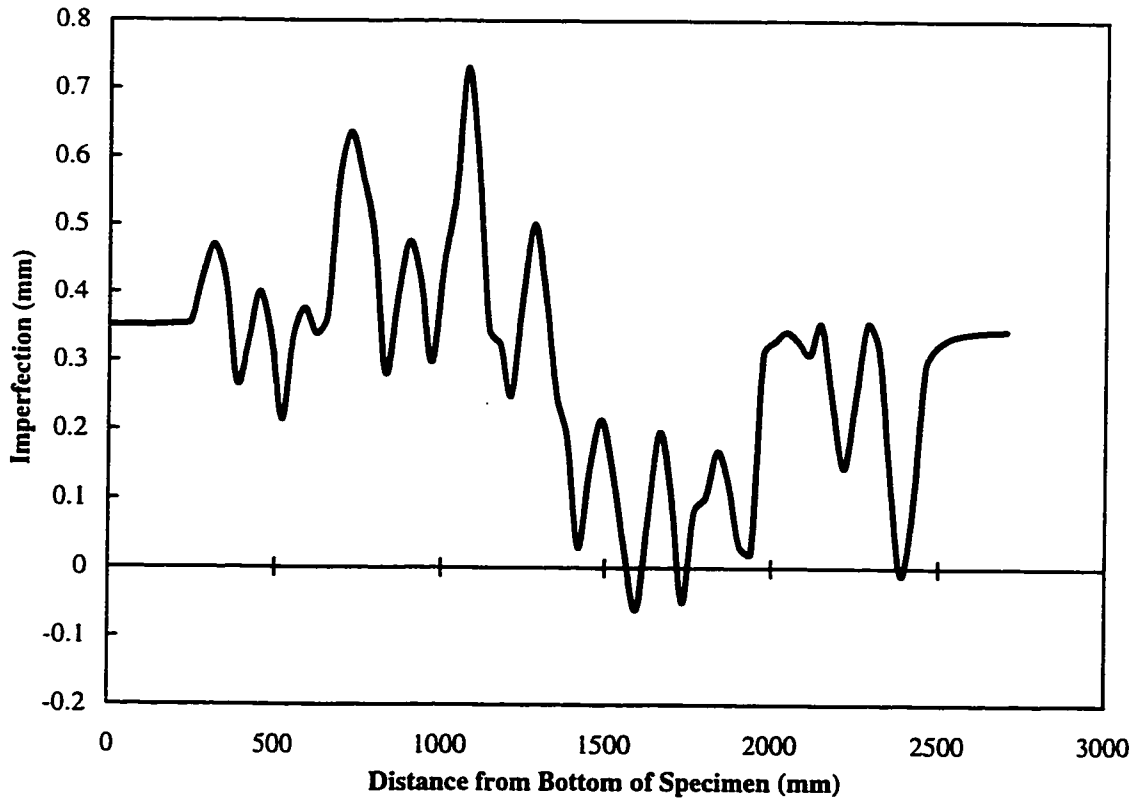

Figure 4.20 Mapped initial imperfections along compression face of C45P80

5. PREDICTION OF TEST RESULTS

The finite element model described in the previous chapter was used to predict the response of the four test specimens. The following sections present a comparison between the analytical results and the experimental results presented in Chapter 3. In addition, the finite element results supplement the change in diameter measurements, which were incomplete during the experiments. A discussion of possible sources of error in the finite element model is then presented.

5.1 FINITE ELEMENT ANALYSIS

To determine the validity of the numerical model, the results of the finite element analysis are compared to the experimental results. The models presented in following are considered representative of the test specimens by trying to accurately model the boundary conditions, incorporating the measured initial imperfections, and using measured material properties. The comparisons between the analytical and experimental results are based on the moment versus curvature relationship, the post-buckling configuration, and the critical compressive strain.

5.1.1 Moment versus Curvature Relationship

The first criterion used for the comparison of results is the global moment versus curvature diagram. The global values are simple to calculate and are less dependent on the location of the local buckle. Since the global moments and curvatures include the effects of the end plates and confining collars used in the test, an assessment of the modelled boundary conditions can therefore be made.

Figure 5.1 shows the experimental and analytical moment versus curvature curves for specimen C45P00. The general shape of the moment versus curvature response is in good agreement with the experimental curve. The initial stiffness of the analytical model also agrees well with that measured during the test. The peak moment obtained from the finite element model is 2033 kN·m compared to the experimental peak moment of 1889 kN·m. The limit point curvature corresponding to the peak moment determined from the analysis is 12.2 $x10^{-6}$ mm^{-1} compared to the experimental value of

7.6 x10^{-6} mm^{-1}. The unstable behaviour following the peak moment and the descending branch for the experimental and analytical results are also similar. The axial load in the analysis of this specimen did not incorporate the reduction inadvertently encountered during the test as discussed in Section 3.5.1.1. The analytical solution, therefore, does not include the discontinuities observed in the experimental result. As explained in Section 5.3, possible causes of the discrepancies between the predicted and measure peak moment and the corresponding limit point curvature are the boundary conditions, magnitude of initial imperfections and material model used in the finite element analysis.

Figure 5.2 shows the experimental and analytical moment versus curvature diagrams for specimen C45P20. The general shape of the analytical response is in all respects similar to the experimental curve. The initial stiffness of the model is also in good agreement with the experimental results. However, curvatures predicted by the numerical model are higher than the experimental values beyond the proportional limit. Excellent agreement between the moment capacities was obtained with a predicted peak moment of 1983 kN·m compared to the experimental peak moment of 1955 kN·m. However, the curvature at the peak moment obtained from the numerical model, 12.2 x10^{-6} mm^{-1}, is greater than the experimental value of 8.9 x10^{-6} mm^{-1}. A comparison of Figure 5.2 with Figure 5.1 indicates that the internal pressure causes a more gradual loss of capacity in the post-buckling range.

Figure 5.3 presents the experimental and analytical moment versus curvature curves for specimen C45P40. The overall response predicted by the finite element analysis is similar to the specimen response observed in the test except for the increased curvatures during loading after the proportional limit at a global moment of approximately 500 kN·m. The peak moment obtained from the finite element model is 1848 kN·m compared to the experimental peak moment of 1952 kN·m. The curvature at the peak moment of the analytical model is 12.2 x10^{-6} mm^{-1} compared to the experimental value of 11.1 x10^{-6} mm^{-1}.

Figure 5.4 shows the experimental and analytical moment versus curvature response for specimen C45P80. In this case, the initial stiffness of the analytical model is less than the corresponding experimental stiffness. However, both the analytical and

experimental curves show the same general response. The moment versus curvature curves for the test specimen and the numerical model are almost parallel in the upward sloping relationship preceding the peak moment and the descending branch following the peak moment. The peak moment obtained from the finite element model is 1591 kN·m compared to the experimental peak moment of 1525 kN·m. The curvature corresponding to the analytical peak moment is 21.9×10^{-6} mm^{-1} compared to the experimental limit point curvature of 17.0×10^{-6} mm^{-1}.

A summary of experimental and analytical peak moment and limit point curvature is presented in Table 5.1. Test-to-FEA ratios are also included. The analytical predictions of moment capacity are all within 7.0 percent of the experimental peak moments. The predicted limit point curvatures, however, are significantly greater than the test results for all specimens, with the greatest difference observed for specimen C45P00. As will be shown in Section 5.3, the finite element analysis is highly sensitive to initial imperfections and material properties.

5.1.2 Post-Buckling Configuration

The post-buckling configurations obtained from the finite element models were compared to the configurations observed during the tests. In order to determine the characteristics of the local deformations from the finite element analysis, it is important that the analytical model be able to predict the buckled configurations observed during the tests. If consistent with the test results, the finite element model may be used to determine serviceability limits for local deformations.

Figure 5.5 shows the predicted local buckle configuration for specimen C45P00. The figure shows that the analytical model developed a "diamond" shape configuration as observed in the test. Also, the location of the main depression in the finite element model was 1250 mm from the bottom of the specimen. This is approximately the same location as the local buckle that developed in the test, which was at 1200 mm from the bottom of the specimen. Figure 5.6 shows a comparison of the analytical and experimental post-buckling configurations for this specimen. In all respects the predicted and experimental buckled configurations for this specimen are similar.

Figure 5.7 presents the predicted local buckle configuration for specimen C45P20. The figure shows that the analytical model has developed a single outward bulge pattern. Although the test specimen developed this local buckling pattern, the location of the bulge crest in the finite element model was 1600 mm from the bottom of the specimen compared to 350 mm from the bottom of the specimen in the test specimen. Figure 5.8 shows a comparison of the analytical and experimental buckled configurations for this specimen. Qualitatively, the buckled configurations for this specimen are similar in geometry although different in location. The configurations shown in the figure are taken at approximately the same global curvature; however, the predicted deformations are somewhat less than the deformations observed in the test specimen because local buckling initiated at a greater curvature for the finite element model. Therefore, for the same curvature, the finite element model has undergone less post-buckling deformation than the test specimen.

Figure 5.9 summarizes the results of an eigenvalue buckling analysis performed for test specimen C45P20. The buckling load analysis was performed in the third load step after the application of the internal pressure and the axial load. The internal pressure and the axial load are taken as the base state loads to which a perturbation load (the bending moment) is added. It is assumed that the response to the perturbation moment is elastic up to the buckling load. This results in as many eigenvalues (buckling moment) and associated eigenmodes (buckled configuration) as degrees of freedom in the model. Figure 5.9 shows the eigenmode and corresponding eigenvalue for modes 1, 2, 5, and 13. It can be seen that buckling modes 1 and 2 are almost identical and consist of a series of waves along the compression face of the pipe, and the maximum wave slightly off-centre. Modes 5 to 13, on the other hand, exhibited waves near the end collars, favouring bulging of the pipe near the end collars. It should be noted that once buckling takes place, only one of these waves develop to a larger magnitude, i.e. localize, while the other waves would either maintain their magnitude or would gradually vanish as the pipe unloads. The eigenvalues (they represent the multipliers by which the perturbation moment applied in step 3 of the analysis is multiplied to obtain the buckling moments) for modes 1, 2, 5, and 13 are 10.8, 10.9, 11.0, and 11.7, respectively. The associated buckling

moments are 10 800, 10 900, 11 000 and 11 700 kN·m compared to the experimental value of 1955 kN·m. Between the first and thirteenth modes, there is therefore only a 8.3 percent difference in buckling load. This has two significant implications: 1) it may be difficult in the load deformation analysis to converge to the lowest mode; and 2) even a slight disturbance may trigger buckling close to the end of the pipe rather than in the middle segment. This latter implication is more important in the testing since only a slight misalignment of the test specimen, or frictional restraint in the loading assemblies could trigger buckling of the test specimens near the ends somewhat similar to eigenmode 5, which has an eigenvalue within 2.0 percent of the value for eigenmode 1. A comparison of Figure 5.7 with Figure 5.9 indicates that the analysis may have converged to a higher mode. The bulge shown in Figure 5.7 corresponds closely to the location of the second crest from the end of the pipe in Figure 5.9. Since the first eigenmode indicates the largest crest near the midsection of the pipe, it is likely that the load deformation analysis has converged to a higher mode.

Figure 5.10 presents the predicted local buckle configuration for specimen C45P40. The analytical model has developed a single outward bulge similar to the one observed in the test. The predicted location of the local buckle, however, differs significantly from the location observed in the test. The test specimen formed a local buckle 400 mm from the bottom of the specimen whereas the predicted local buckle is located at 1900 mm from the bottom of the specimen. Figure 5.11 shows a comparison of the predicted and experimental local buckle configurations for this specimen. As with Figure 5.8, the figures show different magnitudes of deformation because they were taken at different curvatures relative to the limit point curvature.

Figure 5.12 shows the predicted local buckle for specimen C45P80. Excellent agreement between the analytical and experimental results is observed for the post-buckling configuration. As shown in Figure 5.12, the single outward bulge formed approximately 350 mm from the bottom of the specimen just above the bottom confining collar. In comparison the experimental local buckle occurred at 430 mm from the bottom of the specimen. Also, another local buckle is beginning to develop near the top of the finite element configuration, indicating the degree of local disturbances caused by the

confining end collars. Figure 5.13 shows a comparison of the analytical and experimental buckled configurations for this specimen. The edge of the confining collar in the predicted configuration is shown with an arrow.

5.1.3 Critical Strains

The longitudinal compressive strains at the onset of strain localization were determined for the finite element analysis to compare with the experimental results presented in Section 3.5. The local analytical strains were based on element surface strains averaged over a length of one pipe diameter. These values are therefore equivalent to those obtained from strain gauges in the experimental program. Figures 5.14 to 5.17 show the local analytical strains averaged over a length of one pipe diameter versus the global analytical strains, averaged over the length of the model (excluding end collars). This procedure is consistent with the procedure adopted for the test results. The figures exhibit an initial linear response with a 1 to 1 slope indicating essentially uniform strain over the length of the specimens. Figure 5.14 presents the results for specimen C45P00 and demonstrates a slight non-linearity of the local strains prior to the point of significant deviation. In this case, the point of significant deviation from the initial linear behaviour was chosen as the critical strain as indicated in Figure 5.14. The reduction in global and local strains in the later part of the figure is a result of unloading of the specimen as strains localize. All other specimens exhibit relationships with distinct points of deviation as shown in Figures 5.15 to 5.17.

Table 5.2 presents a comparison of the compressive strains at the onset of strain localization determined from the test specimens and the analytical models. The table lists the strains determined from strain gauge measurements presented in Section 3.5, the strains predicted using the finite element model, and the ratio of the experimental to predicted strains. The tabulated data indicate that the predicted compressive strains are generally greater than the experimental values. This is consistent with the differences observed for the predicted and experimental limit point curvatures. The discrepancy between the test values and the predicted values are in the same proportion in both cases.

5.1.4 Change in Diameter

The measured changes in diameter for the test specimens were presented in Section 3.5. The data collected during the tests do not provide a detailed picture of the pipe specimen behaviour because the instrumentation was chosen to provide overall qualitative information. The instrumentation used for the change in diameter measurements was therefore too coarse and the observations regarding the cross-sectional behaviour of the test specimens were not comprehensive. Since the analytical results are in good agreement with the test results, the analytical model is used to provide more details regarding the change in diameter behaviour of the pipe. Although the analytical models did not predict the correct location of the bulging failure of C45P20 and C45P40 test specimens, the local deformations predicted at the bulge were in good agreement with the test results.

Figures 5.18, 5.20, 5.22 and 5.24 show the predicted change in diameter in the plane of bending and transverse to the plane of bending along the length of the models. In addition, Figures 5.19, 5.21, 5.23 and 5.25 present the predicted change in diameter measurements at the cross-section corresponding to the maximum inward change (along with the maximum outward change) as a function of global curvature.

Figure 5.18 (a) shows the predicted values of the change in diameter in the plane of bending along the length of specimen C45P00. Dotted lines show results in the post-buckling range and the heavy solid line shows the results at the peak moment. As shown in Figure 5.5, C45P00 exhibits a "diamond shape" local buckle and the corresponding main depression produces significant cross-sectional distortion in the post-buckling range. Figure 5.18 (a) shows that, for the level of curvature imposed on the model, only decreases in diameter (negative values) are exhibited in the plane of bending. There is, however, a point at approximately 1000 mm from the bottom of the specimen where the deformations reverse direction in the post-buckling range. Figure 5.18 (b) shows the change in diameters in the direction transverse to the plane of bending where the distortions are all outward (positive).

Figure 5.19 shows the predicted change in diameter values in and transverse to the plane of bending for the cross-section at 1250 mm from the bottom of specimen C45P00.

This cross-section corresponds to the location of maximum decrease in diameter for the direction in the plane of bending. In addition, the maximum increase in diameter is shown for the direction transverse to the plane of bending since the maximum values do not coincide in both directions. This figure demonstrates that, up to the limit point curvature, the cross-sectional distortions are of approximately equal value in the inward and outward directions. For this specimen these directions correspond to the in-plane and out-of-plane (transverse) directions, respectively. This implies that the cross-section undergoes ovalisation as discussed in Chapter 3. Also, deformations are shown to increase rapidly following the limit point curvature (indicated in the figure).

Figure 5.20 (a) shows the predicted change in diameter in the plane of bending obtained from the analysis of specimen C45P20. A single bulge shape local buckle was predicted analytically and observed during the testing, as shown in Figure 5.7. Figure 5.20 (a) shows that the predicted changes in diameter follow the same general pattern as shown in Figure 5.18 (a) for specimen C45P00. The magnitude of the inward change, in the plane of bending, is reduced compared to specimen c45P00 and slight expansion of the cross-section, at the location of the single local bulge, is observed in the post-buckling range. Figure 5.20 (b) shows the change in diameter transverse to the plane of bending with all the distortions outward.

Figure 5.21 shows predicted change in diameter in and transverse to the plane of bending for the cross-section at 1660 mm from the bottom of the specimen. This cross-section underwent the maximum inward change in diameter in the plane of bending. In addition, the maximum changes are shown for the direction transverse to the plane of bending since the maximums in the two directions do not occur at the same cross-section. This figure shows that up to the limit point curvature, the inward changes are less than the outward changes in diameter. This is the result of the internal pressure resisting the tendency of the pipe cross-section to flatten. However, the distortions in the pre-buckled range show that some degree of cross-section flattening occurs even with the presence of low levels of internal pressure. The pipe diameter is also shown to increase rapidly after limit point curvature is reached. The reduction in diameter in the plane of bending, however, changes less rapidly compared to specimen C45P00 in Figure 5.19.

Figure 5.22 (a) shows the predicted change in diameter in the plane of bending for specimen C45P40. The predicted and experimentally observed post-buckling configuration of this specimen consists of a single local bulge as shown in Figure 5.9. Figure 5.22 (a) shows that the predicted change in diameter values in the plane of bending follow a similar pattern as the previously presented specimens with the exception that the magnitude of the inward and outward change in diameter is nearly identical after the formation of the local bulge. Figure 5.22 (b) shows the change in diameter transverse to the plane of bending with all distortions outward.

Figure 5.23 shows predicted change in diameters in the plane and transverse to the plane of bending at a cross-section 1660 mm from the bottom of the specimen as a function of the global curvature. This cross-section corresponds to the location where the maximum inward changes occur in the plane of bending. The maximum increase in diameter or outward change, transverse to the plane of bending, is also included. It can be seen that up to the limit point curvature, the inward distortions are small due to the internal pressure resisting inward deformations of the pipe cross-section. Deformations are also shown to increase rapidly following the limit point curvature, particularly transverse to the plane of bending.

Figure 5.24 (a) shows the change in diameter in the plane and transverse to the plane of bending predicted for specimen C45P80. This specimen experimentally and analytically exhibited a single local bulge, as shown in Figure 5.12. Figure 5.24 (a) shows that the predicted change in diameters in the plane of bending result in increased diameters due to the high internal pressure. Also shown in this figure are significant secondary bulges prior to localization of deformations at the most critical section located near the bottom of the specimen. Figure 5.24 (b) shows the change in diameter transverse to the plane of bending with strictly increased diameters.

Figure 5.25 shows the predicted in the plane and transverse to the plane of bending change in diameters at 330 mm from the bottom of the specimen. This cross-section corresponds to the location in the plane of bending where the maximum increase in diameter is observed. The maximum transverse change in diameter is also included. This figure shows that deformations in the plane of bending are slightly less than in the

transverse direction prior to the limit point curvature due to the tendency of the applied moment to flatten the cross-section. The distortions in the post-buckling range are similar in the plane and transverse to the plane of bending and are observed to increase rapidly.

5.1.5 Compression Face Deformations

The experimental observations in Section 3.5 showed a distinct pattern of compression face waves that formed with the imposition of internal pressure and axial load. These deformations are caused by initial imperfections along the compression face. Also, the occurrence of end bulges due to internal pressure was shown. The finite element models also show the development of these characteristics.

Figure 5.26 presents the progression of compression deformations for specimen C45P00. The figure shows the deformations that form upon the application of the axial load. The shape of the deformations remain essentially unchanged until the peak moment is reached, as shown by the curve denoted FEA (2033 kN·m), and a local buckle forms. The compression face displacements measured on the test specimen at the peak moment are also presented for comparison. Good agreement between the measured and predicted displacements is observed.

Figure 5.27 shows the progression of compression face deformations for specimen C45P20. The curve denoted "FEA Axial Load + Pressure" shows bulges near the ends of the specimen. The figure showing the deformed shape at peak moment shows good agreement between the measured and the predicted shapes. Figure 5.27 shows the development of the deformation that ultimately triggers the outward bulge at approximately 1800 mm from the bottom of the specimen as indicated. Figure 4.16 shows the measured initial imperfections along the compression face of this specimen. A comparison of Figure 4.16 and Figure 5.27 indicates that the location of the bulge corresponds to an abrupt change in the configuration of the initial pipe geometry.

The progression of compression face deformations for specimen C45P40 is shown in Figure 5.28. End bulges are more prominent than for the previous specimen due to increased internal pressure. The figure also shows the progression of the deformation that

triggers the single outward bulge at approximately 1900 mm from the bottom of the specimen. Again, a comparison of the measured initial imperfections (Figure 4.18) with the deformed shape shown in Figure 5.28 indicates that the predicted location of the outward bulge corresponds to an abrupt change in the level of imperfection in the initial geometry. The figure showing the deformed shape at peak moment shows good agreement between the measured and predicted shapes.

The progression of compression face deformations for specimen C45P80 is presented in Figure 5.29. End bulges are the most significant features due to the high internal pressure. The figure also shows the progression of the end bulge that subsequently localizes into the single outward bulge at approximately 300 mm from the bottom of the specimen. The figure showing the deformed shape at peak moment shows good agreement between the predicted and measured displacements. Also, two secondary bulges are beginning to form as indicated.

The above analytical results demonstrate the importance of including initial imperfections in the finite element model. It has been shown that at the initial stage of loading, imperfections cause small deformations to develop on the compression face. As loading proceeds, the location of one of the imperfections becomes the critical section and a local buckle forms. Also, the end disturbances due to the boundary restraints are prominent features on the deformed compression face of pressurized pipes. However, the effect of the boundary disturbances does not appear to be as severe in the numerical models as in the experimental test since specimens C45P20 and C45P40 did not form a bulge near the end conditions. The relative magnitudes of the imperfection and boundary effects determine the local buckle location of the models.

It should be recalled that the initial imperfections were measured prior to welding of the specimens to the end plates. This welding process may significantly affect the level and distribution of imperfections in the end region of the test specimens. The imperfections in this region of the test specimens are, therefore, probably different than those included in the finite element models. This effect combined with the end bulges caused by the internal pressure for specimens C45P20 and C45P40 are believed to cause the difference between the observed and predicted locations.

5.2 PREDICTION USING THE PLASTIC EQUATION BY MOHAREB AND MURRAY (1994)

In order to design the test setup, Eq. (2.9) was used to predict the plastic moment capacity of the specimens. The same equation is used here with the measured material properties and wall thickness to update the predictions made during the design stage. The values of yield strength, Fy, of 512 MPa, from the stress versus strain curve given in Table 3.1 and wall thickness of 8.43 mm were therefore used. Table 5.3 presents a comparison of the measured peak moment with predicted values using Eq. (2.9) and the finite element models. The test to predicted ratios presented in Table 5.3 indicate good correlation between the test results and the finite method. The plastic moment equation predicts higher moment capacities for specimens subjected to internal pressure up to 0.4 p_y. This is likely the result of the onset of instability in the test specimen prior to attaining a fully plastic cross-section (on which the equation is based). However, the measured peak moment for specimen C45P80 is 26 percent greater than the predicted capacity using the plastic moment equation. It was observed during this test that the specimen is subjected to strains considerably greater than the yield strain of the material. Strain hardening of the material at high strains is believed to be responsible for the significant increase in moment capacity observed in this test specimen.

The accuracy of the predictions using the plastic equation Eq. (2.9) is limited since the assumption of a fully plastic cross-section may not always be attained with imperfect structures. Also, for a material model that does not exhibit a perfectly plastic plateau, as is the case for these specimens, the selection of a yield value significantly affects the predictions of Eq. (2.9). In this case F_y was chosen to be the stress at 0.5 percent strain.

5.3 IMPROVEMENTS TO THE ANALYTICAL MODEL

The numerical analysis described above included several assumptions that ultimately affected the results. Some of the simplifying assumptions made in the finite element model are: idealised confining collars, accuracy of the measured imperfections, no variation in wall thickness, and material model. An investigation of the effect of some of these assumptions is presented in the following.

The end collars used to support the ends of the test specimen were modelled by increasing the thickness of the elements at the ends of the model. However, it is not known exactly how much restraint was provided by these collars during each test. The use of an effective wall thickness, with elastic-plastic material properties, for end elements in the region of the collars assumed a frictionless contact between the collars and the pipe. This was not the case during the experiments. In addition, bolted connections were used to mount collars reducing the overall stiffness of the collars by an undetermined amount. Different element thickness in the collar region were investigated and it was found that the stiffness of the loading curve, peak moment and limit point curvature were not significantly affected by the changes to these boundary conditions. The slope of the descending branch, however, was significantly affected by a change in stiffness of the end collars. Since the descending branches of the analytical models were in good agreement with the experimental results, it is believed that the effective thickness used in the model provided adequate stiffness. In addition, it is believed that the restraint provided by the collars during the experiments contributed significantly to the location of the local buckle formation due to the development of the end disturbances described in Chapter 3. The end disturbance, or end bulging, in the analytical model did not seem to produce the same destabilising effect near the ends of specimens C45P20 and C45P40. This could contribute to the larger curvature at peak moment observed in the finite element model.

The technique used to measure initial imperfections in the test specimens did not permit a direct measurement of pipe wall radius around the circumference of selected sections. The change in pipe radius rather than the radius itself was measured. The measured imperfections were therefore adjusted so that the average pipe diameter corresponded to the nominal pipe diameter. In reality the average diameter may vary by $\pm$ 1.00% of the nominal pipe diameter according to API specification 5L (1995). This potential variation can change the bending stiffness of the pipe by $\pm$ 3.0 percent based on the resulting change in the moment of inertia. In addition, imperfections were measured prior to installation and welding of the specimens in the test frame. This process can distort the pipe significantly near the ends. Deviations from the measured initial

imperfections used in the analytical model are therefore likely to be more significant. This was not considered in the analysis.

API specifications governing geometric tolerances of line pipe indicate that the wall thickness may vary from -8 percent to +19.5 percent of the nominal wall thickness. Variation of wall thickness within a test specimen can therefore affect the measured initial imperfection pattern. However, current work at the University of Alberta has shown the wall thickness variation within a test specimen to be small. A uniform thickness was therefore used during the analysis and it is believed that this source of error is minimal.

The material model, as will be shown in the following section, has a significant effect on the overall behaviour of the specimens. Small variations of the shape of the stress versus strain curve in the 0.15 percent to 0.5 percent strain region affect the general response up to the limit point. It is also important to accurately define the material properties in the circumferential direction. Flattened tensile coupons were used for this purpose. It is the opinion of the author, that while these types of coupons are acceptable as an industry standard, they do not accurately represent the actual material properties in the circumferential direction. It is believed that the flattening process causes work hardening and induces residual stresses in the material, resulting in the distortion of the stress versus strain curve at the proportional limit of yielding. This is consistent with the results of Lay (1982) who presents a simplified derivation of the residual stresses induced in a pipe due to the forming and the subsequent flattening process. The results of this derivation suggest that the in-service material properties have a higher proportional limit than the flattened tension coupon tests indicate.

5.3.1 Sensitivity Analysis of the Model

An analytical study was performed using the loading conditions and geometry of specimen C45P00 to assess the sensitivity of the model to variations in material properties and magnitude of initial imperfections.

To determine the sensitivity of the model to the material properties, a simplified, tri-linear stress versus strain relationship was used. The tri-linear simplification consisted

of the elastic portion, the first plastic portion from 2000 to 5000 microstrain and the second plastic portion beyond 5000 microstrain. This curve and the average material property curve used to predict the test results are shown in Figure 5.30 in terms of true stress and true strain. The simplified curve shows no proportional limit with a linear relationship up to 0.2 percent strain. This figure also shows that the stress at 0.5 percent strain for the simplified and average material properties is essentially the same at 512 MPa. Both materials use a modulus of elasticity of 225 700 MPa as measured from the tension coupon tests.

The difference between the measured and predicted peak moment and corresponding limit point curvature for specimen C45P00 is quite significant. The magnitude of initial imperfections shown in Figure 4.9 was extrapolated to determine the magnitude of initial imperfections that would produce peak moment and curvature predictions in better agreement with the test results. It was estimated that initial imperfections two to three times those used in the model would be appropriate. An analysis was conducted using an imperfection level of 3.0 times the measured initial imperfections for this specimen. This may seem unreasonable, however the maximum measured imperfection along the compression face for this specimen was only 0.75 mm. With a scaling factor of 3.0, the maximum imperfection along the compression face becomes 2.25 mm. As stated earlier, the imperfections were measured prior to installation of the specimen in the test set-up and welding of the ends. This may have caused changes to the level of imperfections by an amount equal to the scaling factor. It should also be noted that geometric imperfections were included in the analysis but loading imperfections, resulting from misalignment of the test specimens in the test set-up, were not. This may also alter the effect of imperfections in the model.

Figure 5.31 shows the moment versus curvature response from test specimen C45P00 along with three predicted cases. The cases include results using the simplified material model with measured initial imperfections, the imperfections scaled by 3.0 times the measured values with the average material model, and the measured initial imperfections and average material model. The last case is the same as the prediction of the test results presented in Section 5.1.1. This figure demonstrates the extreme

sensitivity of the model to small variations in the material property definition. The simplified material model predicts the loading portion of the experimental curve quite well. However, the peak moment and corresponding limit point curvature are not affected much by the change in the material model. The simplified version of the material model results in a greater stiffness above the proportional limit than the multilinear average version of the material model.

Figure 5.31 shows that the moment versus curvature relationship predicted using the scaled imperfections is in good agreement with the test result. The figure also shows that the magnitude of the initial imperfections does not affect the initial loading curve. These results are consistent with the findings of Section 4.3.

Figure 5.32 shows the predicted moment curvature response for C45P00 using the simplified material properties and initial imperfections 3.0 times the measured values. Excellent agreement with the test results is observed.

All the models used in the sensitivity study developed a "diamond" shape post-buckling configuration located at approximately mid-length of the specimen. Table 5.4 presents a comparison of the experimental peak moment and corresponding limit point curvature with the values predicted in this sensitivity analysis. This table indicates that the simplified material model does not significantly improve the peak moment and limit point curvature, but improves the overall response as seen in Figures 5.31 and 5.32. The analysis with 3.0 times the measured initial imperfections shows a significant improvement in the predicted peak moment and limit point curvature but the response is still softer than the test results. The analysis performed with a combination of the simplified material model and the scaled initial imperfections shows a significant improvement in the pre-buckling response, the peak moment and limit point curvature.

Table 5.1

Comparison of Experimental and Predicted Values for Peak Moment and Limit Point Curvature

	Peak Moment (kN·m)		Limit Point Curvature ($x10^{-6}$ mm^{-1})	
Specimen	Experimental	Finite Element Analysis (Test/Predicted)	Experimental	Finite Element Analysis (Test/Predicted)
C45P00	1889	2033 (0.93)	7.6	12.2 (0.63)
C45P20	1955	1983 (0.99)	8.9	12.2 (0.73)
C45P40	1952	1848 (1.06)	11.1	12.2 (0.91)
C45P80	1525	1591 (0.96)	17.0	21.9 (0.78)

Table 5.2

Critical Compressive Local Strains (με)

Specimen	Experimental Strain Gauges	FEA Strains	Test / Predicted
C45P00	5200	6600	0.79
C45P20	5100	6230	0.83
C45P40	7100	7060	1.01
C45P80	13100	16100	0.81

Table 5.3

Experimental and Predicted Peak Moment

	Peak Moment (kN·m)		
Specimen	**Experimental**	**Finite Element Analysis (Test/ FEA Predicted)**	**Equation 2.9 (Test/Eq.2.9Predicted)**
C45P00	1889	2033 (0.93)	2263 (0.83)
C45P20	1955	1983 (0.99)	2347 (0.83)
C45P40	1952	1848 (1.06)	2226 (0.88)
C45P80	1525	1591 (0.96)	1199 (1.27)

Table 5.4

Sensitivity of Model for Specimen C45P00

Model	**Peak Moment (kN·m) (Test/Predicted)**	**Limit Point Curvature ($x10^{-6}$ mm^{-1}) (Test/Predicted)**
Test Result	1889	7.6
FEA with measured initial imperfections	2033 (0.93)	12.2 (0.63)
FEA with simplified material properties	2065 (0.91)	11.3 (0.67)
FEA with 3 times the measured initial imperfections	1864 (1.01)	10.2 (0.75)
FEA with simplified material model and 3 times the measured initial imperfections	1926 (0.98)	9.33 (0.82)

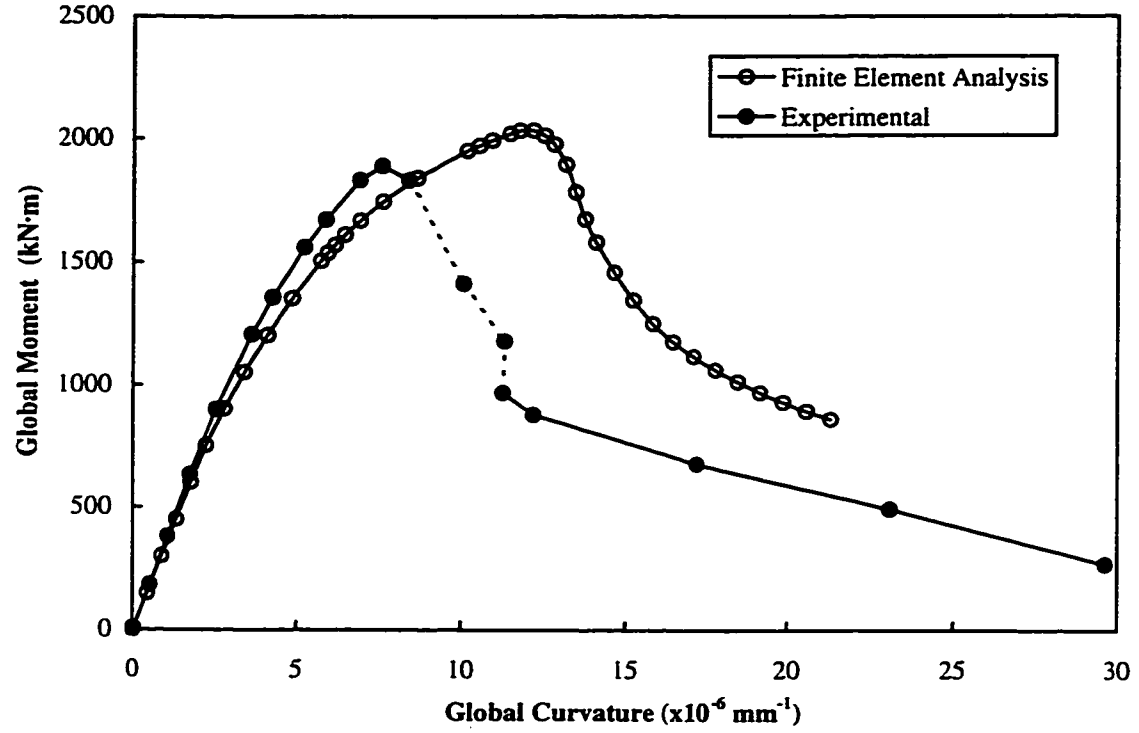

Figure 5.1 C45P00 - Comparison of moment versus curvature relationship

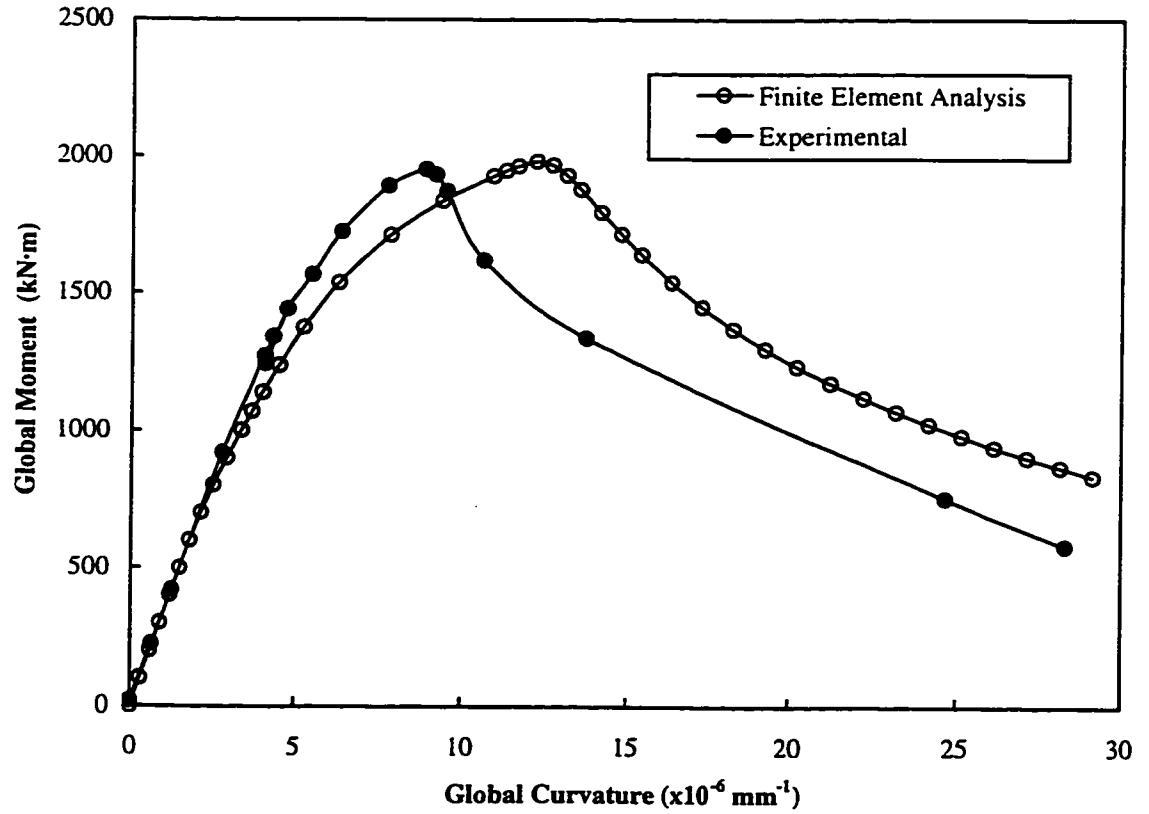

Figure 5.2 C45P20 - Comparison of moment versus curvature relationship

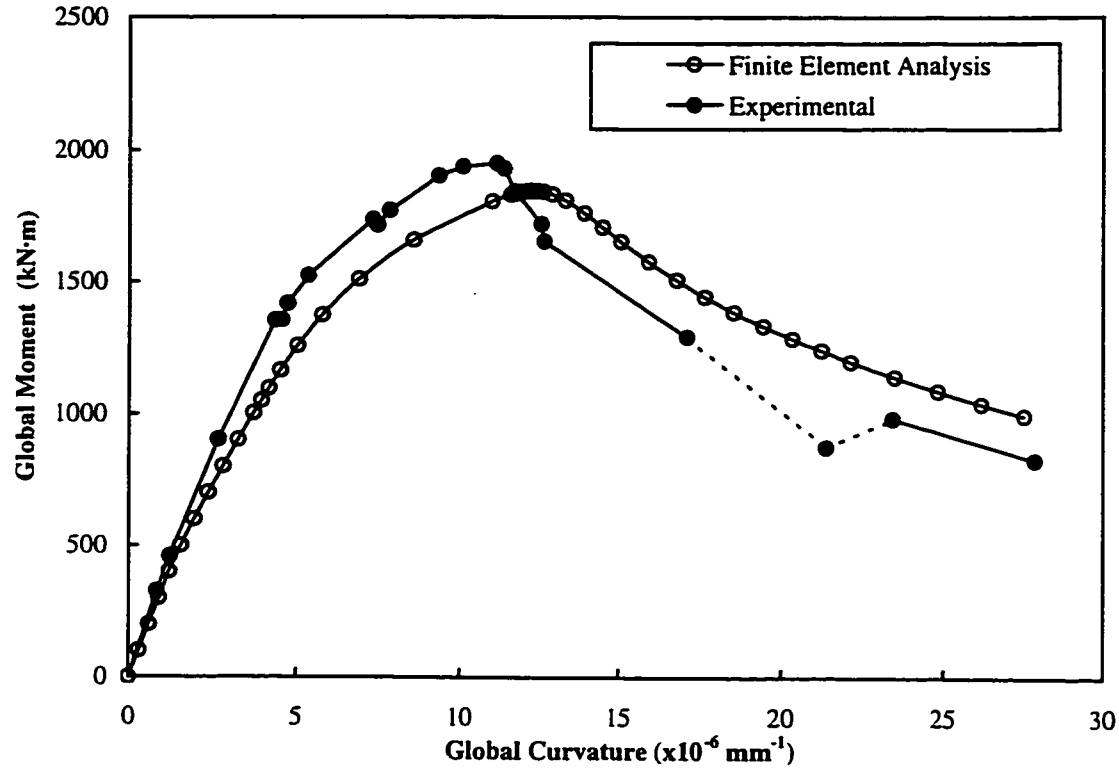

Figure 5.3 C45P40 - Comparison of moment versus curvature relationship

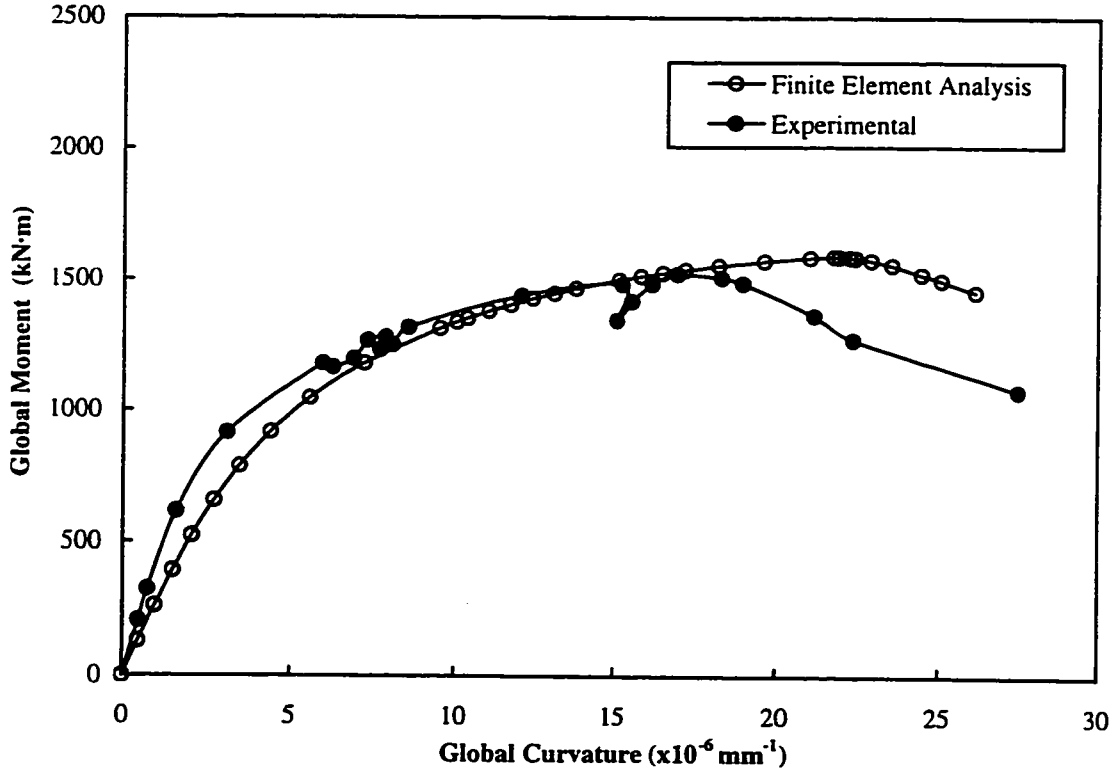

Figure 5.4 C45P80 - Comparison of moment versus curvature relationship

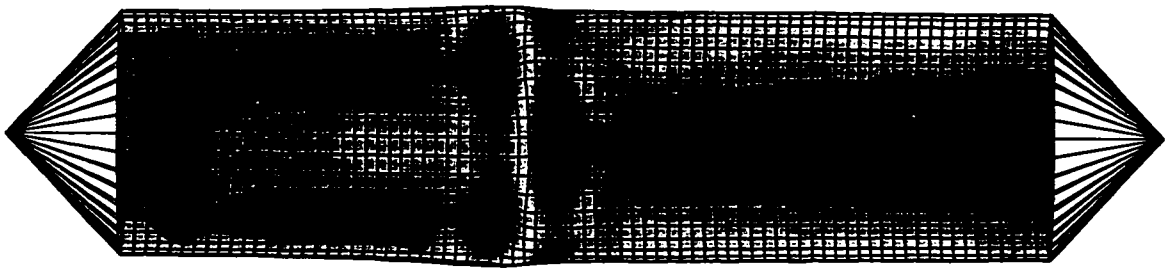

a) Compression Face

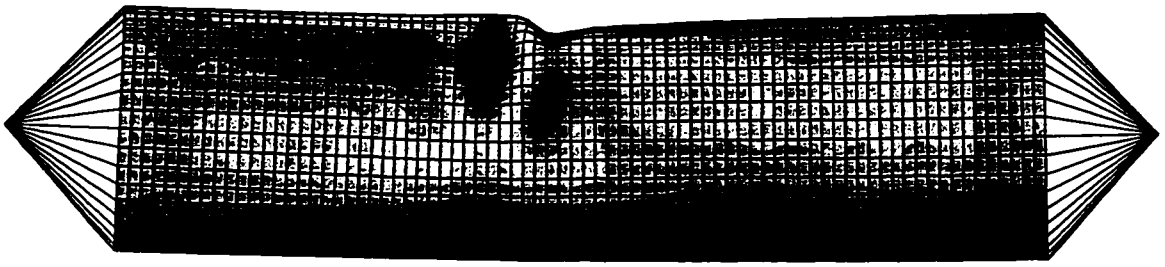

Bottom Top

b) Profile

Figure 5.5 Predicted buckled configuration for specimen C45P00

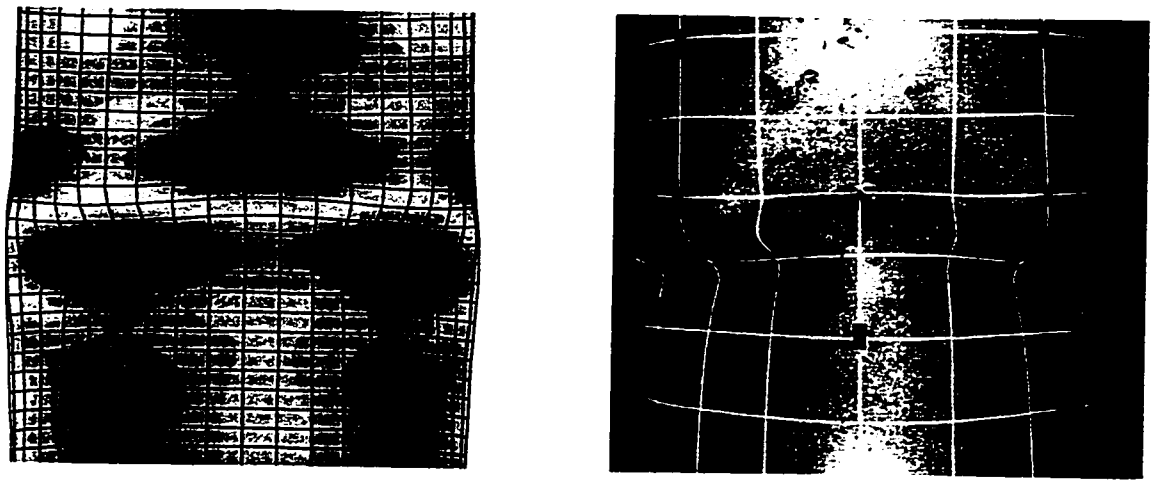

Figure 5.6 Comparison of predicted and experimental configurations for specimen C45P00

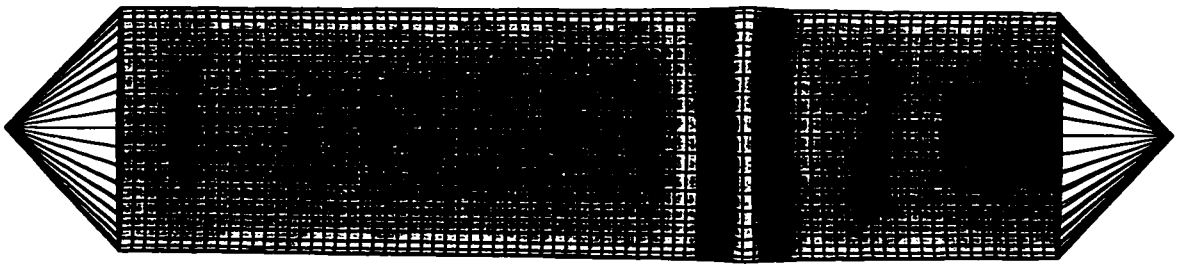

a) Compression face

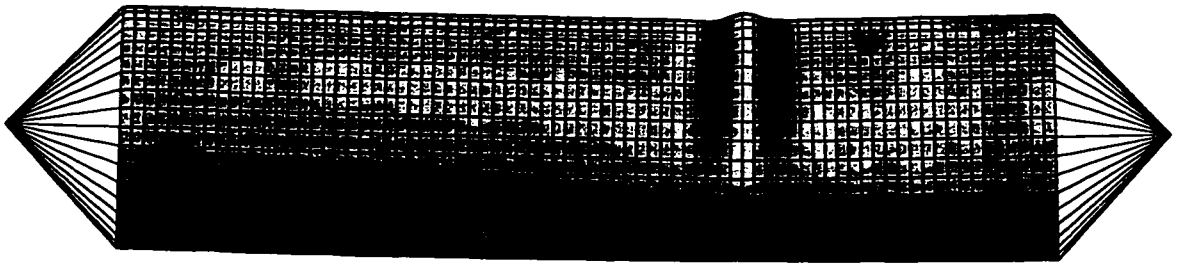

Bottom Top

b) Profile

Figure 5.7 Predicited buckled configuration for specimen C45P20

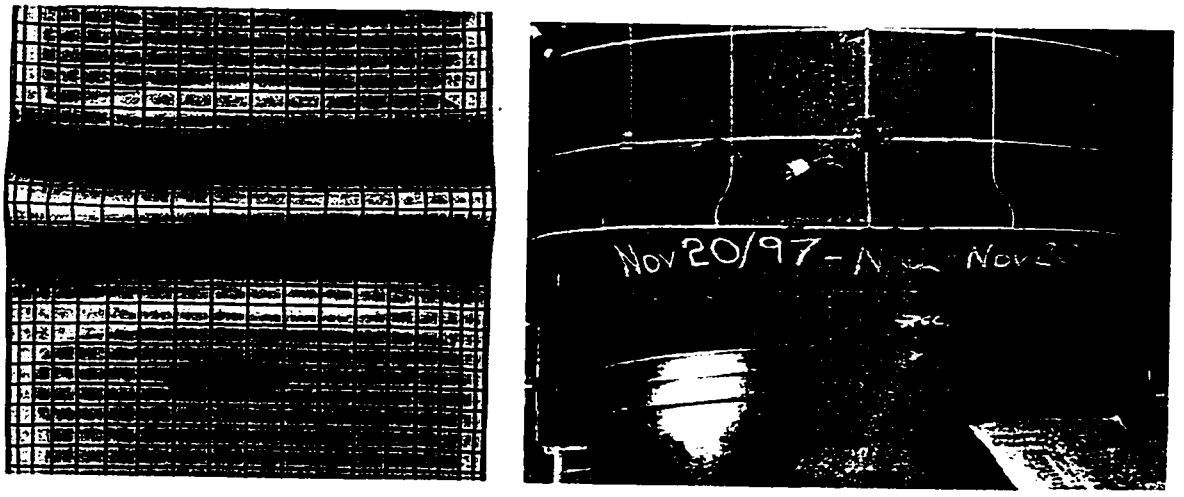

Figure 5.8 Comparison of predicted and experimental configurations for specimen C45P20

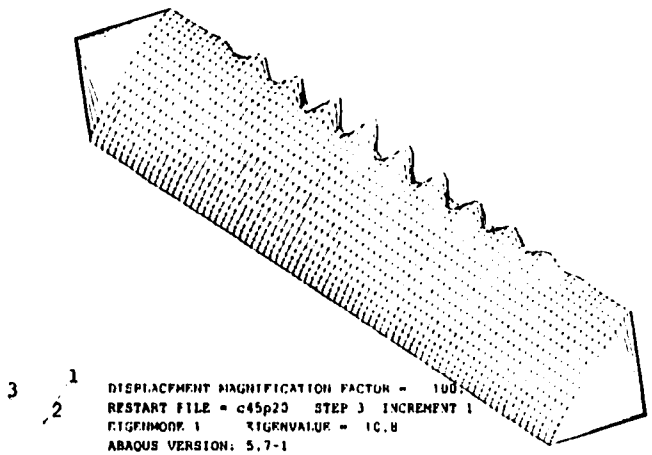

(a) Eigenmode 1

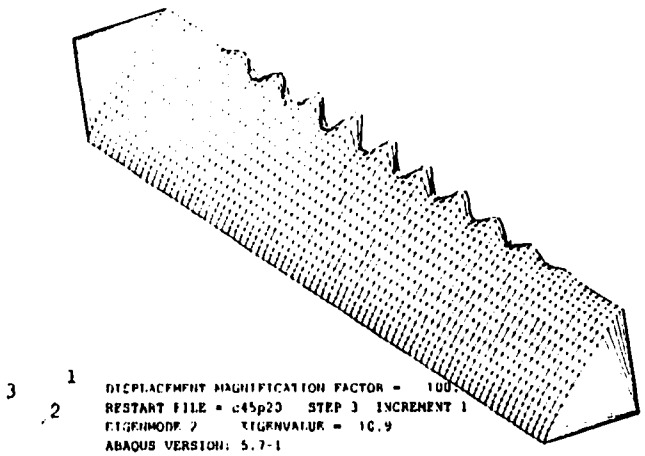

(b) Eigenmode 2

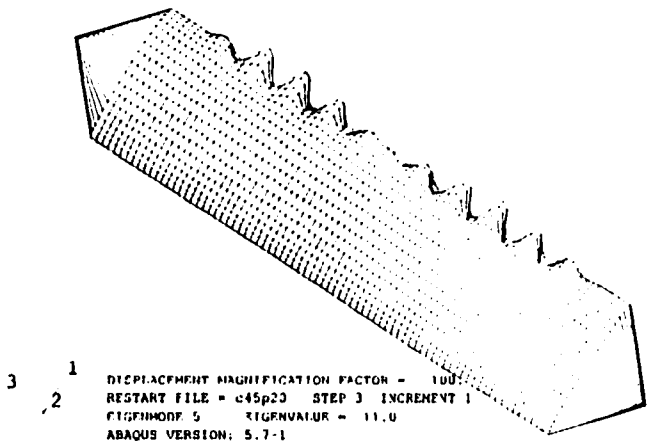

(c) Eigenmode 5

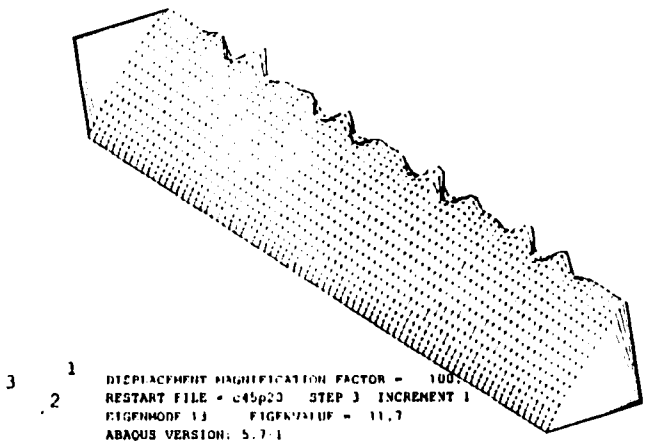

(d) Eigenmode 13

Figure 5.9 Predicted elastic buckling modes for specimen C45P20

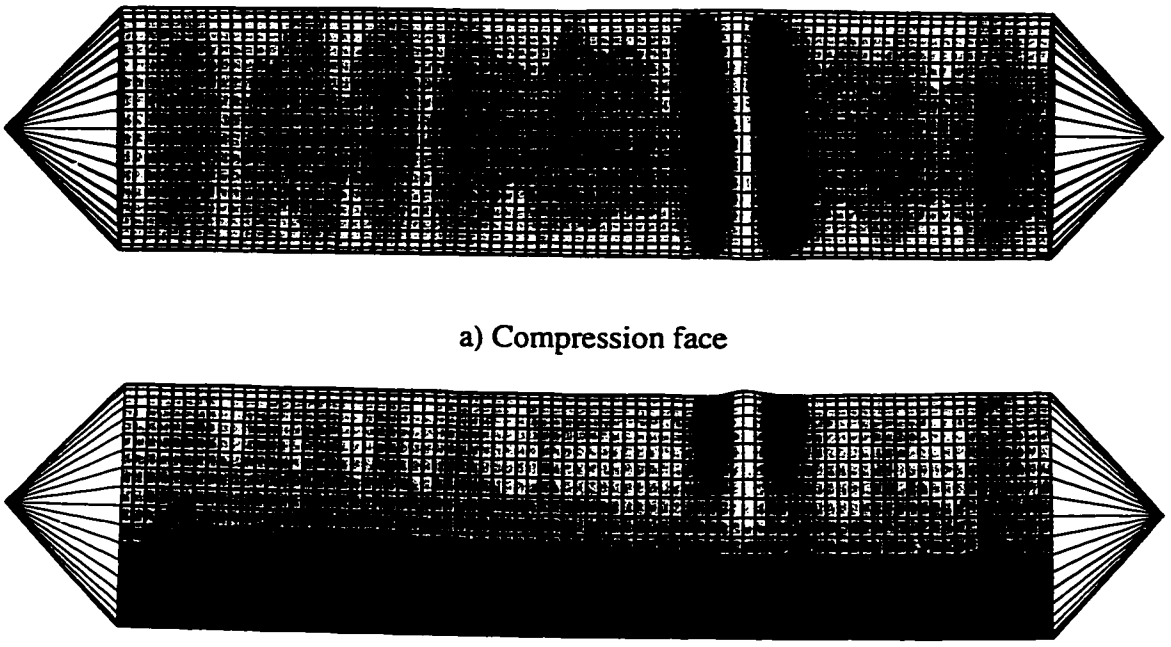

a) Compression face

Bottom Top

b) Profile

Figure 5.10 Predicted buckled configuration for specimen C45P40

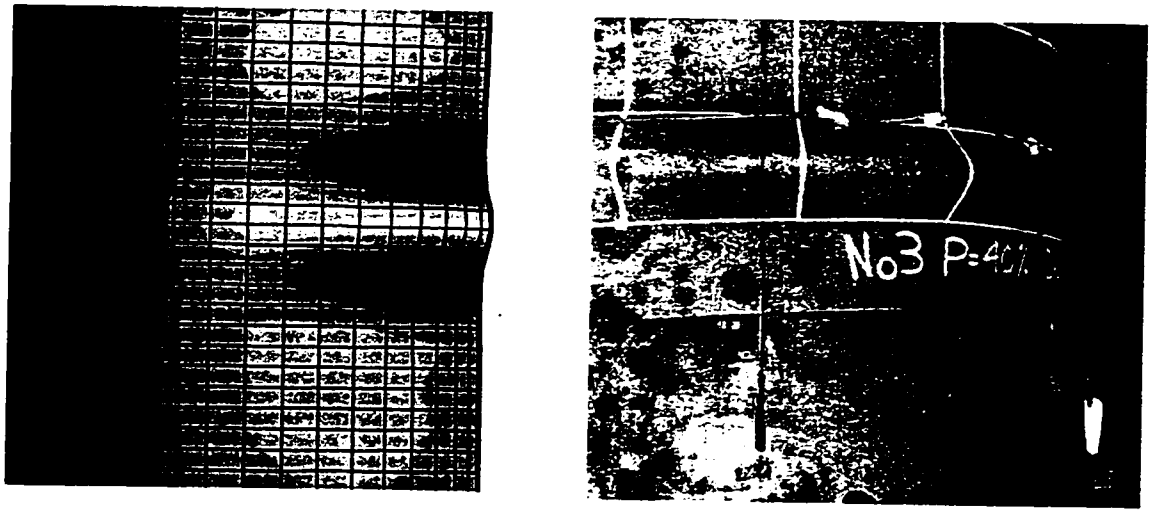

Figure 5.11 Comparison of predicted and experimental configurations for specimen C45P40

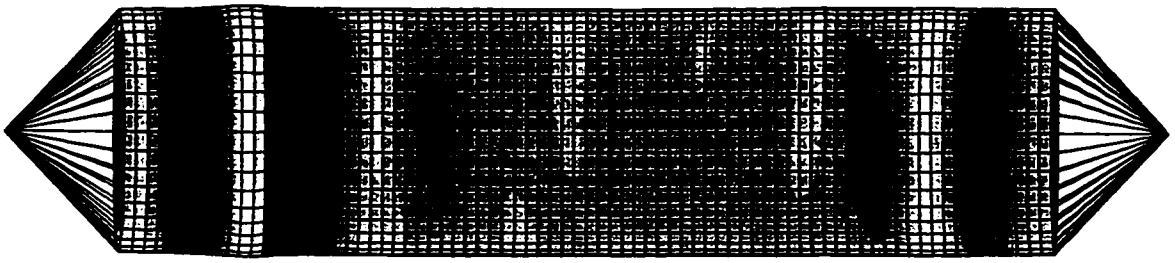

a) Compression face

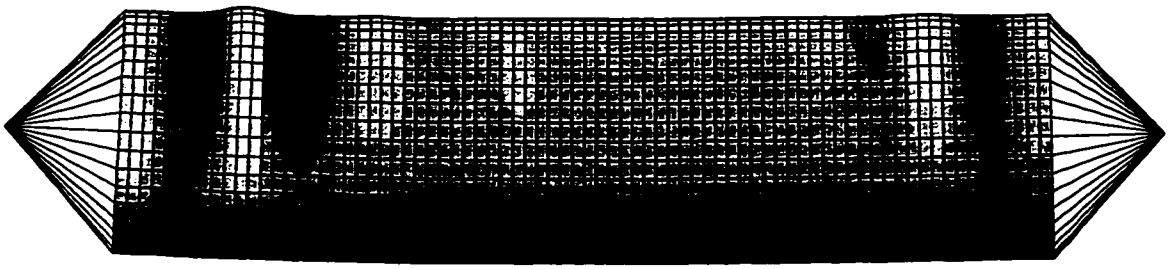

Bottom Top

b) Profile

Figure 5.12 Predicted buckled configuration for specimen C45P80

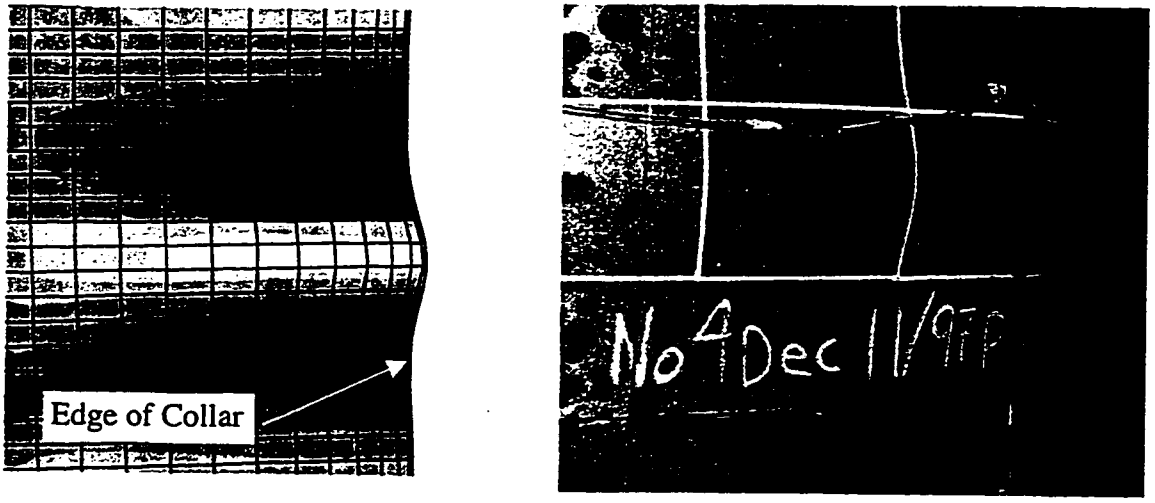

Figure 5.13 Comparison of predicted and experimental configurations for specimen C45P80

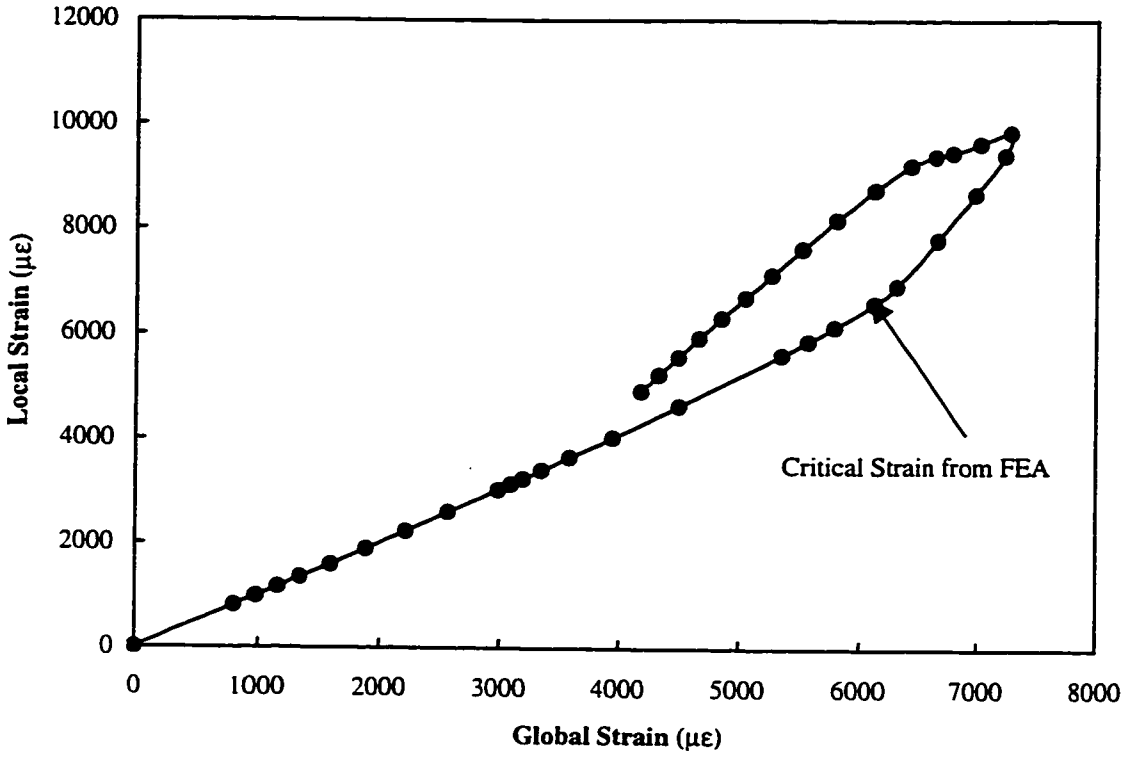

Figure 5.14 C45P00 – Determination of critical compressive strain from FEA

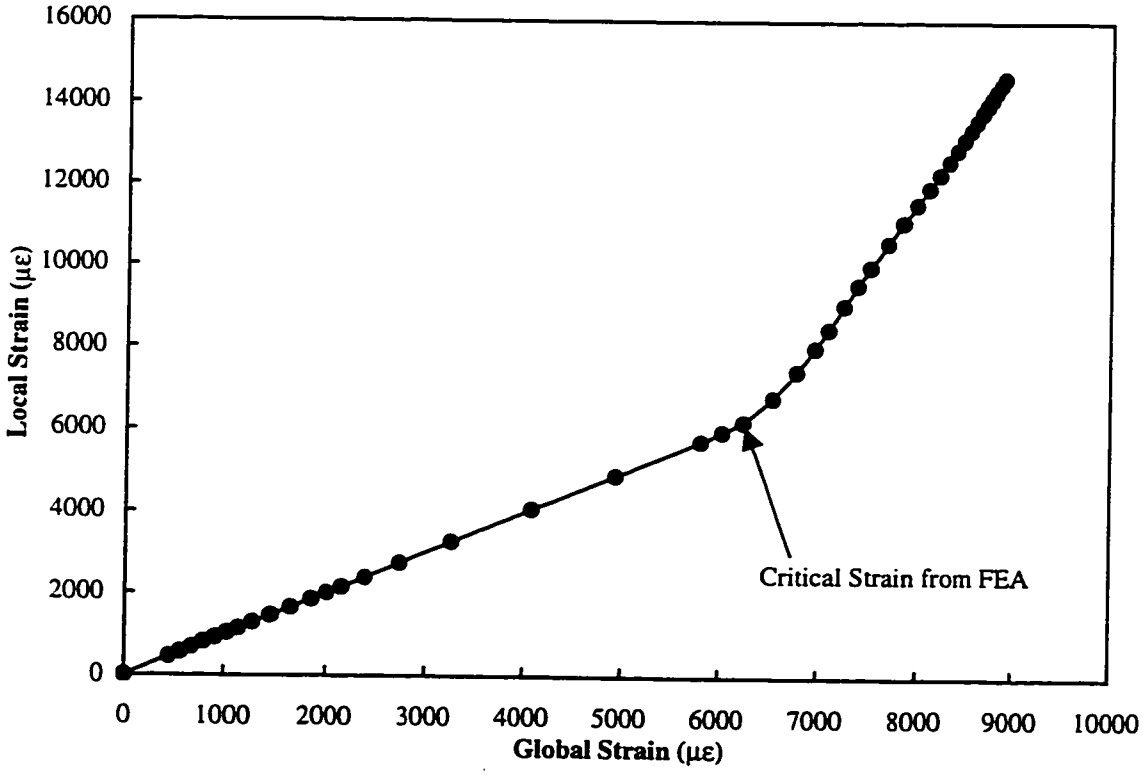

Figure 5.15 C45P20 – Determination of critical compressive strain from FEA

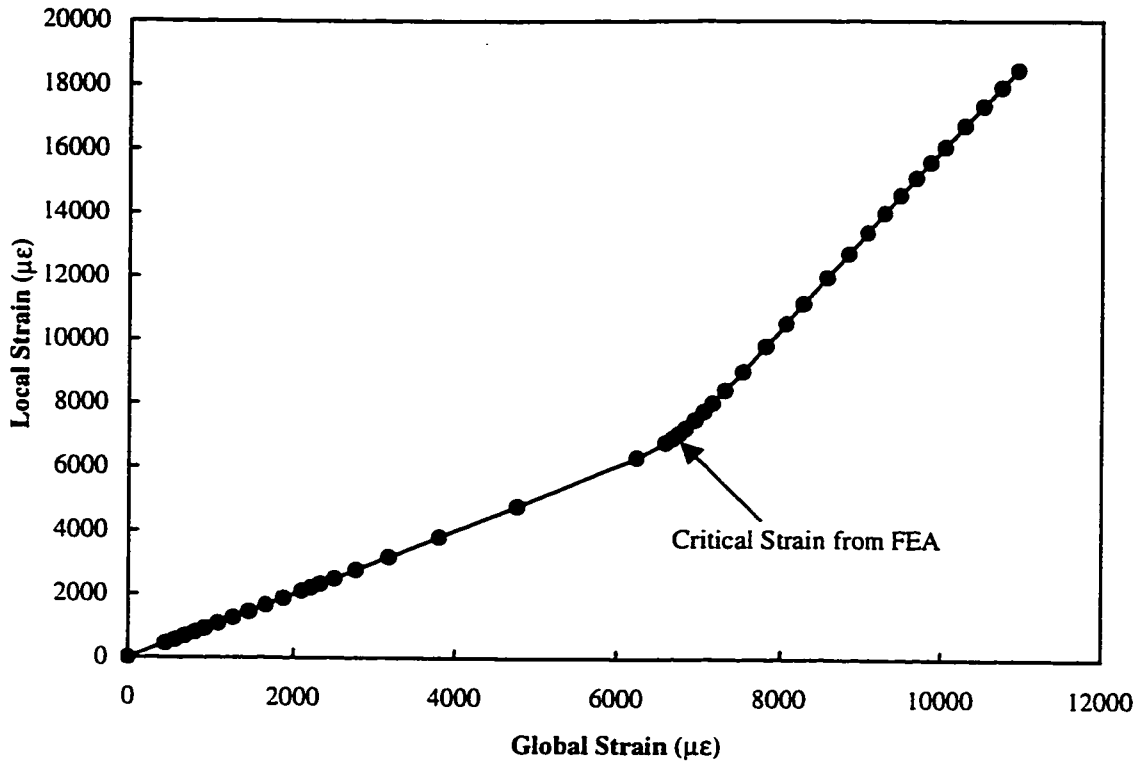

Figure 5.16 C45P40 – Determination of critical compressive strain from FEA

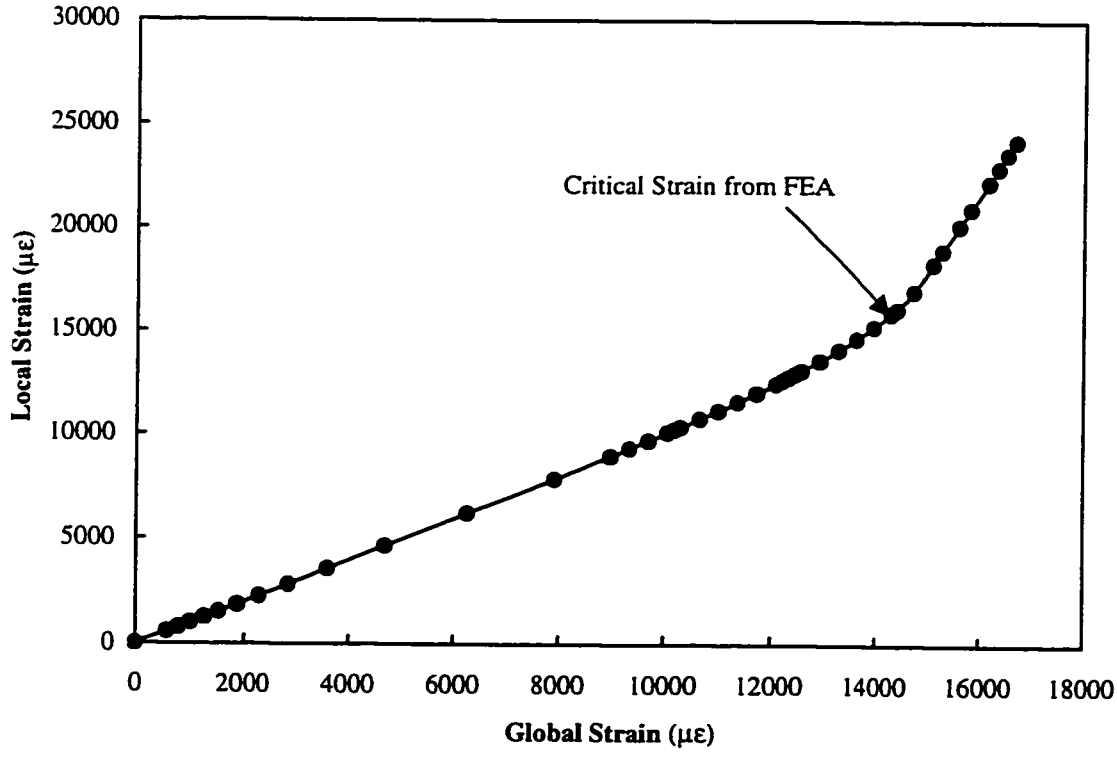

Figure 5.17 C45P80 – Determination of critical compressive strain from FEA

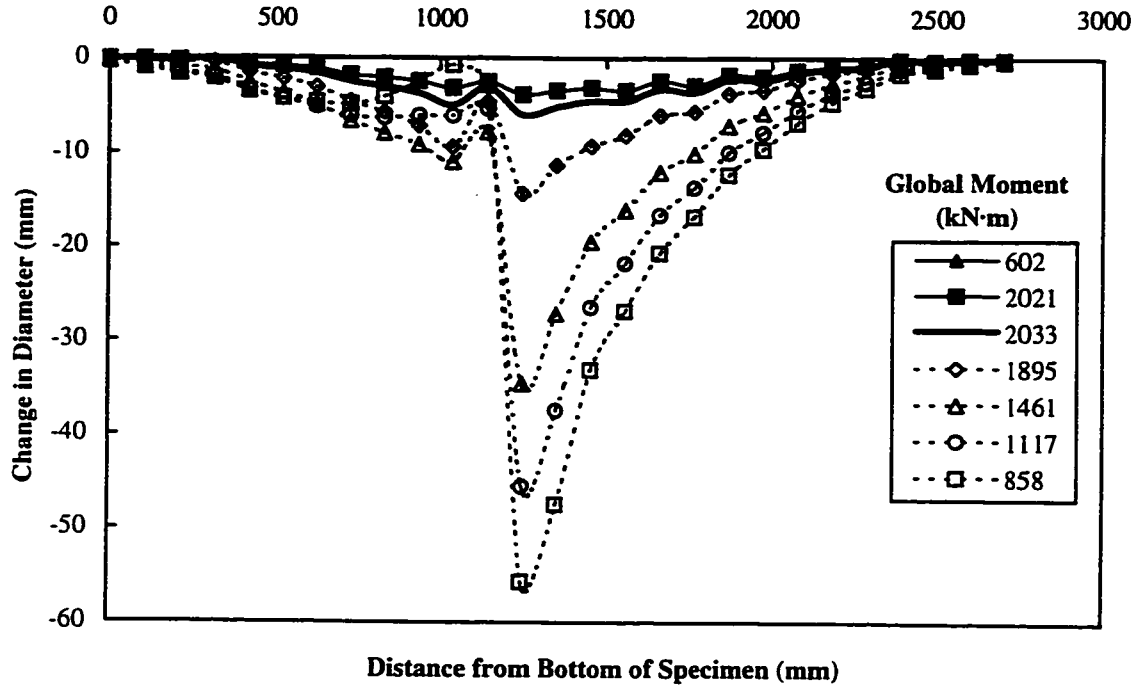

(a) In-plane

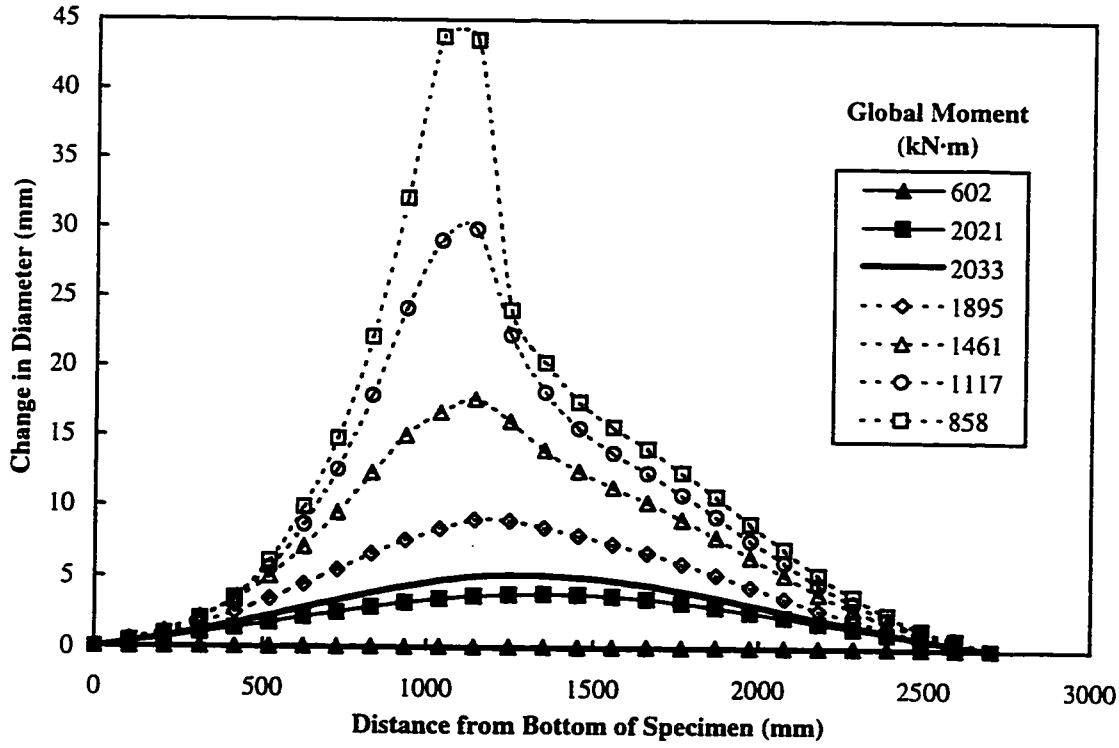

(b) Out-of-Plane

Figure 5.18 C45P00 – Change in diamter results from FEA

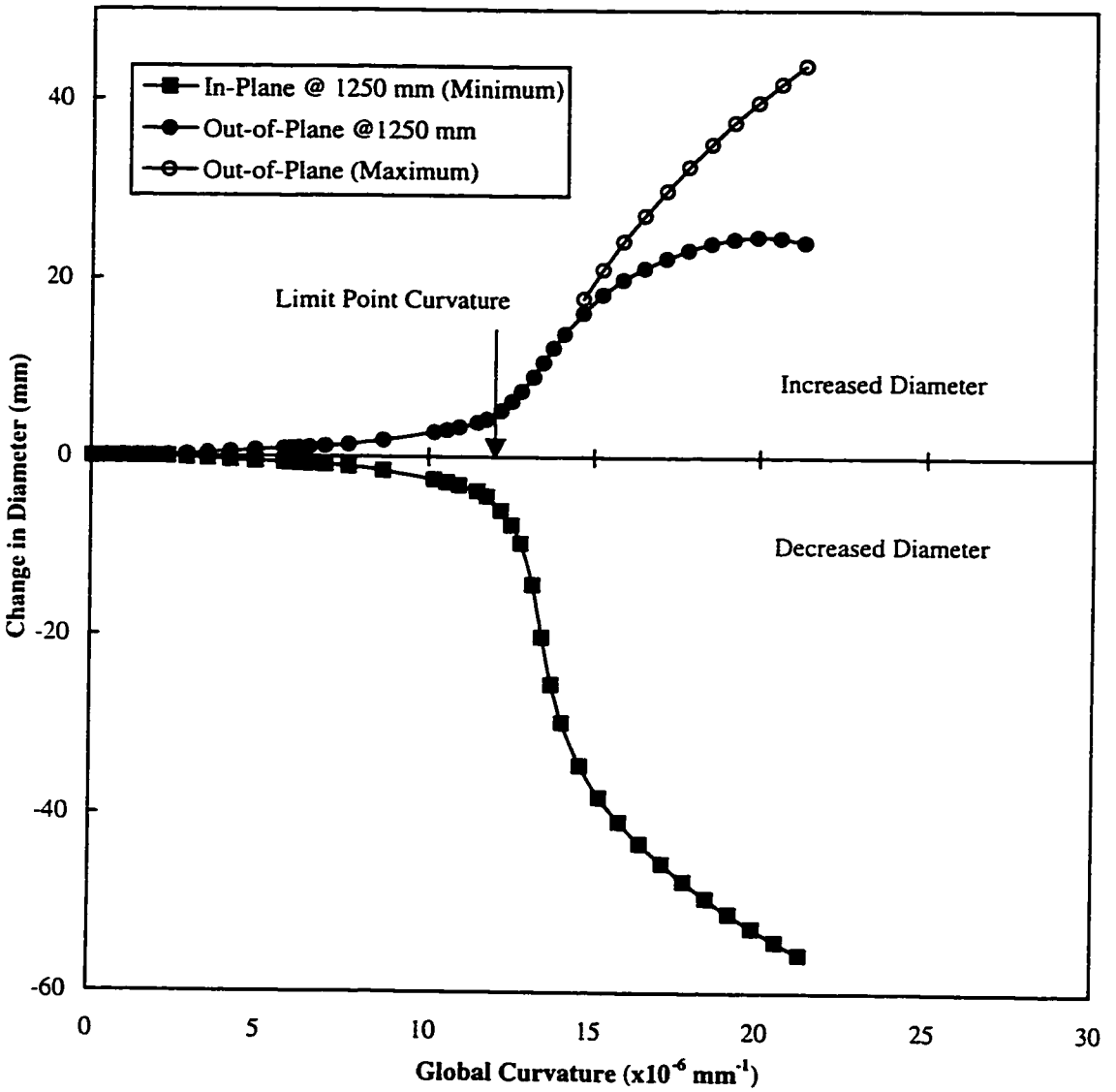

Figure 5.19 C45P00 – Maximum cross-sectional deformations

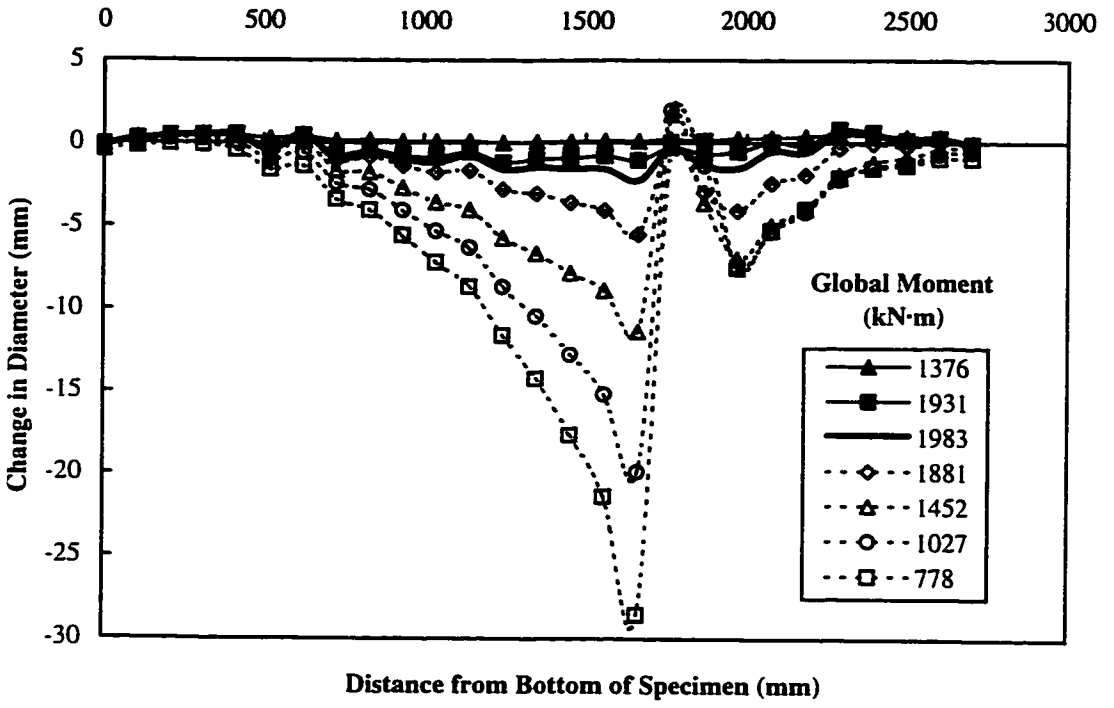

(a) In-plane

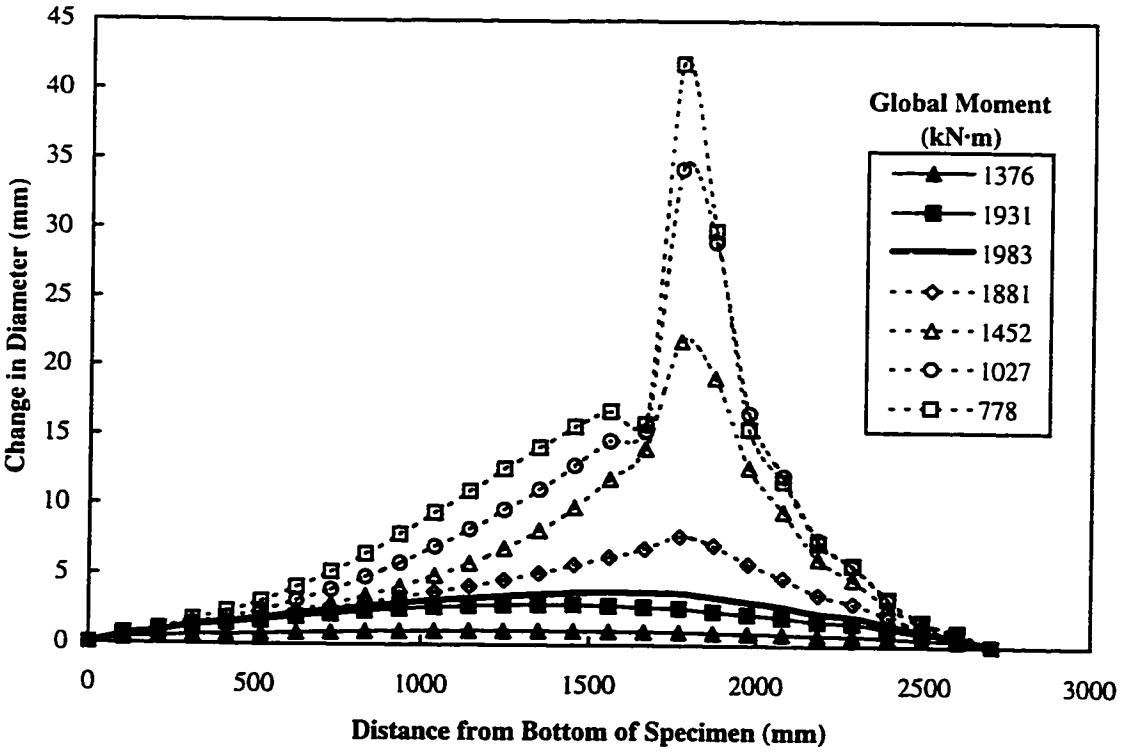

(b) Out-of-Plane

Figure 5.20 C45P20 – Change in diamter results from FEA

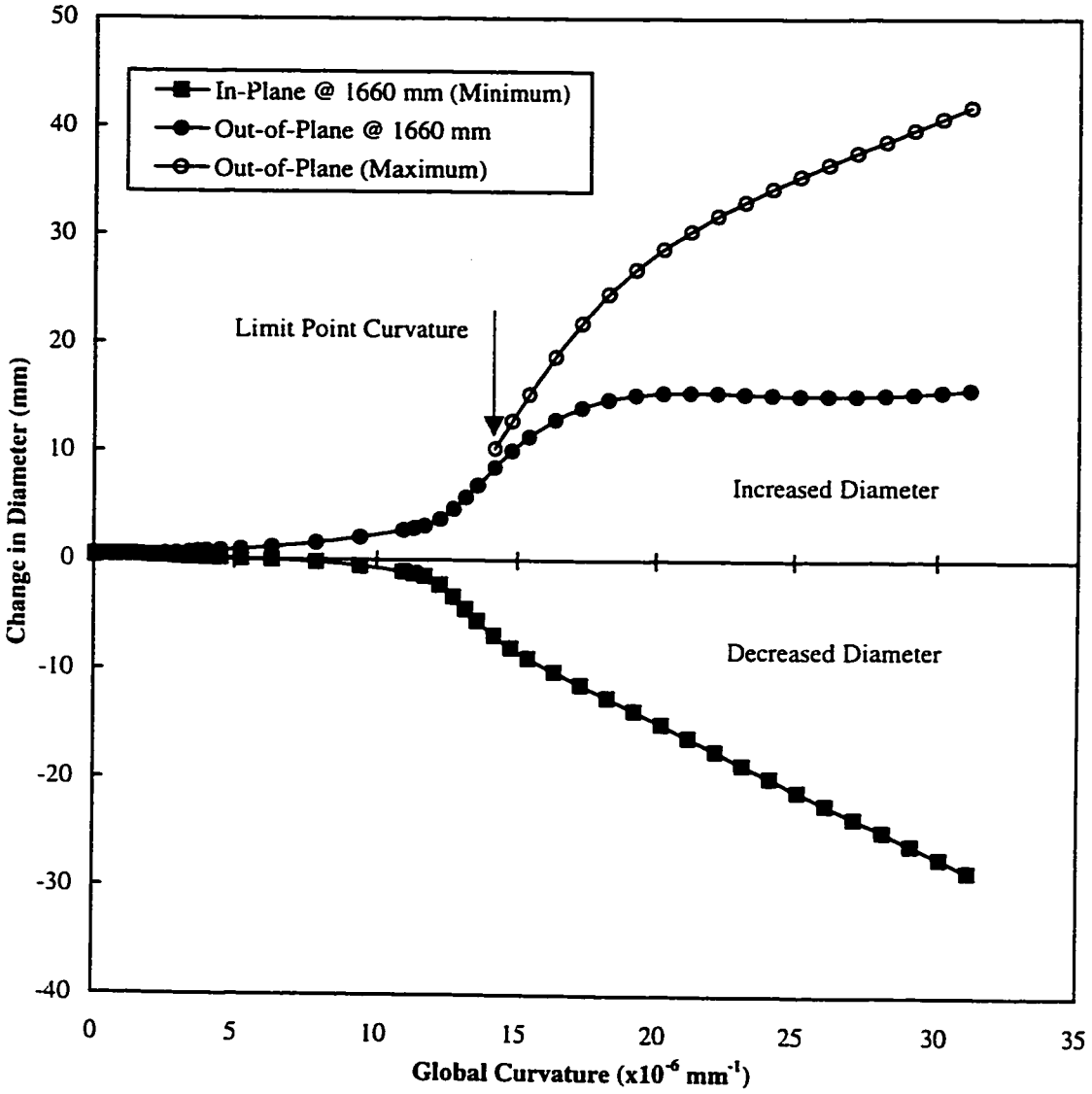

Figure 5.21 C45P20 – Maximum cross-sectional deformations

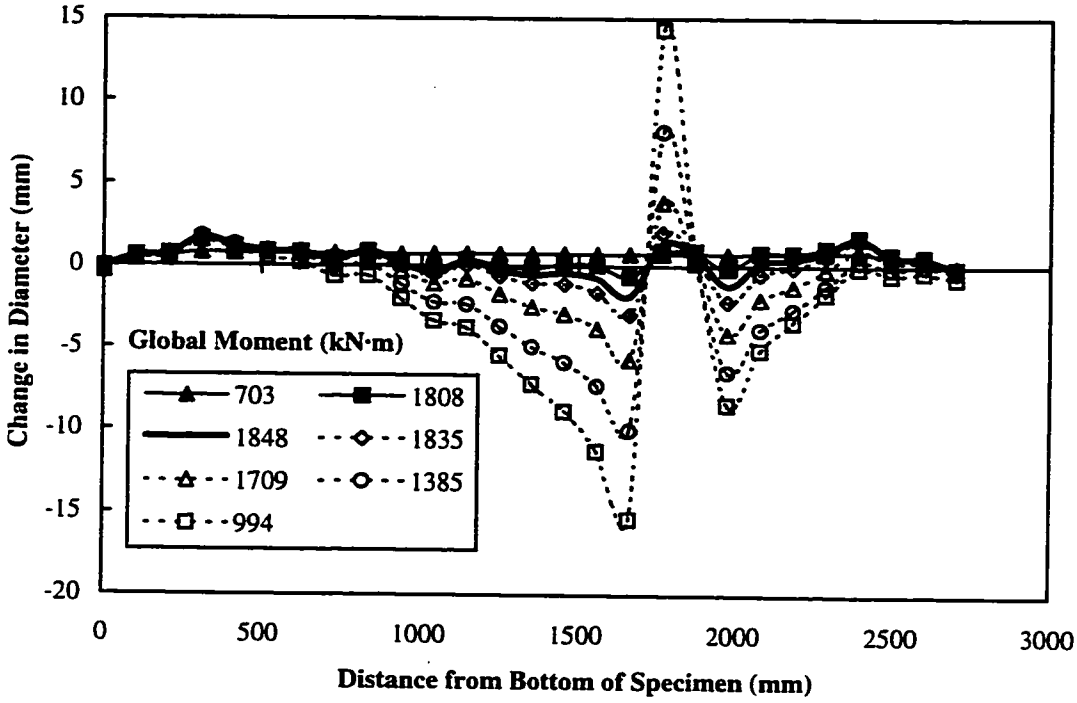

(a) In-plane

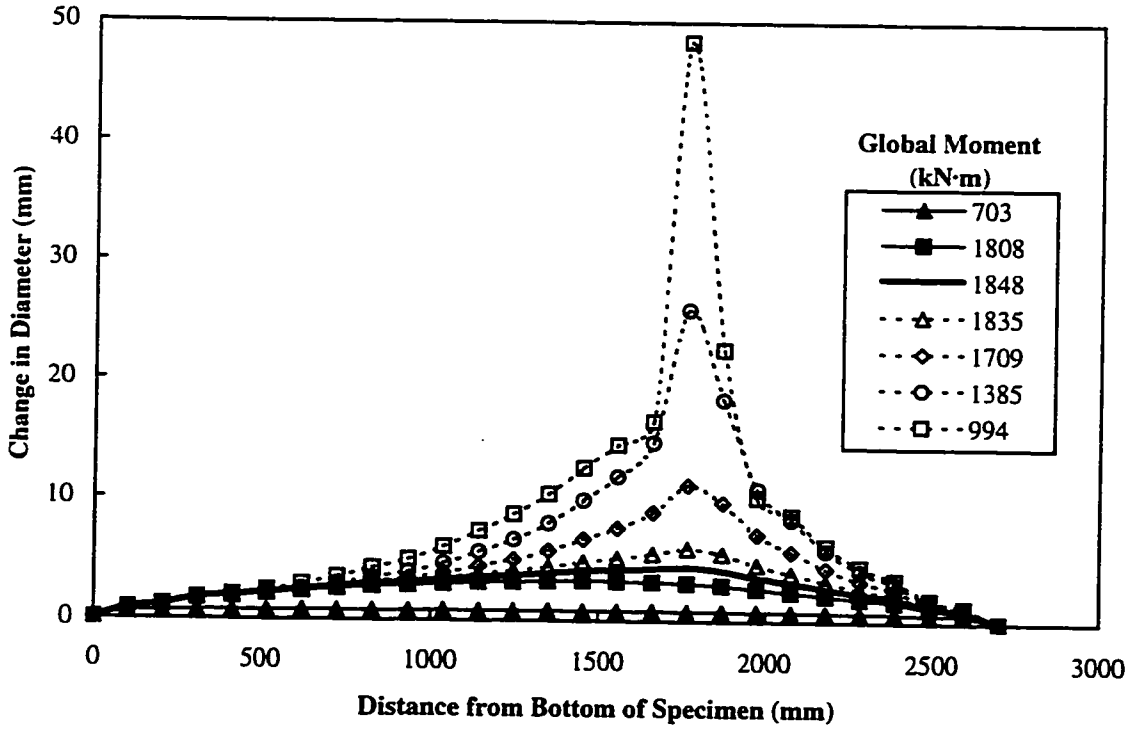

(b) Out-of-Plane

Figure 5.22 C45P40 – Change in diamter results from FEA

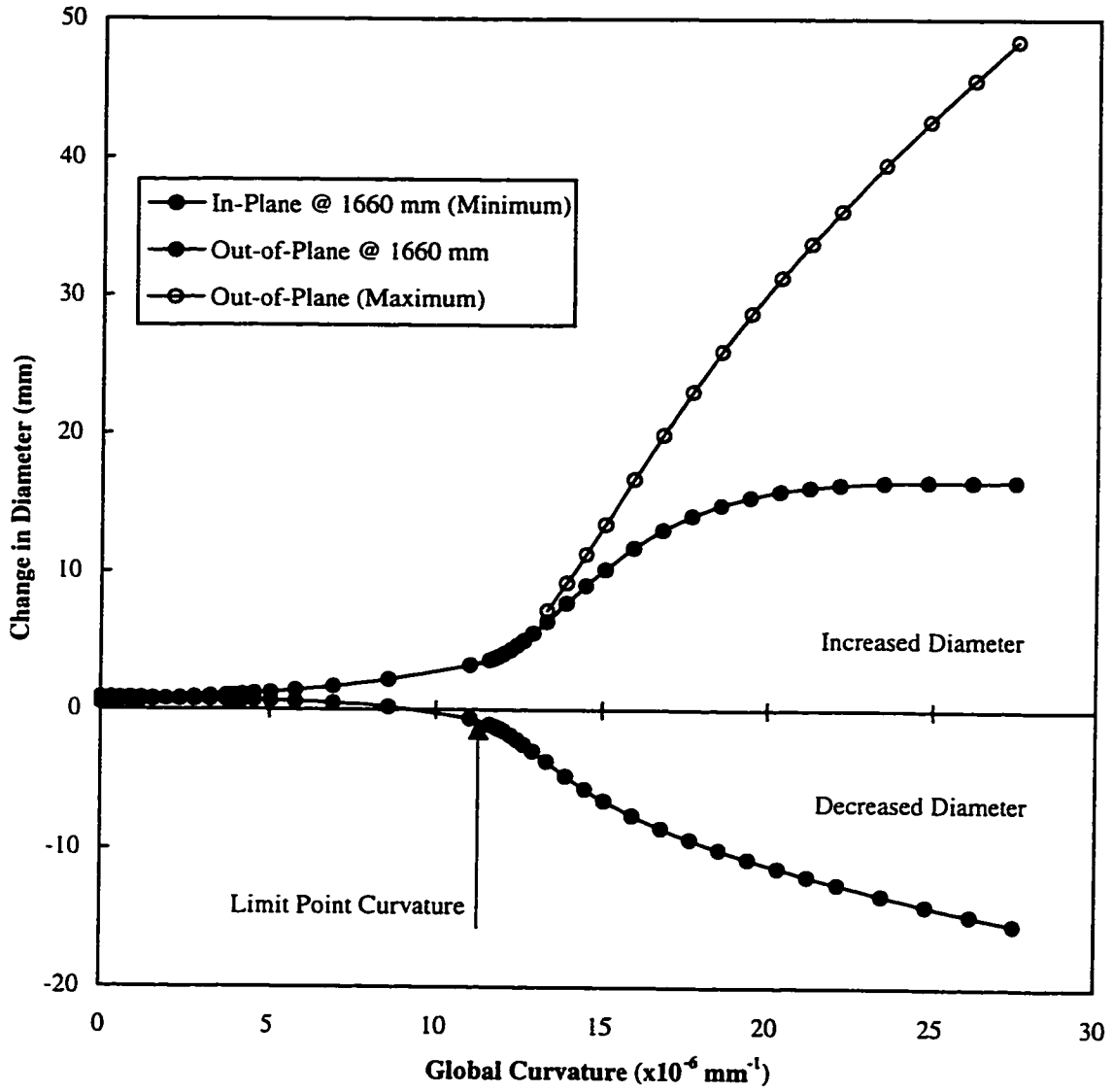

Figure 5.23 C45P40 – Maximum cross-sectional deformations

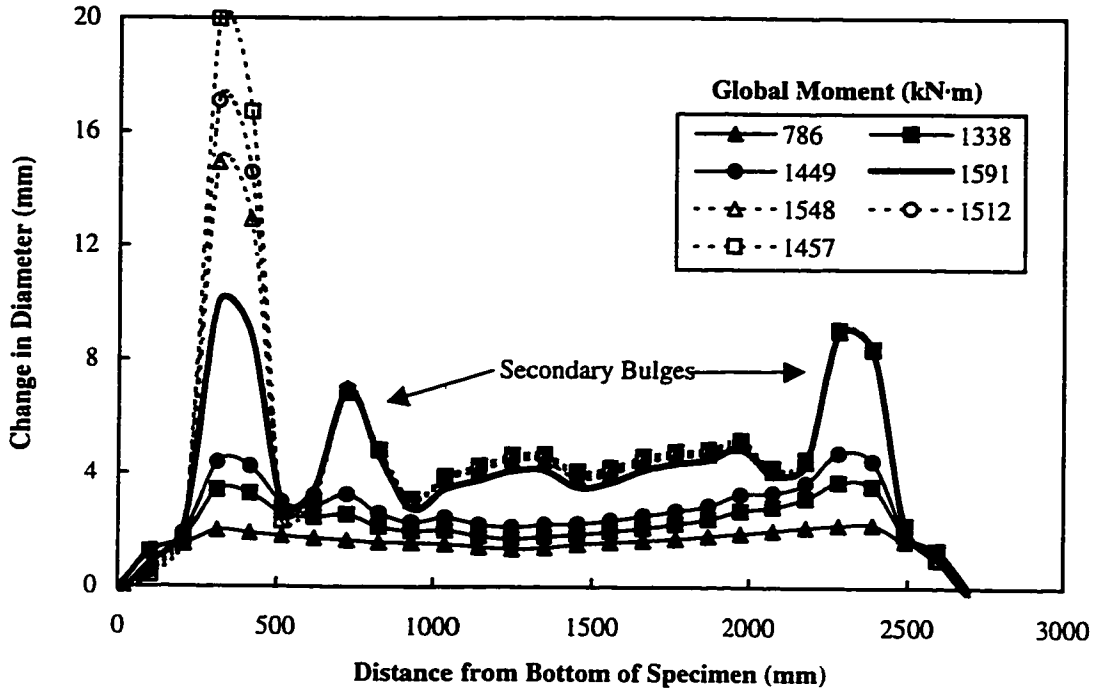

(a) In-plane

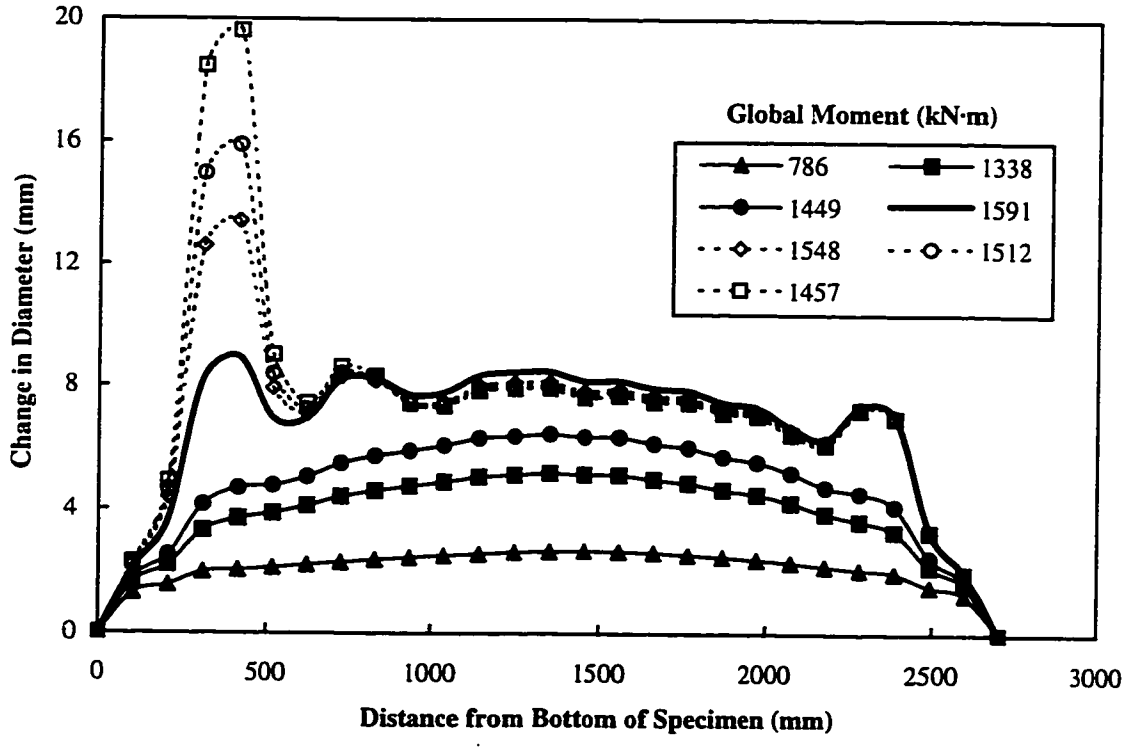

(b) Out-of-Plane

Figure 5.24 C45P80 – Change in diamter results from FEA

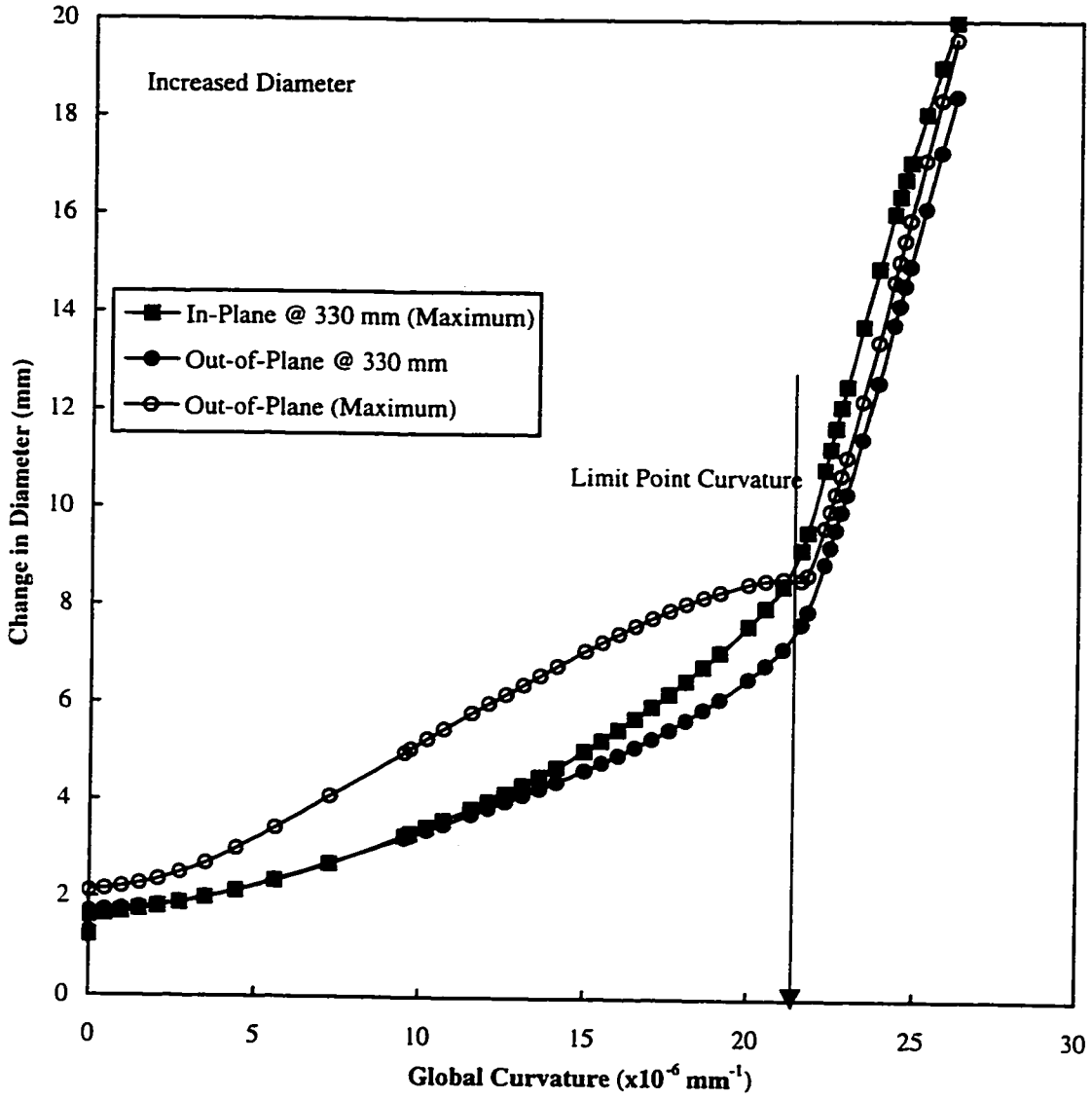

Figure 5.25 C45P80 – Maximum cross-sectional deformations

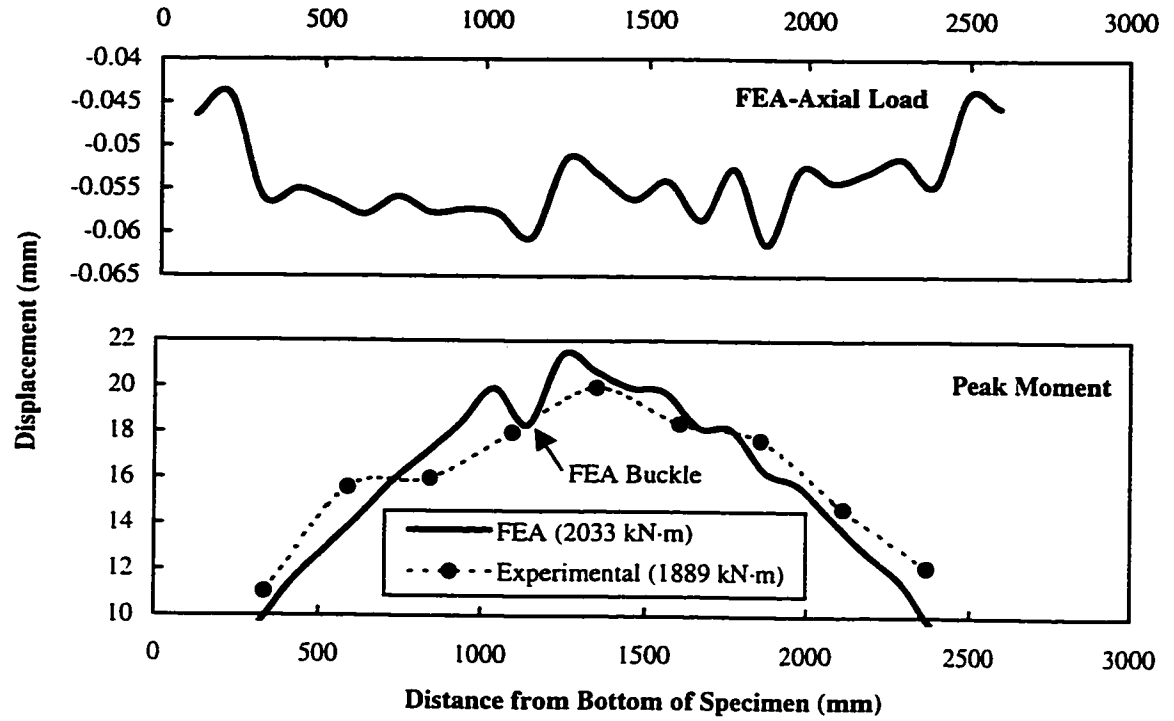

Figure 5.26 C45P00 - Compression face displacements from finite element method

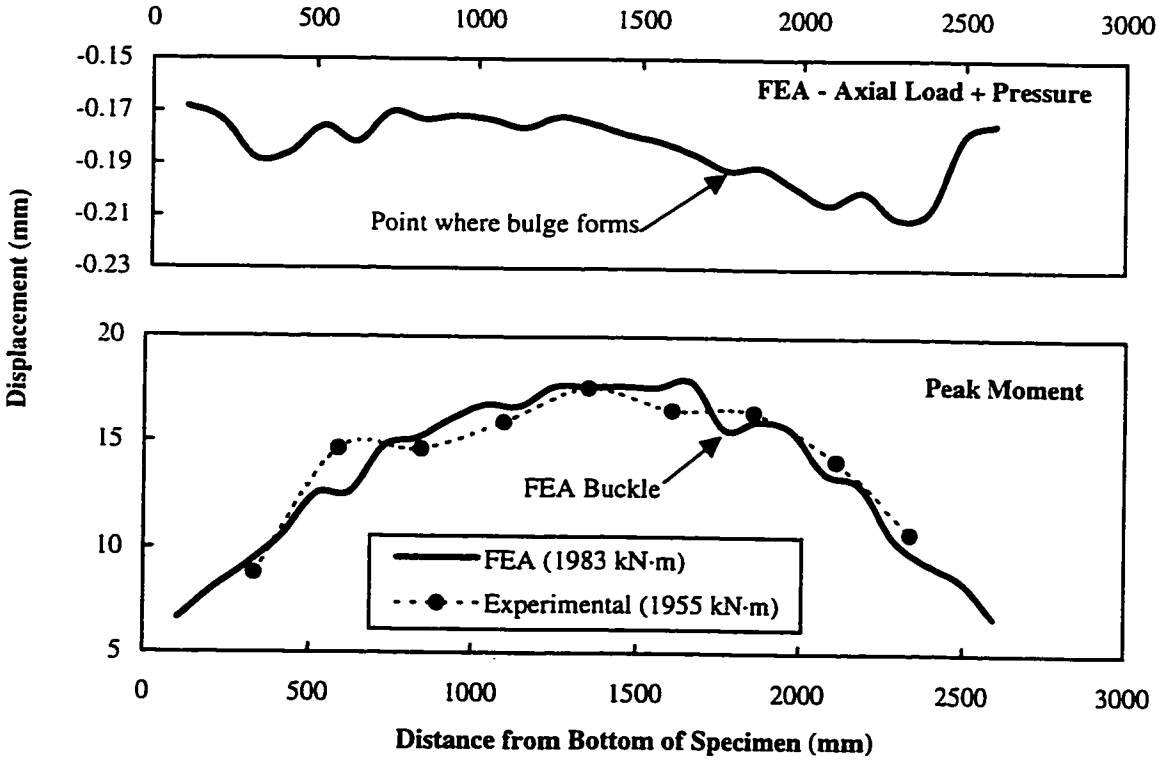

Figure 5.27 C45P20 - Compression face displacements from finite element method

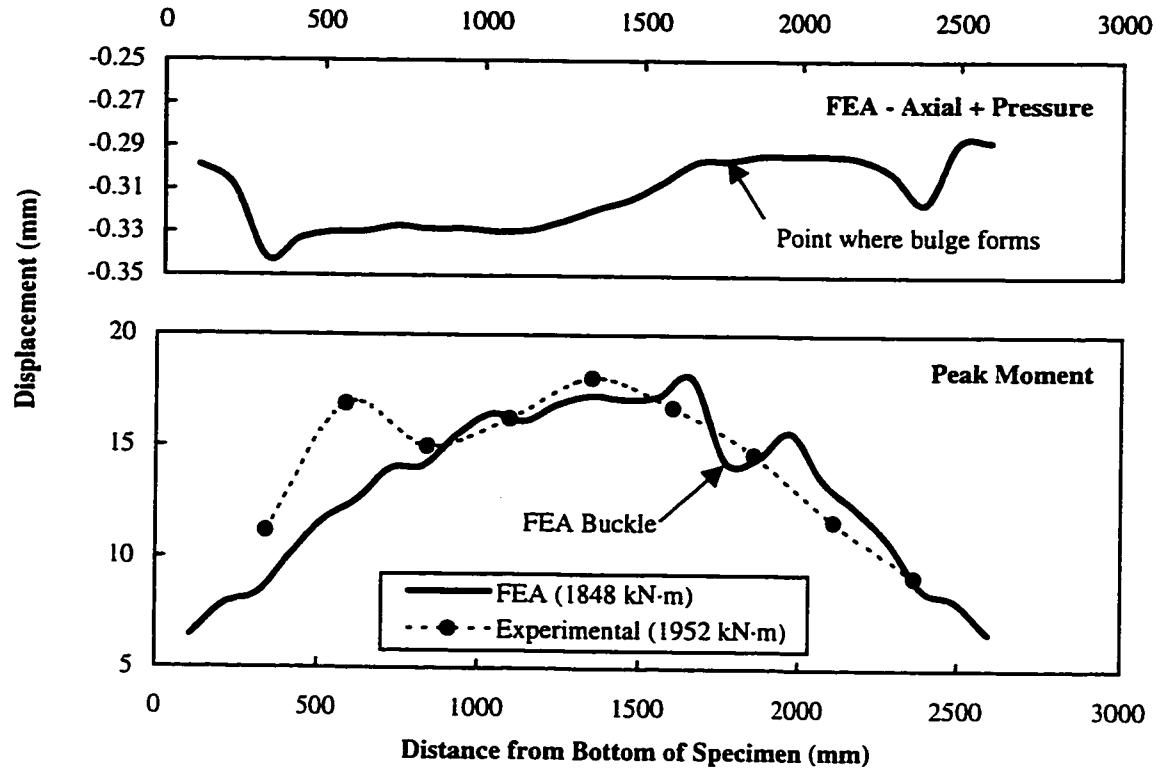

Figure 5.28 C45P40 - Compression face displacements from finite element method

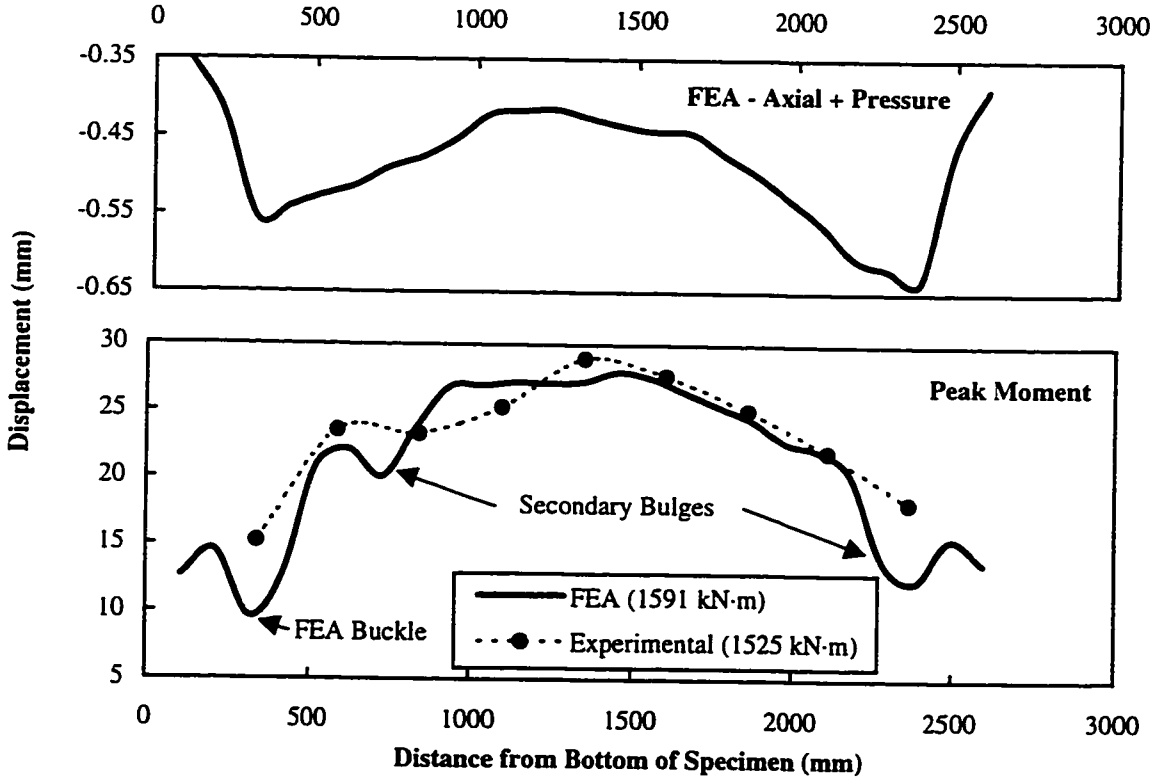

Figure 5.29 C45P80 - Compression face displacements from finite element method

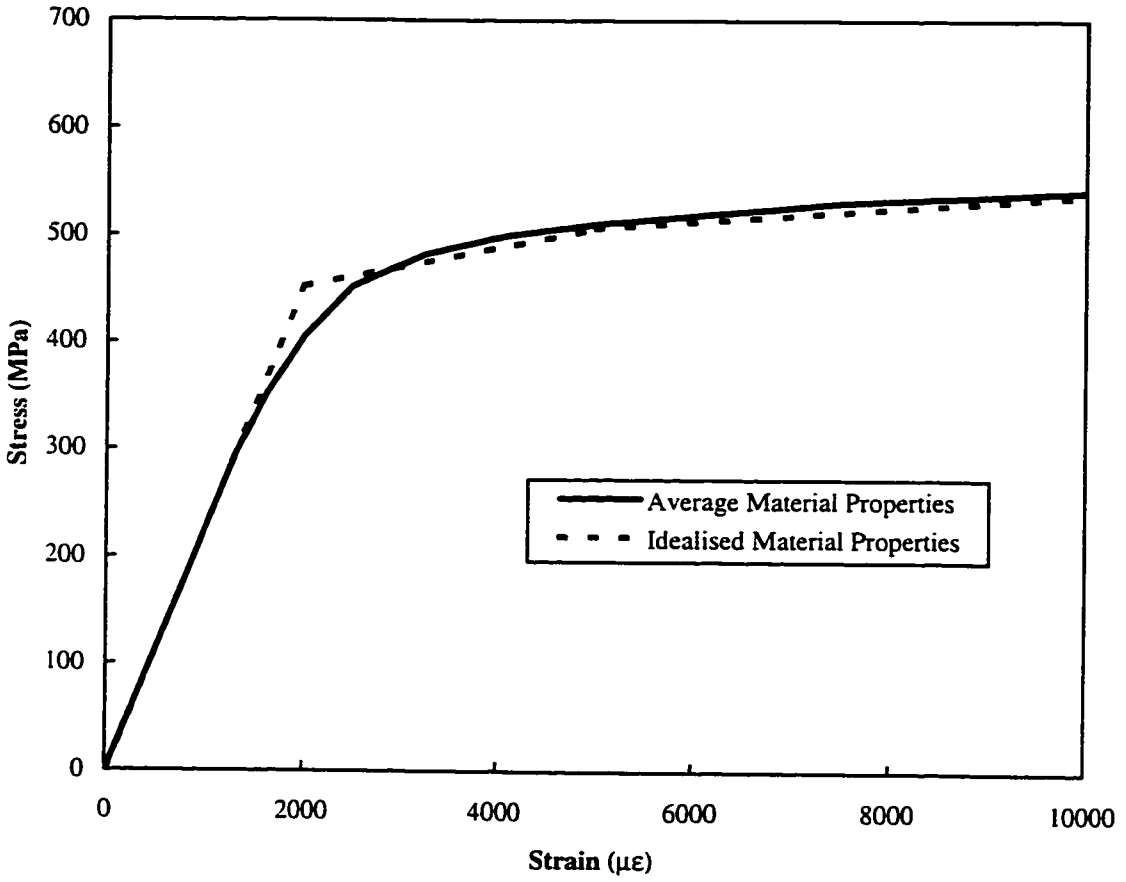

Figure 5.30 Idealized material properties used to study model sensitivity

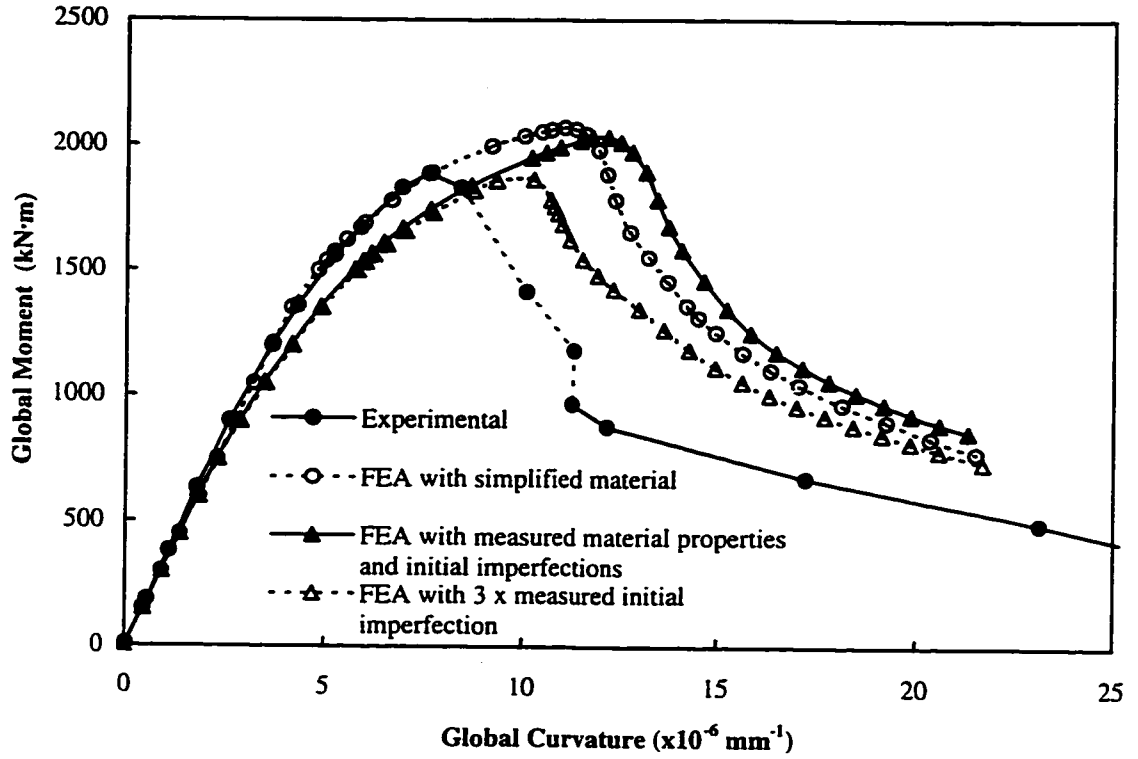

Figure 5.31 Influence of material properties and magnitude of initial imperfections on response of specimen C45P00

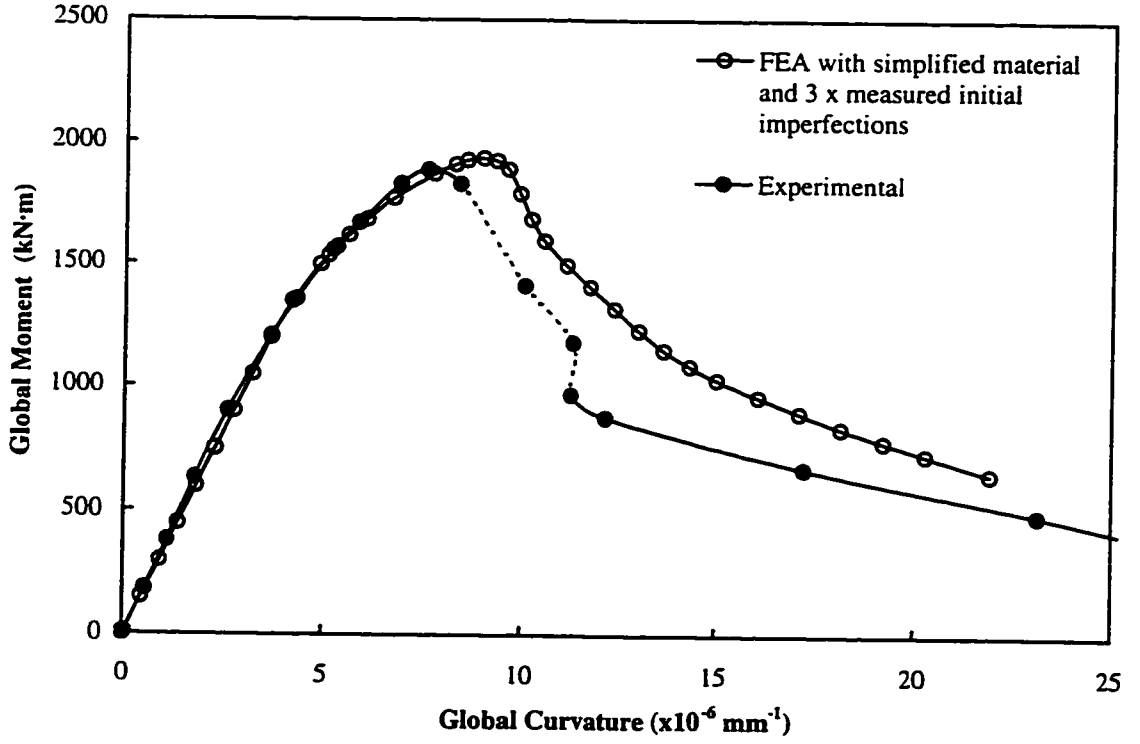

Figure 5.32 Comparison of FEA and experimental

6. CONCLUSIONS AND RECOMMENDATIONS

A series of four full size tests was conducted on pipes with a diameter (762 mm) to thickness (8.3 mm) ratio of 92. The tests were conducted under a combination of loads that are representative of field conditions, namely, internal pressure, axial compression and imposed curvature. The specimens were subjected to internal pressures of 0, 20, 40 and 80 percent pressure causing yield in the hoop direction and a constant axial compression, C_t, equivalent to a temperature difference of 45 degrees Celsius. The test specimens were loaded with end moments until failure. The behaviour of the specimens was recorded with particular attention to deformational aspects. Initial imperfections and material properties were measured to incorporate in a finite element model developed to predict the test results. Analytical studies to determine the effects of mesh size, initial imperfections and variations in material model were also included.

6.1 CONCLUSIONS

1) Two local buckling modes were observed during the test program. The "diamond shape" configuration occurred for the non-pressurized specimen and the "outward bulge" configuration occurred in all the pressurized specimens. This is consistent with previous studies on pipes with lesser D/t values (Mohareb *et al.* 1994).

2) To determine more precisely the pressure at which the local buckling mode changes from the "diamond shape" to the "outward bulge" configuration specimens were tested at 0.0, 0.2, 0.4 and 0.8 p_y. These tests indicate that only small levels of internal pressure are necessary to produce an outward bulge local buckling mode. Specimen C45P20, tested at an internal pressure of 0.20 p_y, failed in the single outward bulge mode whereas specimen C45P00, tested with no internal pressure, failed in the "diamond' shape mode.

3) Compression face strain and displacements measurements on the pressurized specimens showed the development of end bulges during the application of internal pressure and axial load. These bulges, caused by the restraints at the ends of the

specimen, are believed to produce the most critical cross-section causing localization of strains and deformations in this region of the pressurized test specimens.

4) In addition to the bulging of the specimens near the collars due to the internal pressure, it is believed that the conditions at the bottom of the specimen were slightly more severe due to the hydrostatic pressure and self-weight of the test specimen causing failure near the bottom support in all pressurized tests.

5) Moment versus curvature response of the test specimens demonstrated the stabilizing effect of the internal pressure in the post-buckling range. The global curvatures at local buckling and the critical compressive strains also show a general increase with an increase in internal pressure.

6) Specimens subjected to depressurization at an imposed curvature greater than the corresponding limit point curvature for a lower internal pressure did not change configuration during the depressurization cycle.

7) Measured yield strength in the circumferential direction using flattened tension coupon tests was slightly higher than yield strength obtained from longitudinal tension coupon tests. However, the flattening process may modify the stress versus strain behaviour of the circumferential coupon tests. Since the material properties did not differ significantly between the longitudinal and the circumferential directions, the average of the two sets of material properties was used in an isotropic material model for the finite element analysis.

8) A mesh study was performed to determine a suitable mesh size for the finite element model. Since no initial imperfections in geometry were included in the mesh study, the post-buckling configuration was that of the symmetric "diamond shape". A mesh size of 40 elements around the circumference and 78 elements along the length was found to be adequate.

9) The presence of initial imperfections was found to cause important reductions in the limit point curvature and a modest reduction in moment capacity. The analysis showed that imperfections dictate the location of local buckle formation and the mode causing an unsymmetrical "diamond" mode instead of a symmetrical "diamond" mode for a non-pressurized specimen.

10) The global moment versus curvature relationship, post-buckling configuration and critical compressive strains obtained from the analysis were compared to the experimental results to validate the finite element models. Prediction of moment capacity was excellent; predicted curvatures were high, as were critical compressive strains. The predicted buckled configurations agreed well with the experiments but the local buckle location was different for specimen C45P20 and C45P40.

11) An eigenvalue buckling analysis performed for the load conditions of test specimen C45P20 found that the difference between the buckling moment of the first and thirteenth mode was approximately 8.3 percent. It was concluded that 1) the load deformation analysis may not converge to the lowest mode; and 2) a slight disturbance in the test specimen may trigger buckling in a different location than predicted by the analytical model.

12) The change in pipe diameter data obtained from the analysis confirmed a slight flattening of the pipe wall in the in-plane direction and expansion in the out-of-plane direction, (ovalization). The presence of internal pressure reduces the flattening of the cross-section. The change in diameter plots for the four test specimens showed remarkable similarities, even between the different local buckling modes.

13) The end collars used in the tests were modelled analytically. Although their resulting disturbances are prominent features for the pressurized test specimens, their effect did

not seem to be as great in the FEA as evidenced by the buckle location of specimens C45P20 and C45P40 away from the ends.

14) For the D/t ratio investigated in this program, the plastic equation does not account for the instability of the pipe prior to a fully plastic cross-section resulting in higher predicted moment capacity values for specimens C45P00, C45P20 and C45P40. A low predicted capacity for C45P80 is believed to result from a lack of strain hardening material properties in the plastic equation.

15) A sensitivity analysis was conducted for specimen C45P00. Small changes in the shape of the stress versus strain relationship resulted in a significant impact on the overall response of the specimen. Initial imperfections greater than the measured values were attempted and found to give better correlation with the experimental data.

6.2 RECOMMENDATIONS

Several areas of interest were identified as needing further attention. The following list includes recommendations for future work and improvements to the testing and analysis of buried pipelines subjected to combined loads.

1) A comprehensive method needs to be developed that can determine representative material properties in the circumferential direction. Investigation of the possible difference between the compression and tension material response is recommended.

2) The effects of initial imperfections should be investigated analytically including the magnitude and distribution as well as their interaction with parameters such as internal pressure and material properties. The effect of large initial imperfections such as those resulting from the cold bending of pipes in the field should also be investigated.

3) For practical reasons, the initial imperfections used in this investigation were measured before the end plates were welded to the specimens. The welding

distortions were assumed to be negligible. A technique for measuring the initial imperfections following welding of ends of the test specimens is required to test the validity of the assumption made in this program. This is considered increasingly critical for larger D/t pipe.

4) Experimental measurement techniques for curvature, strain, overall displacement, and cross-sectional deformations should ideally model field measurement techniques. This would facilitate a direct comparison between laboratory observations and field data.

5) The influence of welds on the behaviour of pipelines has not been investigated adequately. The weld location, with respect to the extreme fibre for longitudinal, spiral and girth welds should be considered.

6) The end conditions used for experimental testing should be investigated further to determine conditions that have a negligible impact on the pipe behaviour and local buckle formation. In order to minimize the effect of end conditions on local buckling, it is recommended to increase the length of the test specimens so that the second order effects at mid length will be more significant than any possible end effects.

REFERENCES

American Petroleum Institute (1995), *Specification for Line Pipe, API Specification 5L Forty-First Edition*, April.

ASTM Specification A 370 – 94, (1994), *Standard Test Methods and Definitions for Mechanical Testing of Steel Products*, ASTM, March, 1994.

Brazier, L.G., (1927), "On the Flexure of Thin Cylindrical Shells and Other 'Thin Sections'", Proceedings of the Royal Society of London, Series A, Vol. 116 p.104.

Bruschi, R., Monti, P., Bolzoni, G., Tagliaferri,R., (1995a), "Finite Element Method as Numerical Laboratory for Analysing Pipeline Response Under Internal Pressure, Axial Load, Bending Moment," Ocean Mechanics and Arctic Engineering, Volume V, Pipeline Technology, ASME, pp 389-401.

Bruschi, R., Spinazze, M., Tomassini, D., Cuscuna, S., Venzi, S., (1995b) "Failure Modes for Pipelines in Landslide Areas," Ocean Mechanics and Arctic Engineering, Volume V, Pipeline Technology, ASME, pp 65-78.

CAN/CSA-Z662-94, (1994), *Oil and Gas Pipeline Systems*, Canadian Standard Association, Toronto, Ontario, M9W 1R3.

Chen, Q., Elwi, A.E., Kulak, G.L., (1993), "Bending Strength of Longitudinally Stiffened Steel Cylinders", Structural Engineering Report No. 192, Department of Civil Engineering, University of Alberta.

Chen, W.F. and Ross, D.A., (1977). "Tests of Fabricated Tubular Columns." Journal of the Structural Division, ASCE, 103(3), pp 619-633.

Chiou, Y.-J., Chi, S.-Y., (1996), "Numerical Modelling for Buckling of Buried Pipelines Induced by Compressive Ground Failure," Journal of the Chinese Institute of Engineers, Vol 19, No. 3, pp 321-332.

Estefen, S.F., Souza, A.P.F., Alves, T.M.J., (1995), "Comparison Between Limit State Equations for Deepwater Pipelines Under External Pressure and Longitudinal Bending," Offshore Mechanics and Arctic Engineering, Vol. V, Pipeline Technology, ASME pp 431-437.

Hibbit, Karlsson, Sorensen Inc. (1995), "ABAQUS 5.6" Users Manual.

Ibrahim, H., MacGregor, J.G, (1994) "Flexural Behavior of High Strength Concrete Columns", Structural Engineering Report No. 196, Department of Civil Engineering, University of Alberta.

Karamanos, S.A, Tassoulas, J.L., (1996a) "Tubular Members. I: Stability Analysis and Preliminary Results," Journal of Engineering Mechanics, January, pp 64-71.

Karamanos, S.A, Tassoulas, J.L., (1996b) "Tubular Members. II: Local Buckling and Experimental Verification," Journal of Engineering Mechanics, January, pp 72-78.

Kim, H.O. and Velasco, P. (1988), "Review of Pipe Buckling for Arctic Pipeline Design"" Seventh International Conference on Offshore Mechanics and Arctic Engineering, Houston, Texas, February.

Kyriakides, S. and Ju, G.T., (1992), "Bifurcation and Localization Instabilities in Cylindrical Shells under Bending – I. Experiments", International Journal of Solids and Structures, Vol.29, No 9, pp 1117-1142.

Lay, M.G., (1982), *Structural Steel Fundamentals – An Engineering and Metallurgical Primer*, Australian Road Research Board, Victoria, Australia. pp190-196.

Mohareb, M.E., Elwi, A.E., Kulak, G.L., and Murray, D.W., (1994) "Deformational Behaviour of Line Pipe", Structural Engineering Report No. 202, Department of Civil Engineering, University of Alberta.

RockWare Inc., (1988), "MacGridzo Version 2- Contour Mapping and Base Map Plotting for the Macintosh", User Manual.

Schneider, S.P., (1998), "Flexural Capacity of Pressurized Steel Pipe", Journal of Structural Engineering, March, pp 330-340.

Souza, L.T., Murray, D.W., (1994), "Prediction of Wrinkling Behavior of Girth-Welded Line Pipe," Structural Engineering Report No. 197, Department of Civil Engineering, University of Alberta.

Timoshenko, S.P., Gere, J.M., (1961), *Theory of Elastic Stability*, 2nd Edition, McGraw-Hill. pp

Tseng, W., Lee, C., (1995), "Structural Performance Criteria for Fitness-for-Service Evaluations of Underground Natural Gas Pipelines," Second International Conference on Advances in Underground Pipeline Engineering, June 25-28, Bellevue, Washington.

Workman, G.H., (1988) "Manufacturing Residual Stress Effects on Buried Pipeline Structural Response," Seventh International Conference on Offshore Mechanics and Arctic Engineering, Houston, Texas, February 7-12.

Yoosef-Ghodsi, N., Kulak, G.L., and Murray, D.W., (1994) "Behaviour of Girth-Welded Line Pipe", Structural Engineering Report No. 203, Department of Civil Engineering, University of Alberta.

Zhou, Z. and Murray, D.W., (1993) "Numerical Structural Analysis of Buried Pipelines,", Structural Engineering Report No. 181, Department of Civil Engineering, University of Alberta.

Zimmerman, T.J.E., Stephens, M.J., DeGeer, D.D., Chen,Q, (1995) "Compressive Strain Limits for Buried Pipelines", Offshore Mechanics and Arctic Engineering, Volume V, Pipeline Technology, ASME.

IMAGE EVALUATION
TEST TARGET (QA-3)

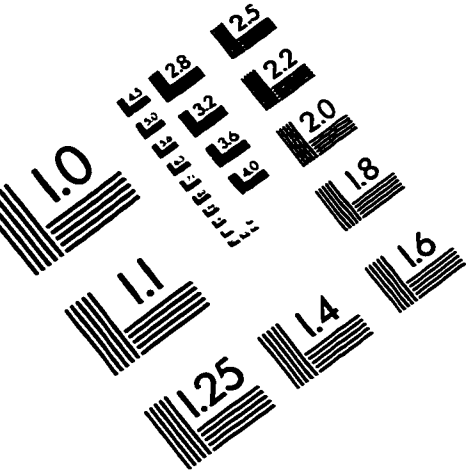

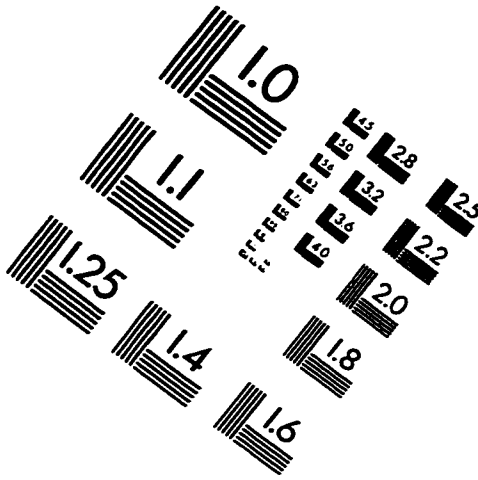

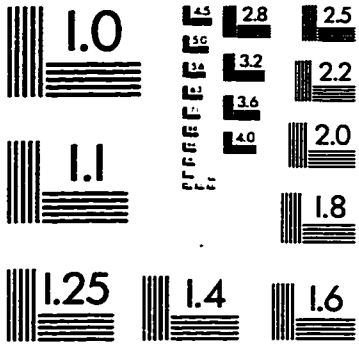

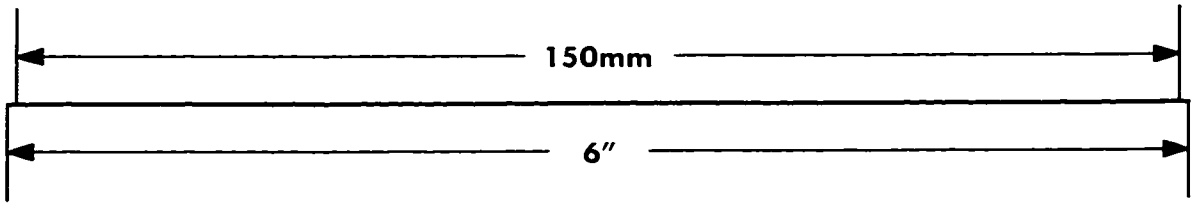

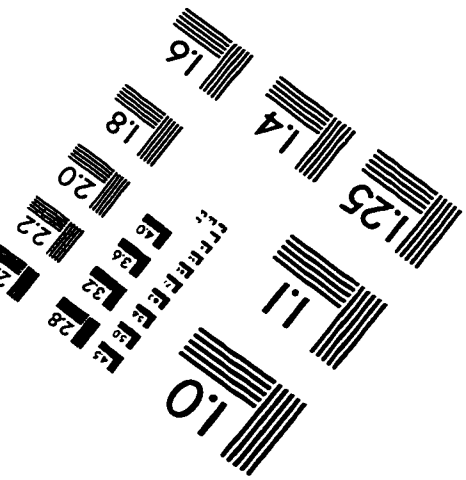

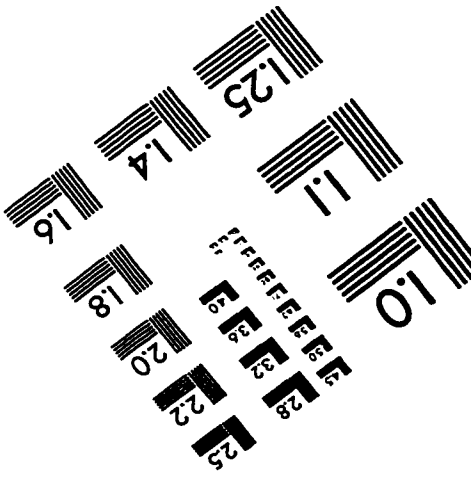

APPLIED IMAGE . Inc
1653 East Main Street
Rochester, NY 14609 USA
Phone: 716/482-0300
Fax: 716/288-5989